

Syracuse University

**SURFACE**

---

Dissertations - ALL

SURFACE

---

12-2013

## Retrieval of Free Space Radiation Patterns through Measured Data in a Non-Anechoic Environment

Weixin Zhao

Follow this and additional works at: <https://surface.syr.edu/etd>



Part of the [Electrical and Computer Engineering Commons](#)

---

### Recommended Citation

Zhao, Weixin, "Retrieval of Free Space Radiation Patterns through Measured Data in a Non-Anechoic Environment" (2013). *Dissertations - ALL*. 10.

<https://surface.syr.edu/etd/10>

This Dissertation is brought to you for free and open access by the SURFACE at SURFACE. It has been accepted for inclusion in Dissertations - ALL by an authorized administrator of SURFACE. For more information, please contact [surface@syr.edu](mailto:surface@syr.edu).

# Abstract

Antenna pattern measurements are usually carried out in an anechoic chamber. However, a good anechoic chamber is very expensive to construct. Previous research has attempted to compensate for the effects of extraneous fields measured in a non-anechoic environment to obtain a free space pattern that would be measured in an anechoic chamber. Existing compensation techniques are like the Test Zone Field compensation method, the Fast-Fourier-Transform-based method, the Matrix Pencil method, and the Antenna Pattern Comparison technique.

This work illustrates and extends a deconvolution methodology which allows the antenna measurement under a non-anechoic test environment and retrieves the free space radiation pattern of an antenna through this measured data; this allows for easier and more affordable antenna measurements.

In this work, we modeled the extraneous fields as the system impulse response of the test environment and utilized a reference antenna to extract the impulse response. Then, we used it to remove the extraneous fields for a desired antenna measured under the same environment and retrieved the ideal pattern. The advantage of this process is that it does not require calculating the time delay to gate out the reflections; therefore, it is independent of the bandwidth of the antenna, and there is no requirement for prior knowledge of the test environment.

This work contributes to the field not by proposing a new methodology for pattern reconstruction but by showing that the deconvolution methodology can analytically remove the effects of extraneous fields in antenna pattern measurements and by extending

this method to antenna pattern measurements under three-dimensional environments. Also, a discussion of the parameters that affect the deconvolution methodology is given in this work. Extensive simulation examples with different environmental settings and with different antennas are presented in this work to demonstrate the applicability of the deconvolution method.

# **Retrieval of Free Space Radiation Patterns through Measured Data in a Non-Anechoic Environment**

By

**Weixin Zhao**

B.S., University of Science and Technology of China, China, 2007

M.S., Syracuse University, USA, 2009

**DISSERTATION**

SUBMITTED IN PARTIAL FULFILLMENT OF THE REQUIREMENTS FOR THE  
DEGREE OF DOCTOR OF PHILOSOPHY IN ELECTRICAL ENGINEERING IN  
THE GRADUATE SCHOOL OF SYRACUSE UNIVERSITY

December 2013

Copyright © Weixin Zhao 2013  
All Rights Reserved

# Acknowledgements

I would like to express my gratitude to several individuals for their great help and support. First of all, I'd like to thank my advisor, Prof. Tapan K. Sarkar for his guidance, patience, and financial support. During my six years of studying with him I was always impressed by his critical thinking, vast knowledge, and attention to detail. And I'd like to thank my co-advisor Prof. Magdalena Salazar Palma for her support and advising in both academic and life. I feel very fortunate to complete this dissertation under their guidance.

I would also like to thank my dissertation committee: Dr. Harvey Schuman, Prof. Jay K Lee, Prof. Tomislav Bujanovic, Prof. Mustafa Cenk Gursoy, and Prof. Shobha K. Bhatia, for serving on the committee despite their tight schedules and their great comments.

I am very thankful to my colleagues in the CEM Lab, Jinhwan Koh, Arijit De, Walid Dyab, Zicong Mei, Latoya Brown, Hongsik Moon, Woojin Lee, Mohammad Abdallah, and Chris Yieung, for helpful discussions with them. Also, great appreciation goes to Daniel García Doñoro, who spent three summers with me in Xi'an working hard on HOBBIES.

Also, I am very lucky to have very good friends like: Zhang Peng, Feng Peijie, Gao Weihua, Sheng Xiang, Jin Chenrui, Li Chaobo, and many others, for their encouragement and help throughout my PhD program. Special thanks go to Chen Yanping, who brings me lots of emotional support.

Last but not least, I would like to express my deepest gratitude to my parents for their love and their sacrifices.

# Table of Contents

<b>List of Figures</b> .....	ix
<b>List of Tables</b> .....	xvi
<b>Abbreviations</b> .....	xvi
<b>1. Introduction</b> .....	1
1.1 Problem Background.....	2
1.2 Originality and Contribution.....	4
1.3 Outlines.....	5
<b>2. Literature Review of Pattern Reconstruction Methodologies</b> .....	7
2.1 Literature Review.....	7
2.2 FFT-Based Method.....	12
<b>3. Deconvolution Method for Radiation Pattern Reconstruction</b> .....	22
3.1 Equations and Derivation.....	23
3.2 Steps Summarized for the Methodology.....	32
3.3 Processing of the Data.....	33
3.4 Simulation Examples.....	36
3.4.1 Example I: One PEC Plate Serves as the Reflector.....	36
3.4.2 Example II: Two PEC Plates Serve as Reflectors.....	44

3.4.3 Example III: Four Connected PEC Plates Serve as Reflectors .....	50
3.4.4 Example IV: Use of a Parabolic Reflector Antenna Serve as the AUT .....	56
<b>4. Discussion on the Deconvolution Method for Radiation Pattern Reconstruction .....</b>	<b>61</b>
4.1 Effect of Different Probe Antennas .....	62
4.1.1 Example I: Use of a Yagi Antenna as the Probe .....	62
4.1.2 Example II: Use of a Parabolic Reflector Antenna as the Probe.....	67
4.1.3 Example III: Use of a Dipole Antenna as the Probe .....	70
4.2 Effect of Different Antenna Size .....	75
4.3 Effect of Different Sizes of PEC Plates.....	82
<b>5. Extension of the Deconvolution Method to Three-Dimensional Pattern Reconstruction.....</b>	<b>90</b>
5.1 Equation and Derivation.....	91
5.2 Steps Summarized for the Methodology .....	95
5.3 Processing of the Data .....	96
5.4 Simulation Examples .....	99
5.4.1 Example I: Four Wide PEC Plates Serve as Reflectors .....	101
5.4.2 Example II: Four PEC Plates and the Ground Serve as Reflectors.....	111
5.4.3 Example III: Six Plates Forming an Unclosed Contour Serve as Reflectors .....	120
5.4.4 Example IV: Antenna Measurement in a Closed PEC Box .....	129
5.4.5 Example V: Six Dielectric Plates Forming a Closed Contour .....	139

<b>6. Conclusion and Future Work</b> .....	147
<b>Appendix A</b> .....	152
<b>Appendix B</b> .....	156
<b>Bibliography</b> .....	159
<b>VITA</b> .....	163

# List of Figures

<b>Figure 1.1</b> Antenna measurement carried out in an anechoic chamber. ....	3
<b>Figure 2.1</b> The radiation pattern measurement system. ....	14
<b>Figure 2.2</b> The radiation pattern measurement model with one PEC plate as the reflector. .....	16
<b>Figure 2.3</b> Dimensions of the helical antenna model with a reflecting plate (AUT). ....	16
<b>Figure 2.4</b> Dimensions of the horn antenna model (Probe). ....	17
<b>Figure 2.5</b> Amplitude pattern of $S_{21}(\phi, f)$ between the helical antenna and the probe. ....	17
<b>Figure 2.6</b> Time domain response corresponding to Figure 2.5. ....	18
<b>Figure 2.7</b> Truncated time domain response. ....	19
<b>Figure 2.8</b> Cleaned pattern of the helical antenna by taking FFT of the truncated time domain response. ....	19
<b>Figure 2.9</b> Amplitude pattern comparison for the helical antenna at 7.6 GHz. ....	20
<b>Figure 2.10</b> Amplitude pattern comparison for the helical antenna at 8.8 GHz. ....	20
<b>Figure 3.1</b> Radiation pattern measurement system diagram. ....	23
<b>Figure 3.2</b> Multiple reflections exist between the AUT and the probe within the azimuth plane. ....	28
<b>Figure 3.3</b> Model of the measurement system with one PEC plate as the reflector. ....	37
<b>Figure 3.4</b> Dimensions of the 6-element yagi antenna model (AUT). ....	37
<b>Figure 3.5</b> Current distribution on the feed dipole of the helical antenna with one PEC plate. ....	38
<b>Figure 3.6</b> Amplitude pattern for the horn antenna with one PEC plate as the reflector. ....	39
<b>Figure 3.7</b> Phase pattern for the horn antenna with one PEC plate as the reflector. ....	40
<b>Figure 3.8</b> Amplitude of the environmental effects when one PEC plate is used as the reflector. ....	40
<b>Figure 3.9</b> Amplitude pattern for the helical antenna with one PEC plate as the reflector. .....	42
<b>Figure 3.10</b> Phase pattern for the helical antenna with one PEC plate as the reflector ...	42
<b>Figure 3.11</b> Amplitude pattern for the yagi antenna with one PEC plate as the reflector	43

<b>Figure 3.12</b> Phase pattern for the yagi antenna with one PEC plate as the reflector .....	43
<b>Figure 3.13</b> Model of the measurement system with two PEC plates as the reflector.....	44
<b>Figure 3.14</b> Current distribution on the feed dipole of the helical antenna with two PEC plates. ....	45
<b>Figure 3.15</b> Amplitude pattern for the horn antenna with two PEC plates as the reflector. ....	46
<b>Figure 3.16</b> Phase pattern for the horn antenna with two PEC plates as the reflector. ....	47
<b>Figure 3.17</b> Amplitude of the environmental effects when two PEC plates are used as the reflector. ....	47
<b>Figure 3.18</b> Amplitude pattern for the helical antenna with two PEC plates as the reflector. ....	48
<b>Figure 3.19</b> Phase pattern for the helical antenna with two PEC plates as the reflector..	48
<b>Figure 3.20</b> Amplitude pattern for the yagi antenna with two PEC plates as the reflector. ....	49
<b>Figure 3.21</b> Phase pattern for the yagi antenna with two PEC plates as the reflector. ....	49
<b>Figure 3.22</b> Model of the measurement system with four PEC plates as the reflector. ....	50
<b>Figure 3.23</b> Current distribution on the feed dipole of the helical antenna with four PEC plates. ....	51
<b>Figure 3.24</b> Amplitude pattern for the horn antenna with four PEC plates as the reflector. ....	52
<b>Figure 3.25</b> Phase pattern for the horn antenna with four PEC plates as the reflector. ....	52
<b>Figure 3.26</b> Amplitude of the environmental effects when four PEC plates are used as the reflector. ....	53
<b>Figure 3.27</b> Amplitude pattern for the helical antenna with four PEC plates as the reflector. ....	54
<b>Figure 3.28</b> Phase pattern for the helical antenna with four PEC plates as the reflector.	54
<b>Figure 3.29</b> Amplitude pattern for the yagi antenna with four PEC plates as the reflector. ....	55
<b>Figure 3.30</b> Phase pattern for the yagi antenna with four PEC plates as the reflector.....	56
<b>Figure 3.31</b> Model of a parabolic reflector antenna with its feeding component. ....	57
<b>Figure 3.32</b> Amplitude pattern for the parabolic reflector antenna.....	58

<b>Figure 3.33</b> Phase pattern for the parabolic reflector antenna. ....	58
<b>Figure 3.34</b> Amplitude pattern for the new parabolic reflector antenna. ....	60
<b>Figure 3.35</b> Phase Amplitude pattern for the new parabolic reflector antenna. ....	60
<b>Figure 4.1</b> Model of the measurement system with a yagi as the probe. ....	63
<b>Figure 4.2</b> Amplitude pattern for the horn antenna system with a yagi as the probe. ....	64
<b>Figure 4.3</b> Phase pattern for the horn antenna system with a yagi as the probe. ....	64
<b>Figure 4.4</b> Amplitude pattern for the helical antenna with a yagi as the probe. ....	65
<b>Figure 4.5</b> Phase pattern for the helical antenna with a yagi as the probe. ....	65
<b>Figure 4.6</b> Amplitude pattern for the yagi antenna with a yagi as the probe. ....	66
<b>Figure 4.7</b> Phase pattern for the yagi antenna with a yagi as the probe. ....	66
<b>Figure 4.8</b> Model of the measurement system with a parabolic reflector as the probe. ..	67
<b>Figure 4.9</b> Amplitude pattern for the horn antenna with a parabolic reflector as the probe. .....	68
<b>Figure 4.10</b> Phase pattern for the horn antenna with a parabolic reflector as the probe..	68
<b>Figure 4.11</b> Amplitude pattern for the parabolic reflector antenna with a parabolic reflector as the probe. ....	69
<b>Figure 4.12</b> Phase pattern for the parabolic reflector antenna with a parabolic reflector as the probe. ....	69
<b>Figure 4.13</b> Model of the measurement system with a dipole as the probe. ....	70
<b>Figure 4.14</b> Amplitude pattern for the horn antenna with a dipole as the probe. ....	71
<b>Figure 4.15</b> Phase pattern for the horn antenna with a dipole as the probe. ....	71
<b>Figure 4.16</b> Amplitude pattern for the helical antenna with a dipole as the probe. ....	72
<b>Figure 4.17</b> Phase pattern for the helical antenna with a dipole as the probe. ....	72
<b>Figure 4.18</b> Amplitude pattern for the yagi antenna with a dipole as the probe. ....	73
<b>Figure 4.19</b> Phase pattern for the yagi antenna with a dipole as the probe. ....	73
<b>Figure 4.20</b> The new model of the measurement system with four PEC plates. ....	76
<b>Figure 4.21</b> Dimensions of a new horn antenna model (Probe). ....	76
<b>Figure 4.22</b> Dimensions of a new helical antenna model with a reflecting plate (AUT). 76	
<b>Figure 4.23</b> Dimensions of a new 6-element yagi antenna model (AUT). ....	77
<b>Figure 4.24</b> Current distribution on the feed dipole of the helical antenna. ....	78
<b>Figure 4.25</b> Amplitude pattern for the horn antenna with the new model. ....	78

<b>Figure 4.26</b> Phase pattern for the horn antenna with the new model.....	79
<b>Figure 4.27</b> Amplitude of the environmental effects with the new model. ....	79
<b>Figure 4.28</b> Amplitude pattern for the helical antenna with the new model.....	80
<b>Figure 4.29</b> Phase pattern for the helical antenna with the new model. ....	81
<b>Figure 4.30</b> Amplitude pattern for the yagi antenna with the new model. ....	81
<b>Figure 4.31</b> Phase pattern for the yagi antenna with the new model. ....	82
<b>Figure 4.32</b> Comparison of the reconstructed patterns for the helical antenna under different number of PEC plates.....	83
<b>Figure 4.33</b> Comparison of the reconstructed patterns for the Yagi antenna under different number of PEC plates.....	84
<b>Figure 4.34</b> Comparison of the models with different PEC plate widths. ....	86
<b>Figure 4.35</b> Comparison of the reconstructed patterns for the helical antenna under three PEC plate width settings. ....	87
<b>Figure 4.36</b> Comparison of the reconstructed patterns for the yagi antenna under three PEC plate width settings. ....	88
<b>Figure 5.1</b> Multiple reflections exist in the whole spatial domain.....	92
<b>Figure 5.2</b> Model of a new parabolic reflector antenna with its feeding component. ...	100
<b>Figure 5.3</b> Model of the measurement system with four very wide PEC plates.....	101
<b>Figure 5.4</b> Three-dimensional plot of the ideal and non-ideal radiation patterns of the horn antenna.....	102
<b>Figure 5.5</b> Three-dimensional plot of the ideal and non-ideal radiation patterns of the yagi antenna. ....	102
<b>Figure 5.6</b> Three-dimensional plot of the ideal and non-ideal radiation patterns of the parabolic reflector antenna.....	103
<b>Figure 5.7</b> Current distribution on the feed dipole of the yagi antenna with four very wide PEC plates. ....	104
<b>Figure 5.8</b> Current distribution on the feed dipole of the parabolic reflector antenna with four wide PEC plates as the reflector.....	104
<b>Figure 5.9</b> Three-dimensional plot of the reconstructed pattern for the yagi antenna. ...	106
<b>Figure 5.10</b> Three-dimensional plot of the reconstructed pattern for the parabolic reflector antenna.....	106

<b>Figure 5.11</b> Comparison of the reconstructed patterns for the yagi antenna along different phi angles with four wide PEC plates as the reflector. ....	107
<b>Figure 5.12</b> Comparison of the reconstructed patterns for the yagi antenna along different theta angles with four wide PEC plates as the reflector.....	108
<b>Figure 5.13</b> Comparison of the reconstructed patterns for the parabolic reflector antenna along different phi angles with four wide PEC plates as the reflector.....	109
<b>Figure 5.14</b> Comparison of the reconstructed patterns for the parabolic reflector antenna along different theta angles with four wide PEC plates as the reflector. ....	110
<b>Figure 5.15</b> Model of the measurement system with four PEC plates and the ground as the reflector. ....	112
<b>Figure 5.16</b> Three-dimensional plot of the ideal and non-ideal radiation patterns of the horn antenna.....	113
<b>Figure 5.17</b> Three-dimensional plot of the ideal and non-ideal radiation patterns of the yagi antenna. ....	113
<b>Figure 5.18</b> Three-dimensional plot of the ideal and non-ideal radiation patterns of a parabolic reflector antenna.....	113
<b>Figure 5.19</b> Current distribution on the feed dipole of the yagi antenna with four PEC plates and the ground as the reflector. ....	114
<b>Figure 5.20</b> Three-dimensional plot of the reconstructed pattern for the yagi antenna.	115
<b>Figure 5.21</b> Three-dimensional plot of the reconstructed pattern for the parabolic reflector antenna.....	115
<b>Figure 5.22</b> Comparison of the reconstructed patterns for the yagi antenna along different phi angles with four PEC plates and the ground as the reflector. ....	116
<b>Figure 5.23</b> Comparison of the reconstructed patterns for the yagi antenna along different theta angles with four PEC plates and the ground as the reflector. ....	117
<b>Figure 5.24</b> Comparison of the reconstructed patterns for the parabolic reflector antenna along different phi angles with four PEC plates and the ground as the reflector. ....	118
<b>Figure 5.25</b> Comparison of the reconstructed patterns for the parabolic reflector antenna along different theta angles with four PEC plates and the ground as the reflector.....	119
<b>Figure 5.26</b> Model of the measurement system with six PEC plates forming an unclosed contour. ....	121

<b>Figure 5.27</b> Three-dimensional plot of the ideal and non-ideal radiation patterns of the horn antenna.....	122
<b>Figure 5.28</b> Three-dimensional plot of the ideal and non-ideal radiation patterns of the yagi antenna.....	122
<b>Figure 5.29</b> Three-dimensional plot of the ideal and non-ideal radiation patterns of the parabolic reflector antenna.....	122
<b>Figure 5.30</b> Current distribution on the feed dipole of the yagi antenna with six PEC plates as the reflector.....	123
<b>Figure 5.31</b> Three-dimensional plot of the reconstructed pattern for the yagi antenna.	124
<b>Figure 5.32</b> Three-dimensional plot of the reconstructed pattern for the parabolic reflector antenna.....	124
<b>Figure 5.33</b> Comparison of the reconstructed patterns for the yagi antenna along different phi angles with six PEC plates as the reflector.....	125
<b>Figure 5.34</b> Comparison of the reconstructed patterns for the yagi antenna along different theta angles with six PEC plates as the reflector.....	126
<b>Figure 5.35</b> Comparison of the reconstructed patterns for the parabolic reflector antenna along different phi angles with six PEC plates as the reflector.....	127
<b>Figure 5.36</b> Comparison of the reconstructed patterns for the parabolic reflector antenna along different theta angles with six PEC plates as the reflector.....	128
<b>Figure 5.37</b> Model of the measurement system within a closed PEC box.....	130
<b>Figure 5.38</b> Three-dimensional plot of the ideal and non-ideal radiation patterns of the horn antenna (antenna in a closed PEC box).....	131
<b>Figure 5.39</b> Three-dimensional plot of the ideal and non-ideal radiation patterns of the yagi antenna (antenna in a closed PEC box).....	131
<b>Figure 5.40</b> Three-dimensional plot of the ideal and non-ideal radiation patterns of the parabolic reflector antenna (antenna in a closed PEC box).....	131
<b>Figure 5.41</b> Current distribution on the feed dipole of the yagi antenna.....	132
<b>Figure 5.42</b> Three-dimensional plot of the reconstructed pattern for the yagi antenna.	134
<b>Figure 5.43</b> Three-dimensional plot of the reconstructed pattern for the parabolic reflector antenna.....	134

<b>Figure 5.44</b> Comparison of the reconstructed patterns for the yagi antenna along different phi angles (antennas within a closed PEC box). .....	135
<b>Figure 5.45</b> Comparison of the reconstructed patterns for the yagi antenna along different theta angles (antennas within a closed PEC box). .....	136
<b>Figure 5.46</b> Comparison of the reconstructed patterns for the parabolic reflector antenna along different phi angles (antennas within a closed PEC box). .....	137
<b>Figure 5.47</b> Comparison of the reconstructed patterns for the parabolic reflector antenna along different theta angles (antennas within a closed PEC box). .....	138
<b>Figure 5.48</b> Model of the measurement system within a closed box with 6 dielectric plates. ....	140
<b>Figure 5.49</b> Current distribution on the feed dipole of the yagi antenna when the test environment is a closed box with 6 dielectric plates. ....	141
<b>Figure 5.50</b> Comparison of the patterns for the yagi antenna along different phi angles when the test environment is a closed box with 6 dielectric plates. ....	143
<b>Figure 5.51</b> Comparison of the patterns for the yagi antenna along different theta angles when the test environment is a closed box with 6 dielectric plates. ....	144
<b>Figure 5.52</b> Comparison of the patterns for the parabolic reflector antenna along different phi angles when the test environment is a closed box with 6 dielectric plates. ....	145
<b>Figure 5.53</b> Comparison of the patterns for the parabolic reflector antenna along different theta angles when the test environment is a closed box with 6 dielectric plates. ....	146
<b>Figure A.1</b> Data mapping illustration. ....	155
<b>Figure B.1</b> Points of complex roots at the unit circle.....	157

# List of Tables

**Table 4.1** Reconstruction error for the helical antenna in the angular domain at 1.5 GHz  
..... 89

**Table 4.2** Reconstruction error for the yagi antenna in the angular domain at 1.5 GHz . 89

## Abbreviations

APC	Antenna Pattern Comparison
AUT	Antenna under Test
CATR	Compact Antenna Test Range
FDTD	Finite-Difference Time-Domain
FFT	Fast Fourier Transform
FMM	Fast Multipole Method
MoM	Method of Moments
MPM	Matrix Pencil Method
NAPC	Novel Antenna Pattern Comparison
OGT	Oversampled Gabor Transform
PEC	Perfect Electric Conductor
RF	Radio Frequency
SME	Spherical Mode Expansion
TZF	Test Zone Field

# Chapter 1

## Introduction

Antennas are used in many ways, including in communication devices, radars, and satellites. For simple antennas, one can use analytical methods to analyze, synthesize, and design them. For many other antennas, due to their complex structures, they cannot be studied analytically. Thus, numerical computation methods like Method of Moments (MoM), Fast Multipole Method (FMM), Finite Element Method (FEM), and Finite-Difference Time-Domain (FDTD), have been developed in recent decades to numerically compute the radiation characteristics of such antennas.

However, to complement numerical computational techniques antenna measurement is a necessary step for the testing of an antenna to characterize it or to ensure that an antenna meets certain design specifications. Researchers are usually interested in antenna gain, efficiency, radiation pattern, VSWR, polarization, beamwidth, and so on.

A facility used to test and evaluate antennas is referred to as an antenna range. In general, there are two basic types of antenna ranges: the reflection range and the free-space range [1]. The reflection range is usually of an outdoor type where the ground is the reflection surface, while the free-space range is designed to minimize the reflections from the surrounding environment. It includes elevated ranges, slant ranges [2], anechoic chambers, compact ranges [3], and near-field ranges [4]. Each type of range has its own unique features and scope of applications.

For the anechoic chamber, the measurement is carried out inside the chamber, which is covered by RF absorbers. The RF absorbers will provide a reflection coefficient of  $-40$  dB for the incident wave and are used to approximate the free space environment. Inside the chamber, the test antenna is placed in the free space far-field region of a probe antenna. The far field (Fraunhofer) distance  $d$  of an antenna is commonly taken as  $2D^2 / \lambda$  where  $D$  is the maximum overall dimension of the antenna and  $\lambda$  is the wavelength of operation [1]. For a large antenna, the far field distance  $d$  will be relatively large, and the size of the chamber required to carry out an indoor far-field range measurement will be large. Thus, near-field ranges were developed. The principle of near-field techniques is to use a probe to measure the field generated by an antenna at a short distance over a surface close to the antenna. Then analytical methods are used to calculate the far-field from the measured near-field. The measurement using the compact range will use a reflector to approximate an incident plane-wave field at a short distance. This is very useful when testing antenna systems at low frequencies (i.e., when the far field distance is too large) or when the antenna to be characterized is large.

## 1.1 Problem Background

The anechoic chamber is a commonly used facility for the antenna far-field pattern measurement, as it provides an indoor environment and an all-weather capability. First, let us look at the normal antenna measurement carried out in the anechoic chamber (shown in Figure 1.1). Inside the chamber, the AUT (antenna under test) is mounted on the AUT tower, which provides rotation along theta and phi directions, while a probe

antenna is placed at a distance away from the AUT. The walls and the floor of the room will be covered by RF absorbers to eliminate various reflected fields. Also, the mechanical devices present inside the chamber will be covered with RF absorbers to reduce the reflection and diffraction contributions and increase the measurement accuracy. The network analyzer is used to provide the RF signal and to measure the response received on the probe antenna. The positioner automatically controls the rotation of the AUT to generate a 3-dimensional radiation pattern.

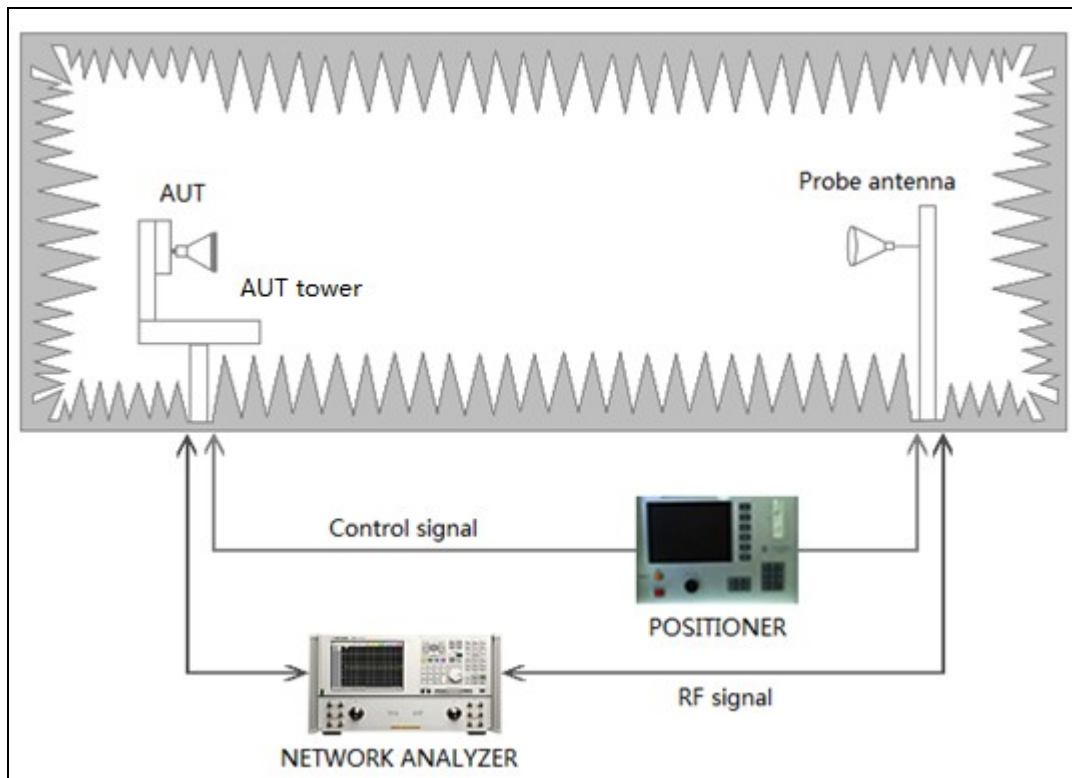


**Figure 1.1** Antenna measurement carried out in an anechoic chamber.

However, it is very expensive to construct an anechoic chamber. Further, to measure the radiation pattern of large antenna arrays mounted on their platforms (i.e., radar antenna array mounted on an aircraft), an indoor anechoic chamber with sufficient size would be

prohibitively expensive to build. The following questions arise: How is an accurate antenna measurement carried out without using an anechoic chamber? Is it possible that one can measure the radiation pattern of the AUT in a non-anechoic environment and then do some processing to remove the artifacts of the environment? In this work, we propose a methodology to generate a far-field pattern for the AUT that will be obtained in an anechoic environment using data measured for the AUT in a non-anechoic environment.

A large amount of research has been done to address this problem. They have used various approaches to compensate for the reflections that will occur naturally in a non-anechoic environment and generate a pattern that will approximate the free space radiation pattern. The purpose of this work is to reconstruct the free space radiation pattern using the data measured in a non-anechoic environment so that antenna pattern measurements can be carried out in any environment. As a result, the cost of the measurement will be cheaper and the measurement will be easier.

Note that, antenna measurement techniques include far-field techniques and near-field techniques and they perform the far-field and near-field measurement, respectively. In this work, we only consider the far-field measurement. And the word “pattern” within the work indicates the far-field radiation pattern of an antenna.

## **1.2 Originality and Contribution**

The contribution of this work is not to propose a new methodology for pattern reconstruction, but to prove and to illustrate the deconvolution method can analytically

remove the effects of extraneous fields in antenna pattern measurements. And this method is extended to antenna pattern measurements under three-dimensional environments, which is not studied in any other work. Also, the limitations and effectiveness of the method are discussed and illustrated through numerical simulation examples within this work. Extensive simulation examples with different environmental settings and different antennas are presented in this work to demonstrate the applicability of the deconvolution method.

### **1.3 Outlines**

This dissertation is presented in six chapters. The first chapter provides several basic concepts of antenna measurements, as well as the background and the motivation of this research. Concepts such as the anechoic chamber setup and the different types of antenna ranges for the measurement are introduced to help demonstrate the problem. The originality and contribution of this work is clearly stated within this chapter.

Chapter 2 reviews in the literature the existing methodologies for solving the antenna pattern reconstruction problem, such as the Fast Fourier Transform (FFT)-based methods. Also, the disadvantages for those methodologies are given in this chapter. The deconvolution method that is to be presented in details does not have those disadvantages.

Chapter 3 presents the deconvolution method in two dimensional (2D) environments and models the environmental effects as impulse responses of the test environment. It

first characterizes the environment using a reference antenna and then uses this signature to remove unwanted effects from a subsequent test for the AUT through a deconvolution processing. Numerical simulation examples are given to illustrate the performance of the method.

Chapter 4 provides a discussion on the limitations of the deconvolution method and parameters that affect its performance. First, different probe antennas are chosen to change the antenna effect. Then, different sizes of antennas and a different simulation frequency are applied in the simulation model. Also, the test environment is changed by using different sizes of PEC plates. The deconvolution method is evaluated to reveal its limitations and effectiveness under different conditions.

Chapter 5 describes the extension of the deconvolution method to three-dimensional (3D) environments and aims to extract the radiation pattern of the AUT under practical test environments with reflections from all spatial angles. Several simulation examples are given to illustrate the pattern reconstruction in a 3D environment.

Chapter 6 summarizes the work and discusses directions for future work.

The two appendixes at the end give detailed explanations for problems that one may run into during actual data processing using the deconvolution method. Appendix A explains why one needs to perform the data mapping for 3D pattern reconstruction. Appendix B explains how to remove the NA value when processing the data.

# Chapter 2

## Literature Review of Pattern Reconstruction Methodologies

### 2.1 Literature Review

In the past, researchers have introduced methods for reducing the undesired reflection and diffraction of signals from the walls and objects located inside an anechoic chamber. This chapter first gives a general review of previous works on antenna pattern reconstruction. Then, the FFT-based method is introduced with more details to follow for the purposes of generating a better understanding of the problem and for comparison with the deconvolution method.

Most of the existing pattern reconstruction methods can be divided into three categories based on the information that is used [6]. In the first category, the technique is to use the test-zone field for pattern correction, while in the second category the technique is to use time or frequency responses for correction. The third category's technique is to use the spatial response of the test antenna.

The Test Zone Field (TZF) compensation method [7]-[12] and the deconvolution method [13]-[16] are techniques of the first category. For the TZF compensation method, the test zone field is measured over a spherical surface encompassing the test zone using

a TZF probe. But this field is distorted due to extraneous fields, which are caused by reflection and diffraction responses and by the leakage of the range probe. This method provides a way to analytically remove the effect of extraneous fields in antenna pattern measurements. A spherical mode expansion (SME) of the measured test zone field is used in antenna measurements to compensate for the effects of the extraneous fields.

This method basically consists of two steps. The first step is to measure the response of a reference antenna (with known radiation characteristics) in the test zone, and expand the measured TZF into spherical modes. This step is to use the measured results to calculate the coefficients for the test zone incident fields. Then in the second step, one replaces the reference antenna as the AUT and carries out the measurement again. By utilizing the measurement data and the calculated coefficients of the TZF, the radiation pattern of the AUT can be calculated. Several papers have been presented for this method, applying a matrix inversion or the FFT (Fast Fourier Transform) technique to calculate the unknown coefficients.

The deconvolution method also uses the test-zone field information and the first work was presented in 1976, but no detail information was found in the work. In [14], a primary source was used to illuminate the AUT, and several secondary sources were used to imitate the environmental effects. The convolution relation between the far-field response of the AUT and the source distribution were given but without any proof. The method was verified through numerical simulations and a pilot experiment. In [15], the method was illustrated for correcting antenna measurement errors in compact antenna test ranges. The reaction theorem was applied to the AUT and the compact range antenna system to deduce the convolution equation. Measurement results of a standard horn were

presented to illustrate the method. In [16], the deconvolution method was derived from the time domain convolution, and transitioned into the angular domain convolution by introducing the concept of the impulse response of the test environment. Numerical simulation results were presented and compared with results of the FFT-based method. All the previous work on the deconvolution method was limited to the two-dimensional case. In this work, derivation of the deconvolution method in the three-dimensional case will be given along with numerical simulation examples.

As the time and frequency responses of the test antenna contain similar information, different techniques utilizing either the time or the frequency domain data fall into the second category. Typical methods include the FFT-based method, the Matrix Pencil method, and equalization methods.

The FFT-based method generates the time domain response of a non-anechoic environment from its frequency response by applying the Inverse Fourier Transform [17]-[18]. In the time domain, the direct signal from the transmitting antenna is detected and gated to eliminate undesired late-time echoes which are reflection and diffraction components. Then, apply the Fourier Transform to this truncated time domain response and one can obtain a cleaned radiation pattern containing only the direct signal at the desired frequency. This method can also be used to characterize the level of reflections of the anechoic chamber [19]-[20], due to the fact that the RF absorbers can reduce but not remove the reflections or diffractions.

However, a major disadvantage of this methodology is that we need to determine the time taken by the fields to travel along a line-of-sight path (direct path) from the AUT to the probe antenna and the shortest time needed for the fields to travel through other paths

besides the direct one. This can be difficult especially when the measurement site has multiple objects that are close to the direct path. Also, to have sufficient time domain resolution to perform the time gating, a large bandwidth of the measurement data is required in the frequency domain.

Another method that also applies the idea of time gating is to directly measure the far-field antenna pattern in the time domain [21]. By using the data from a single measurement in the time domain, range evaluation, pattern reconstruction and pattern error correction can be performed. However, it is difficult to carry out measurements in the time domain as a large bandwidth of the signal is required.

The Matrix Pencil method and the Oversampled Gabor Transform (OGT) essentially achieve similar goals as the FFT-based method but they require less bandwidth [22]-[25]. These two methods are based on the matrix-pencil or the oversampled Gabor-transform and decompose the measured frequency response into several propagation components in the form of complex exponential functions over selected frequency intervals. By extracting the component contributed from the direct path of propagation and by suppressing other components, the approximated free space radiation pattern can be obtained.

P. S. H. Leather and D. Parson present an equalization technique to correct the effects of unwanted signals. A special measurement is carried out for the non-anechoic environment where an antenna is to be tested to determine the parameters of the equalizer [26]-[31]. By applying the idea of a matched filter, they used the adaptive equalizer to calculate the actual channel characteristics and to adjust its coefficients appropriately to approximate the free space condition. This method needs to have a training procedure

that transmits the ideal signal to the environment, collects the responses, and records differences between the ideal signal and the received responses to calculate the coefficients. These coefficients can then be used to cancel the effects of the environment on the desired AUT.

Techniques of the third category include methods like the antenna pattern comparison (APC), novel antenna pattern comparison (NAPC) [33], and adaptive array strategies [34]. The APC technique was designed for measuring the reflectivity level in an anechoic chamber [32], but it can also be used to correct the measured pattern of an antenna. This technique measures the pattern of an antenna several times at different sites inside a room. Then, the recorded patterns are adjusted and superimposed so that the main-lobes cover each other and the corrected antenna pattern is obtained by taking the average of the measured patterns. The NAPC technique requires measuring the antenna pattern twice at two different locations in the test zone. During one pattern measurement, the antenna location is fixed in the target zone; during the second pattern measurement, the antenna is moved as a function of the pattern angle and the corrected pattern is given by the average of the two responses. As for the adaptive array strategy, those spurious signals are considered as the interference signals and the direction of arrival (DOA) algorithm is applied to identify and remove them.

Also, several other techniques are developed and are considered suitable in a hologram based compact antenna test range (CATR) at sub-millimeter wavelengths (e.g., the feed scanning APC technique, the feed scanning APC technique [35], the frequency shift technique [36], and the correction technique based on an adaptive array algorithm [37]).

The purpose of this paper is to present a deconvolution-based technique and to extend the method to be used in three-dimensional environments. Part of the work is from the previously published paper [16] and is presented in Chapter 3.

## **2.2 FFT-Based Method**

As previously mentioned, the FFT-based method is used to eliminate the reflections and diffractions existing in a measurement chamber. The idea of this method is straightforward. The measurement data from the AUT is taken in the frequency domain over a range of frequencies and can be transformed to the time domain data through FFT. Since RF absorbers cannot absorb the wave completely, the received responses at the probe would be a combination of the direct path signal as well as the reflection and diffraction contributions from walls and mechanical devices in the room. The direct path signal and the reflection signals would travel along different paths. The direct path signal is the dominant signal and travels along the direct path between the AUT and the probe, thus arriving at the probe first, while other reflection signals arrive later. Those late signals are called late-time echoes in the time domain. Based on prior knowledge of the test environment, one can calculate the time taken by the signal travelling on a direct path and also the time taken by the signal traveling on the shortest reflection path (paths besides the direct path). By eliminating late time echoes in the time domain and transforming the truncated data to the frequency domain, researchers can obtain a clean radiation pattern approximating the free space radiation pattern.

In an anechoic environment, the direct path signal between the AUT and the probe is the only measured signal. The channel in the frequency domain is then characterized by a constant amplitude response, independent of the frequency and with a linear phase. However, in a non-anechoic environment, the above is not true when reflected and diffracted fields are present due to the environment. And the influences of the reflection and diffraction contributions exist in both amplitude and phase of the antenna responses. The main idea of the FFT-based method is that after a certain time period there should not be any desired direct path signal. This time period can be calculated based on the knowledge of the measurement environment, specifically, the distance between the AUT and the probe. This has been described in detail in [17]-[18].

The diagram of an antenna measurement system in an anechoic chamber is shown in Figure 2.1. It contains one probe antenna and one AUT with a finite distance in between. A metal plate is placed as a reflector at one side of the antennas. The direct path between the AUT and the probe is the straight line connecting two antennas, and the shortest path to the reflector can be obtained by drawing the image of the probe and by connecting it with the AUT. During the simulation or measurement, the AUT will act as the transmitter (port 1), and it will rotate along the axis of itself in an azimuth angle  $\phi$ , while the probe will be the receiver (port 2). And the  $S_{21}(\phi, f)$  parameter is recorded to generate the radiation pattern of the AUT. Typical far-field antenna measurements are performed with the AUT operating in the receiving mode, excited by an incident plane wave. Reciprocity implies that the AUT works equally well as transmitters or receivers [5]. In this work, we rotate the AUT and operate it as a transmitter. And the  $S_{21}(\phi, f)$  parameter is recorded to form the radiation pattern

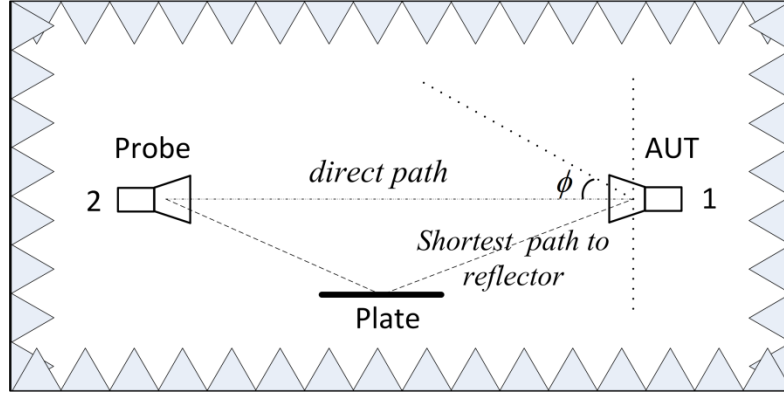


**Figure 2.1** The radiation pattern measurement system.

Here, we summarize the steps of the FFT-based method:

- (1). Measure the response (both amplitude and phase) in the frequency domain covering the bandwidth from, for example, 6 GHz to 12 GHz. In other words, measure  $S_{21}(\phi, f)$  between the two antennas in the presence of the metal plate as shown in Figure 2.1.
- (2). Apply the Inverse Fourier Transforms (IFFT) to  $S_{21}(\phi, f)$  in the frequency domain to obtain the time domain response  $S_{21}(\phi, t)$ .
- (3). Once in the time domain, the signal is truncated and the direct ray contribution between the transmitting antenna and the receiving antenna should be approximately retained. By estimating the time delay between the direct path contribution and the shortest reflected path contribution, the minimal bandwidth for measurement can be calculated so as to have sufficient resolution in the time domain and to perform the time gating.
- (4). Then, the truncated time domain data is transformed to the frequency domain by applying the FFT to obtain the processed frequency domain data  $S'_{21}(\phi, f)$ .

To illustrate the performance of the FFT-based method, one simulation example is presented here, and this example can also be found in previous paper [16]. The setup of the model is shown in Figure 2.2 and the far field condition is satisfied. The rotation (in azimuth plane) angle  $\phi$  of the AUT changes from  $-90^\circ$  to  $90^\circ$  with a  $2^\circ$  step. A powerful full-wave EM simulation software HOBBIES (Method of Moments based) [38] is used to simulate all the electromagnetic effects in the model. The frequency of operation is changed from 6 GHz to 12 GHz, in a step of 0.05 GHz, to characterize the non-anechoic environment. This can be calculated through the time delay. The time delay is the time difference between the direct path signal and the shortest reflection path signal and can be easily calculated to be  $\Delta t = 7.45ns$  for this simulation example. So the minimum bandwidth needed for the frequency sweep can be obtained as the reciprocal of the time delay (i.e.,  $BW = 1/\Delta t$ ). However, to achieve a better truncation precision in time, a higher bandwidth is recommended to obtain a higher resolution in the time domain. For that, it is necessary to use  $BW \approx 5/\Delta t$ . Therefore, we choose the frequency sweep from 6 GHz to 12 GHz.

A metal plate sized  $0.5\text{ m} \times 0.2\text{ m}$  was used in the far-field of the measurement environment. The AUT is a helical antenna whose dimensions are shown in Figure 2.3. The helical antenna is fed at the junction of the wire helix and the circular PEC backplane. The diameter of the wire is  $0.5\text{ mm}$ . A standard gain horn antenna is used as the probe antenna, whose dimensions are shown in Figure 2.4. A monopole with the length of  $9.5\text{ mm}$  and the diameter of  $0.5\text{ mm}$  is used to feed the horn and is located at a distance of  $7.5\text{ mm}$  away from the end of the horn.

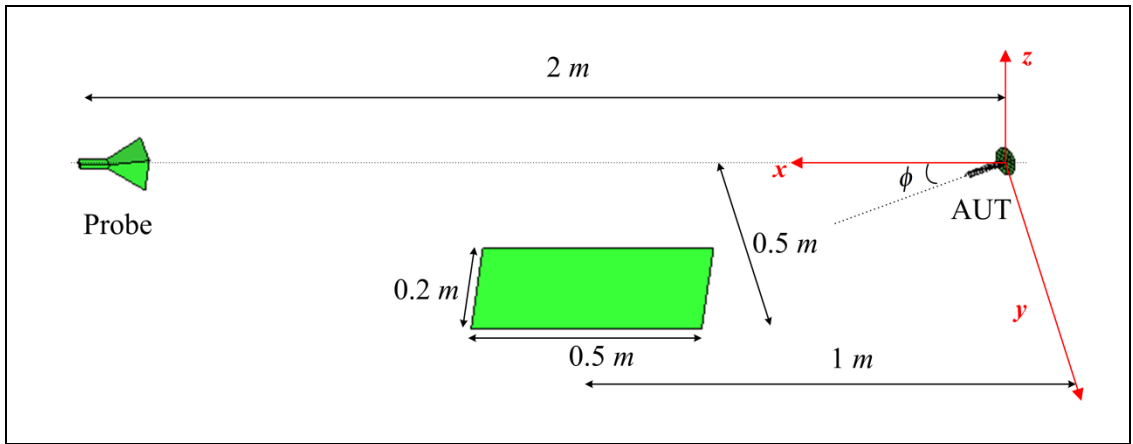


**Figure 2.2** The radiation pattern measurement model with one PEC plate as the reflector. (the AUT is a helical antenna; the probe antenna is a horn antenna)

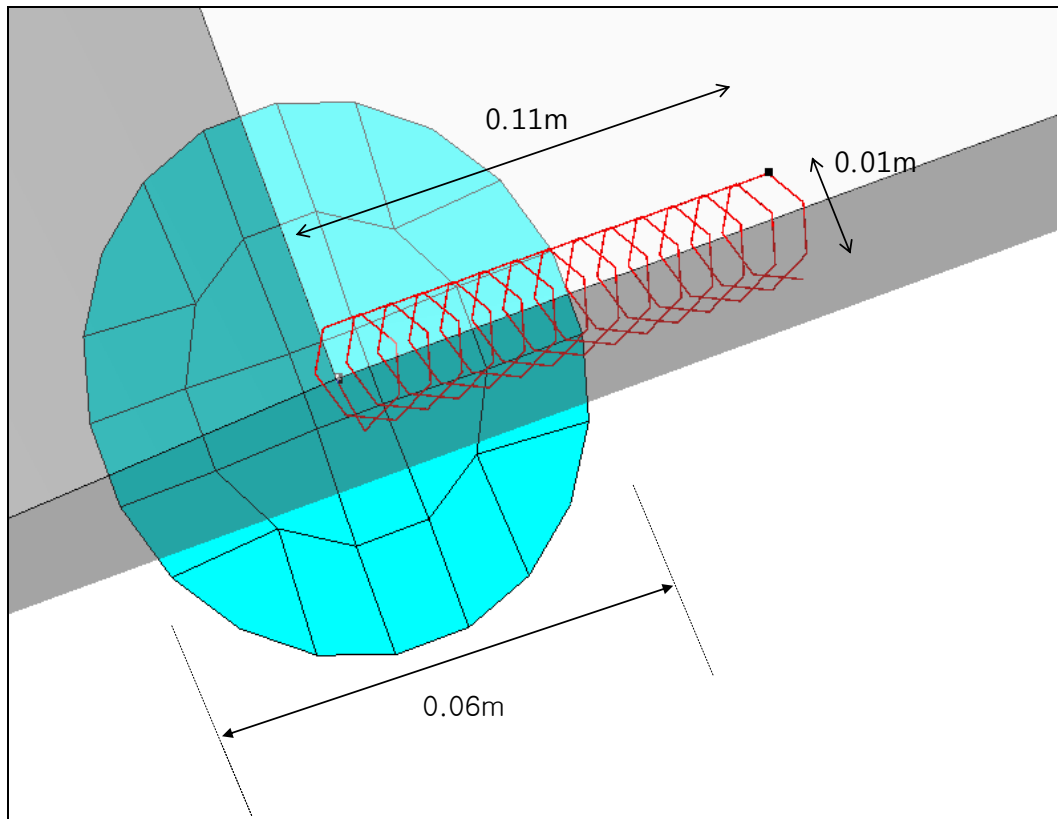


**Figure 2.3** Dimensions of the helical antenna model with a reflecting plate (AUT).

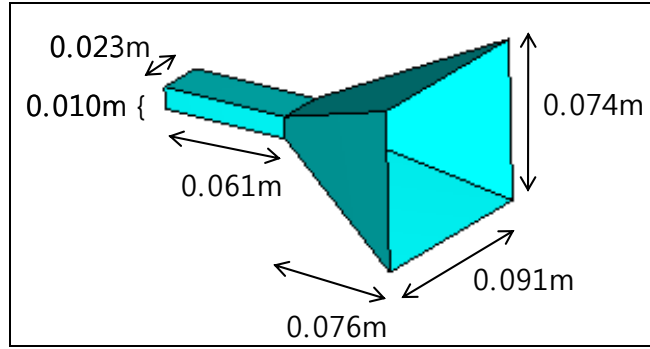


**Figure 2.4** Dimensions of the horn antenna model (Probe).

In the simulation model, the AUT is rotated along the azimuth angle  $\phi$  from  $-90^\circ$  to  $90^\circ$  with a  $2^\circ$  step in the frequency range of 6 to 12 GHz. For each azimuth angle and each frequency point, the simulated  $S_{21}(\phi, f)$  data is collected and the amplitude response, which is in the frequency domain for various rotation angles, is shown in Figure 2.5. It is seen that the various reflected and diffracted fields from the reflector are primarily located in the region covering azimuth angles ranging from  $20^\circ \sim 40^\circ$ , which is the region where the main beam of the AUT is reflected by the metal plate.

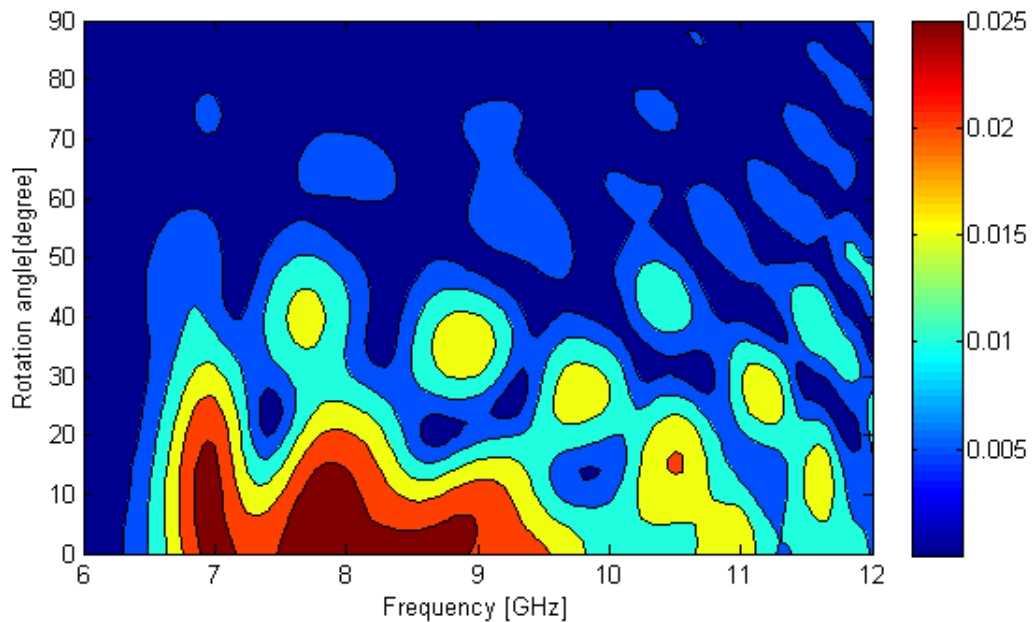


**Figure 2.5** Amplitude pattern of  $S_{21}(\phi, f)$  between the helical antenna and the probe.

Then, the Inverse FFT is applied to this data and the corresponding time domain data is shown in Figure 2.6. From Figure 2.2, it is easy to realize that the shortest time for the fields to propagate from the AUT to the probe is about  $7.45 \text{ ns}$ . Any received signal beyond that would be the reflections and diffractions of the radiated fields and should be removed.

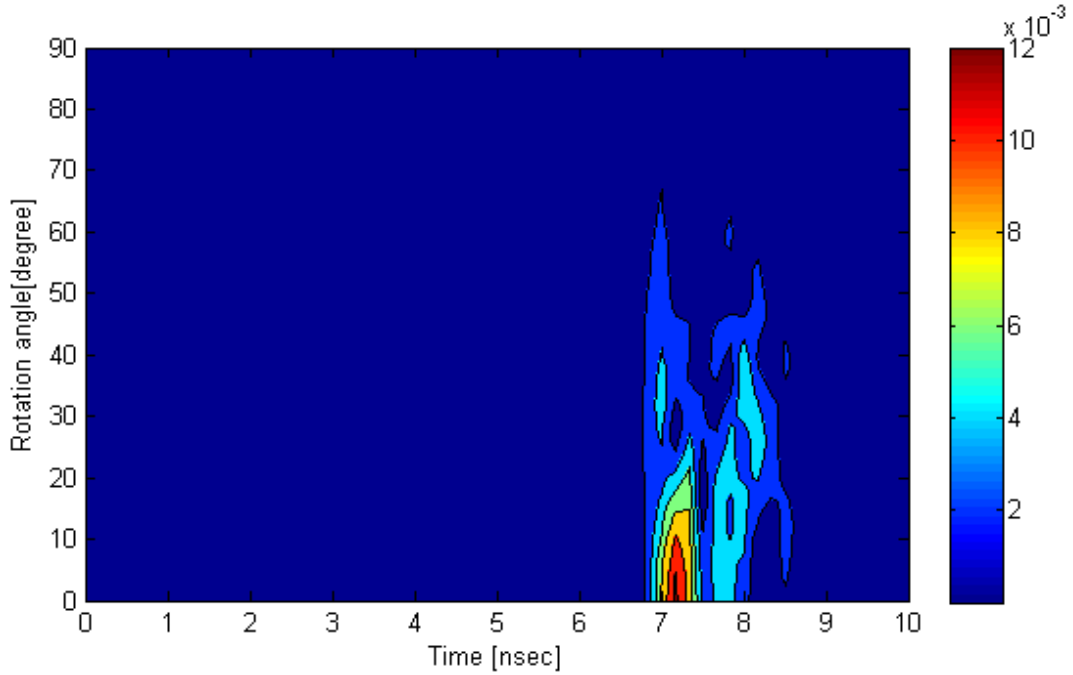


**Figure 2.6** Time domain response corresponding to Figure 2.5.

As mentioned above, we need to truncate the data beyond  $7.45 \text{ ns}$ . As the minimum time interval is  $1/6 \text{ ns}$  under the current bandwidth setting, we will truncate the data towards the closest data point, which is  $7.5 \text{ ns}$  (as shown in Figure 2.7). After truncating the time domain signal from  $7.5 \text{ ns}$ , the processed signal is transformed back to the frequency domain by applying the FFT. The cleaned pattern in the frequency domain is shown in Figure 2.8. It is observed that most of the reflected and diffracted fields in the angular range of  $20^\circ \sim 40^\circ$  have been reduced. To see the performance of the FFT-based method more clearly, a comparison is made for the helical antenna among the ideal

pattern, the FFT-based pattern and the reflected pattern (pattern with reflection contributions), for the patterns at 7.6 GHz and 8.8 GHz, shown in Figures 2.9 and 2.10, respectively.

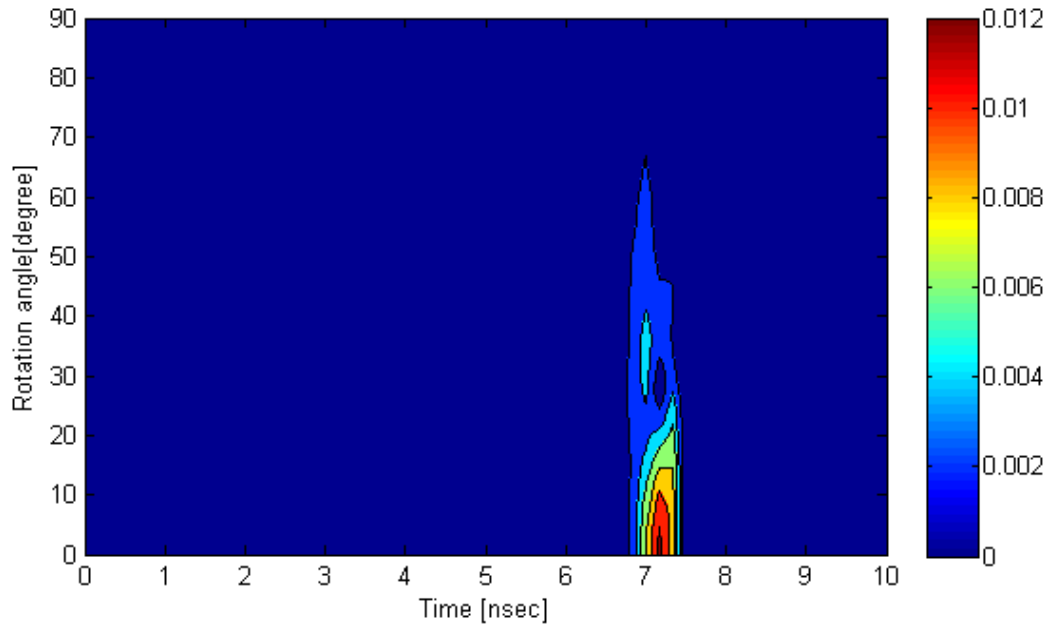


**Figure 2.7** Truncated time domain response.

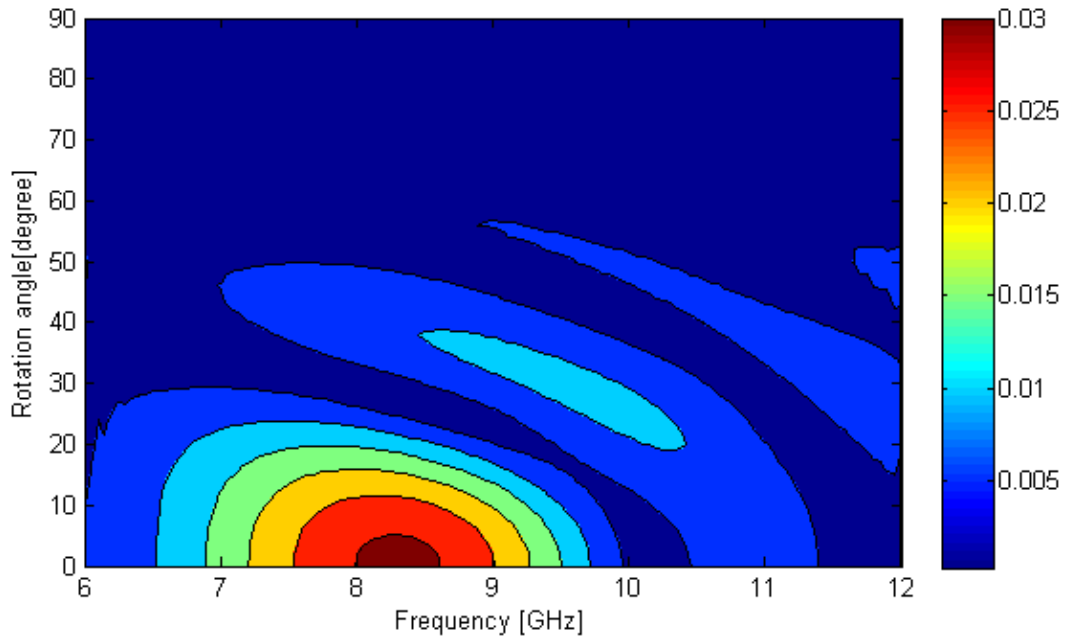


**Figure 2.8** Cleaned pattern of the helical antenna by taking FFT of the truncated time domain response.

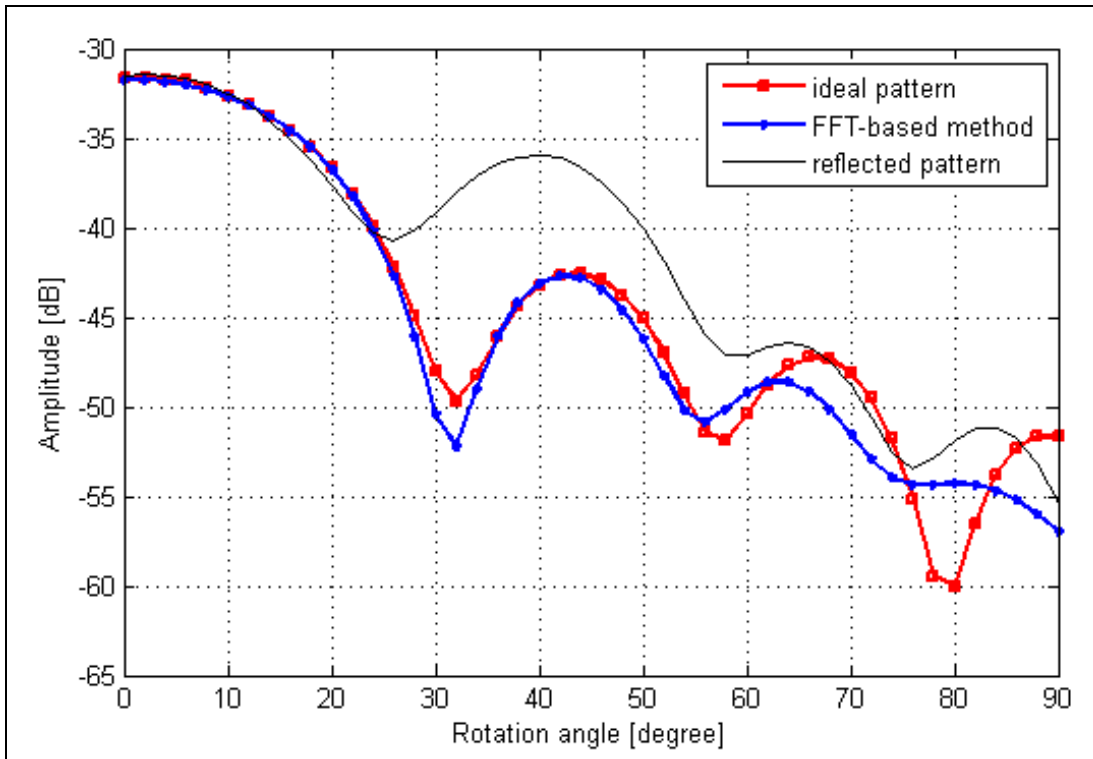


**Figure 2.9** Amplitude pattern comparison for the helical antenna at 7.6 GHz.

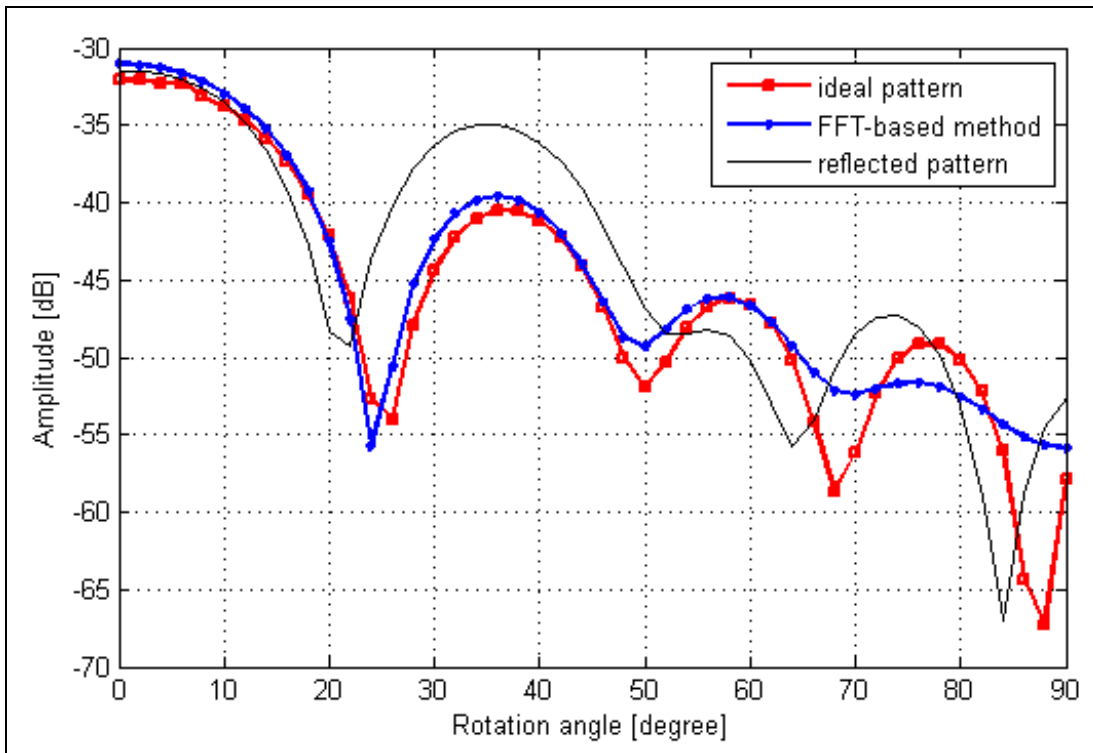


**Figure 2.10** Amplitude pattern comparison for the helical antenna at 8.8 GHz.

The black line termed *reflected pattern* is the result of the reflection contributions, while the reconstructed pattern is indicated by the blue line termed *FFT-based pattern*. The red line termed *ideal pattern* is the reference pattern. One can observe that after the truncation process the processed patterns give acceptable results compared with the ideal patterns. And the FFT-based method has removed a major part of the reflection contributions.

A problem with the FFT-based method is that one needs to determine the time delay between the time take by the direct path and the time taken by the shortest reflection path. This is not an easy task especially when multiple paths are present.

## Chapter 3

# Deconvolution Method for Radiation Pattern Reconstruction

Considerable developments have taken place in the area of antenna measurements during recent years. And the accuracy of the measurement results is affected by factors like the Signal to Noise Ratio (SNR) of the measured data, the data processing algorithms, the precision of the test equipments and also the quality of the measurement environment. Large efforts have been made to improve the measurement facility but it is usually limited by the available budget. For example, use of high quality absorbing materials in the anechoic chamber is costly. This work is focused on antenna pattern reconstruction through deconvolution method.

The concept of the deconvolution method and some results have been reported in [13]-[15]. In this work, we will present and prove the method from a different point of view, followed by the governing equations to implement this method and numerical examples to illustrate the process. Note that in this chapter the deconvolution method is applied in 2D test environment<sup>1</sup>. Extensions of the method to 3D test environment will be given in chapter 5.

---

<sup>1</sup> Part of this chapter previously appeared in: Jinhwan Koh, De, A., T. K. Sarkar, Hongsik Moon, **Weixin Zhao**, M. Salazar-Palma, "Free Space Radiation Pattern Reconstruction from Non-Anechoic Measurements Using an Impulse Response of the Environment," *IEEE Transactions on Antennas and Propagation*, vol.60, no.2, pp.821-831, Feb. 2012 [16].

### 3.1 Equations and Derivation

Consider making antenna measurement inside a regular room instead of an anechoic chamber. The received signal at the probe is affected by the environment (walls, floor, ceiling, and so on) and we call this as the environmental effects. As shown in Figure 3.1, the AUT and the probe work as the transmitting and receiving antenna, respectively. The distance between two antennas satisfies the far field condition since the far-field pattern of an AUT is considered. The AUT will rotate during the measurement and  $S_{21}(f, \phi)$  will be measured at a fixed frequency  $f$  for each rotating angle  $\phi$  ( $\phi$  will be the azimuth angle since the AUT rotates along the azimuth plane). The radiation pattern of the AUT is proportional to  $S_{21}(f, \phi)$ , as a function of the AUT rotation angle. Here,  $S_{21}(f, \phi)$  contains information for both the antenna far-field pattern and the environmental effects.

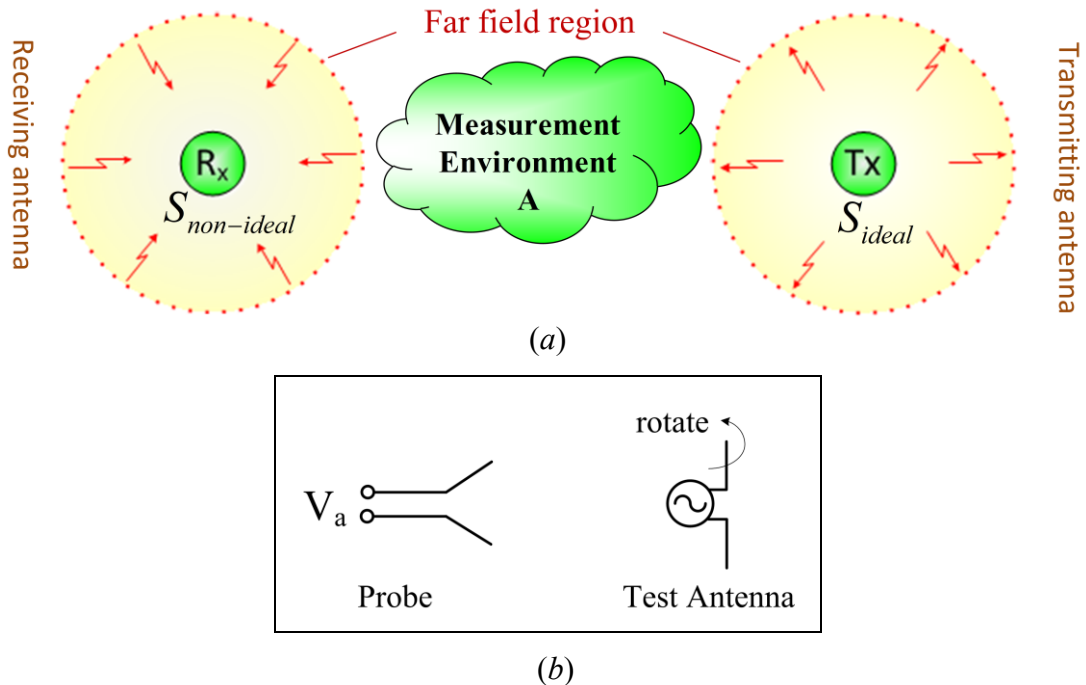


**Figure 3.1** Radiation pattern measurement system diagram.

Many physical processes can be represented by, and successfully analyzed assuming linear time-invariant (LTI) systems as models [39]. And from the time domain point-of-view, the output of the system is simply the convolution of the system input and the impulse response of the system. When the transmitter in a room generates a signal  $x(t)$ , it will be affected by the room and received by the receiver as  $y(t)$ . Suppose the impulse response of the room system is  $h(t)$ , then we know that:

$$y(t) = x(t) * h(t), \quad (3.1)$$

where  $*$  represents a convolution in the time domain, and in the frequency domain it will be:

$$Y(f) = X(f) \cdot H(f), \quad (3.2)$$

where  $Y(f)$ ,  $X(f)$  and  $H(f)$  are the Fourier transforms of  $y(t)$ ,  $x(t)$  and  $h(t)$ , respectively. Thus, for antenna measurement inside a room, the received signal at the probe will be a convolution of the transmitted signal (from the AUT) with the room impulse response. Note that, this relationship is between the time domain and the frequency domain; moreover, both the AUT and the probe are fixed in the spatial domain.

Now, let's analyze the situation when the AUT rotates during the measurement. The reflections from the room may be strong at some angles, and weak for some other angles. For each rotation angle  $\phi$ , the AUT transmits signal along all directions and the probe also receives signal from all directions (assume that there are  $n$  directions for one cut in the plane). The signal which is transmitted along direction  $i$  travels along a certain path and is received from direction  $j$ . We define this path as  $ji$ . And the corresponding environmental effect along this path is defined as  $h_{ji}$ . So the total signals received at the probe along direction 1 will be a summation of the signals from the transmitter radiating in all

directions and through paths  $h_{11}, h_{12}, \dots, h_{1n}$ . Then, we will have:

$$R_x^1 = h_{11}T_x^1 + h_{12}T_x^2 + \dots + h_{1i}T_x^i + \dots + h_{1n}T_x^n, \quad (3.3)$$

where  $R_x^1$  is the signal received at the probe along direction 1

$T_x^i$  is the signal transmitted at the AUT along direction  $i$

$h_{1i}$  is the environmental effect along the path  $1i$

$n$  is the number of directions that are considered

Similarly, there will be a signal received at the probe from direction 2, 3, until  $n$ . And there will be corresponding equations for  $R_x^2, R_x^3, \dots, R_x^n$ .

$$\begin{aligned} R_x^1 &= h_{11}T_x^1 + h_{12}T_x^2 + \dots + h_{1i}T_x^i + \dots + h_{1n}T_x^n \\ R_x^2 &= h_{21}T_x^1 + h_{22}T_x^2 + \dots + h_{2i}T_x^i + \dots + h_{2n}T_x^n \\ &\vdots \\ R_x^n &= h_{n1}T_x^1 + h_{n2}T_x^2 + \dots + h_{ni}T_x^i + \dots + h_{nn}T_x^n \end{aligned} \quad (3.4)$$

and we can write them in the matrix form as:

$$\begin{bmatrix} R_x^1 \\ \vdots \\ R_x^n \end{bmatrix} = \begin{bmatrix} h_{11} & \cdots & h_{1n} \\ \vdots & \ddots & \vdots \\ h_{n1} & \cdots & h_{nn} \end{bmatrix} \cdot \begin{bmatrix} T_x^1 \\ \vdots \\ T_x^n \end{bmatrix} \quad (3.5)$$

where  $R_x^1 \dots R_x^n$  stand for the signals received at the receiver from all  $n$  directions;

$T_x^1 \dots T_x^n$  stand for the signals sent by the transmitter along all  $n$  directions;  $h_{ji}$  stands for the environmental effect for the path that the signal is transmitted along direction  $i$  and is received along direction  $j$ .

So for each azimuth (rotation) angle  $\phi_1$ ,  $S_{21}(\phi_1)$  is a summation of the received

signals as  $R_x^1 + R_x^2 + \dots + R_x^n$  (at  $\phi_1$ ). By using  $h_1$  to represent the summation of  $h_{11}, h_{21},$  until  $h_{n1}$ , and also other  $h_{ji}$  terms, we can write  $S_{21}(\phi_1)$  as a summation of  $T_x^1 h_1 + T_x^2 h_2 + \dots + T_x^n h_n$ :

$$S_{21}(\phi_1) = R_x^1 + R_x^2 + \dots + R_x^n \text{ (at } \phi_1) = \text{sum} \left\{ \begin{array}{l} T_x^1 (h_{11} + h_{21} + \dots + h_{n1}) \\ T_x^2 (h_{12} + h_{22} + \dots + h_{n2}) \\ \vdots \\ T_x^n (h_{1n} + h_{2n} + \dots + h_{nn}) \end{array} \right. \begin{array}{l} h_1 \\ h_2 \\ \vdots \\ h_n \end{array} \quad (3.6)$$

$$= T_x^1 h_1 + T_x^2 h_2 + \dots + T_x^n h_n$$

where,

$$\begin{aligned} h_1 &= h_{11} + h_{21} + \dots + h_{n1} \\ h_2 &= h_{12} + h_{22} + \dots + h_{n2} \\ &\vdots \\ h_n &= h_{1n} + h_{2n} + \dots + h_{nn} \end{aligned} \quad (3.7)$$

Then, we rotate the AUT every 1 degree, the angle  $\phi$  changes from  $\phi_1$  to  $\phi_2$ . The corresponding field component transmitted along direction 1 will then be transmitted along direction 2. And we can get a similar equation for  $S_{21}(\phi_2)$  as presented earlier:

$$S_{21}(\phi_2) = \text{sum} \left\{ \begin{array}{l} h_1 T_x^1 + h_2 T_x^2 + \dots + h_n T_x^{n-1} + h_{n+1} T_x^n \\ h_2 T_x^1 + h_3 T_x^2 + \dots + h_n T_x^{n-1} + h_{n+2} T_x^n \\ \vdots \\ h_{n2} T_x^1 + h_{n3} T_x^2 + \dots + h_{nn} T_x^{n-1} + h_{n+1} T_x^n \end{array} \right. \quad (3.8)$$

$$= T_x^1 h_2 + T_x^2 h_3 + \dots + T_x^n h_1$$

similarly, we can get such expressions for every single  $\phi$  and write them in the matrix form as:

$$\begin{bmatrix} S_{21}(\phi_1) \\ \vdots \\ S_{21}(\phi_n) \end{bmatrix} = \begin{bmatrix} h_1 & h_2 & \cdots & h_n \\ h_2 & h_3 & \cdots & h_1 \\ \vdots & & & \vdots \\ h_n & h_1 & \cdots & h_{n-1} \end{bmatrix} \cdot \begin{bmatrix} T_x^1 \\ \vdots \\ T_x^n \end{bmatrix} = (h_1, h_2, \dots, h_n) \otimes_{\phi} (T_x^1, T_x^2, \dots, T_x^n) \quad (3.9)$$

It is easy to observe that the  $[h]$  matrix is shifted by one element for each row in Eq. (3.9). So the multiplication of matrix  $[h]$  and vector of  $[T_x]$  will be a convolution of two vectors. As we know,  $(T_x^1, T_x^2, \dots, T_x^n)$ , which is the signal transmitted by the AUT, forms the free space radiation pattern of the AUT; while  $(S_{21}(\phi_1), S_{21}(\phi_2), \dots, S_{21}(\phi_n))$ , which is the actual signal received by the probe in the presence of the environment, forms the non-ideal radiation pattern. We can then conclude that the measured non-ideal signal can be represented as an angular convolution between the ideal signal and the environmental responses at the frequency  $f$ , as shown in Eq. (3.10), where  $\otimes_{\phi}$  represents a convolution in the angular domain.

$$P_{non-ideal\ AUT}(\phi, f) = P_{ideal\ AUT}(\phi, f) \otimes_{\phi} A(\phi, f) \quad (3.10)$$

The above derivation of equation (3.10) is not very rigorous while the following derivation is more rigorous, and it also can be found in previous paper [16]. We first assume an AUT can generate an ideal pencil beam pattern (the radiated signal will be along one direction in the far field). As shown in Figure 3.2, the signal which is transmitted along  $\phi$  experiences multiple reflections from Object 1 and Object 2 in the azimuth plane. Note that we assume that the objects do not change size or positions in time (time invariant). The received time domain signal at the probe, when the AUT is rotated through  $\phi$ , is unique with respect to other angles. Therefore the time domain

response along angle  $\phi$  can be described as an impulse response along  $\phi$  or a spatial signature of  $\phi$ . The reason we have the pencil beam assumption here is that the environment affects the radiated signal differently along different angles, and we first consider the environmental effects in one direction only.

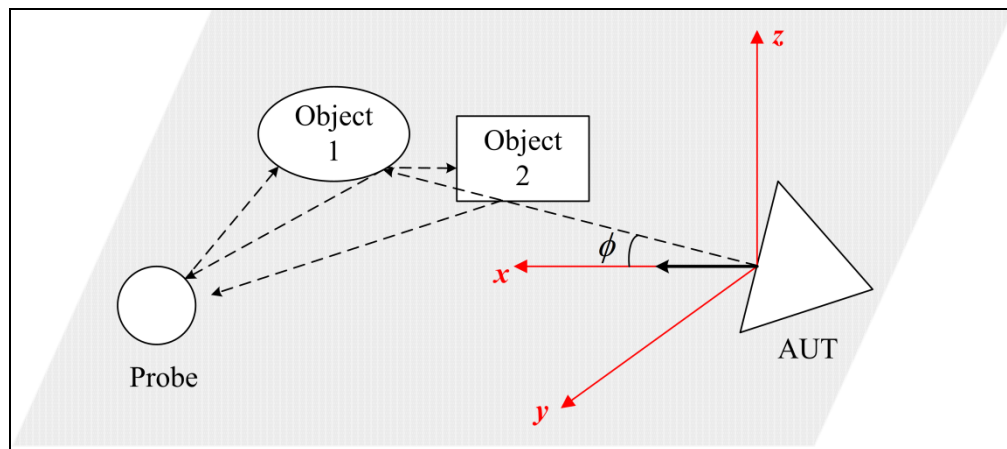


**Figure 3.2** Multiple reflections exist between the AUT and the probe within the azimuth plane.

The measured signal at the probe, which contains various reflections, can be represented as a time convolution of the ideal signal (without any reflection) and the impulse response along  $\phi_L$ , which can be written as:

$$P_{non-ideal}(\phi_L, t) = P_{ideal}(\phi_L, t) \otimes A(\phi_L, t) \quad (3.11)$$

or

$$P_{non-ideal}(\phi_L, f) = P_{ideal}(\phi_L, f) \cdot A(\phi_L, f) \quad (3.12)$$

where  $\otimes$  denotes a time convolution, and

$P_{non-ideal}(\phi_L, t)$  is the non-ideal time domain signal at the probe in the presence of the reflections for the angle  $\phi_L$ ;

$P_{non-ideal}(\phi_L, f)$  is the non-ideal frequency domain signal at the probe in the presence of the reflections for the angle  $\phi_L$ ;

$P_{ideal}(\phi_L, t)$  is the ideal time domain signal without any reflection for the angle  $\phi_L$ ;

$P_{ideal}(\phi_L, f)$  is the ideal frequency domain signal without any reflection for the angle  $\phi_L$ ;

$A(\phi_L, t)$  is the impulse response of the environment with objects present when the AUT has a pencil beam pointing along the angle  $\phi_L$ ;

$A(\phi_L, f)$  is the frequency domain response of the environment with objects present when the AUT has a pencil beam pointing along the angle  $\phi_L$ .

Note that  $A(\phi_L, t)$  represents the contribution of various reflections from the environment along the angle  $\phi_L$  and is independent of the particular AUT.

In a real situation, the AUT will radiate towards every direction in the spatial domain and cannot have an ideal pencil beam pattern. We define the impulse response of the environment along the rotation angle  $\phi_L$  as  $\hat{A}(\phi_L, f)$  when the AUT does not have an ideal pencil beam pattern. Then, using (3.12) we have:

$$P_{non-ideal}(\phi_L, f) = P_{ideal}(\phi_L, f) \cdot \hat{A}(\phi_L, f) \quad (3.13)$$

here,  $\hat{A}(\phi_L, f)$  is the frequency domain impulse response along the angle of  $\phi_L$  when the AUT does not have an ideal pencil beam pattern, which is more practical.

Now,  $\hat{A}(\phi_L, f)$  contains information of the beam pattern of the AUT as well as the environmental effects at  $\phi_L$ . However, we need the true impulse response  $A(\phi_L, f)$  or

$A(\phi_L, t)$ , which is independent of the beam pattern of the AUT. Then  $\hat{A}(\phi_L, f)$  can be considered as a convolution in the angular domain of the normalized beam pattern and the true impulse response. That is,

$$\hat{A}(\phi_L, f) = \frac{P_{ideal}(\phi, f)}{P_{ideal}(\phi_L, f)} \otimes_{\phi} A(\phi, f) \Big|_{\phi=\phi_L} \quad (3.14)$$

Here,  $P_{ideal}(\phi, f)$  is the ideal pattern of an antenna without any reflection from the environment at the frequency  $f$ , and  $\otimes_{\phi}$  is the convolution operator in the angular domain. When the AUT doesn't have an ideal pencil beam pattern, it radiates the wave towards different directions, and be affected differently by the environment. And the combination of such effects is equal to the term  $\hat{A}(\phi_L, f)$ . By substituting (3.14) into (3.13) we have,

$$P_{non-ideal}(\phi_L, f) = P_{ideal}(\phi, f) \otimes_{\phi} A(\phi, f) \Big|_{\phi=\phi_L} \quad (3.15)$$

For a general angle of  $\phi$ , we have:

$$P_{non-ideal}(\phi, f) = P_{ideal}(\phi, f) \otimes_{\phi} A(\phi, f) \quad (3.16)$$

which leads to the same conclusion as (3.10).

Therefore, the beam pattern of the AUT in the presence of reflections can be considered as a convolution in the angular domain between the ideal beam pattern of the AUT and the impulse response of the environment. And we know that taking FFT will transform the convolution in the angular domain to the multiplication in the other domain, which we can name as the angle-frequency domain. Thus the impulse response  $A(\phi, f)$  can easily be calculated by taking the IFFT of (3.16) using the measurement data of a

reference antenna whose ideal pattern is known. Once  $A(\phi, f)$  is calculated, the ideal pattern  $P_{ideal}(\phi, f)$  of the AUT can be obtained for any antenna measured in the same environment through (3.16). This requires two assumptions: First, the environment is unchanged during measurements for the reference antenna and the AUT. Second, because both the probe and the AUT are considered as part of the environment, sizes of the reference antenna and the AUT need to be similar. In this way, the change of antenna will not cause a sudden change of the environment.

Also, one condition needs to be mentioned is the AUT inside the environment should radiate as if it is located in the free space, and in other words, the current distribution on the AUT should remain close to the ideal one. The reason is that we are reconstructing the radiation pattern of the AUT to approximate the free space radiation pattern. If the current distribution on the antenna has been dramatically changed by the environment, then the radiation pattern will also be changed. And after the reconstruction, the reconstructed pattern will be a pattern that has been affected by the environment. To satisfy this condition, the AUT should be positioned with a “safe” distance away from the environment, to minimize the changes in the current on the AUT due to the environment. A reference for this “safe” distance can be the free space far-field distance, which is commonly taken as  $2D^2/\lambda$ , where  $D$  is the maximum overall dimension of the antenna and  $\lambda$  is the wavelength of operation [1].

## 3.2 Steps Summarized for the Methodology

After getting Eq. 3.16, we designed a procedure to demonstrate this procedure through simulation. We will use HOBBIES [38] as the EM simulation tool for all examples presented in this work. In the software, we constituted the radiation pattern measurement model containing an AUT, a probe antenna, and PEC plates which serve as the environment. We first carried out the simulation in a non-anechoic environment using two reference (standard) antennas, whose ideal patterns are known, and performed a deconvolution to compute the environmental response  $A$ . Then, we carried out the simulation for the AUT in the same environment and estimated its free space radiation pattern through the environmental response  $A$  that we extracted from the reference antenna. The entire procedure can be summarized into 4 steps:

- 1) At a fixed frequency, measure the reference (standard) antenna response  $P_{non-ideal}(\phi, f)$  in a non-anechoic environment. Also the reference antenna response  $P_{ideal}(\phi, f)$  is known.
- 2) Calculate  $A(\phi, f)$  using the equation  $P_{non-ideal}(\phi, f) = P_{ideal}(\phi, f) \otimes_{\phi} A(\phi, f)$ .
- 3) At the same frequency, replace the reference antenna with the AUT and keep the rest of the environment unchanged, measure the AUT in the same way as in step (1), and let  $P_{non-ideal\ AUT}(\phi, f)$  be the result.
- 4) Obtain the ideal response of the AUT,  $P_{ideal\ AUT}(\phi, f)$ , through deconvolution using:

$$P_{non-ideal\ AUT}(\phi, f) = P_{ideal\ AUT}(\phi, f) \otimes_{\phi} A(\phi, f)$$

From the above procedures, we can see that the deconvolution method only requires a single frequency measurement, and it is independent of the bandwidth of the antenna; while the FFT based approach require broadband characteristics for the antenna. And the deconvolution method requires no prior knowledge of the system or the test environment. Most importantly, it doesn't require the antenna radiation pattern measurement to be carried out in an anechoic chamber.

### **3.3 Processing of the Data**

Specifically, the following procedures are the rules of thumb for setting up simulation models and processing the simulated data generated through numerical electromagnetics code:

1. In this work, all simulation examples will be carried out using HOBBIES to perform the full wave EM simulation. First, build the simulation model for the antenna radiation pattern measurement system which consists of an AUT (transmitting antenna), a probe (receiving antenna) and reflectors. The reflectors will reflect the radiated fields from the AUT and can be modeled by the PEC plates around the antennas.
2. In HOBBIES, set the operation mode as “ANTENNA (one generator at a time)”, and set an excitation port for both the AUT and the probe. During the simulation, the AUT and the probe will be the transmitter and the receiver, respectively. To simulate the antenna measurement process, the AUT rotates along itself in the azimuth plane for a step of  $1^\circ$ , and for each rotation angle the model is simulated and the  $S_{21}$  data is collected.

3. The  $S_{21}$  data along each azimuth angle  $\phi$  forms the radiation pattern of the AUT. When the AUT rotates one loop in the azimuth plane, there will be 360 data points, i.e.  $-180^\circ, -179^\circ, -178^\circ, \dots, 179^\circ$ . and then the measured data will repeat this sequence. Therefore, the ideal pattern  $P_{ideal}(\phi, f)$  and the non-ideal pattern  $P_{non-ideal}(\phi, f)$  as well as the environmental effects  $A(\phi, f)$ , are all periodic sequences of period 360 in  $\phi$  angle domain. Note that if the model is symmetrical (both the environment and the antennas are symmetrical) in the azimuth plane, we can then reduce the number of simulation points by half.
4. As described in Section 3.2, we first use a reference antenna as the AUT and simulate the antenna within a non-anechoic environment to obtain the non-ideal radiation pattern of the reference antenna  $P_{non-ideal-Ref}(\phi, f)$ . Also, we can obtain the ideal radiation pattern of the reference antenna  $P_{ideal-Ref}(\phi, f)$  by simulating the model without the environment (the antenna would be like in the free space without the non-anechoic environment). In reality, we can obtain the ideal pattern of the reference antenna through its datasheet. Similarly, by replacing the reference antenna with the desired AUT and carry out the simulation, we can obtain the ideal pattern  $P_{ideal-AUT}(\phi, f)$  and the non-ideal pattern  $P_{non-ideal-AUT}(\phi, f)$  for the desired AUT. The ideal pattern  $P_{ideal-AUT}(\phi, f)$  will be the goal of the reconstructed pattern.
5. Now we need to apply (3.16) to reconstruct the radiation pattern of the AUT. According to Section 3.2.4 of [40], the convolution of two periodic sequences is the multiplication of the corresponding discrete Fourier series. Let  $\tilde{x}_1(n)$  and  $\tilde{x}_2(n)$  be the two periodic sequences of period  $N$  with the discrete Fourier series denoted by

$\tilde{X}_1(k)$  and  $\tilde{X}_2(k)$ , respectively. It can be written as:

$$\tilde{x}_3(n) = \sum_{m=0}^{N-1} \tilde{x}_1(m)\tilde{x}_2(n-m) \quad (3.17)$$

$$\tilde{X}_3(k) = \tilde{X}_1(k)\tilde{X}_2(k) \quad (3.18)$$

6. From (3.16) we have the following equations:

$$P_{non-ideal-Ref}(\phi, f) = P_{ideal-Ref}(\phi, f) \otimes_{\phi} A(\phi, f) \quad (3.19)$$

$$P_{non-ideal-AUT}(\phi, f) = P_{ideal-AUT}(\phi, f) \otimes_{\phi} A(\phi, f) \quad (3.20)$$

Therefore, by taking the FFT of both sides of (3.19), the angular convolution operator will become the multiplication operator. We can derive the environment effects  $A(\phi, f)$  as:

$$A(\phi, f) = \text{iffit} \left( \frac{\text{fft}(P_{non-ideal-Ref}(\phi, f))}{\text{fft}(P_{ideal-Ref}(\phi, f))} \right) \quad (3.21)$$

7. Take the FFT of both sides of (3.20) and substitute the environment effects  $A(\phi, f)$  into the equation, we get:

$$\begin{aligned} P_{ideal-AUT}(\phi, f) &= \text{iffit} \left( \frac{\text{fft}(P_{non-ideal-AUT}(\phi, f))}{\text{fft}(A(\phi, f))} \right) \\ &= \text{iffit} \left( \frac{\text{fft}(P_{non-ideal-AUT}(\phi, f)) \cdot \text{fft}(P_{ideal-Ref}(\phi, f))}{\text{fft}(P_{non-ideal-Ref}(\phi, f))} \right) \end{aligned} \quad (3.22)$$

Note that the division and multiplication in (3.21) and (3.22) are element by element operations on vectors. All data processing can be performed off-line using a commercial software package (MATLAB 7, The MathWorks Inc., Natick, MA, 2000). In MATLAB, the function  $Y=\text{fft}(X)$  returns the Discrete Fourier Transform

(DFT) of vector  $X$ , computed with a Fast Fourier Transform (FFT) algorithm. Similarly, the function  $Y=\text{ifft}(X)$  returns the Inverse Discrete Fourier Transform (IDFT) of vector  $X$ .

8. Compare the reconstructed pattern of the AUT from (3.22) with the simulated result

$$P_{ideal-AUT}(\phi, f).$$

## 3.4 Simulation Examples

### 3.4.1 Example I: One PEC Plate Serve as a Reflector

To verify the idea, numerical examples were simulated using different antennas, a horn antenna, a helical antenna, and a Yagi antenna. The horn antenna is set to be the reference antenna and the probe antenna for all the examples. It is interesting to observe that in this methodology the probe antenna need not be small. The goal is to remove the effects of the extraneous fields due to the presence of PEC reflectors and retrieve the free space radiation pattern of the helical antenna and the Yagi antenna. For all the examples, we assume that the environment does not vary with time.

The simulation model, shown in Figure 3.3, is a model similar to the first example shown in Figure 2.2. The model includes two antennas; on the right side is a horn antenna as the probe, while on the left side is the AUT. There are two different AUTs, Figures 2.3 and 3.4 give dimensions of the helical antenna and the 6-element yagi antenna. And Figure 2.4 shows the dimensions of the horn antenna (reference antenna and the probe antenna). The PEC plate serves as the reflector, and is 1.25 meter away from the two antennas. As mentioned in Section 3.1, one condition needs to be satisfied is that the

current distribution on the feed dipole should remain close to the ideal one. And an approximation for the “safe” distance would be the free space far-field distance  $2D^2 / \lambda$ , which is 1.12 meter ( $D$  is 0.155 meter as the largest diagonal size of the antennas). So we designed the distance between the PEC plate and the antenna to be 1.25 meter. Figure 3.5 gives the real and imaginary part of the current distribution on the feed dipole of the helical antenna, and it shows that they are not affected by the PEC plate (the current distribution on the other antenna is omitted due to limited space).

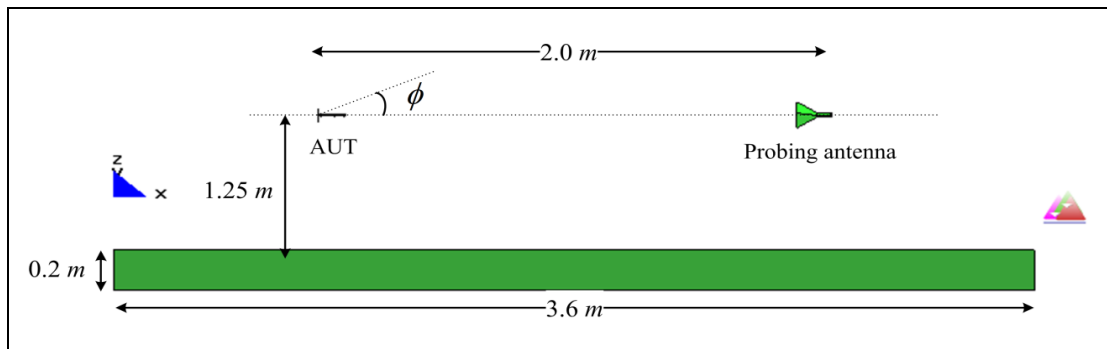


**Figure 3.3** Model of the measurement system with one PEC plate as the reflector.

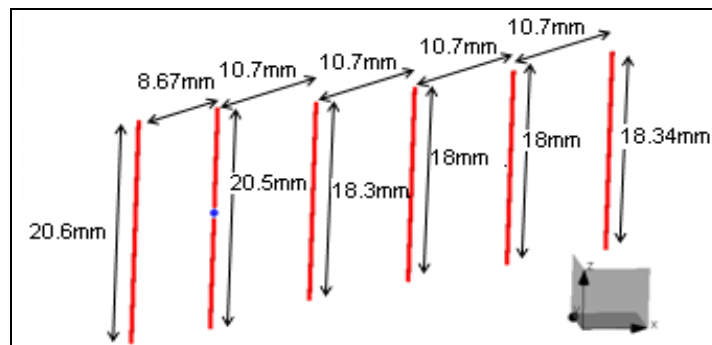


**Figure 3.4** Dimensions of the 6-element yagi antenna model (AUT).

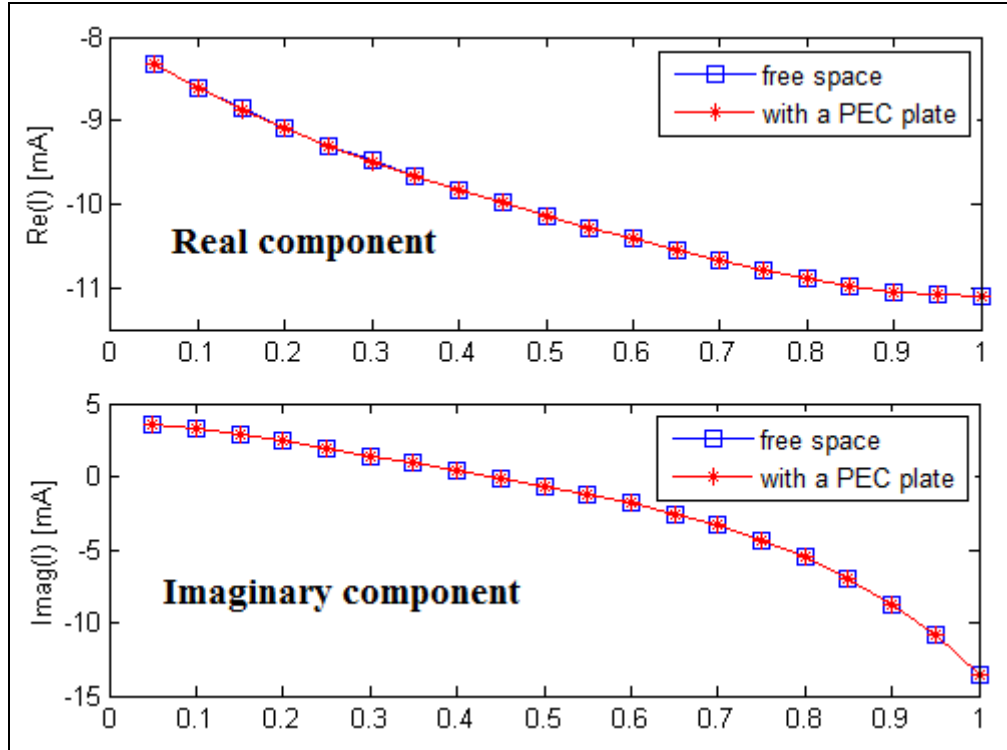
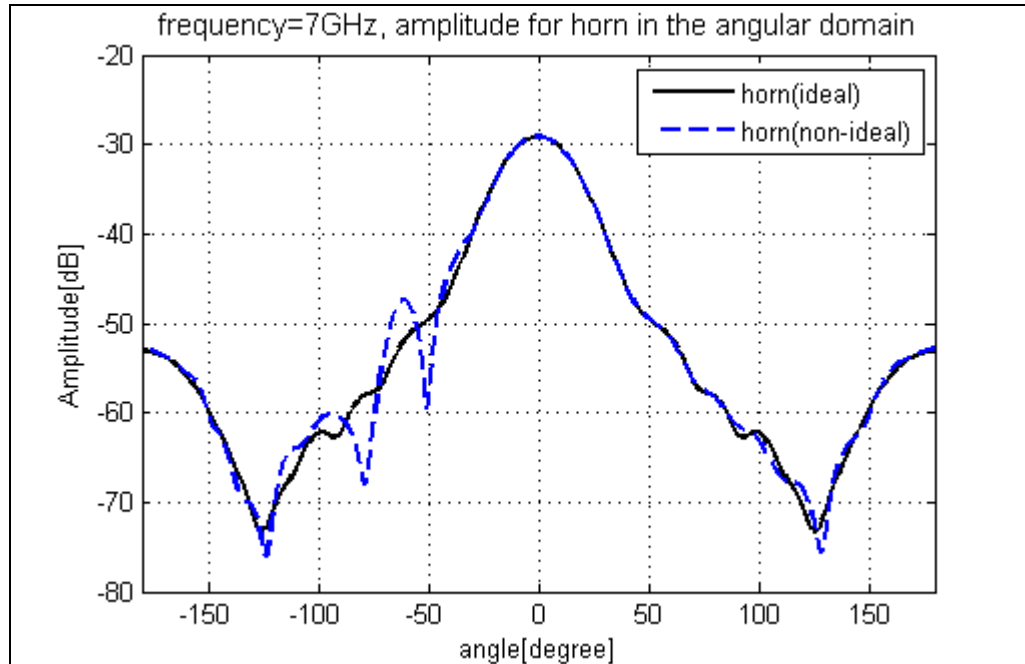


**Figure 3.5** Current distribution on the feed dipole of the helical antenna with one PEC plate.

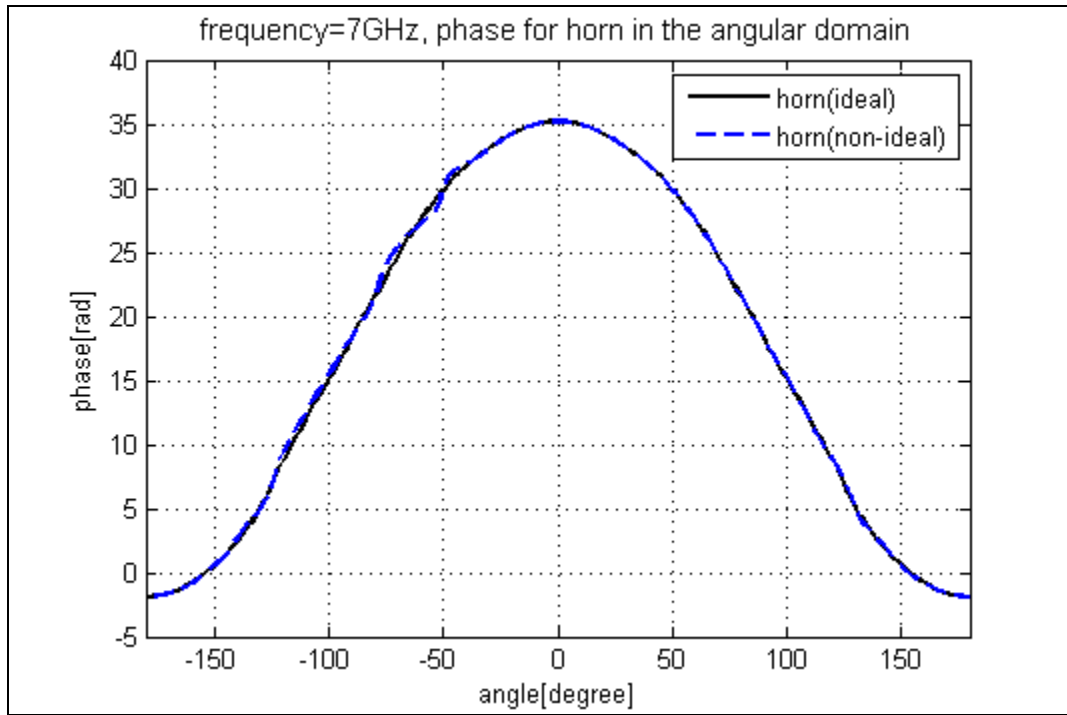
The numerical simulations and the simulation data processing followed the procedures as described in Section 3.3. The azimuth angle  $\phi$  of the AUT was varied from  $-180^\circ$  to  $179^\circ$  with a  $1^\circ$  step. The  $S_{21}$  data was collected at each azimuth angle  $\phi$  to form the plot of the radiation pattern. Equation 3.22 was used to calculate the reconstructed pattern for the AUT. And the reconstructed results were compared with the simulated ideal pattern of the AUT to illustrate the performance of the deconvolution method.

Note that using the PEC plate instead of a dielectric plate as the reflector is to increase the level of reflections and make the environmental effects as strong as possible. Therefore the presence of PEC plates will greatly distort the radiation pattern of the AUT and the performance of the deconvolution method on pattern reconstruction can be demonstrated more clearly.

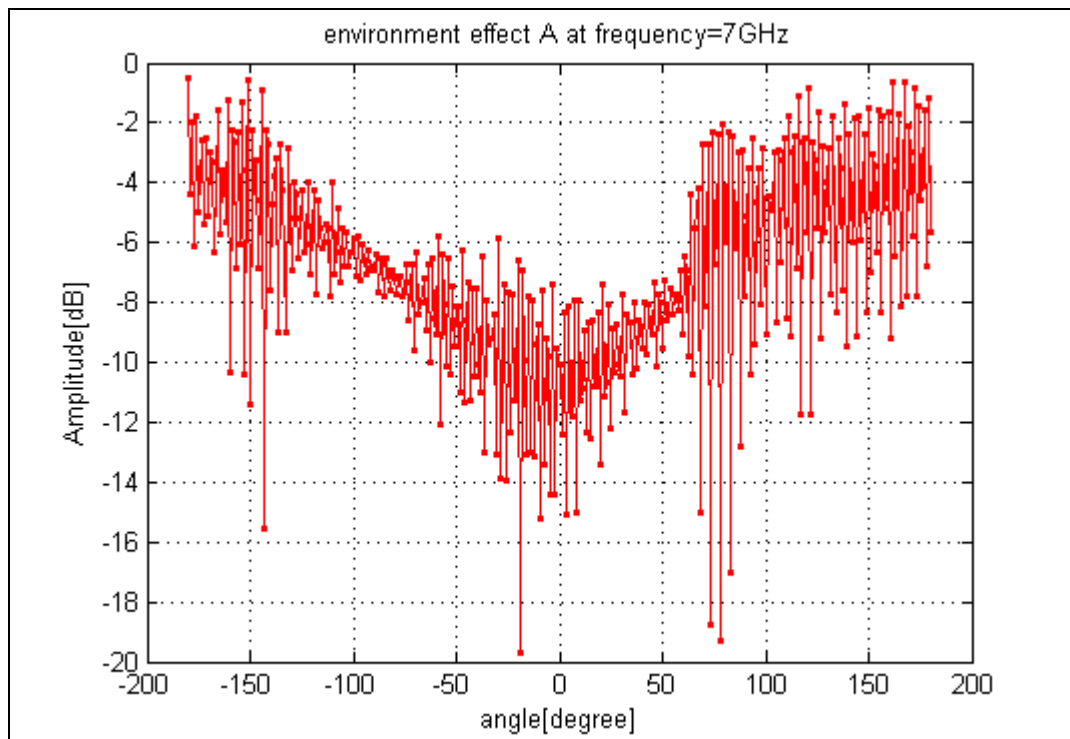
Figure 3.6 shows the comparison of the amplitude pattern for the horn antenna with and without the PEC reflector at 7 GHz; while Figure 3.7 shows the phase component of the radiation pattern. The blue dashed line termed *non-ideal* is the result in the presence of the PEC reflector, while the black line is for the free space radiation pattern. It is easy to observe the difference of the two curves due to the reflection between the azimuth angles  $-40^\circ$  and  $-130^\circ$ , where the main beam of the horn antenna is pointing at the PEC plate. The environmental response  $A(\phi, f)$  extracted from the model is shown in Figure 3.8.



**Figure 3.6** Amplitude pattern for the horn antenna with one PEC plate as the reflector.



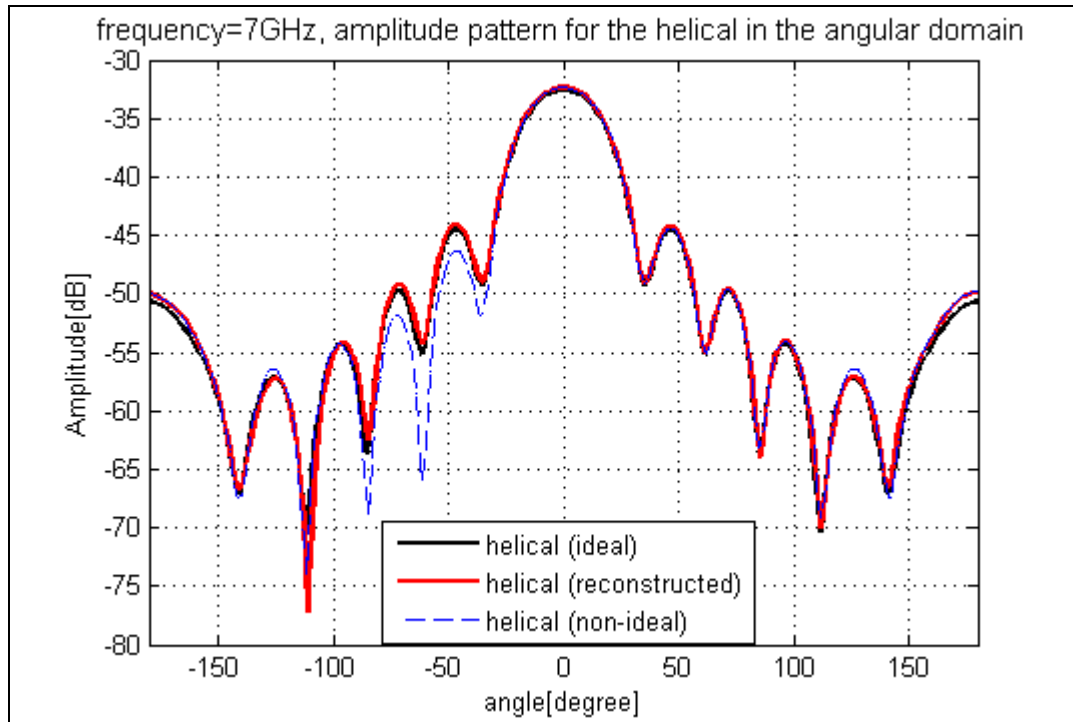
**Figure 3.7** Phase pattern for the horn antenna with one PEC plate as the reflector.



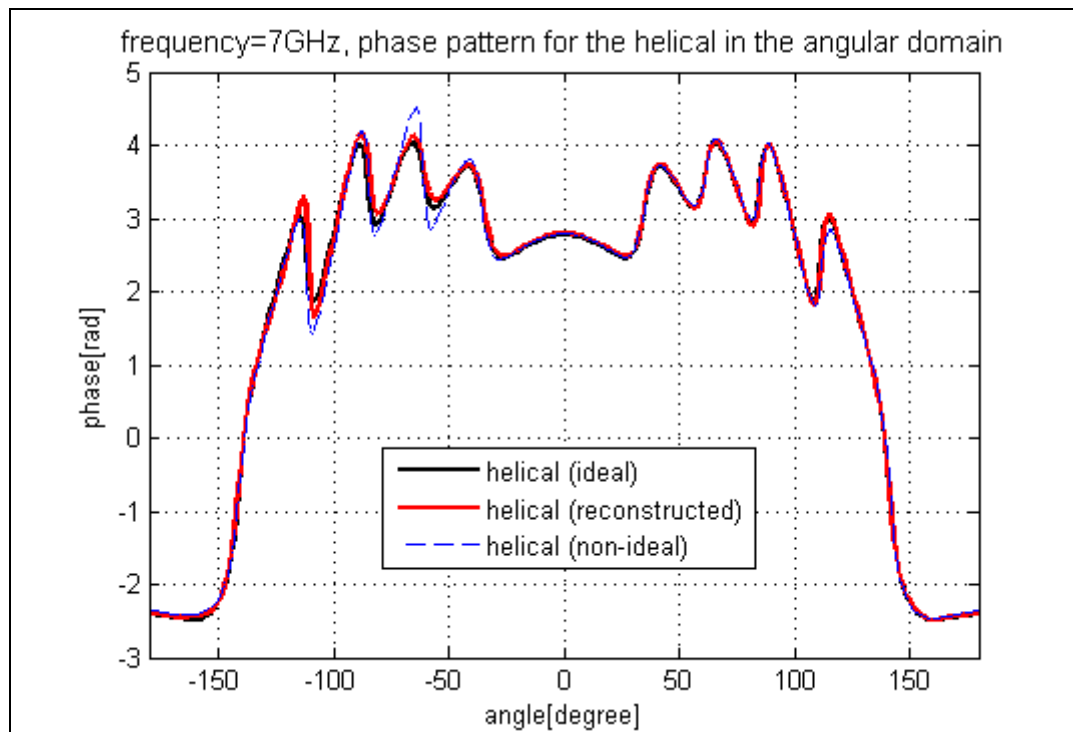
**Figure 3.8** Amplitude of the environmental effects when one PEC plate is used as the reflector.

Figure 3.9 shows the comparison of the amplitude pattern for the helical antenna with and without the PEC reflector at 7 GHz; while Figure 3.10 shows the phase component. The blue dashed line termed *non-ideal* is the result in the presence of the PEC reflector while the reconstructed pattern is indicated by the red line termed *reconstructed*. We want to reconstruct the pattern from this non-ideal data, and by substituting the environmental response data, we can obtain a clean pattern for the helical antenna. We can see that the reconstructed pattern is very close to the ideal pattern of the helical antenna. Therefore, it indicates that the reflections and diffractions caused by the PEC plate have been extracted out by using the deconvolution method. Compared with the result of FFT-based method shown in Figure 2.9 and Figure 2.10, the deconvolution method generates better results.

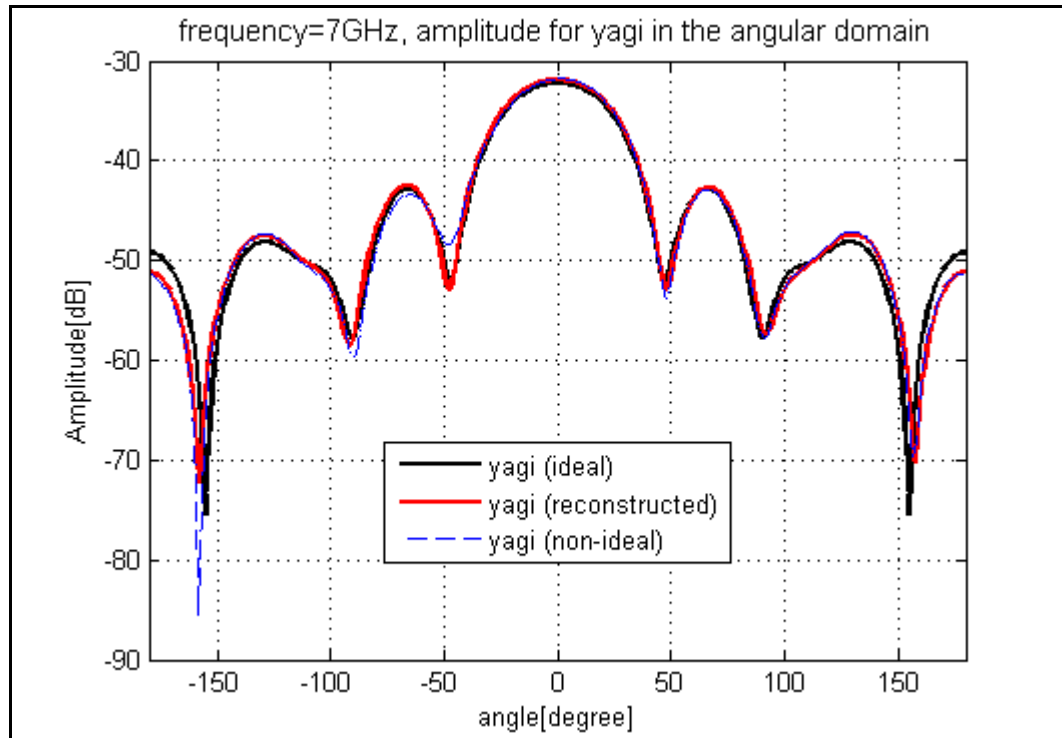
Similarly, we can also apply the deconvolution method to reconstruct a clean radiation pattern for the 6-element yagi antenna using data measured in a non-anechoic environment. For the same environment, we replace the helical antenna with the 6-element yagi antenna. And by substituting the environmental response data, we can similarly obtain a clean pattern for the yagi. Figure 3.11 shows the comparison of the amplitude pattern for the yagi antenna with and without the PEC reflector at 7 GHz; while Figure 3.12 shows the phase component. Again, we can observe that the reconstructed pattern has greatly reduced the presence of the undesired reflections from the plates in the measurements, and the processed result is very close to the ideal pattern of the yagi antenna.



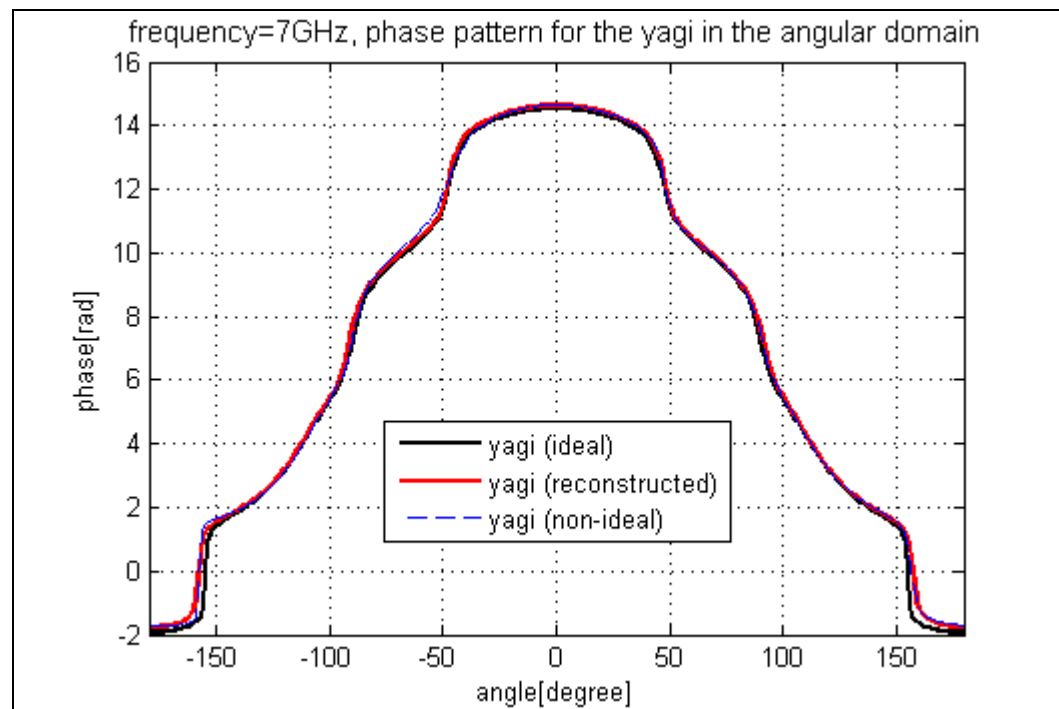
**Figure 3.9** Amplitude pattern for the helical antenna with one PEC plate as the reflector.



**Figure 3.10** Phase pattern for the helical antenna with one PEC plate as the reflector



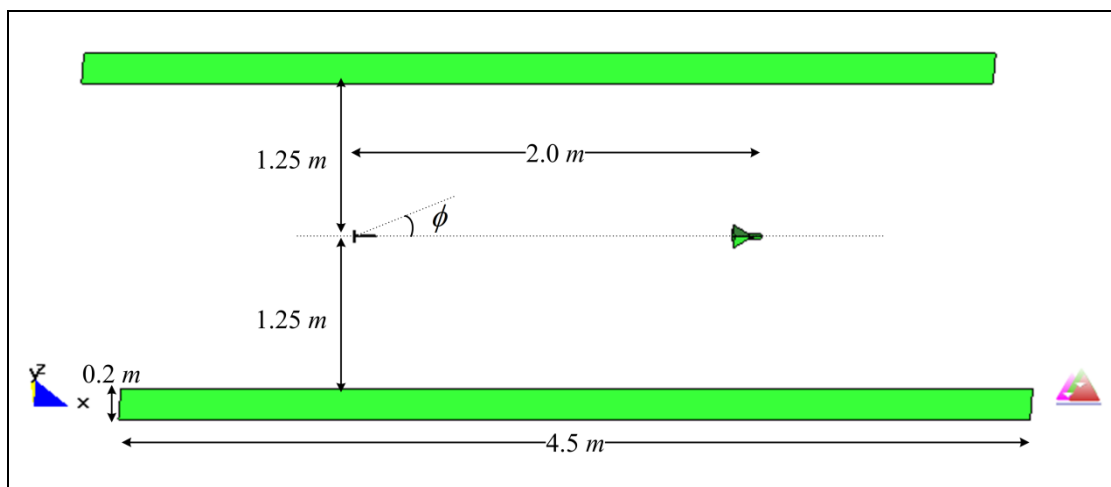
**Figure 3.11** Amplitude pattern for the yagi antenna with one PEC plate as the reflector



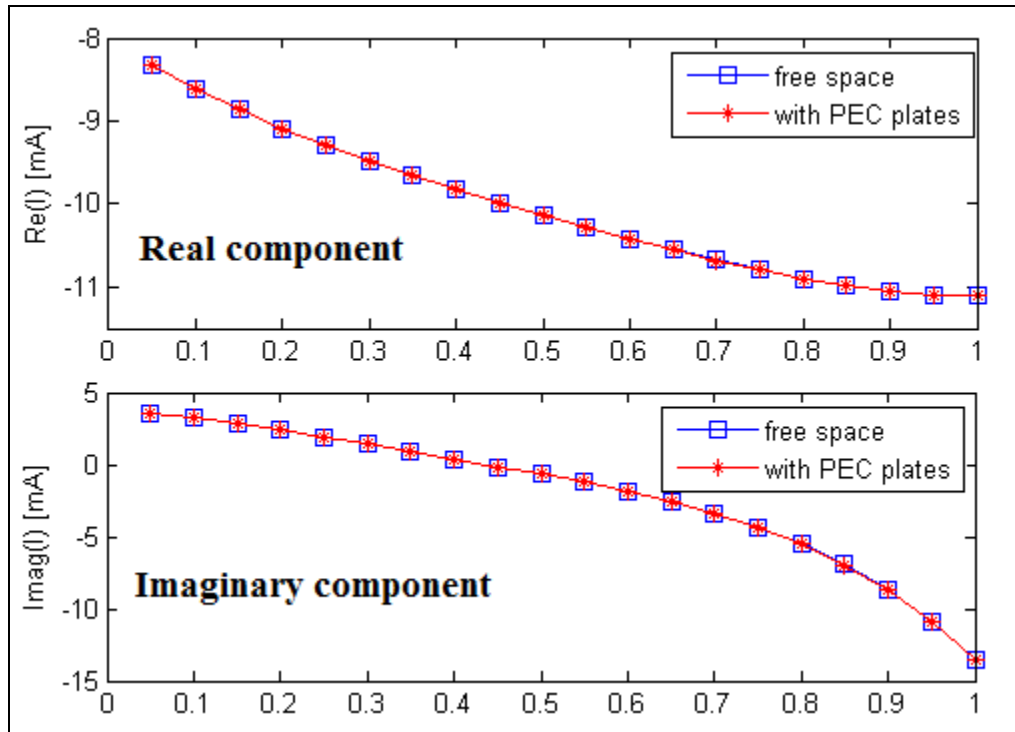
**Figure 3.12** Phase pattern for the yagi antenna with one PEC plate as the reflector

### 3.4.2 Example II: Two PEC Plates Serve as Reflectors

The previous example has shown the pattern reconstruction for the helical antenna and the 6-element yagi antenna using the data generated in a non-anechoic environment. That example presents a simple case with the presence of only one PEC plate, which is a very simple environment. To evaluate the deconvolution method using more complicated cases, we present the second example with two PEC plates as reflectors. Figure 3.13 shows the schematic diagram of the model, two PEC plates have the same size and are located at symmetric positions towards the antennas (the symmetry is applied to reduce the number of simulation points by half). The same procedure is applied as in Section 3.4.1 to reconstruct the radiation pattern for the helical antenna and the 6-element yagi antenna. Again, we need to check the current distribution on the feed dipole of the helical antenna. Figure 3.14 indicates that the current distribution is not affected by the PEC plates.



**Figure 3.13** Model of the measurement system with two PEC plates as the reflector.



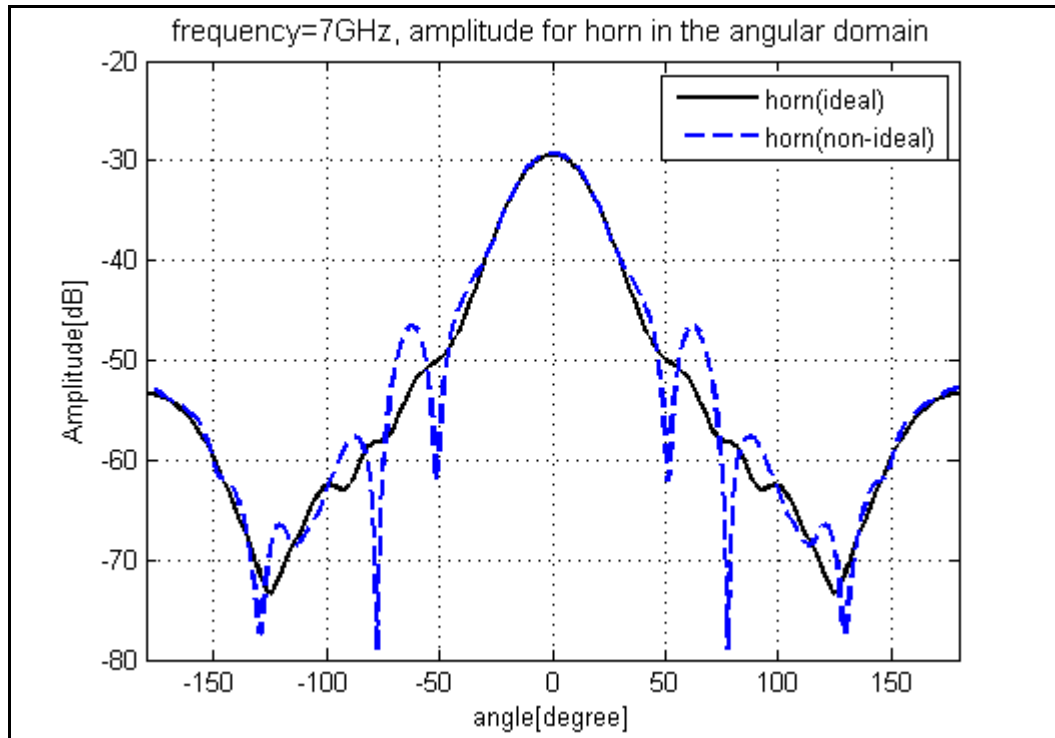
**Figure 3.14** Current distribution on the feed dipole of the helical antenna with two PEC plates.

Figure 3.15 shows the comparison of the amplitude pattern for the horn antenna with and without the PEC reflector at 7 GHz; while Figure 3.16 shows the phase component of the pattern. The blue dashed line indicates the result in the presence of the PEC reflectors. It is easy to observe that there are large reflections between the azimuth angles range  $[-40^\circ, -130^\circ]$  and  $[40^\circ, 130^\circ]$ , where the main beam of the horn antenna is pointing at the PEC plates. The environmental response  $A(\phi, f)$  extracted from the model is shown in Figure 3.17.

Figure 3.18 shows the comparison of the amplitude pattern for the helical antenna with and without the PEC reflector at 7 GHz; while Figure 3.19 shows the phase component of the pattern. The blue dashed line termed *non-ideal* indicates the result in the presence of the PEC reflector, the reconstructed pattern is indicated by the red line termed *reconstructed*.

Compared with the example in Section 3.4.1, the reflected response for this example is stronger. Still, we see that the reconstructed pattern is very close to the ideal pattern. This indicates that the echoes caused by the PEC plates have been successfully compensated by using the deconvolution method.

Similarly, we also applied the deconvolution method to reconstruct a clean radiation pattern for the 6-element yagi antenna. Figure 3.20 shows the comparison of the amplitude pattern for the yagi antenna with and without the PEC reflector at 7 GHz; while Figure 3.21 shows the phase component of the pattern. Again, we can observe that the reconstructed pattern is very close to the ideal pattern of the yagi antenna.



**Figure 3.15** Amplitude pattern for the horn antenna with two PEC plates as the reflector.

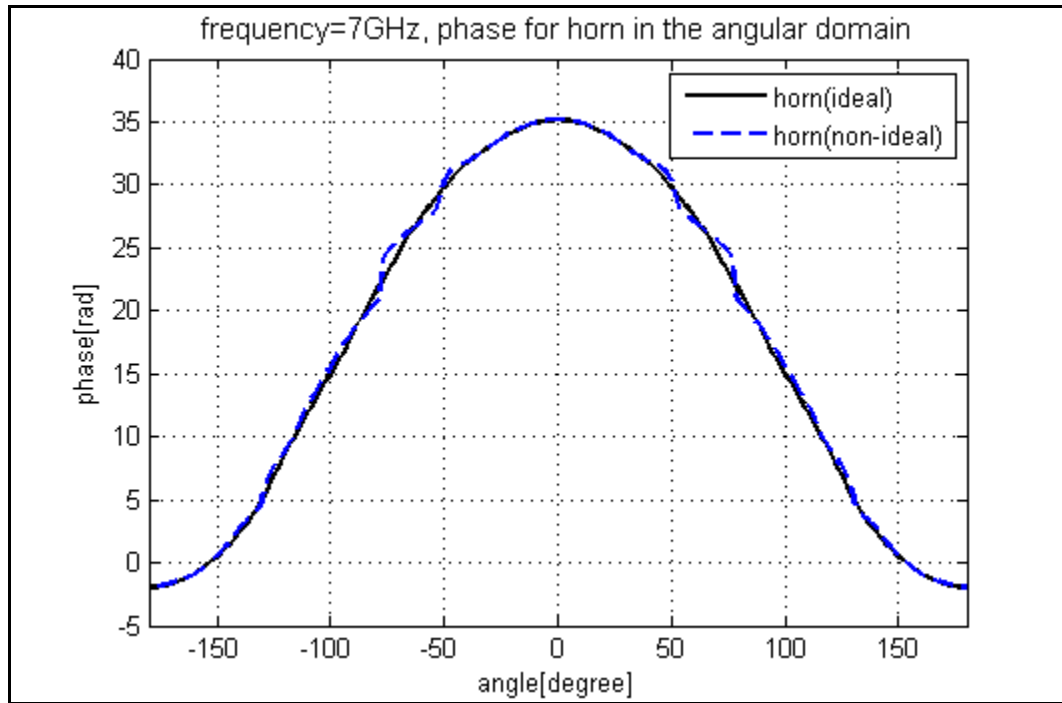


**Figure 3.16** Phase pattern for the horn antenna with two PEC plates as the reflector.

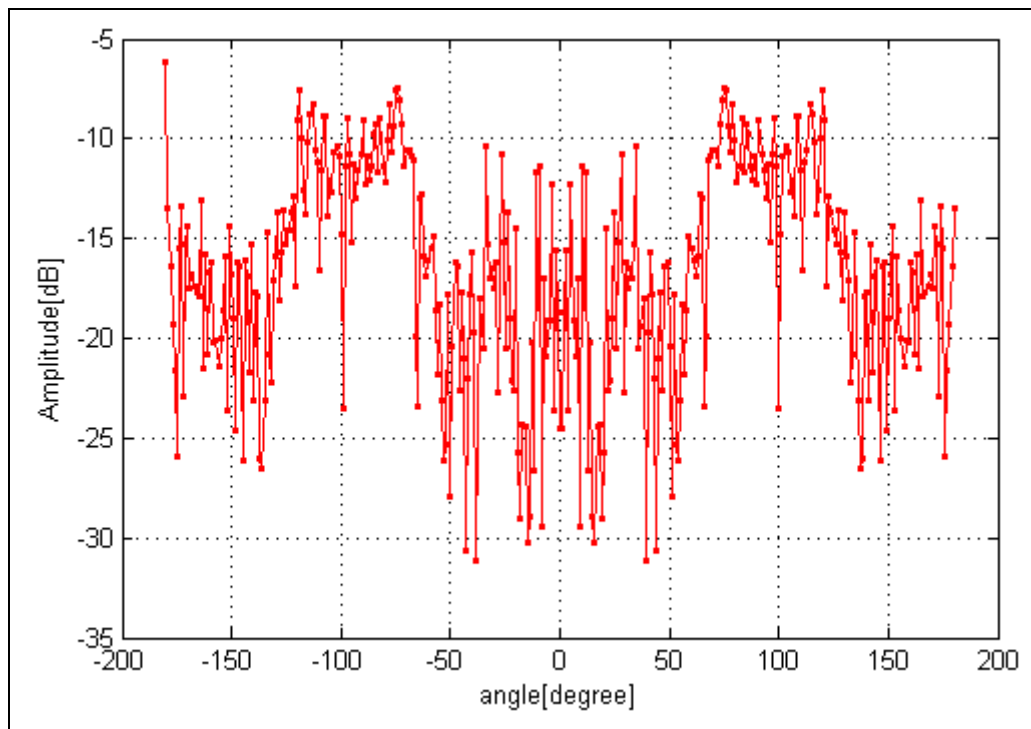


**Figure 3.17** Amplitude of the environmental effects when two PEC plates are used as the reflector.

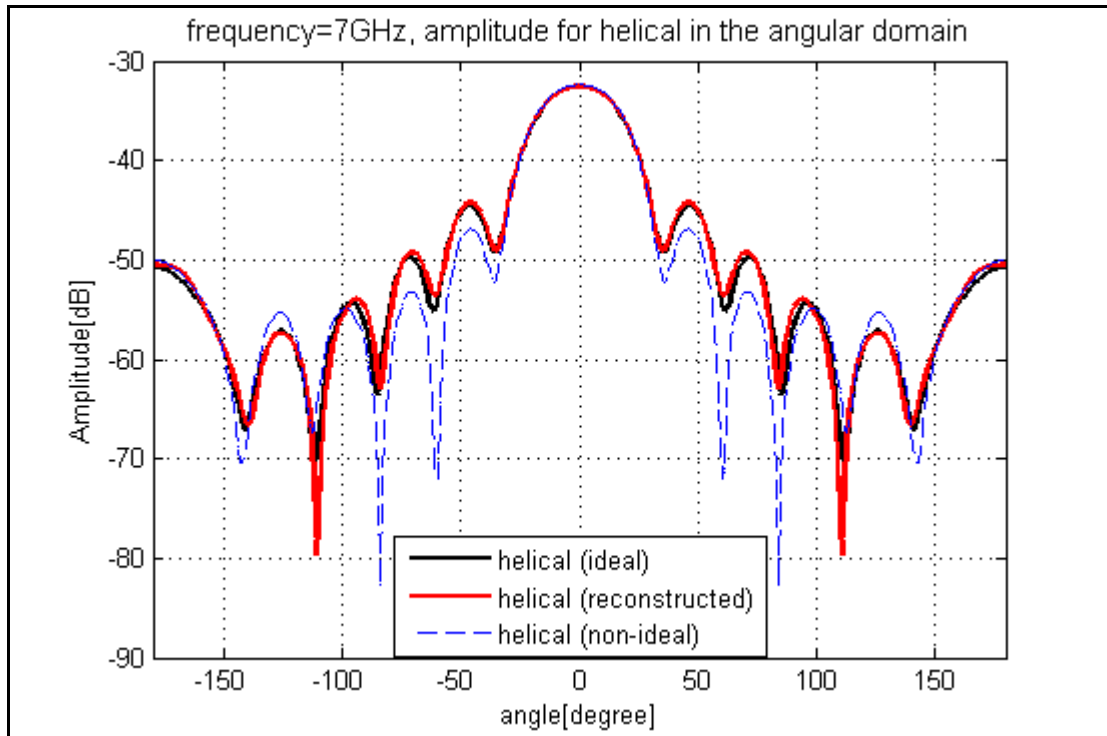


**Figure 3.18** Amplitude pattern for the helical antenna with two PEC plates as the reflector.

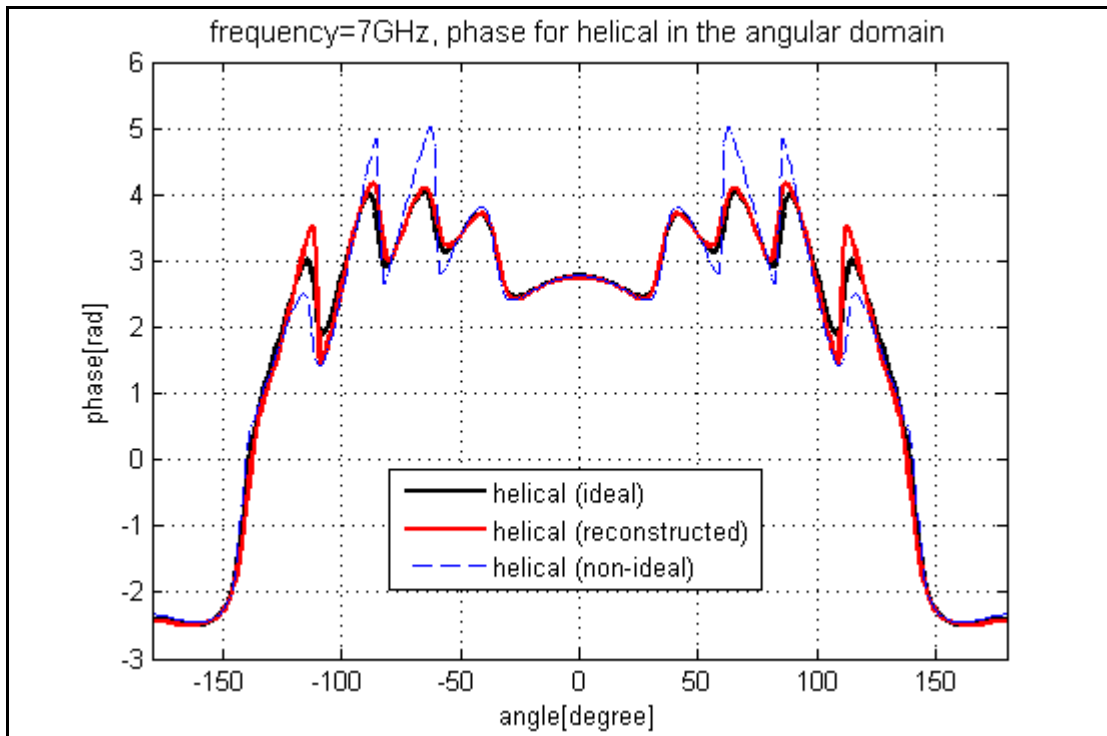


**Figure 3.19** Phase pattern for the helical antenna with two PEC plates as the reflector.

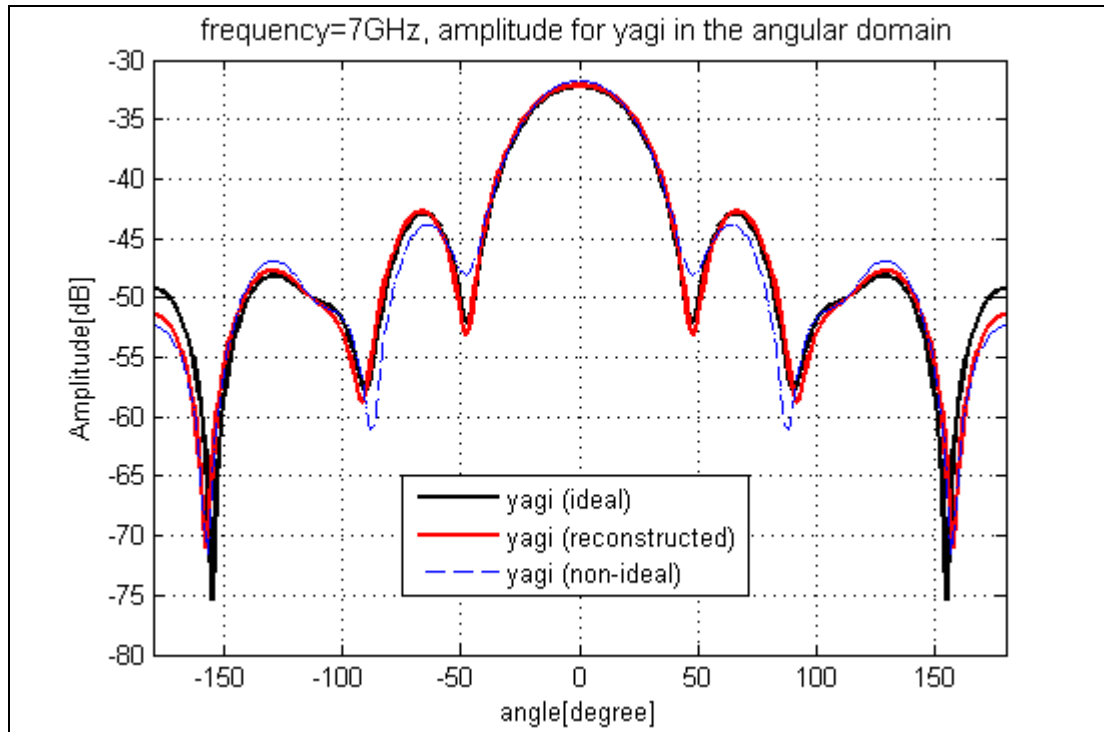


**Figure 3.20** Amplitude pattern for the yagi antenna with two PEC plates as the reflector.

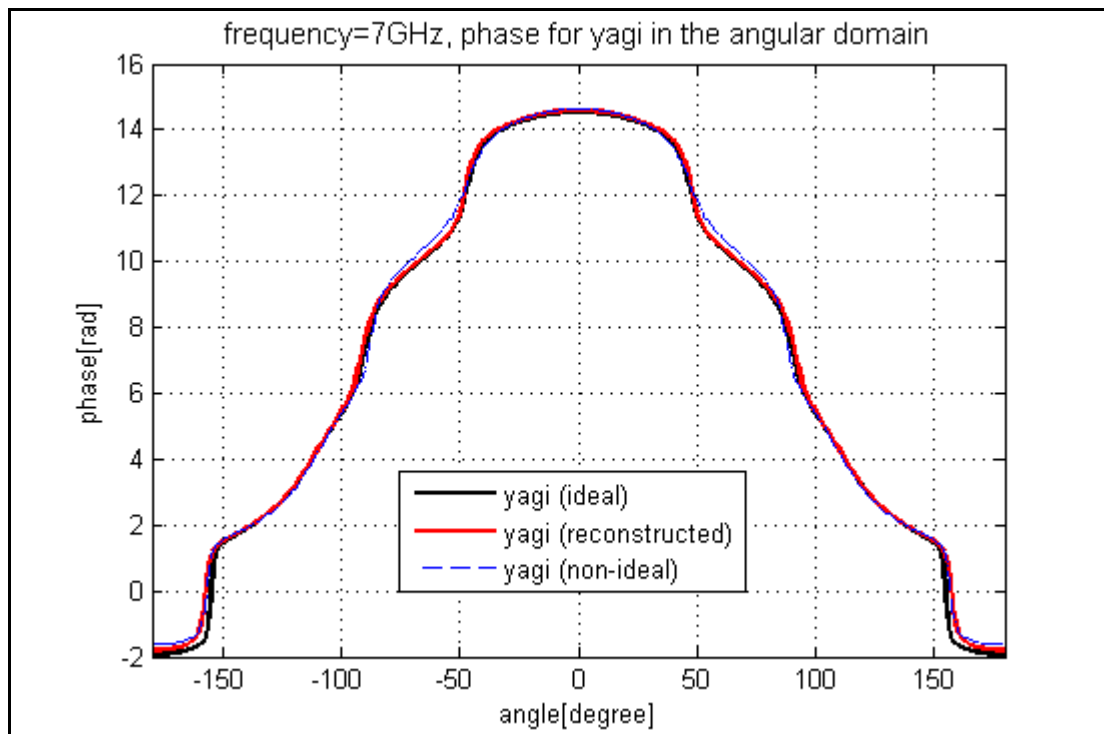


**Figure 3.21** Phase pattern for the yagi antenna with two PEC plates as the reflector.

### 3.4.3 Example III: Four Connected PEC Plates Serve as Reflectors

This third example presents a more complicated case, to fully evaluate the deconvolution method for the pattern reconstruction from the data measured in a non-anechoic environment. This example uses four connected PEC plates as the reflectors around the antenna, as shown in Figure 3.22. Four PEC plates form a rectangular contour enclosing the AUT and the probe antenna. The entire model is  $4.5\text{ m}$  long and  $2.5\text{ m}$  wide. Similarly, we need to check the current distribution on the feed dipole of the helical antenna. Figure 3.23 shows that the current distribution is slightly affected by the PEC plates.

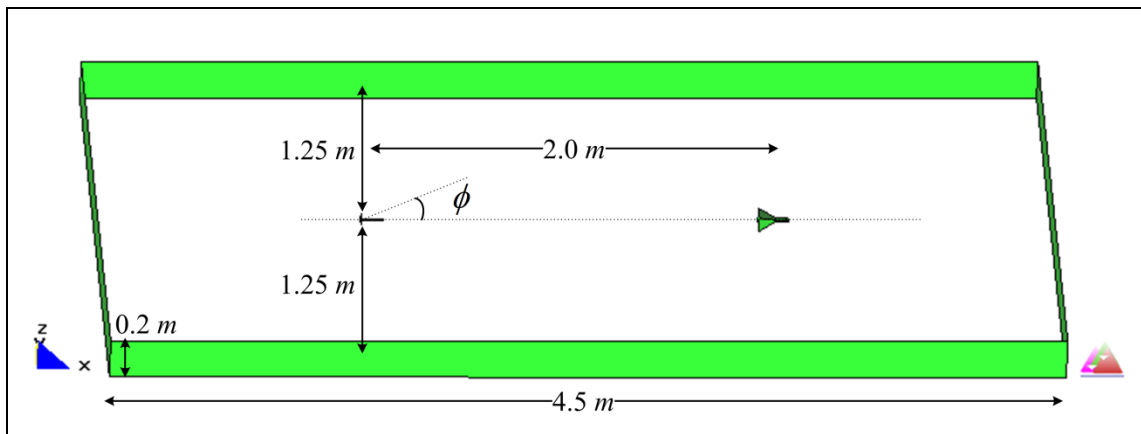


**Figure 3.22** Model of the measurement system with four PEC plates as the reflector.

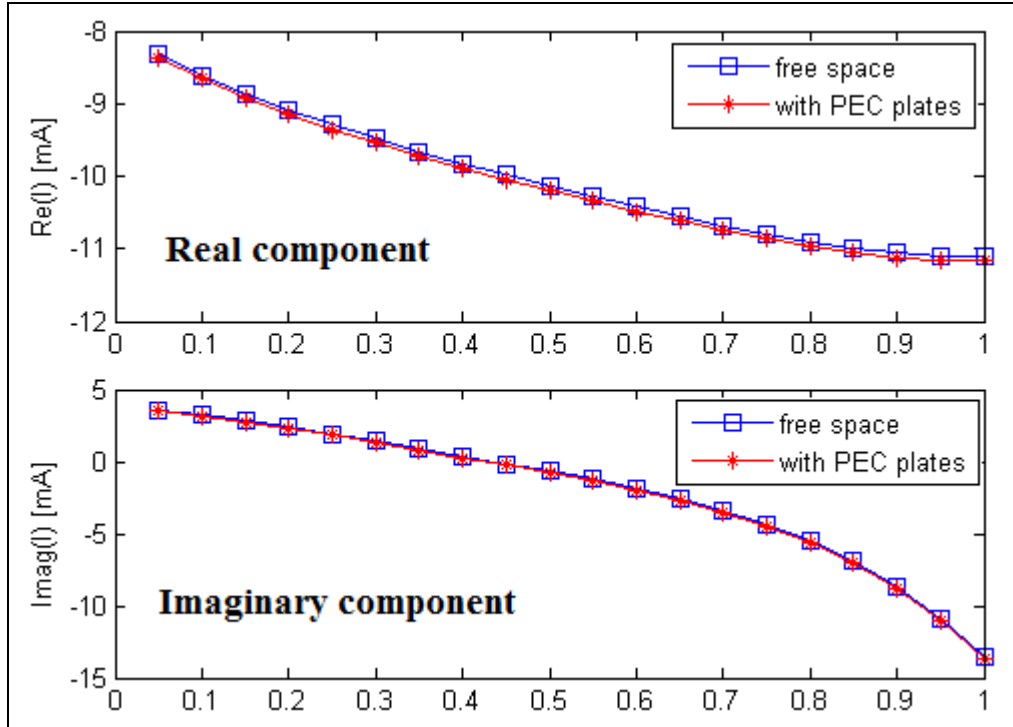


**Figure 3.23** Current distribution on the feed dipole of the helical antenna with four PEC plates.

The same procedure was carried out to reconstruct the radiation pattern for the helical antenna and the 6-element yagi antenna. Figure 3.24 shows the comparison of the amplitude pattern for the horn antenna with and without the PEC reflector at 7 GHz; while Figure 3.25 shows the phase component of the pattern. The blue dashed line termed *non-ideal* is the result in the presence of the PEC reflectors. It is easy to observe that the reflection responses affect the radiation pattern of the antenna for all azimuth angles; especially the back lobe level of the pattern has been greatly increased due to the PEC plates. The environmental response  $A(\phi, f)$  extracted from the model is shown in Figure 3.26.

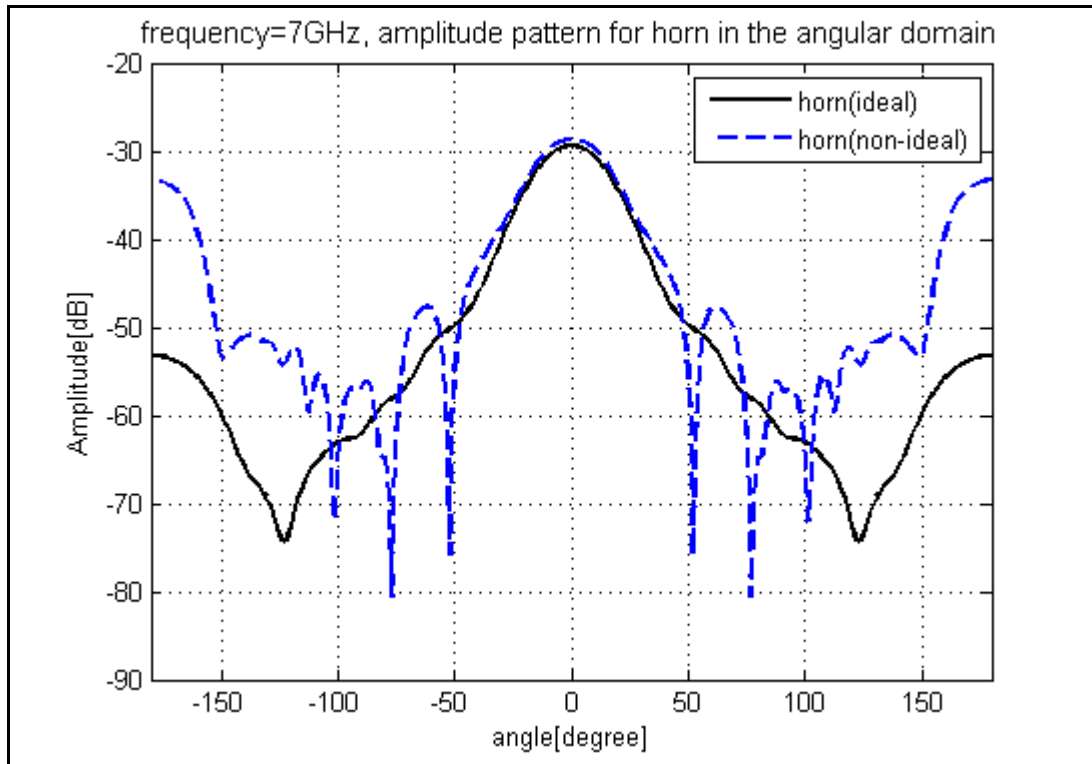


**Figure 3.24** Amplitude pattern for the horn antenna with four PEC plates as the reflector.

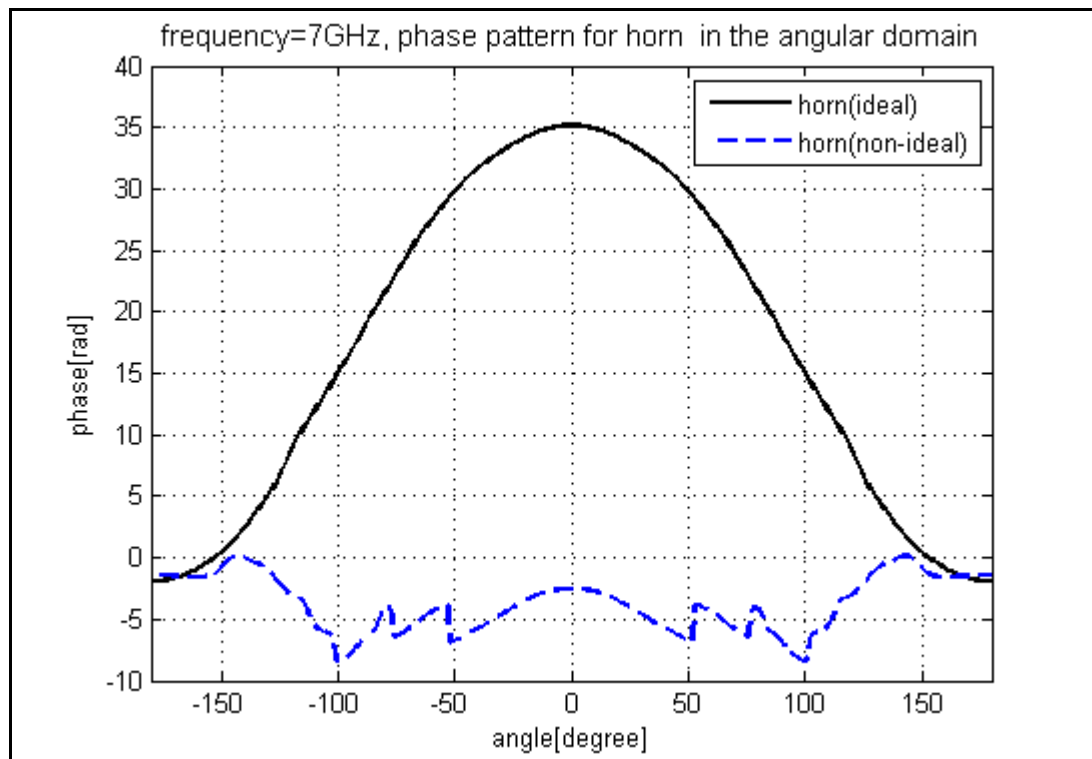


**Figure 3.25** Phase pattern for the horn antenna with four PEC plates as the reflector.

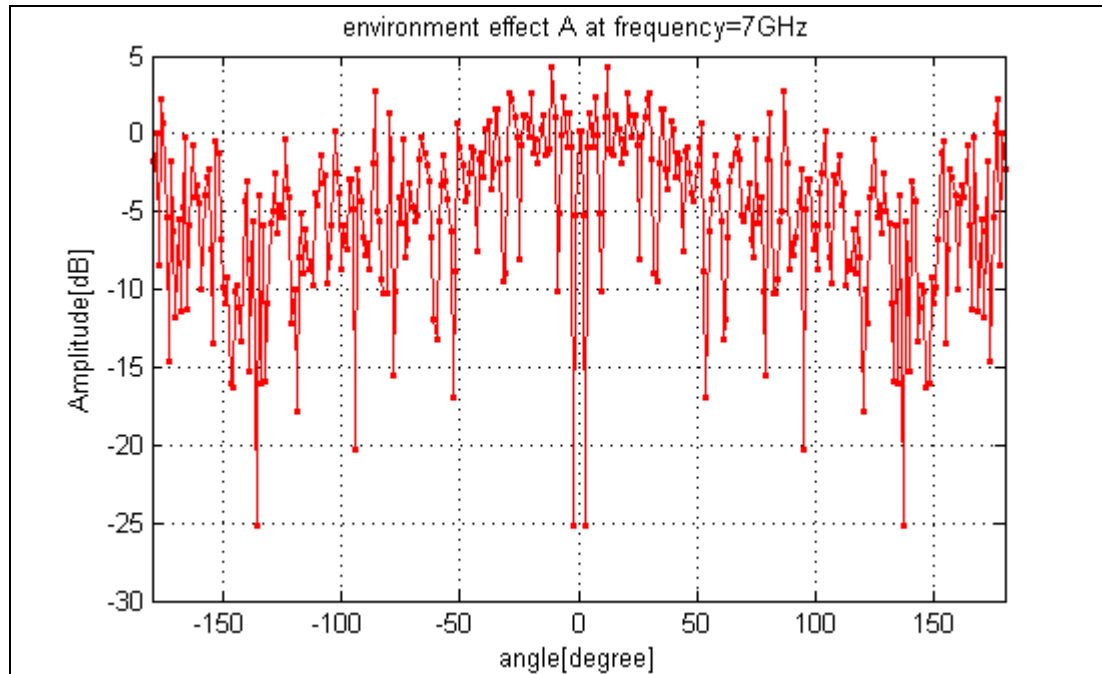


**Figure 3.26** Amplitude of the environmental effects when four PEC plates are used as the reflector.

The reconstructed pattern for the helical antenna is given in Figures 3.27 and 3.28. Figure 3.27 shows the comparison of the amplitude pattern with and without the PEC reflectors at 7 GHz; while Figure 3.28 shows the phase component. The blue dashed line termed *non-ideal* is the result in the presence of the PEC reflector, while the reconstructed pattern is indicated by the red line termed *reconstructed*. Compared with the example in Section 3.4.2, the reflected responses from the PEC plates for this example are much stronger for the back lobe level. However, deconvolution method still obtains a very good reconstructed pattern which is close to the ideal pattern of the helical antenna. This indicates that the reflection and diffraction contributions caused by the PEC plates have been successfully compensated by using the deconvolution method.

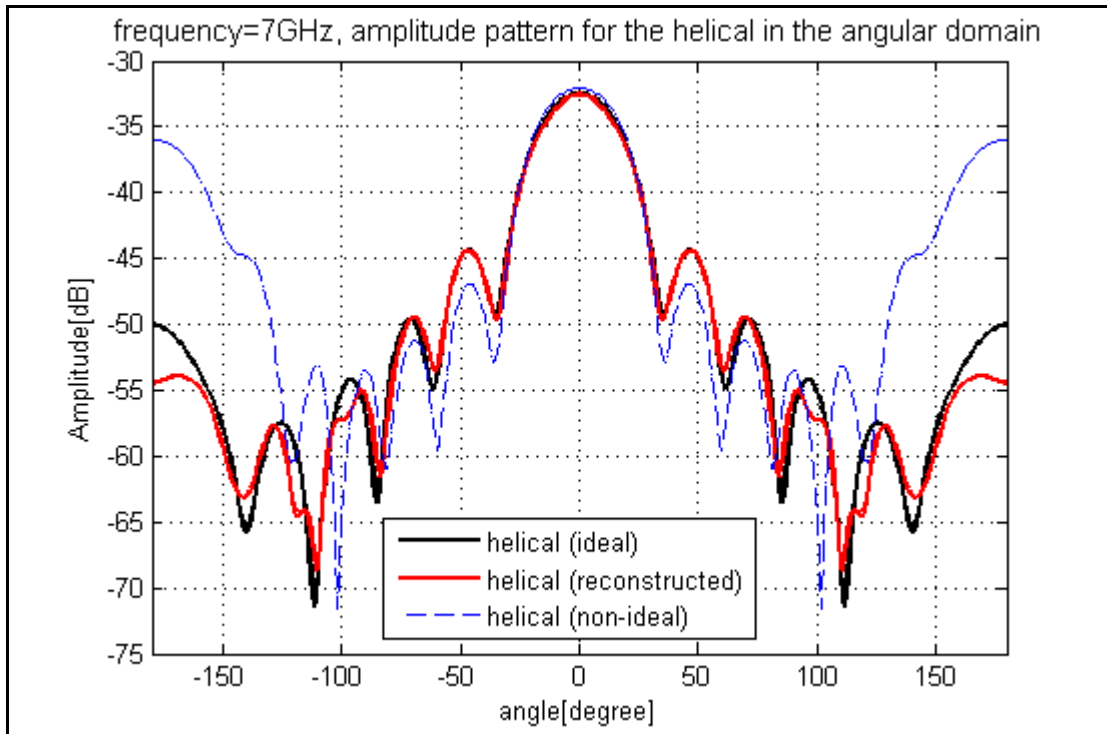


**Figure 3.27** Amplitude pattern for the helical antenna with four PEC plates as the reflector.

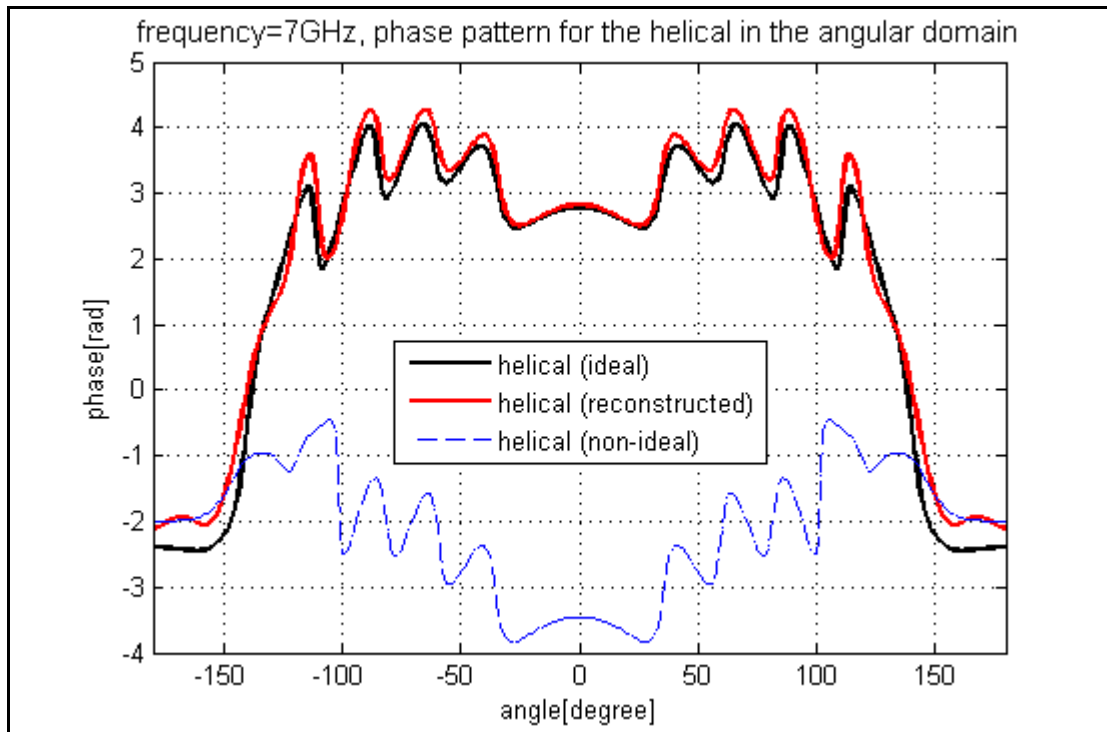


**Figure 3.28** Phase pattern for the helical antenna with four PEC plates as the reflector.

Similarly, we also applied the deconvolution method to reconstruct the pattern for the 6-element yagi antenna from its non-anechoic measured data. Figure 3.29 shows the comparison of the amplitude pattern for the yagi antenna with and without the PEC reflectors at 7 GHz; while Figure 3.30 shows the phase component of the pattern. Again, it is seen that the reconstructed pattern is very good.

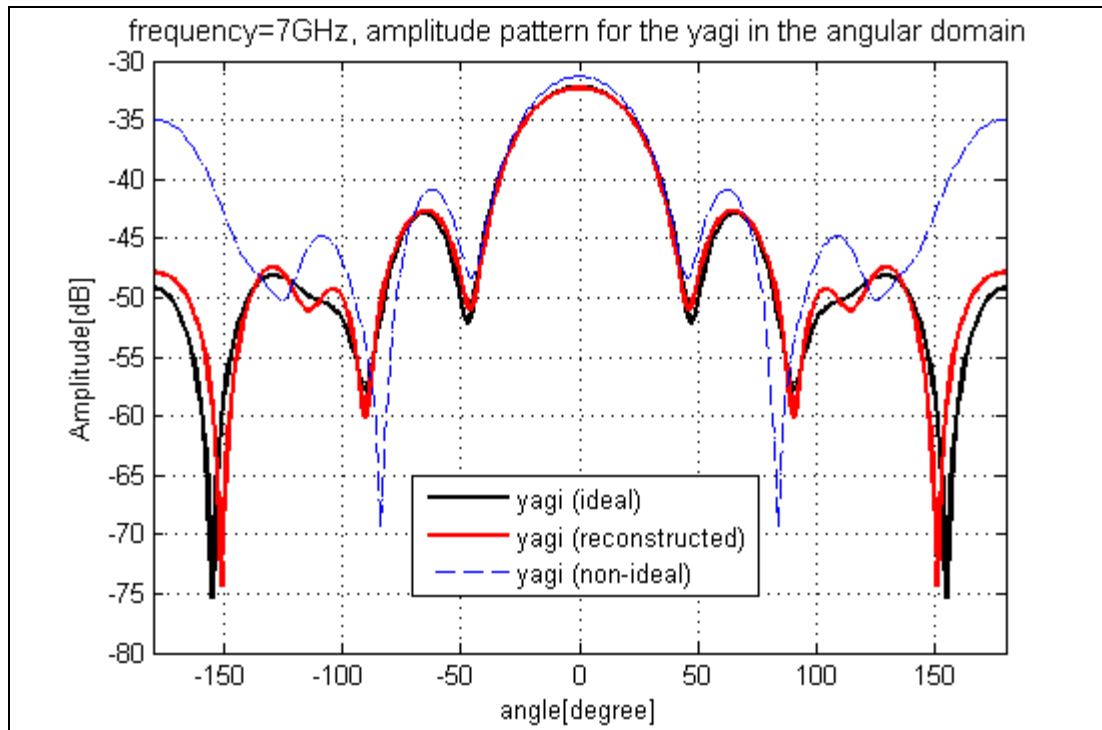


**Figure 3.29** Amplitude pattern for the yagi antenna with four PEC plates as the reflector.

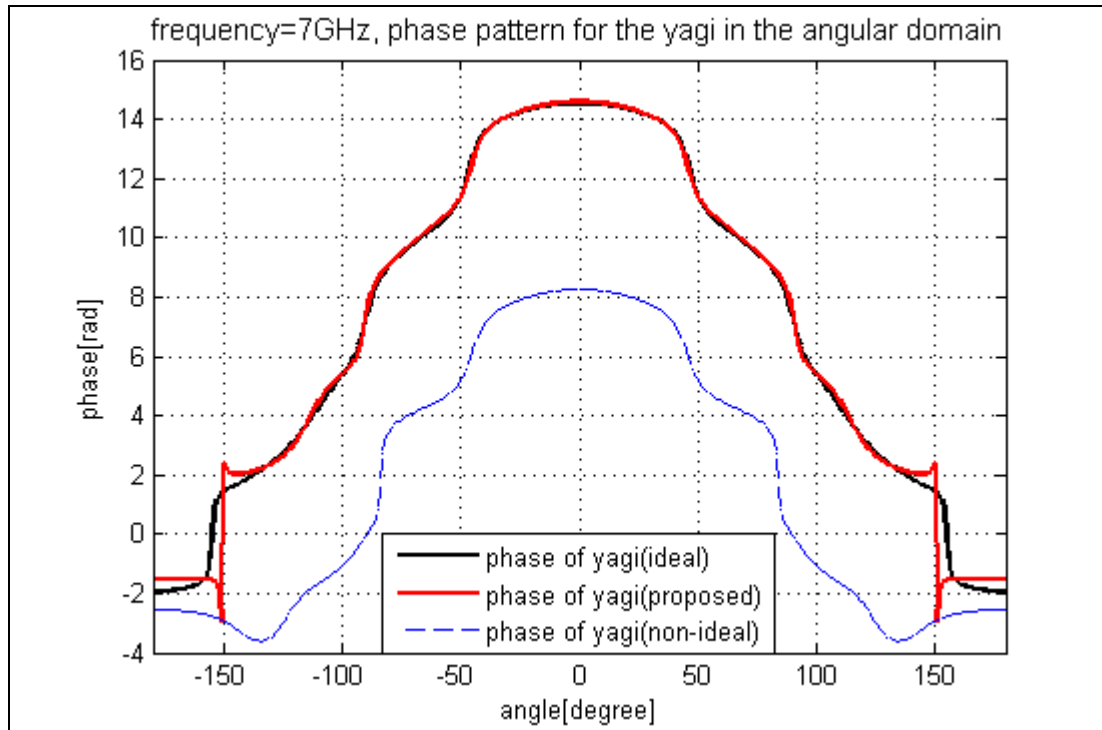


**Figure 3.30** Phase pattern for the yagi antenna with four PEC plates as the reflector.

#### 3.4.4 Example IV: Use of a Parabolic Reflector Antenna as the AUT

Previous examples have shown the deconvolution method working under three different environmental settings to reconstruct the pattern of a helical antenna and a yagi antenna. To better illustrate the applicability of the deconvolution method, we'd like to introduce a parabolic reflector antenna to be the AUT as an example for the pattern reconstruction. Figure 3.31 shows the model of a parabolic reflector antenna with its feeding component. The dish diameter  $D$  was first designed to be  $0.16\text{ m}$ , while the depth  $d$  was  $0.04\text{ m}$ , so the focal length  $f$  was calculated as  $f = D^2 / 16d = 0.04\text{ m}$ . The feeding element is a dipole antenna positioned at the focal point inside a waveguide.

By replacing the AUT as the parabolic reflector antenna, we carried out the same

reconstruction procedure to retrieve the radiation pattern of the AUT. Figure 3.32 shows the comparison of the amplitude pattern for the parabolic reflector antenna with and without the PEC plates at 7 GHz; while Figure 3.33 shows the phase component of the radiation pattern. The blue dashed line termed *non-ideal* is the result in the presence of PEC plates, the reconstructed pattern is indicated by the red line termed *reconstructed*. It is seen that the reconstructed pattern using the deconvolution method is close to the ideal pattern for the main lobe but does not fit well for the side lobes and the back lobe.

To find out the reason, we first look at the far-field distance for this parabolic reflector antenna which is  $2D^2/\lambda = 1.20$  meter ( $D$  is 0.16 meter as the diagonal size of the antenna). And the distance between the reflector and PEC plates is  $1.25 - 0.16/2 = 1.17$  m, which is smaller than the free space far-field distance in this model. This means the PEC plates are not in the free space far-field region of the parabolic reflector antenna, and this may distort the radiation pattern.

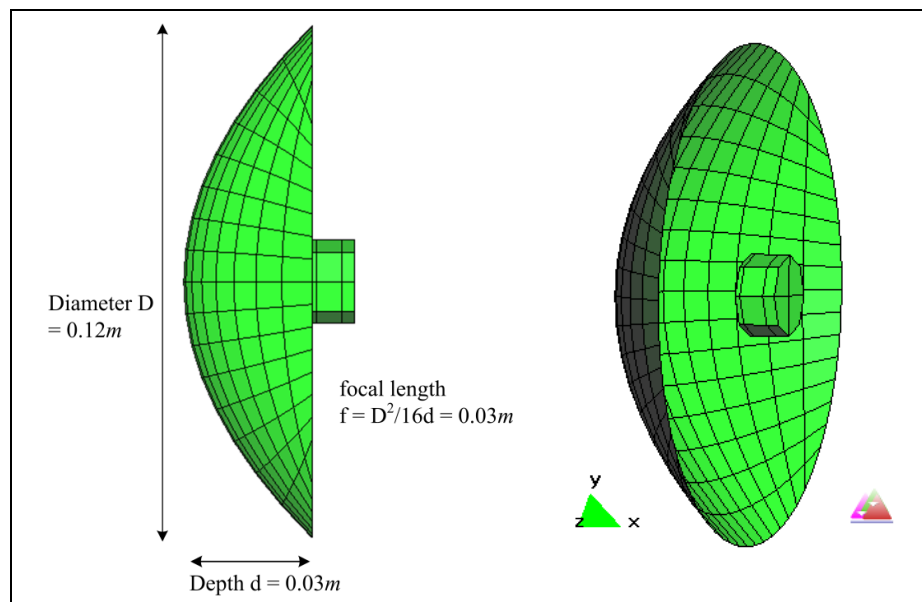


**Figure 3.31** Model of a parabolic reflector antenna with its feeding component.

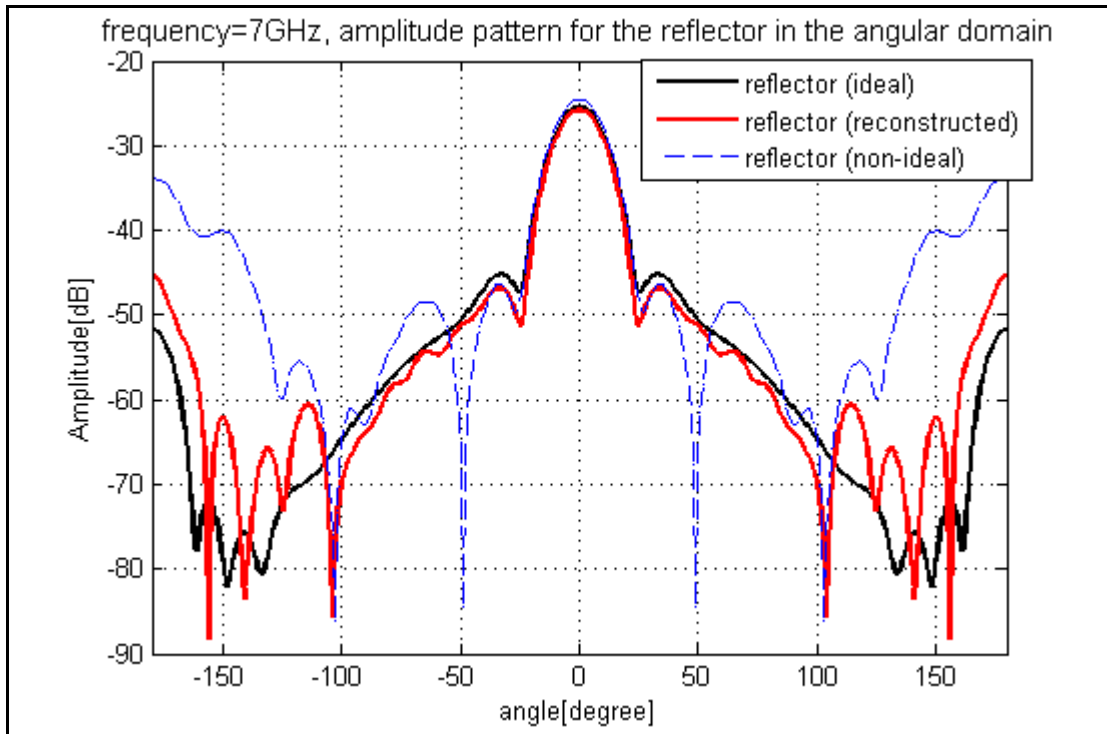


**Figure 3.32** Amplitude pattern for the parabolic reflector antenna.

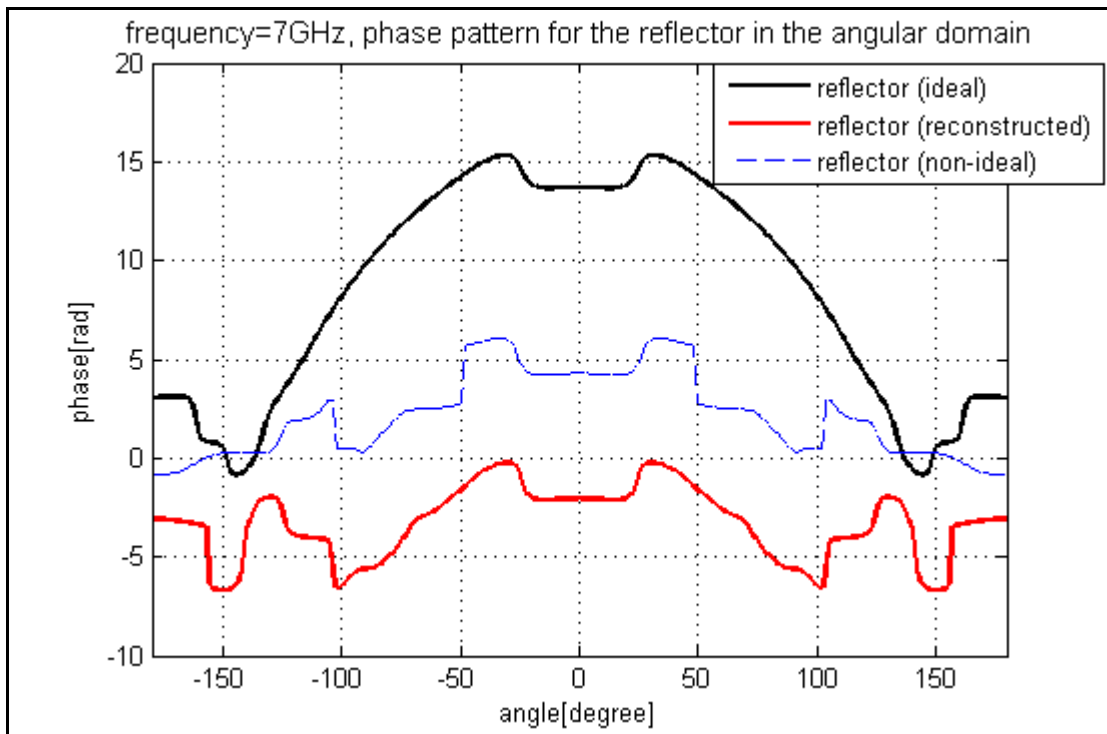


**Figure 3.33** Phase pattern for the parabolic reflector antenna.

Thus, the parabolic reflector antenna was re-designed and reduced in size to be of diameter  $D = 0.12 \text{ m}$ , depth  $d = 0.03 \text{ m}$ , and focal length as  $0.03 \text{ m}$ . so that the free space far-field distance is reduced to be  $2D^2 / \lambda = 0.67 \text{ meter}$  ( $D$  is  $0.12 \text{ meter}$  as the diagonal size of the antenna). Then, the distance between the reflector antenna and PEC plates is  $1.25 - 0.12/2 = 1.19 \text{ m}$ , which is larger than the free space far-field distance in the new model.

The same pattern reconstruction procedure was carried out for the new parabolic reflector antenna. Figure 3.34 shows the comparison of the amplitude pattern for the new parabolic reflector antenna with and without the PEC plates at  $7 \text{ GHz}$ ; while Figure 3.35 shows the phase component of the radiation pattern. The blue dashed line termed *non-ideal* is the result in the presence of PEC plates, the reconstructed pattern is indicated by the red line termed *reconstructed*. We can observe that the reconstructed pattern using the deconvolution method has been greatly improved for both the side lobes and the back lobe when compared with the previous parabolic reflector antenna model.

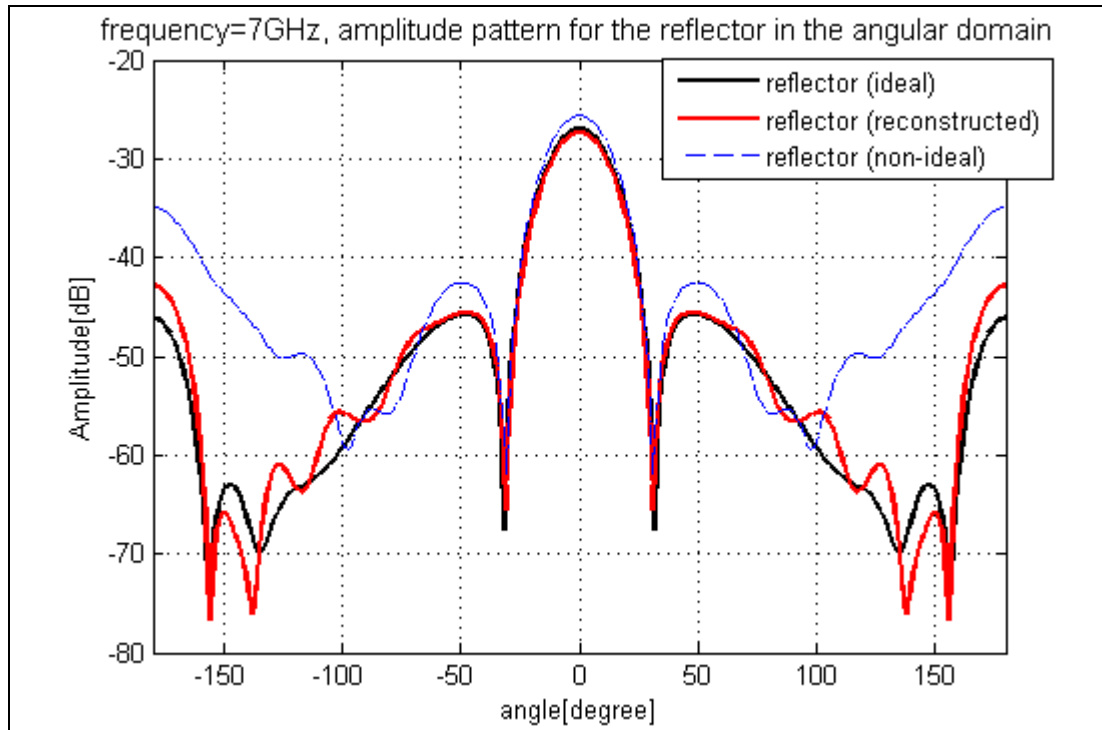


**Figure 3.34** Amplitude pattern for the new parabolic reflector antenna.

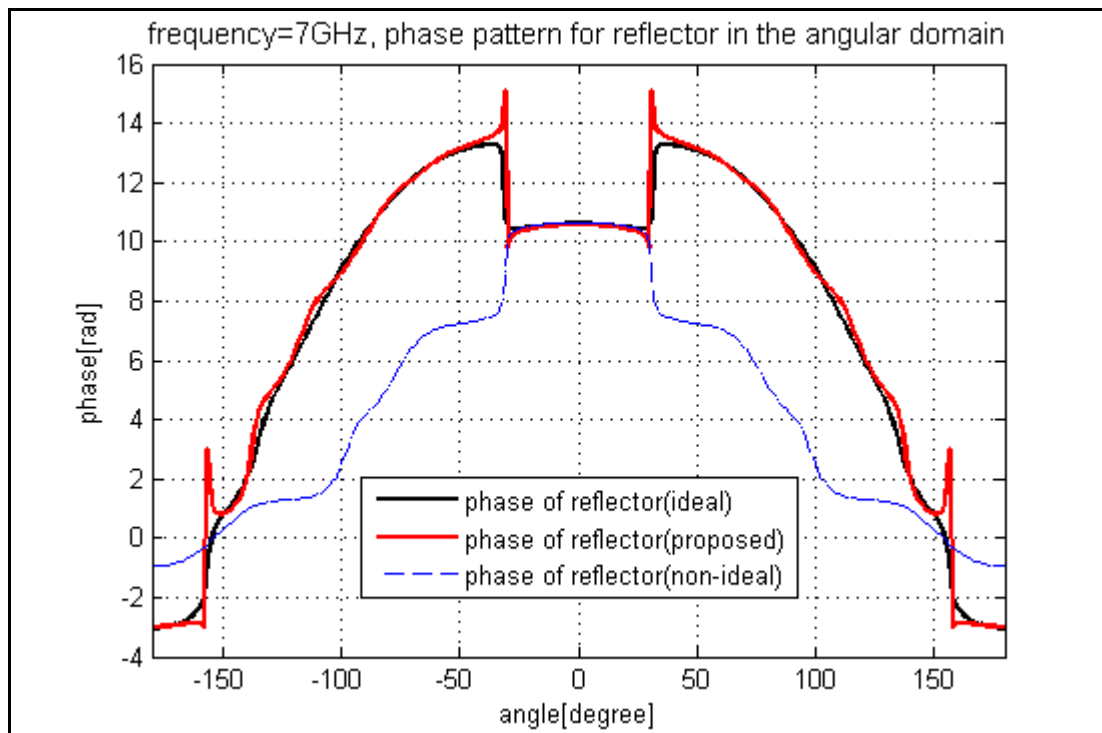


**Figure 3.35** Phase Amplitude pattern for the new parabolic reflector antenna.

## **Chapter 4**

# **Discussion on the Deconvolution Method for Radiation Pattern Reconstruction**

The previous chapter has introduced the deconvolution method to reconstruct the free space radiation pattern of an antenna using data measured in a non-anechoic environment. Numerical examples have been presented to show that under different environmental setup, the deconvolution method has successfully reconstructed the radiation pattern for a helical antenna, a 6-element yagi antenna, and a parabolic reflector antenna. Those examples demonstrate the general idea of the deconvolution method and give us the confidence to carry out more comprehensive analysis on it.

The deconvolution method is a general methodology for pattern reconstruction. In this chapter, we will present more examples to analyze the applicability of the method and find out what factors would limit its performance. We will first discuss the effect of different probe antennas, and then we will use different sizes of antennas to evaluate the method. After that, we will change the environmental effects by changing the size of PEC plates and compare the reconstructed results.

## 4.1 Effect of Different Probe Antennas

Previously, we have presented numerical examples with different AUTs to test the deconvolution method. For all those examples, we have used a standard gain horn antenna as the probe. Here, we will choose different probe antennas to change the effect of the probe and repeat the simulation examples to verify this method.

### *4.1.1 Example I: Use of a Yagi Antenna as the Probe*

For this example, we will keep the environmental setting as 4 PEC plates, the same as that in the example of Section 3.4.3, but replace the probe antenna with the yagi antenna, as shown in Figure 4.1. The reconstruction procedure is the same as before. We first used a standard gain horn as the AUT. With the presence of four PEC plates, we obtained a distorted radiation pattern of the horn in the simulation and can therefore extract the environmental effects based on its ideal pattern. Then, we replaced the horn with the helical/yagi antenna as the AUT, and we got the distorted radiation pattern of the helical/yagi antenna. By substituting the environmental effects, we can derive the free space radiation pattern of the helical/yagi antenna. The size for the yagi and the helical antenna are the same as in previous examples, as shown in Figures 3.4 and 2.3, respectively (for simplicity, we use the same yagi antenna as the probe and the AUT).

Figures 4.2 and 4.3 present the received pattern for the horn antenna. Figure 4.2 shows the comparison of the amplitude pattern for the horn antenna with and without the four PEC plates; while Figure 4.3 shows the phase component. The reconstructed results for the helical antenna are shown in Figures 4.4 and 4.5. Figure 4.4 shows the comparison of the

amplitude pattern; while Figure 4.5 shows the phase component.

Similarly, we also applied the deconvolution method to reconstruct a clean radiation pattern for the yagi antenna. The comparison of the amplitude pattern for the yagi antenna with and without the PEC plates is given in Figure 4.6; while Figure 4.7 shows the phase component.

When compared with examples in Section 3.4.3, where the horn antenna is used as the probe, the reconstructed results by using the yagi antenna as the probe also obtain a pattern well approximated to the ideal pattern of the AUT.

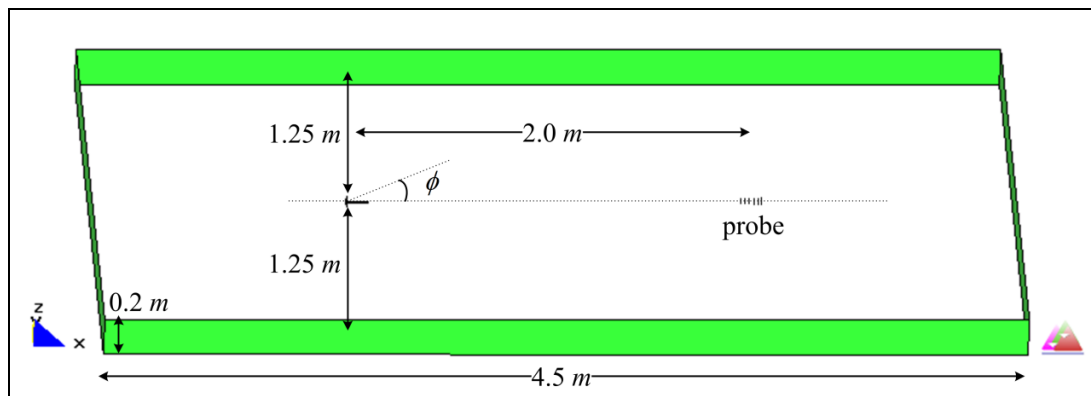


**Figure 4.1** Model of the measurement system with a yagi as the probe.

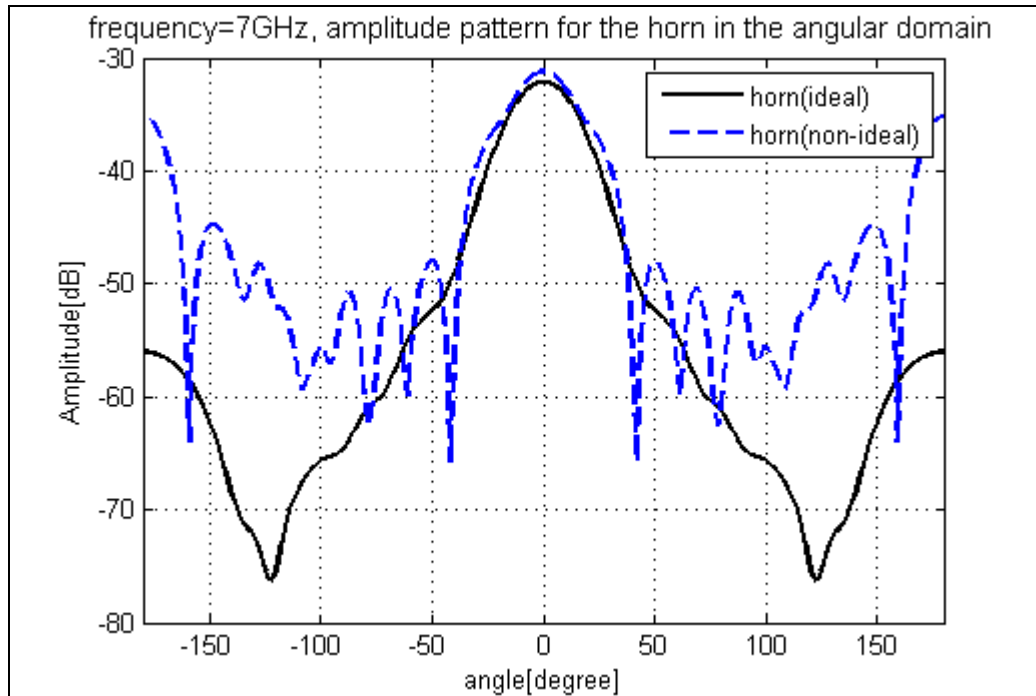


**Figure 4.2** Amplitude pattern for the horn antenna system with a yagi as the probe.

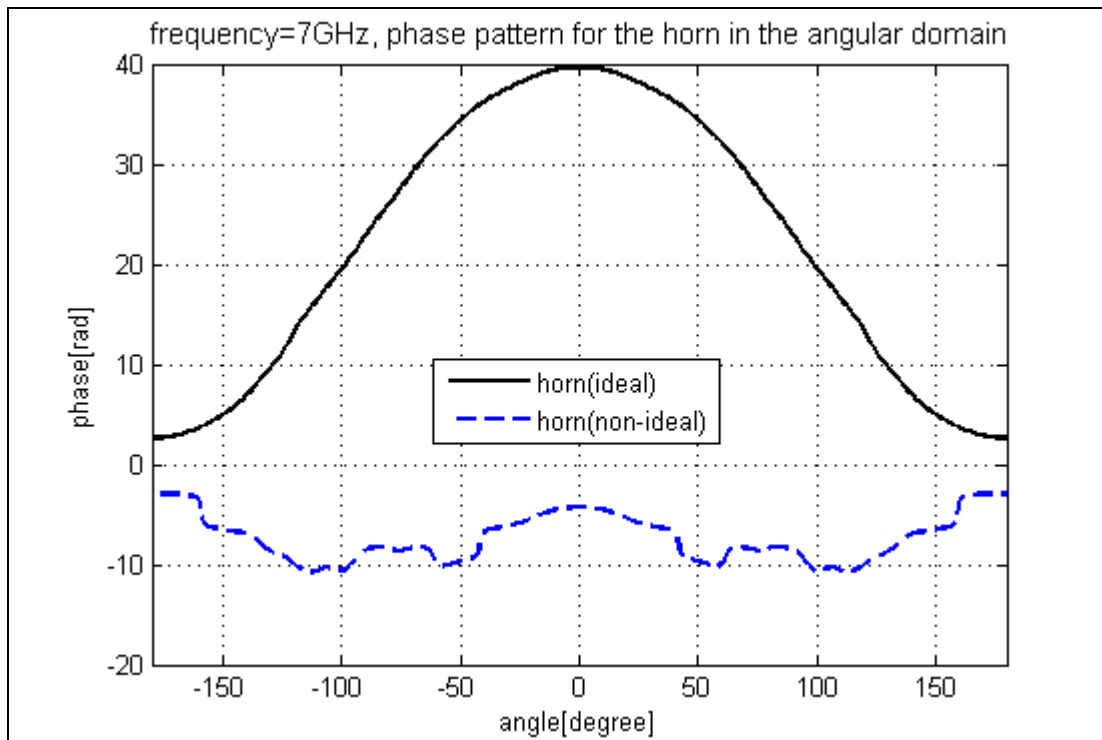


**Figure 4.3** Phase pattern for the horn antenna system with a yagi as the probe.

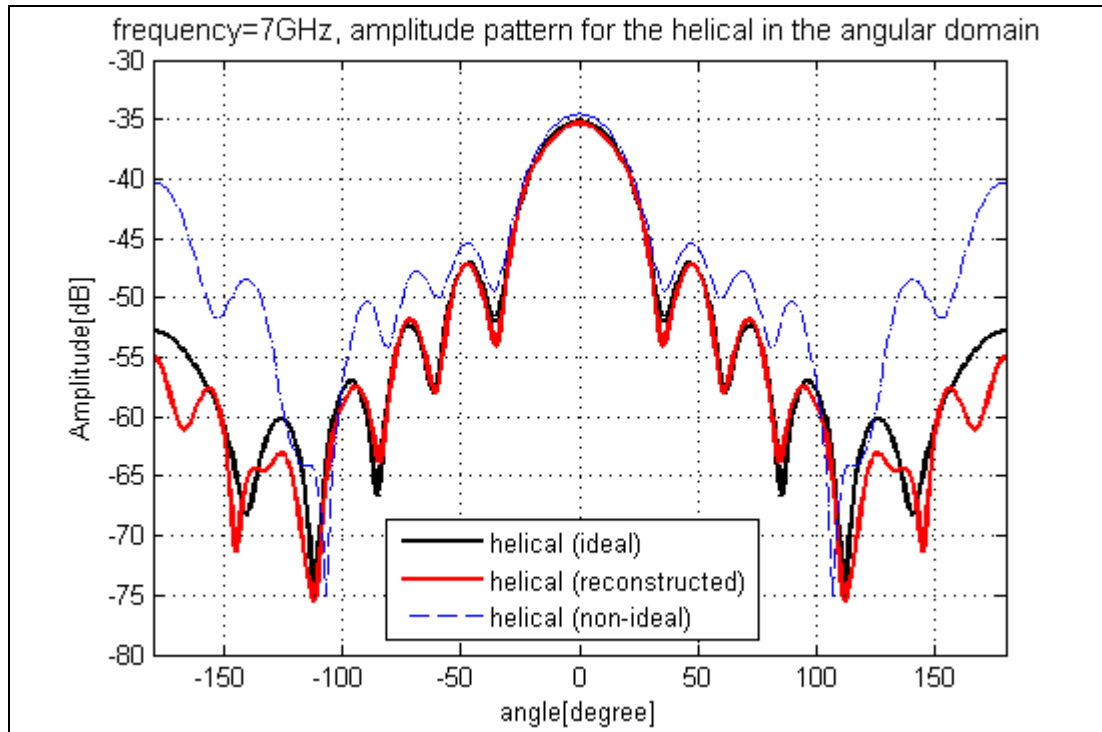


**Figure 4.4** Amplitude pattern for the helical antenna with a yagi as the probe.

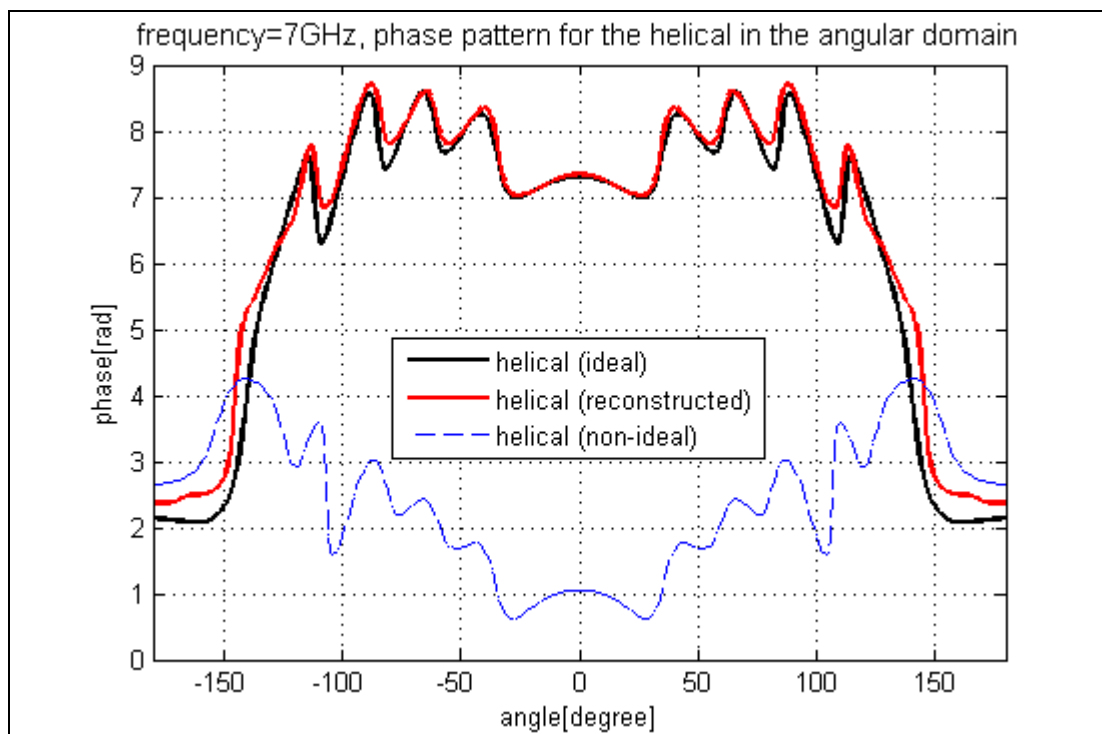


**Figure 4.5** Phase pattern for the helical antenna with a yagi as the probe.

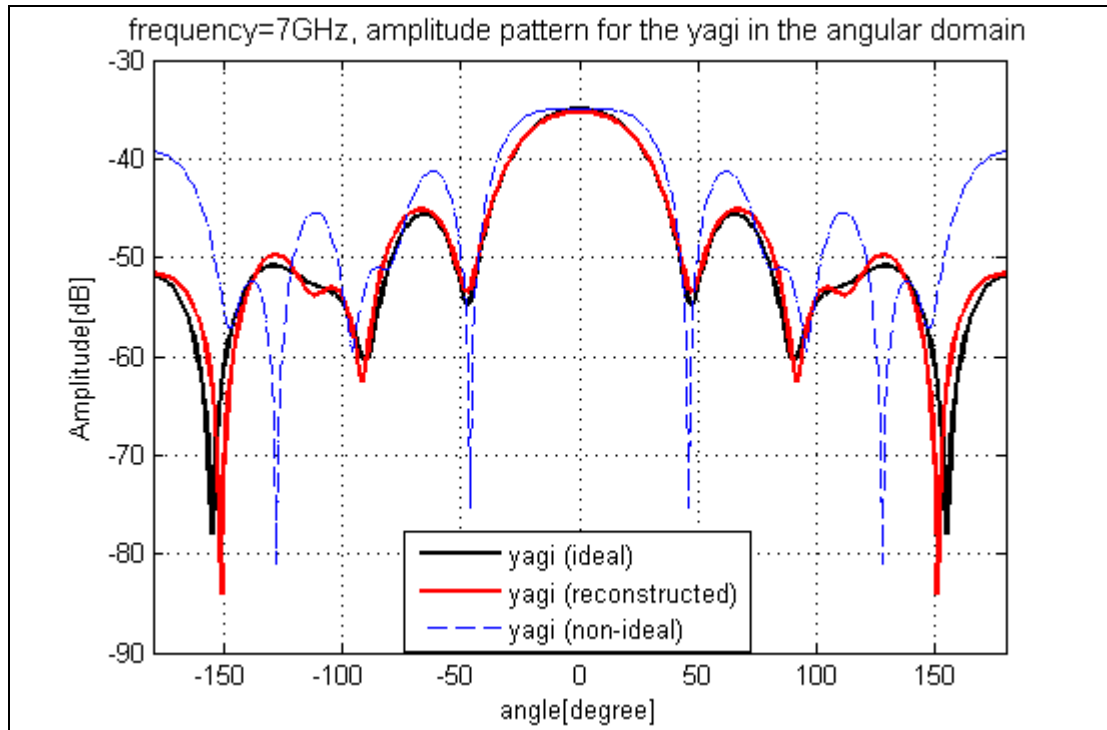


**Figure 4.6** Amplitude pattern for the yagi antenna with a yagi as the probe.

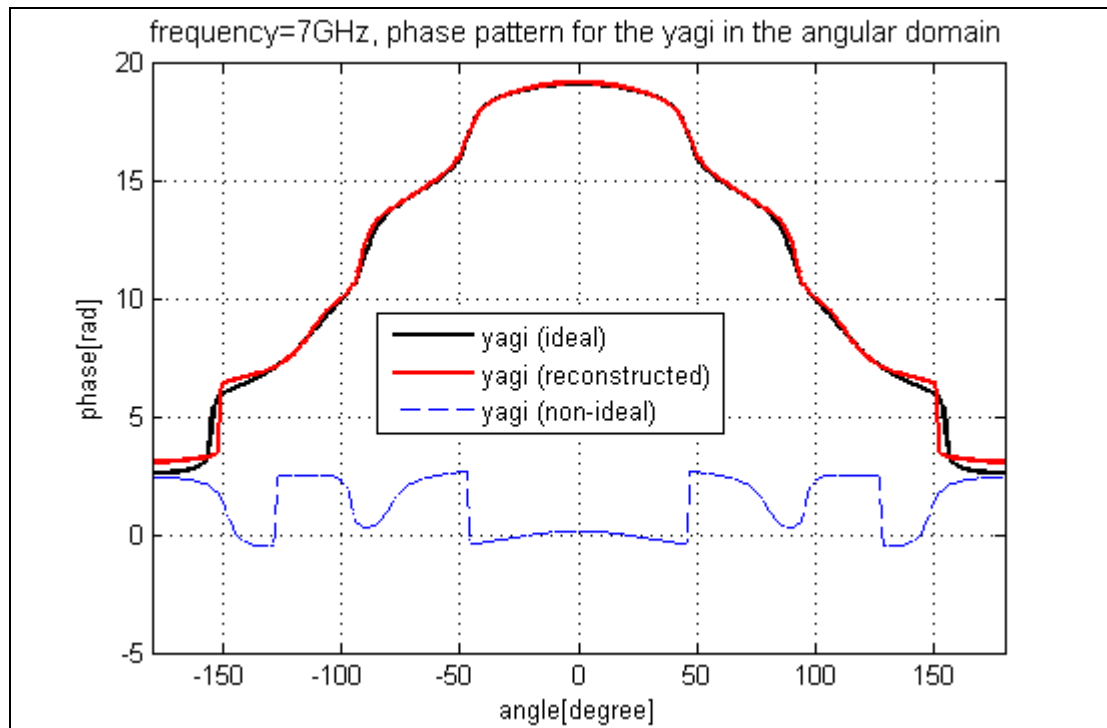


**Figure 4.7** Phase pattern for the yagi antenna with a yagi as the probe.

#### 4.1.2 Example II: Use of a Parabolic Reflector Antenna as the Probe

The previous example has shown that choosing the yagi antenna as the probe does not affect the reconstructed results. For this example, we'd like to use a parabolic reflector antenna as the probe, and observe if this would make any difference for the deconvolution method. The size of the parabolic reflector antenna is just the same as in previous examples, as shown in Figure 3.31. The model for the simulation is shown in Figure 4.8. And the AUT for this example is also a parabolic reflector antenna with the same size as the probe, for simplicity.

The same procedure was applied to reconstruct the radiation pattern for the parabolic reflector antenna. Since we have illustrated the procedures before, we will only present the reconstructed result for the parabolic reflector antenna (AUT). The received responses at the probe are shown in Figures 4.9 and 4.10. The reconstructed results for the parabolic reflector antenna are shown in Figures 4.11 and 4.12 for the amplitude and the phase component of the radiation pattern, respectively. From those figures, we can observe that when the parabolic reflector antenna is used as the probe, the reconstructed pattern is still well approximated to the ideal pattern.

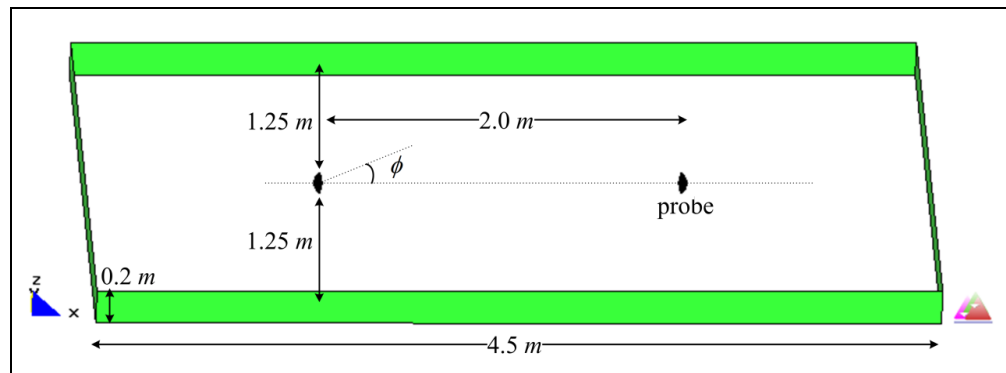


**Figure 4.8** Model of the measurement system with a parabolic reflector as the probe.

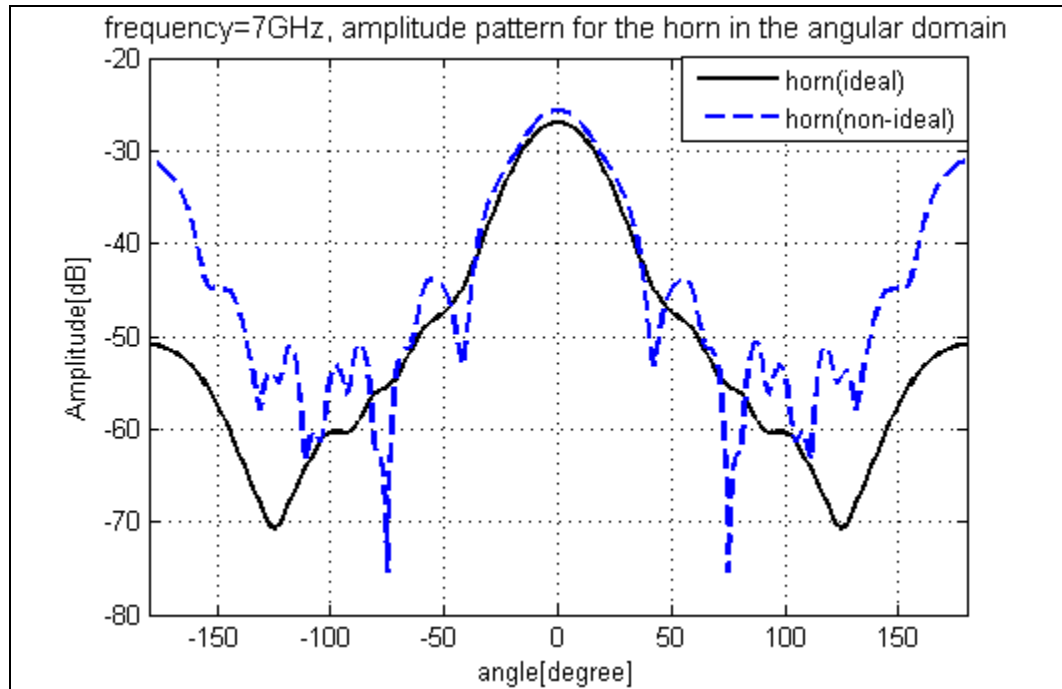


**Figure 4.9** Amplitude pattern for the horn antenna with a parabolic reflector as the probe.

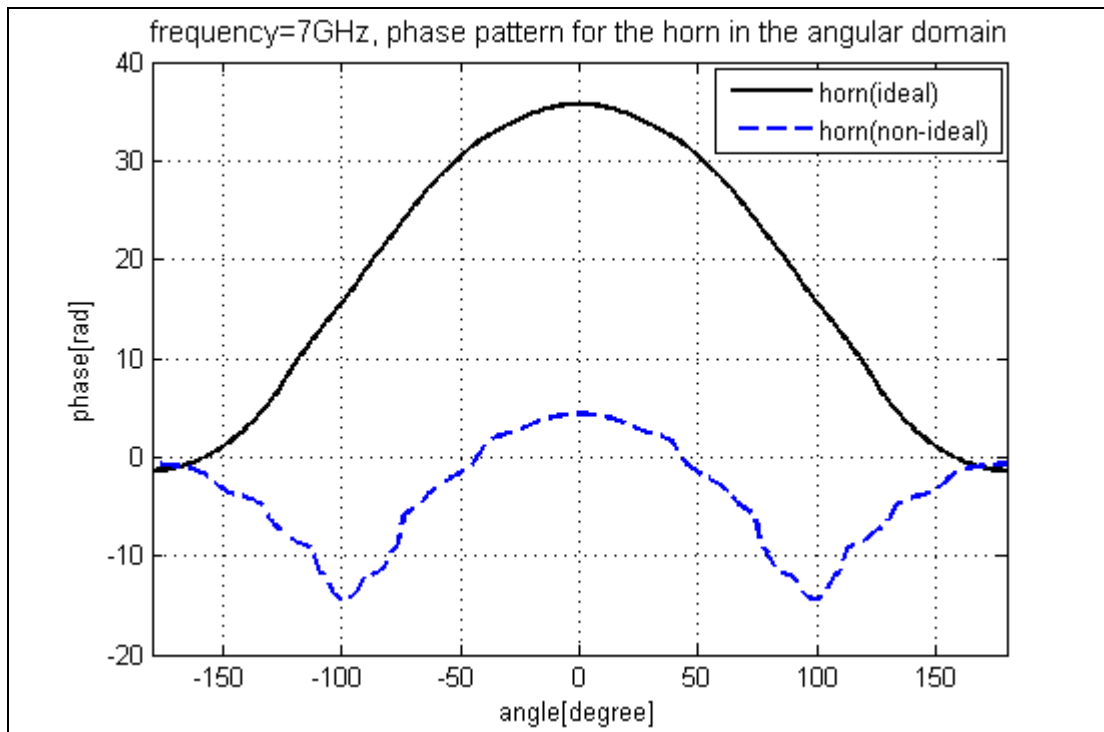


**Figure 4.10** Phase pattern for the horn antenna with a parabolic reflector as the probe.

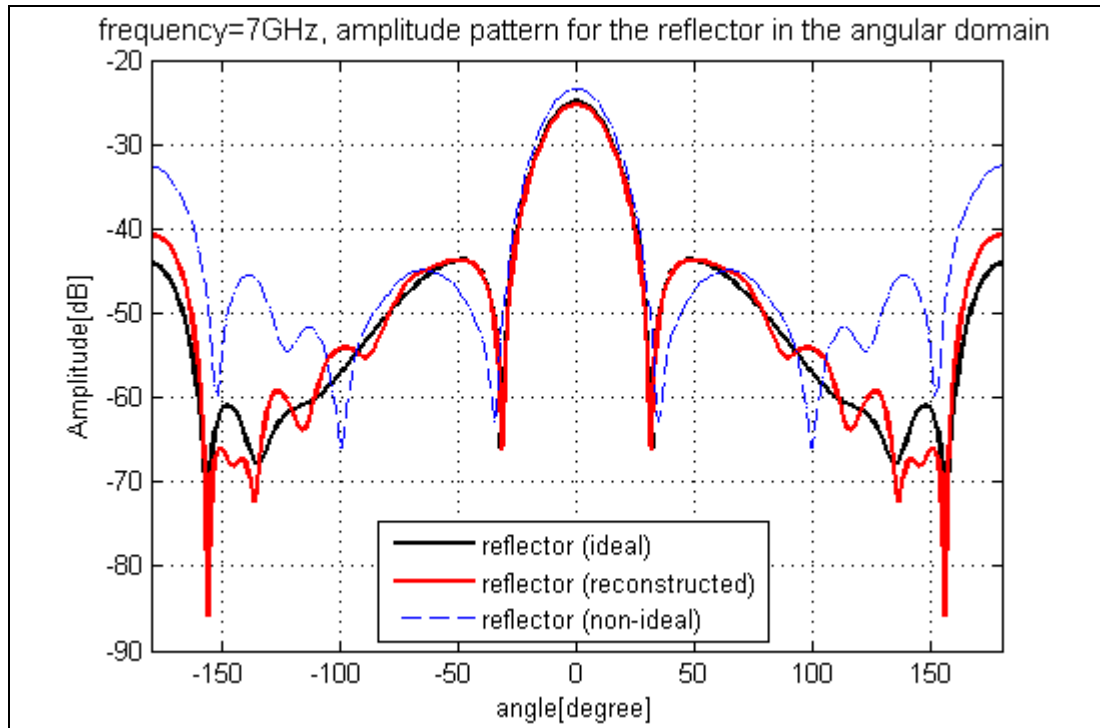


**Figure 4.11** Amplitude pattern for the parabolic reflector antenna with a parabolic reflector as the probe.

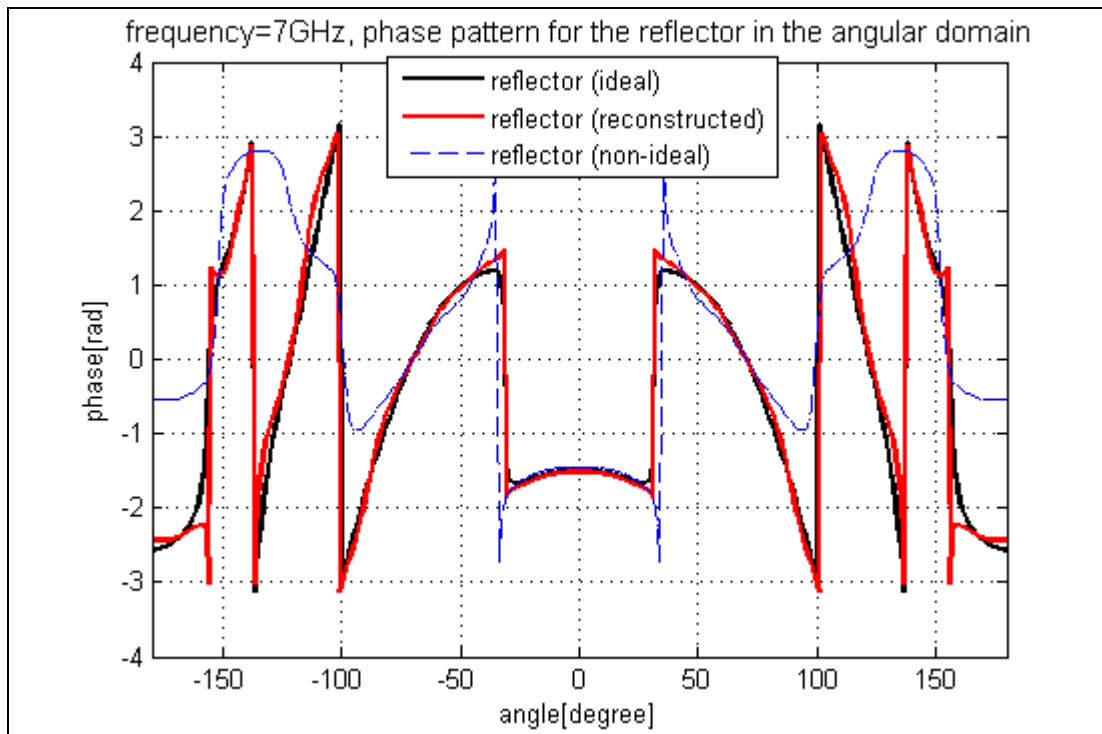


**Figure 4.12** Phase pattern for the parabolic reflector antenna with a parabolic reflector as the probe.

### 4.1.3 Example III: Use of a Dipole Antenna as the Probe

The previous two examples have well supported the deconvolution method for pattern reconstruction. However, not all types of antennas may be suitable for the probe antenna.

For this example, we'd like to use a dipole antenna as the probe, and observe the reconstructed results. The simulation model is shown in Figure 4.13. The dipole antenna is a half-wave dipole with the length of  $2\text{ cm}$  (simulation frequency is  $7\text{ GHz}$ ) and the radius of  $0.18\text{ mm}$ . The AUTs of this example are the same helical antenna and the yagi antenna as used in previous examples. The standard gain horn antenna is used as the reference antenna to derive the environmental effects. The reconstruction procedure is the same as described in the previous examples.

Figure 4.14 shows the comparison of the amplitude pattern for the horn antenna with and without the four PEC plates; while Figure 4.15 shows the phase component. The reconstructed results for the helical antenna and the yagi antenna are shown in Figures 4.16 ~ 4.19. The comparison of the amplitude pattern for the helical / yagi antenna is shown in Figure 4.16 / 4.18; while Figure 4.17 / 4.19 shows the phase component.

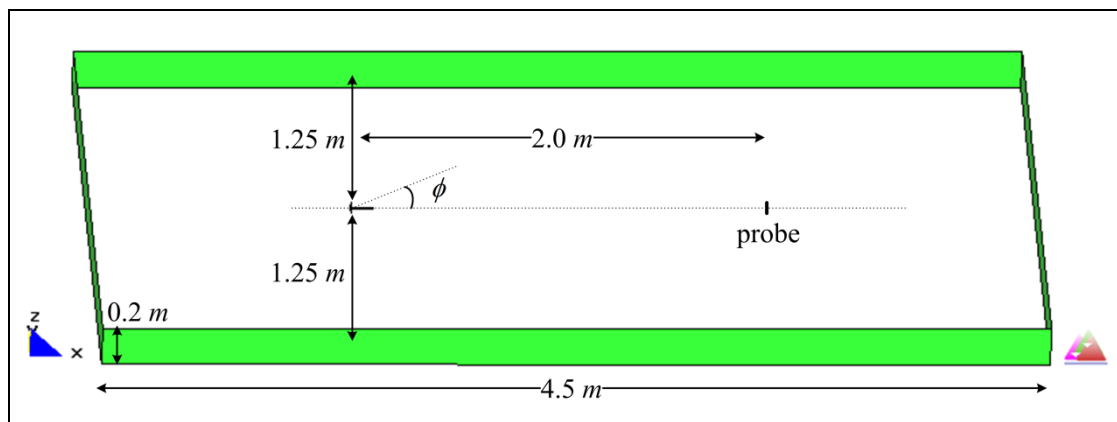


**Figure 4.13** Model of the measurement system with a dipole as the probe.

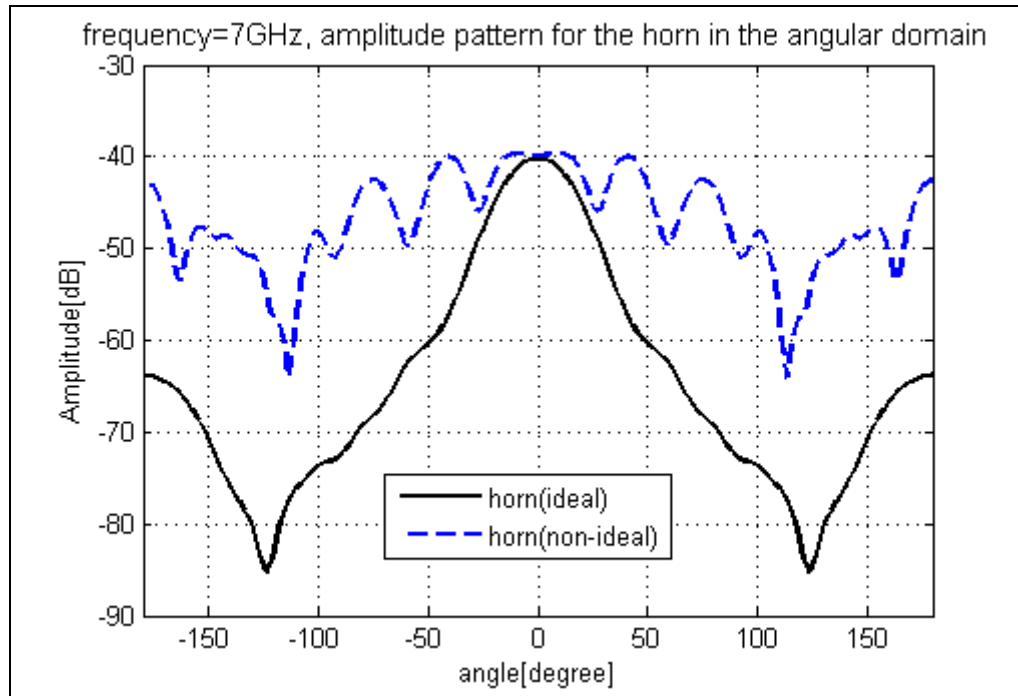


**Figure 4.14** Amplitude pattern for the horn antenna with a dipole as the probe.

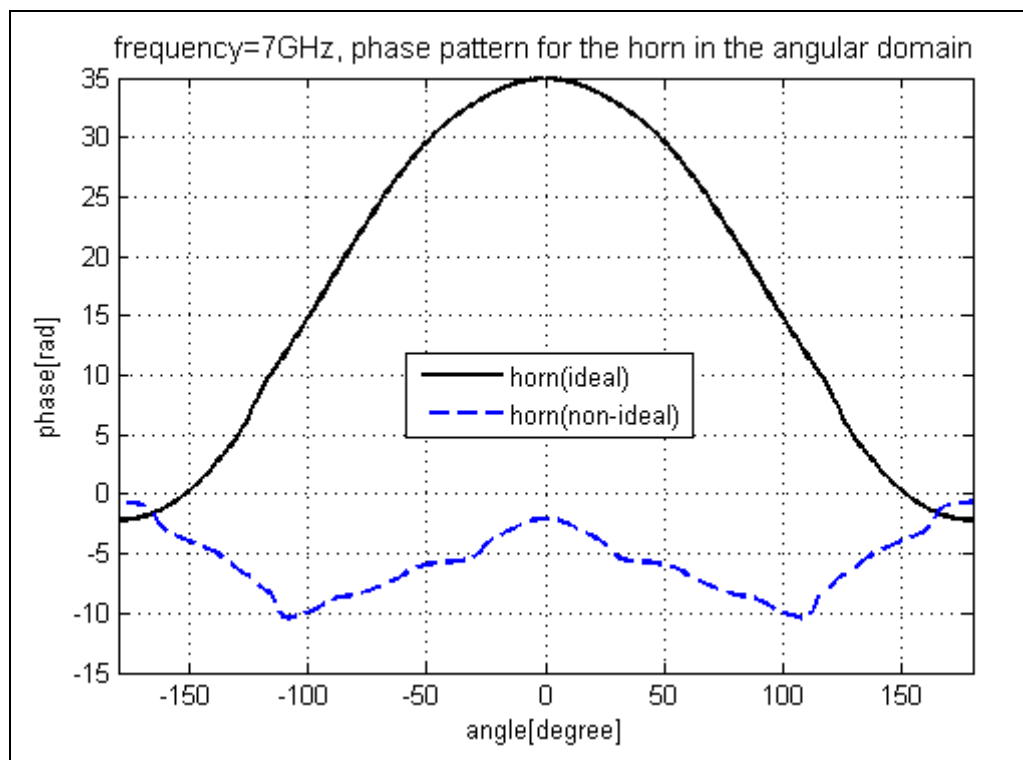


**Figure 4.15** Phase pattern for the horn antenna with a dipole as the probe.

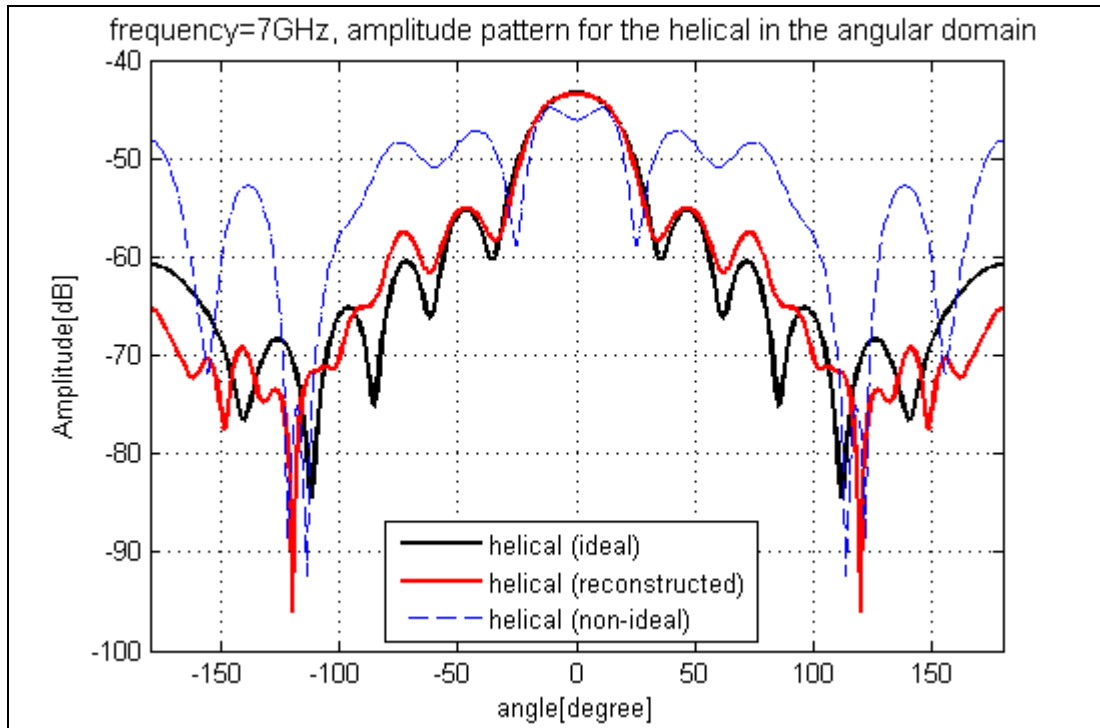


**Figure 4.16** Amplitude pattern for the helical antenna with a dipole as the probe.

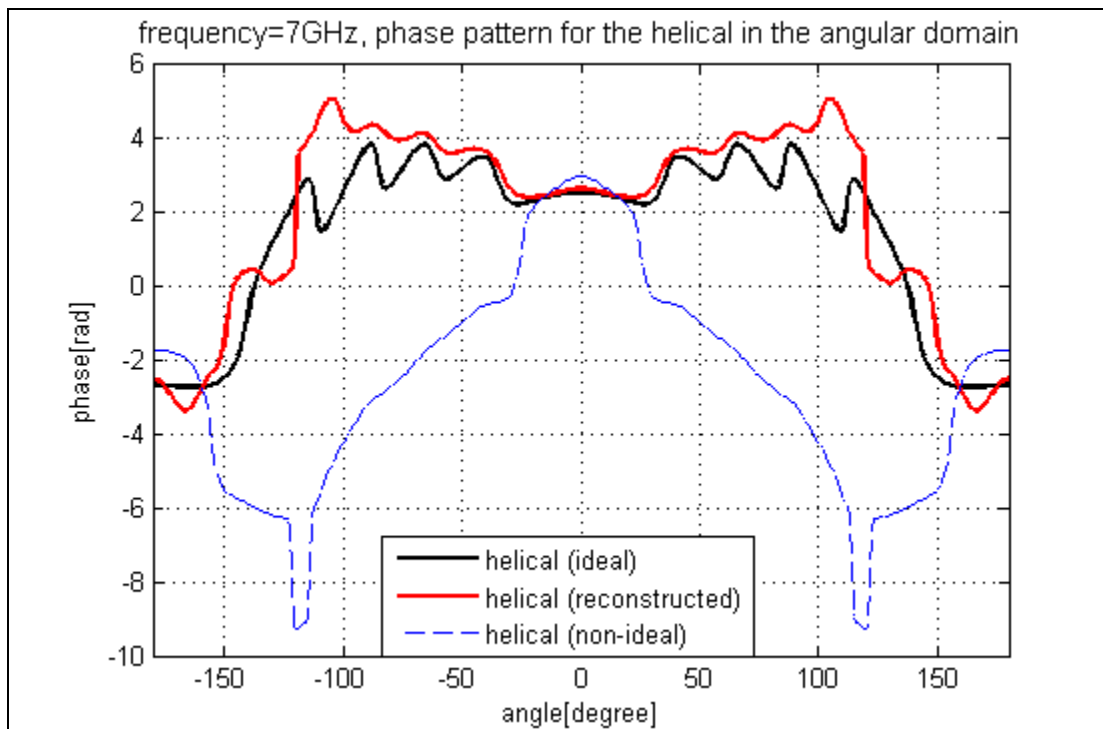


**Figure 4.17** Phase pattern for the helical antenna with a dipole as the probe.

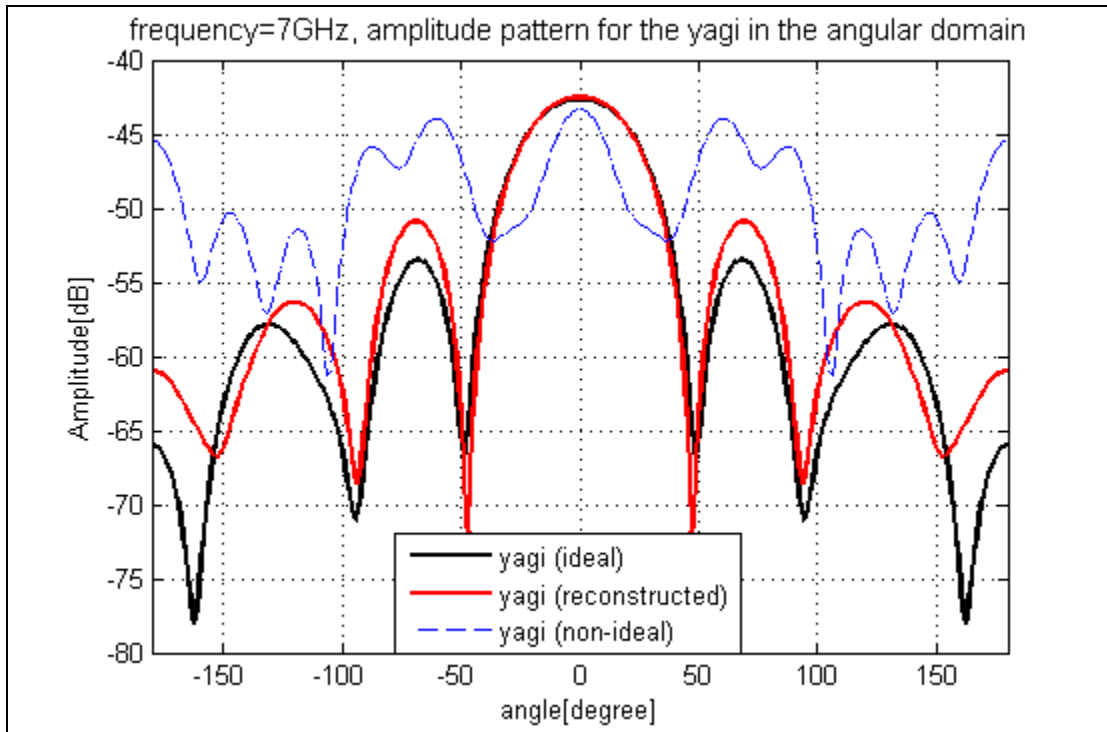


**Figure 4.18** Amplitude pattern for the yagi antenna with a dipole as the probe.

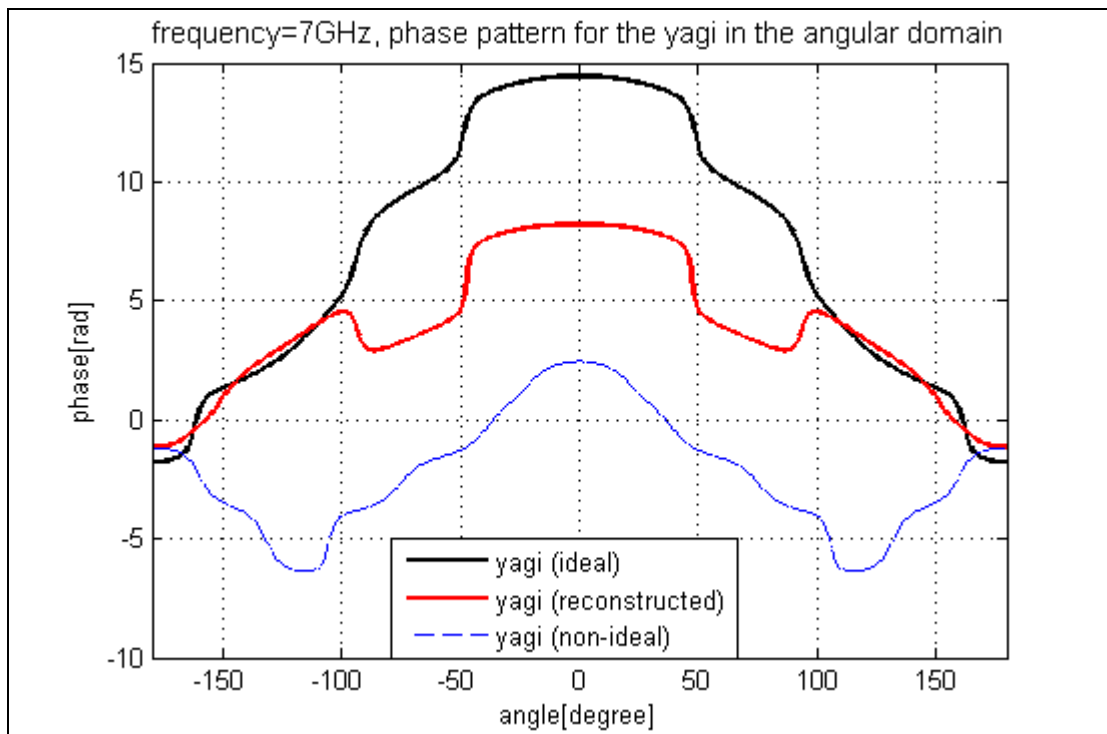


**Figure 4.19** Phase pattern for the yagi antenna with a dipole as the probe.

From those figures, we can observe that the distorted patterns are totally different from the free space radiation patterns. The reconstructed results are not as good as previous two examples, and only the main lobe of the pattern is well reconstructed. We realize that when a dipole is used as the probe, due to its omni-directional property along the plane, it receives responses from the environment and the AUT equally. When the reflection responses are large enough, the direct response from the AUT will be overwhelmed by the reflection responses, and thus generating distorted reconstructed results. Therefore, the probe antenna required for the pattern reconstruction needs to be an antenna with a proper front-to-back ratio.

The two examples in Section 4.1.1 and Section 4.1.2 show that with a different probe the effect of the probe antenna to the received signal is different. As shown in Figure 4.2 and Figure 4.9, under the same environment but with a different probe the received non-ideal signals are different due to the probe effect. However, this effect will be cancelled and will not affect the reconstructed result. The deconvolution method requires one to perform two tests, one for a reference antenna and the other for the AUT. During the two tests, the same probe will be used to collect the signal, thus resulting in the same probe effect for two tests, and this effect can be cancelled out.

Note that the reference antenna used for extracting the environmental effects should not be any omni-directional antenna either. If the reference antenna generates an omni-directional radiation pattern, the received signal at the probe will be a constant value when the reference antenna rotates in the azimuth plane. No matter how the environment changes, the received pattern will not reveal the change of the environment.

## 4.2 Effect of Different Antenna Size

In this Section, we'd like to show examples for different simulation frequencies, and using different electrical sizes for the antennas to show that the deconvolution method is a general method and works for different sizes of antennas. Previous examples are all under the operating frequency of 7 GHz, the current example will change the frequency to be 1.5 GHz. And we re-designed all antennas used in the simulation to let them work at this new frequency.

The new model for the measurement system also has four PEC plates as the reflectors around the antenna, which is shown in Figure 4.20. Four PEC plates form a rectangular contour enclosing the probe and the AUT. A horn antenna is still used as the probe, and the AUTs are a 6-element yagi and a helical antenna with a back plate. New models of the horn, helix, and the yagi antenna are shown in Figures 4.21, 4.22, and 4.23, respectively. For the operation frequency of 1.5 GHz, those antennas now have different electrical sizes. In previous examples, the horn, the helix, and the yagi antenna models have the largest electrical sizes as  $3.6 \lambda$ ,  $2.7 \lambda$ , and  $1.3 \lambda$ , respectively; while new models now have the largest electrical sizes as  $1.5 \lambda$ ,  $1.6 \lambda$ , and  $1.3 \lambda$ , respectively. And their radiation properties are different from the previous models (except the yagi, whose electrical size is almost the same). In the model, both antennas are kept under a 2 meter distance, which is  $10 \lambda$ , away from the four PEC plates; while in the old model, the distance is  $29 \lambda$ .

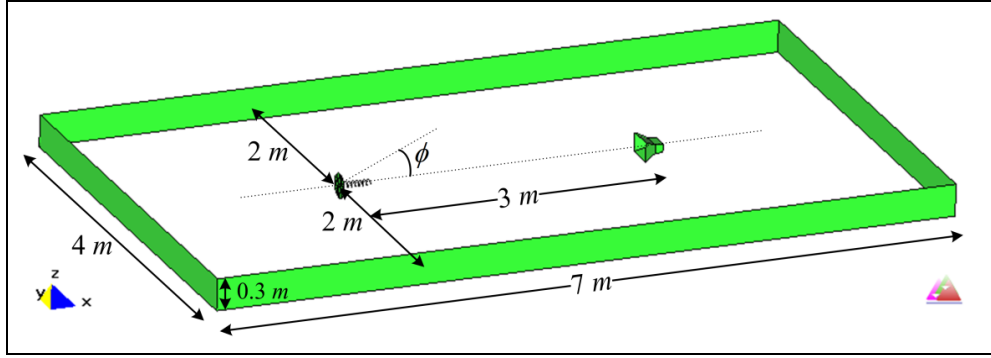


**Figure 4.20** The new model of the measurement system with four PEC plates.

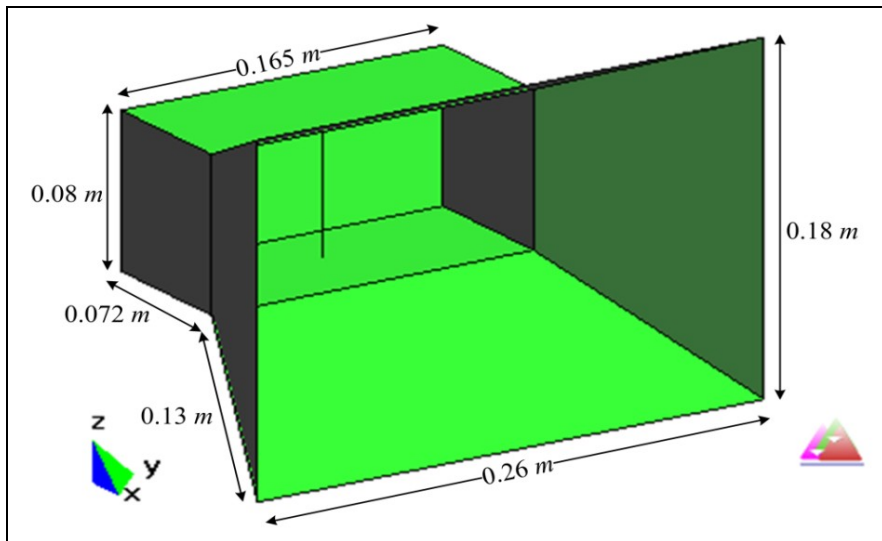


**Figure 4.21** Dimensions of a new horn antenna model (Probe).

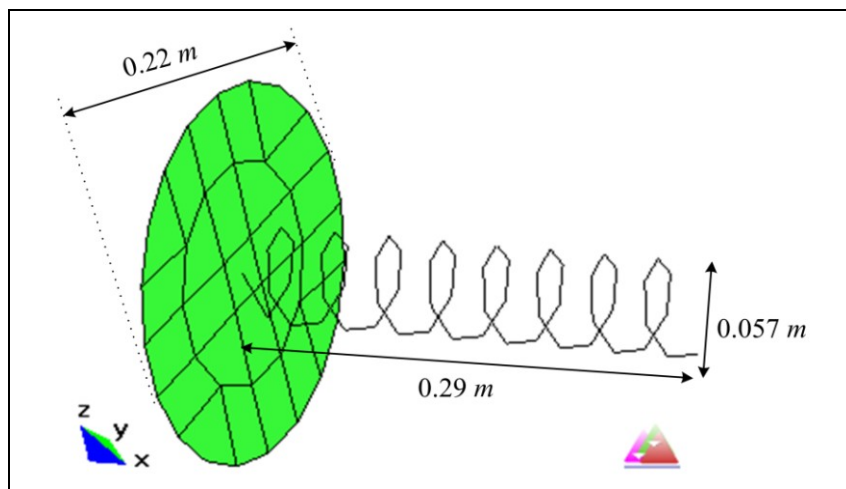


**Figure 4.22** Dimensions of a new helical antenna model with a reflecting plate (AUT).

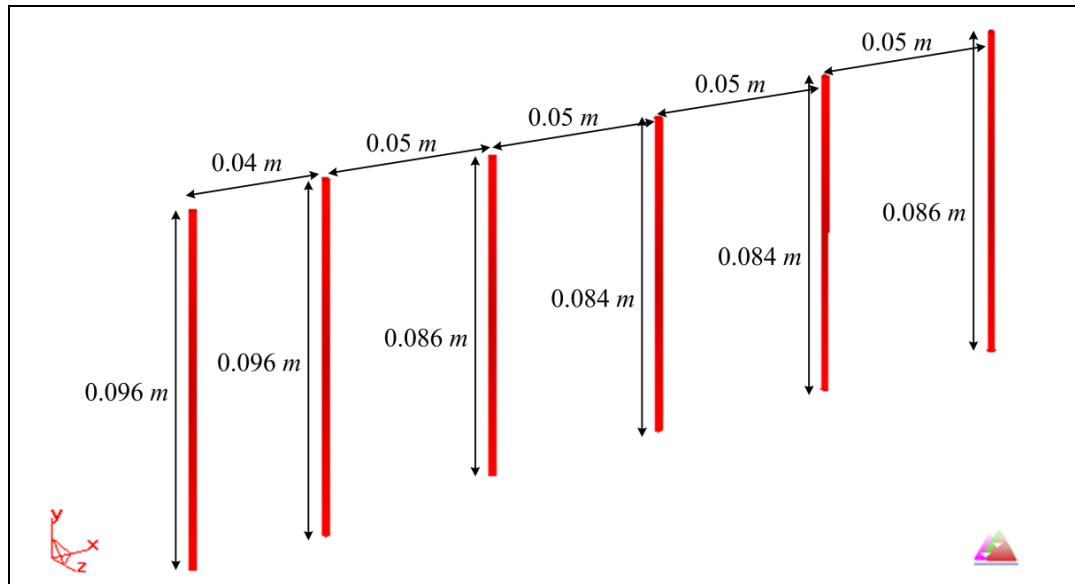


**Figure 4.23** Dimensions of a new 6-element yagi antenna model (AUT).

For this new model of the measurement system, it also needs to satisfy the condition that the current distribution on the feed dipole of the AUT should not change dramatically with the environment. Figure 4.24 shows that the current distribution on the feed dipole of the helical antenna is barely affected by the PEC plates (the current distribution on other antennas is omitted).

The same pattern reconstruction procedure was carried out for this example. Figure 4.25 shows the comparison of the amplitude pattern for the horn antenna with and without the PEC reflector at 1.5 GHz; while Figure 4.26 shows the phase component of the radiation pattern. The extracted environmental response  $A(\phi, f)$  is shown in Figure 4.27.

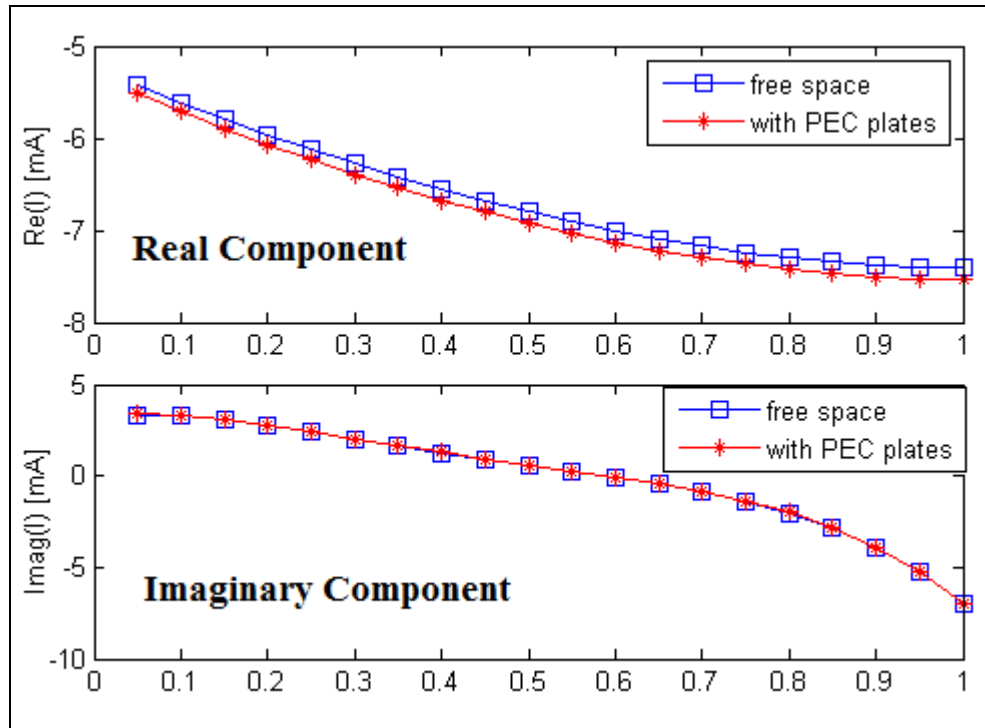


**Figure 4.24** Current distribution on the feed dipole of the helical antenna.

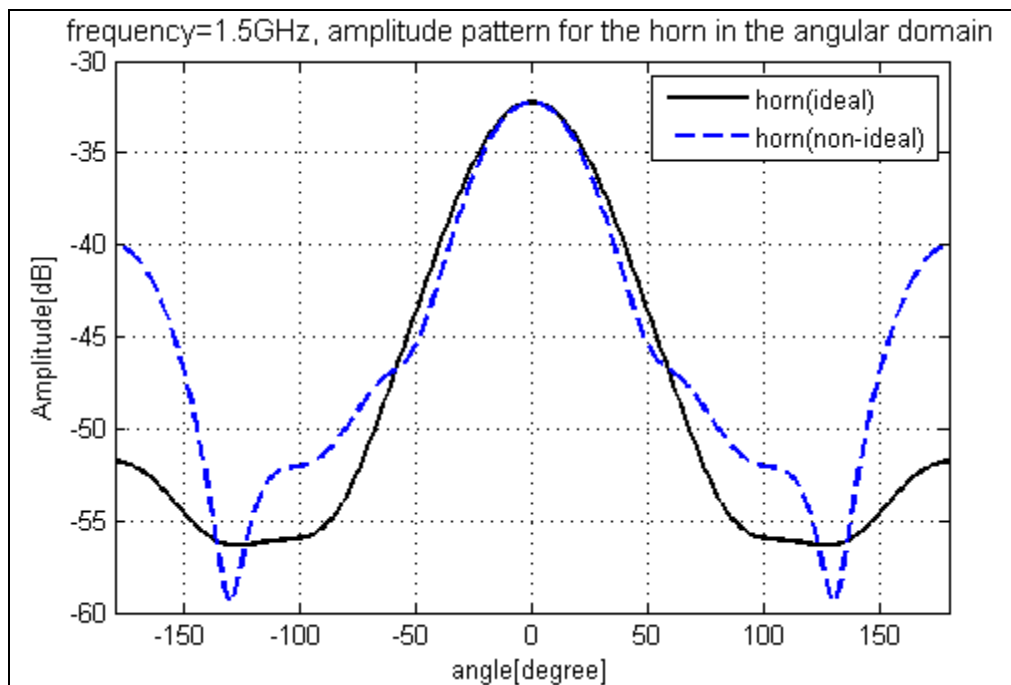


**Figure 4.25** Amplitude pattern for the horn antenna with the new model.

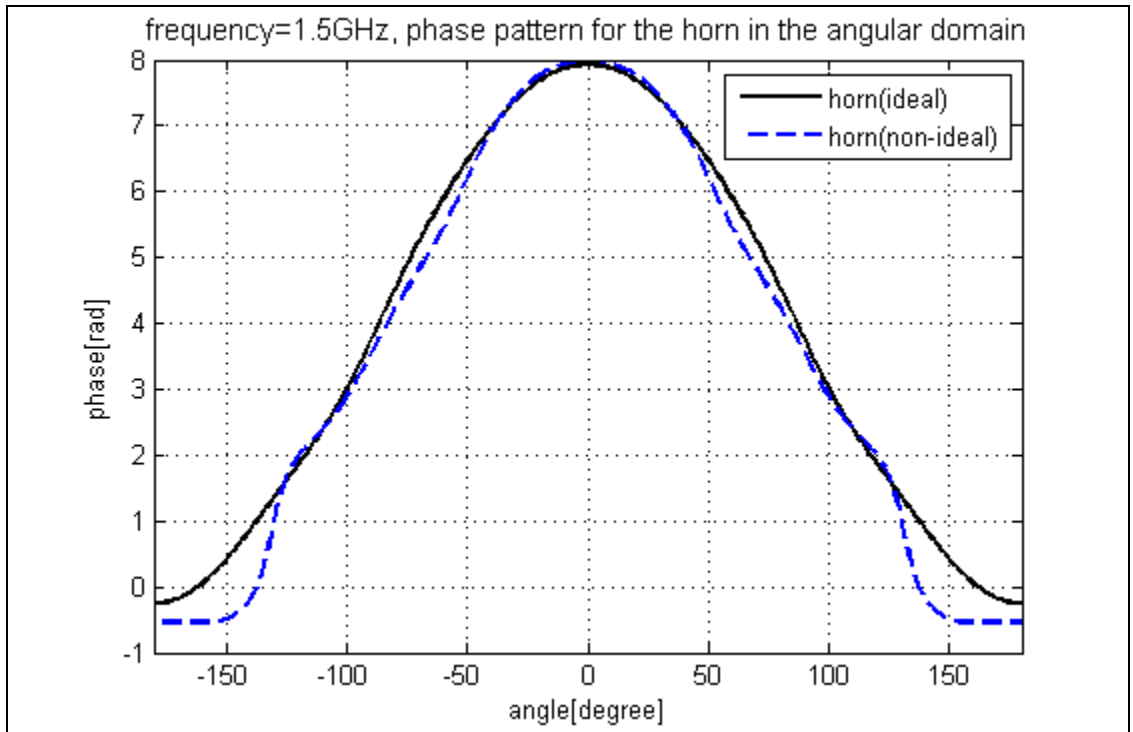


**Figure 4.26** Phase pattern for the horn antenna with the new model.

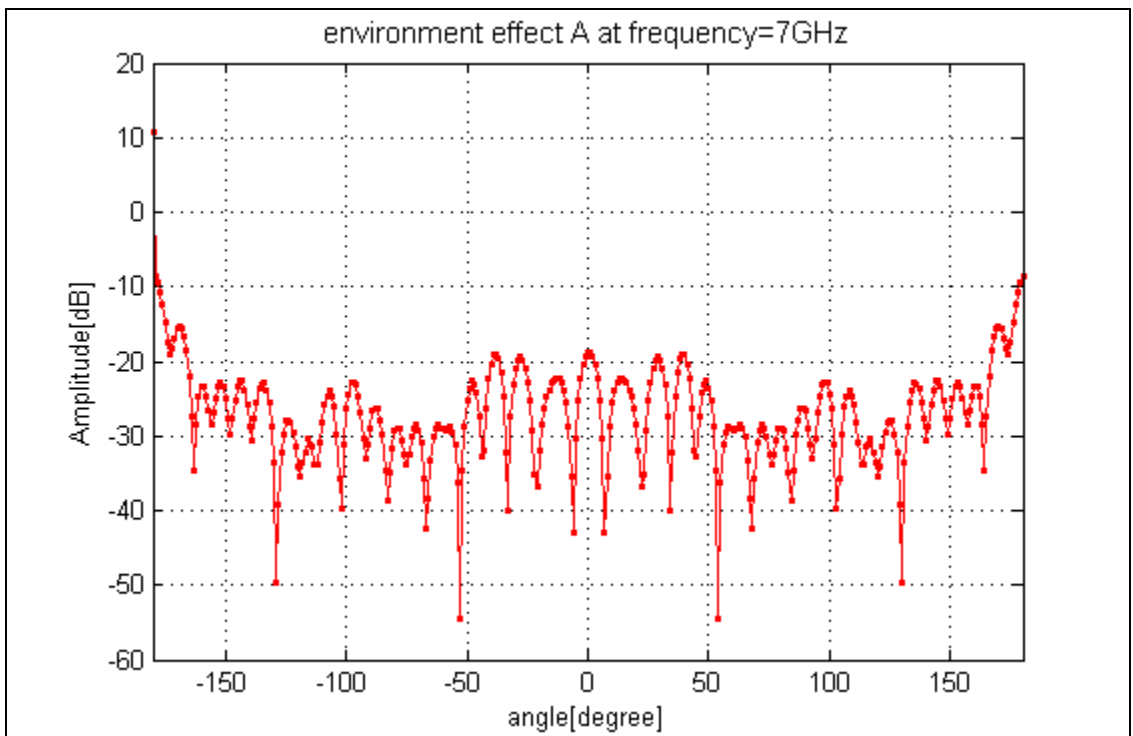


**Figure 4.27** Amplitude of the environmental effects with the new model.

The reconstructed results are shown through the following figures. Figure 4.28 gives the comparison of the amplitude pattern for the helical antenna; while Figure 4.29 shows the phase component of the radiation pattern. The comparison of the amplitude pattern for the yagi antenna is shown in Figure 4.30; while the phase component is given in Figure 4.31. When compared with the examples in the previous chapter, under this new environment, the reconstructed patterns using the deconvolution method are still well approximated to the ideal patterns of the AUTs. This example indicates that the deconvolution method can successfully reconstruct the radiation pattern for different electrical sizes of antennas operating at different frequencies.

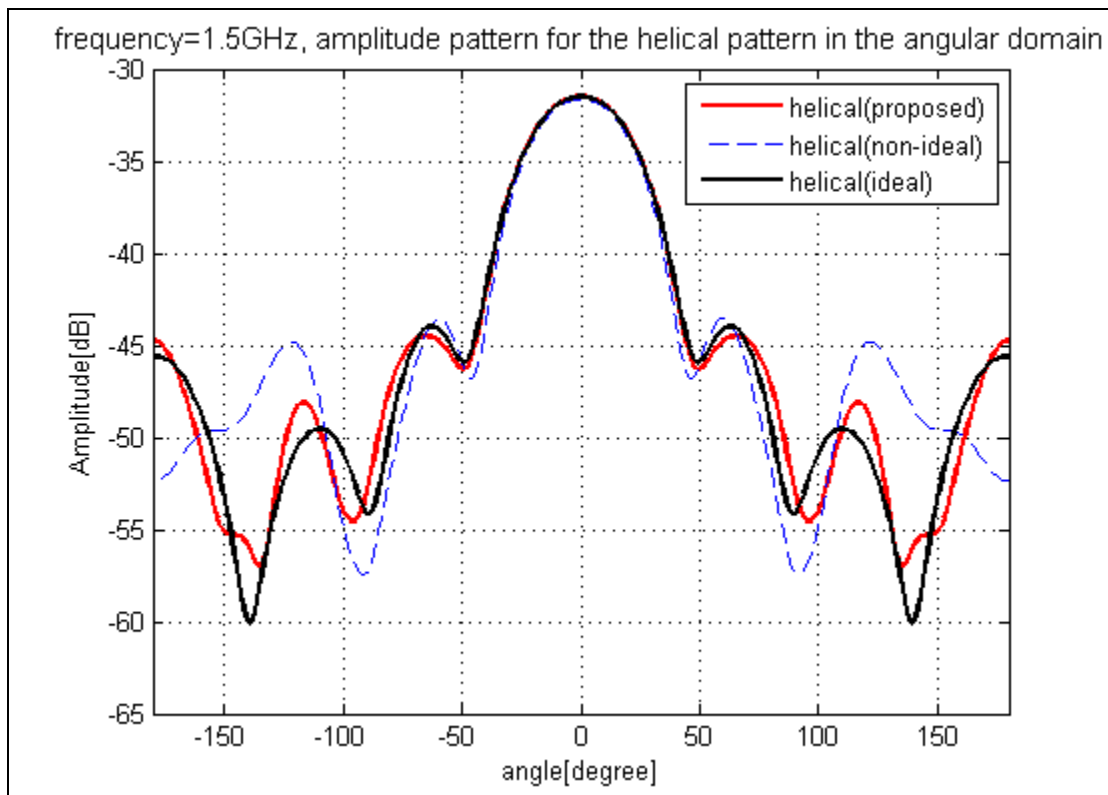


**Figure 4.28** Amplitude pattern for the helical antenna with the new model.

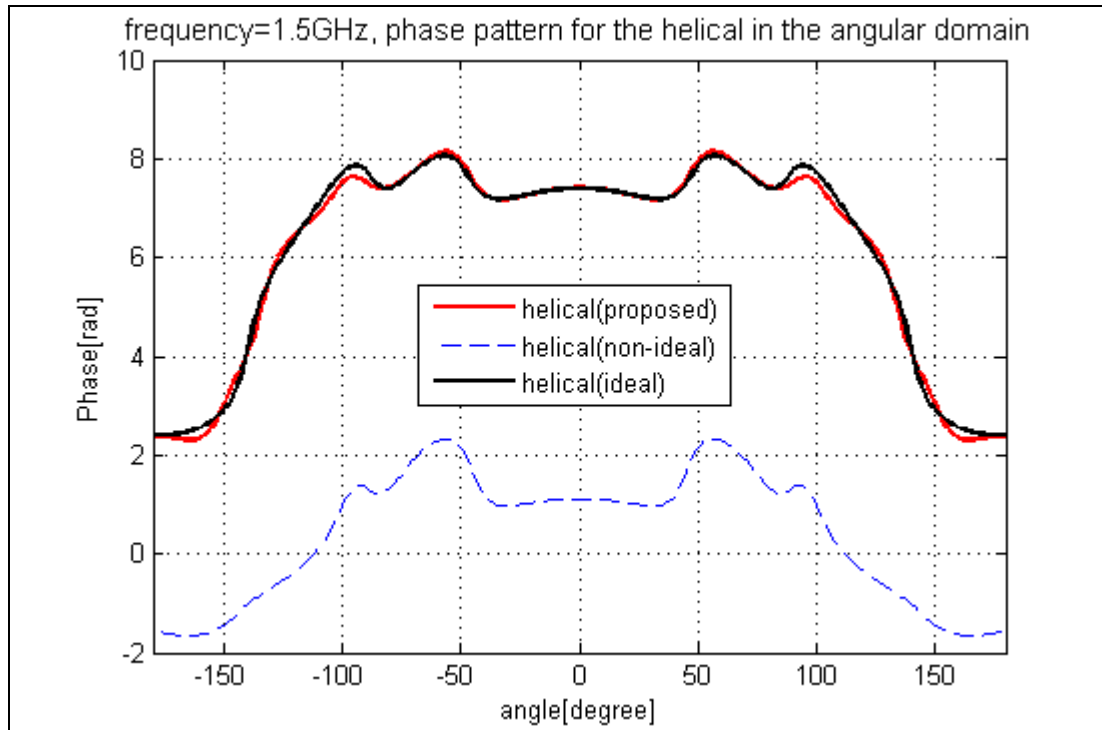


**Figure 4.29** Phase pattern for the helical antenna with the new model.

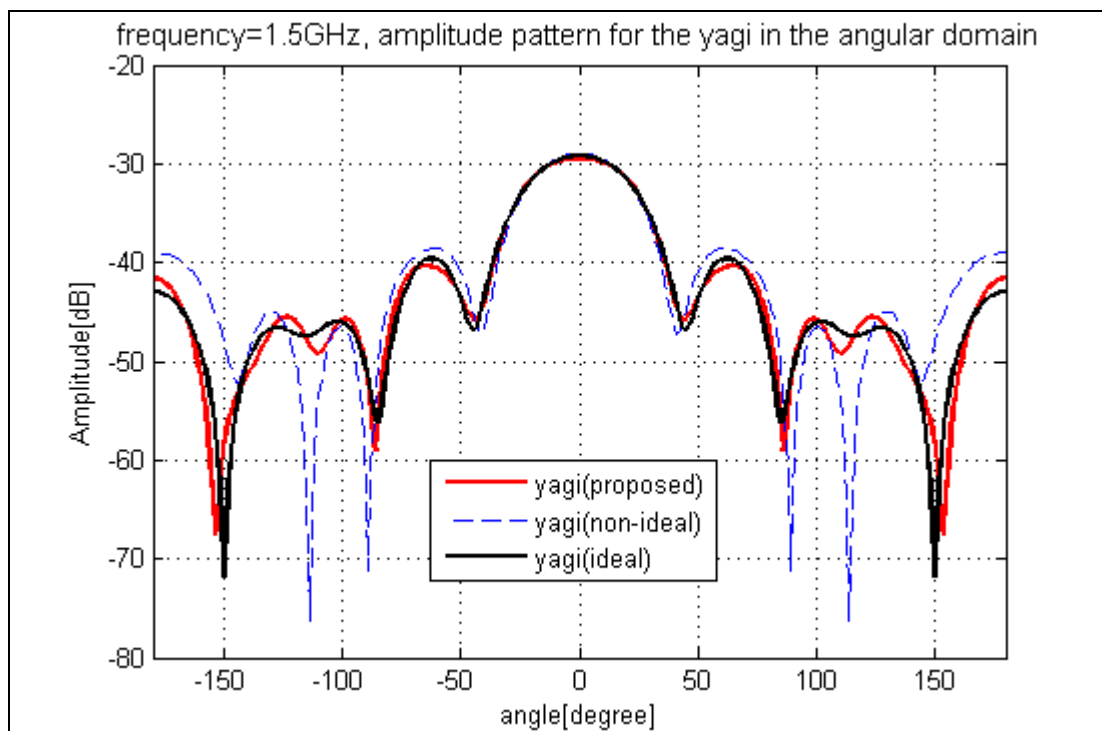


**Figure 4.30** Amplitude pattern for the yagi antenna with the new model.

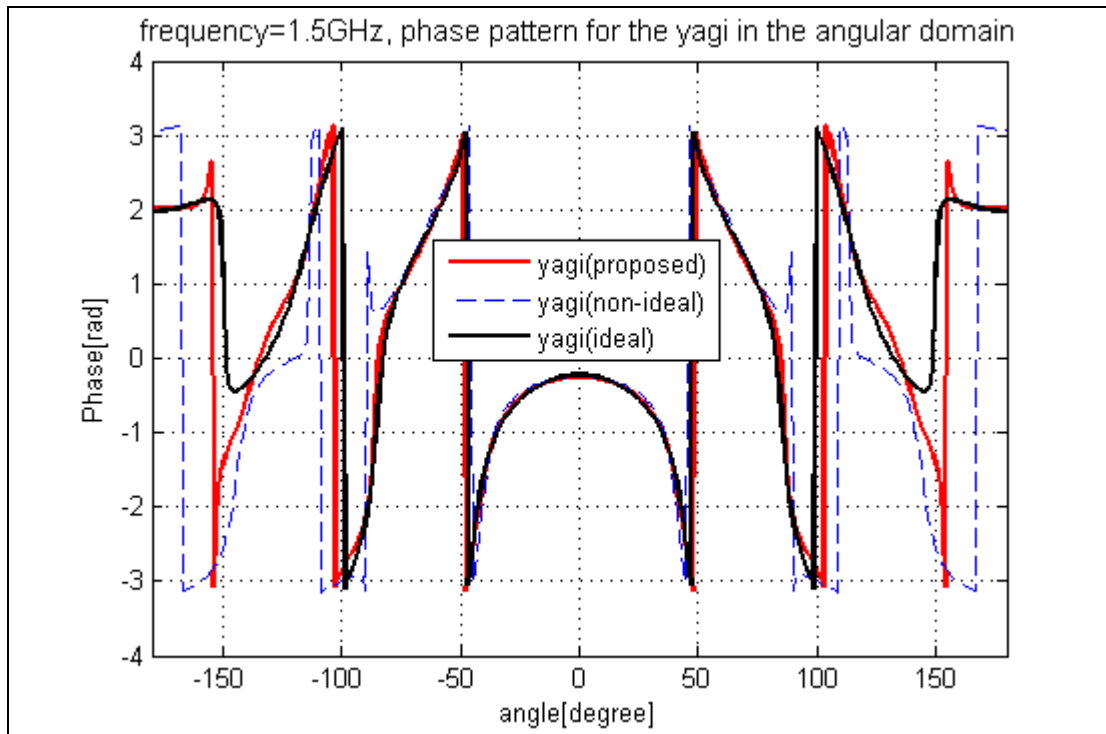


**Figure 4.31** Phase pattern for the yagi antenna with the new model.

### 4.3 Effect of Different Sizes of PEC Plates

The purpose of the deconvolution method is to retrieve the ideal radiation pattern using the data measured in a non-anechoic environment. An important question would be: **How would the environment itself affect the performance of the pattern reconstruction?**

In previous examples, we started from the simplest example with only one PEC plate, and increased to two plates, and to four plates. During this process, the applicability of the deconvolution method on pattern reconstruction regarding the effect of different environments has been shown. Figures 4.32 and 4.33 give comparisons of the reconstructed results for the helical antenna and the yagi antenna when the number of the

PEC plates increase. The left side show the amplitude patterns while the right side show the phase patterns. The units and axes are the same as in the previous examples. Note that these two figures are results summarized from previous examples in Chapter 3.

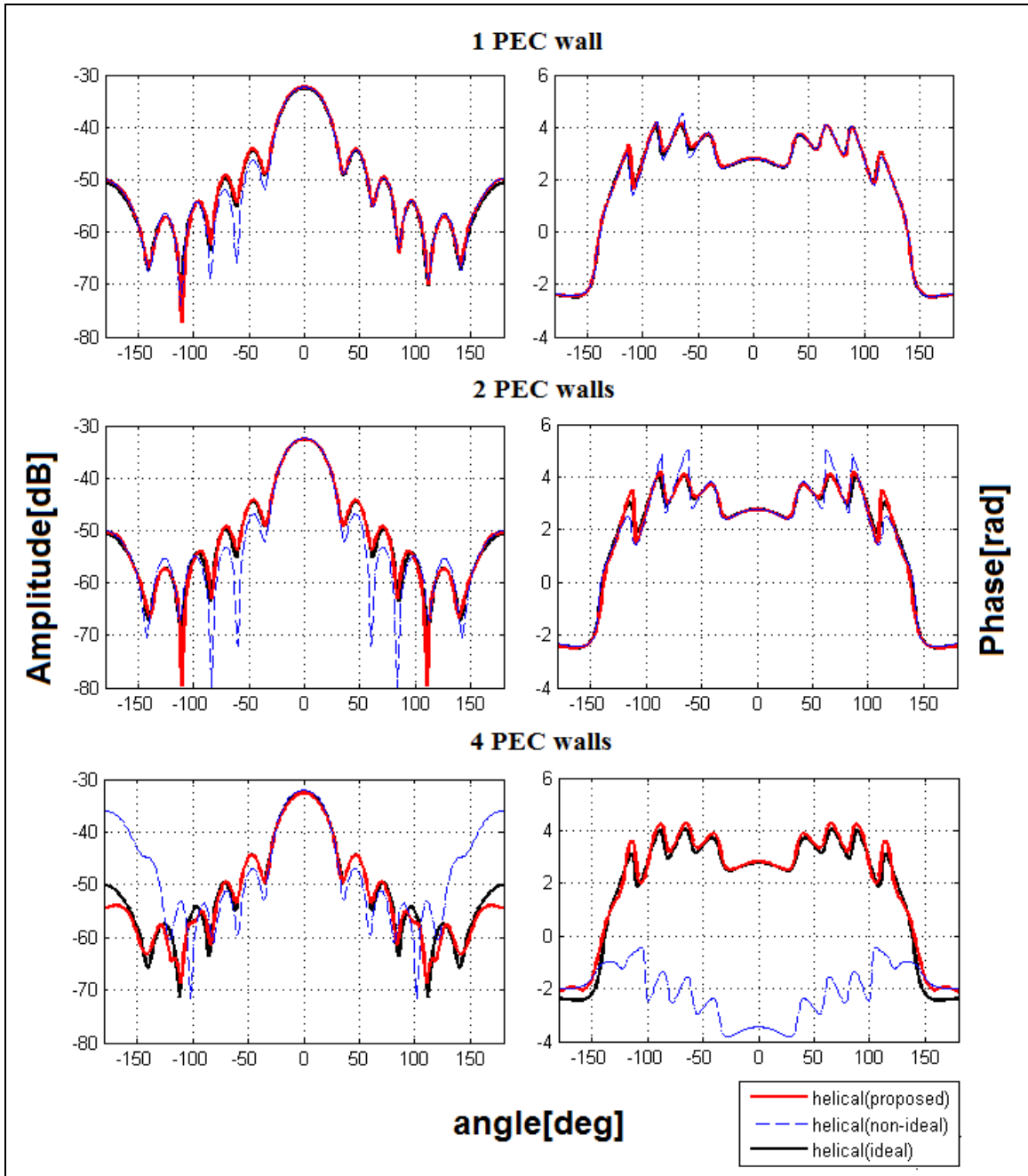


**Figure 4.32** Comparison of the reconstructed patterns for the helical antenna under different number of PEC plates.

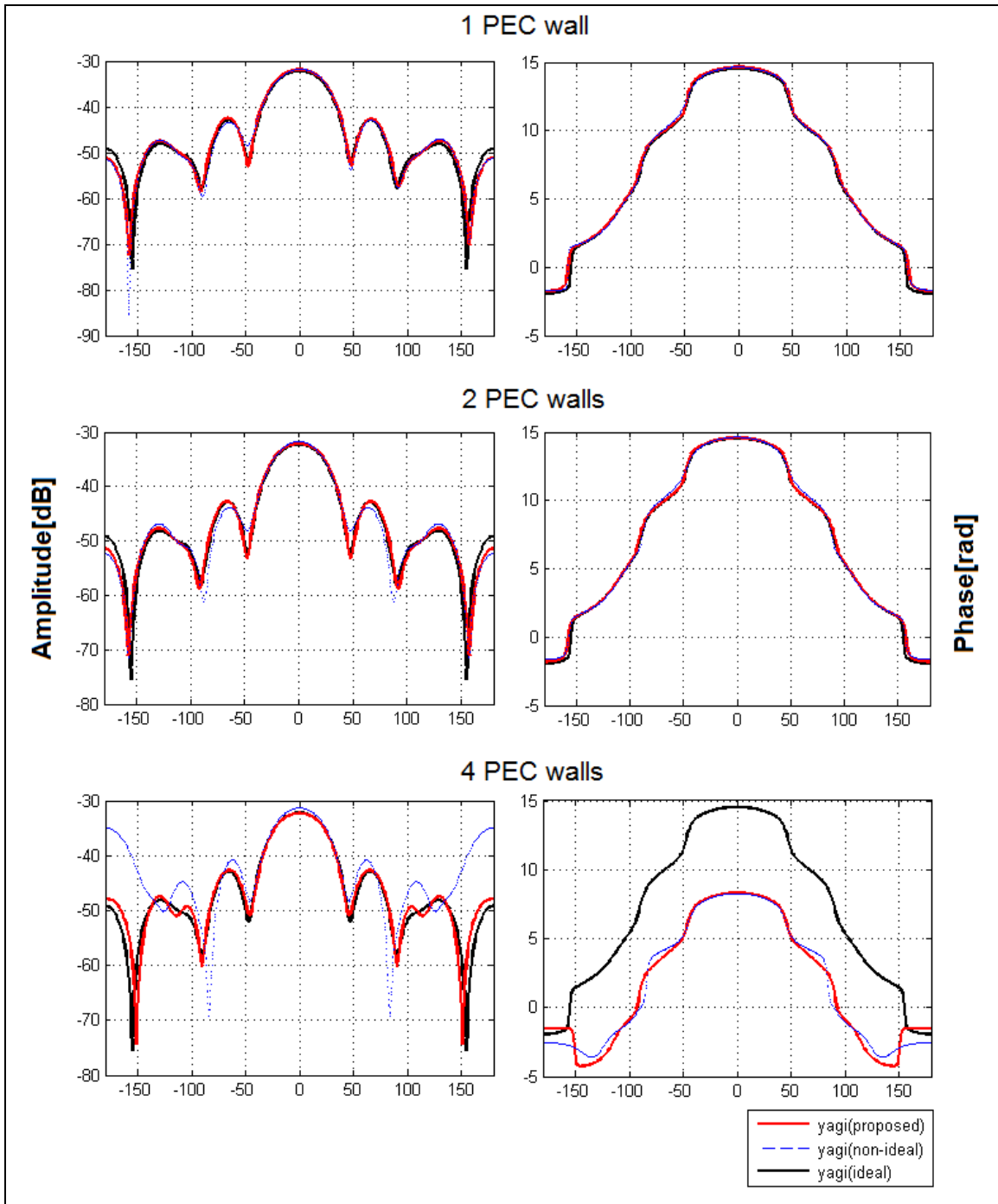


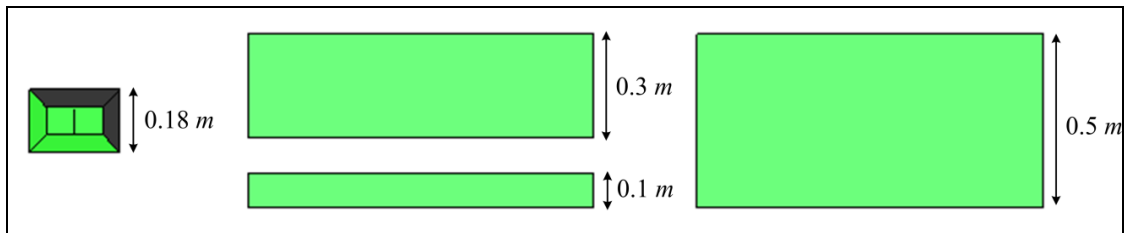
**Figure 4.33** Comparison of the reconstructed patterns for the Yagi antenna under different number of PEC plates.

It is shown that when there is only one PEC plate, the reconstructed results are always the best for both AUTs; while the reconstructed results are always the worst when there are

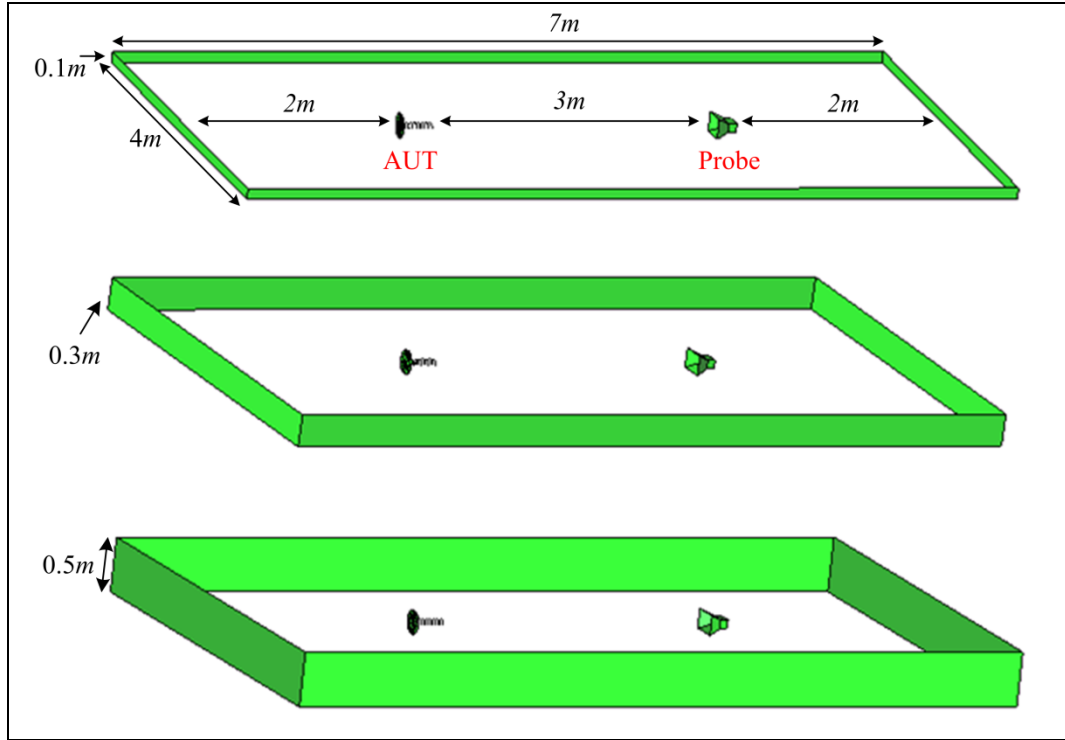
four PEC plates. It indicates that when the number of PEC plates increase, the environment gets more complicated, there are more reflections and diffractions, and the reconstructed results will get worse.

To look deeper into the question that how different environments affect the pattern reconstruction quality, we need to further change the environmental effects. One way is to add more PEC objects between the antennas and the PEC plates. However, if the object is set too close to the antennas, this may change the current distribution on the AUT and affect the reconstructed results. Another way is to increase the width of the PEC plates and generate stronger reflections.

The following example is to illustrate how the pattern reconstruction is affected by the width of the PEC plates. For comparison purposes, we will use the model in Section 4.2 and use that result as a reference. In Section 4.2, the AUTs and the probe antenna are newly designed and the simulation frequency is 1.5 GHz. Four PEC plates form a contour around the AUT and the probe. The helical antenna and the yagi antenna are the AUTs; while the horn antenna is the probe. We will keep those settings in the following example, but change the width of the PEC plates from 0.3 m to be 0.1 m and 0.5 m, respectively. Figure 4.34 shows the model using different widths of PEC plates. It is seen that when the plate width is 0.1 m, it is of a relatively narrow strip compared to the antenna size; when the width is 0.5 m, it is relatively wide.



(a)



(b)

**Figure 4.34** Comparison of the models with different PEC plate widths.

The pattern reconstruction procedure is the same as described in the previous examples. And the reconstructed results are shown in Figures 4.35 and 4.36. The two figures list the comparisons of the reconstructed results under different width settings when the AUTs are the helical antenna and the yagi antenna, respectively. And they clearly show that the reflections gets stronger and the reconstructed results get worse when the PEC plate width gets increased. We also calculated and compared the error between the ideal pattern and the reconstructed pattern with respect to the rotation angle  $\phi$  under the three width settings. And the error is defined as:

$$error(\phi) = |S_{21}(\phi) - S'_{21}(\phi)| \quad (4.1)$$

where  $S_{21}(\phi)$  is the ideal pattern of the AUT and  $S'_{21}(\phi)$  is the reconstructed pattern of

the AUT. The results for the helical antenna and the yagi antenna are shown in Table 4.1 and Table 4.2, respectively. The Mean / STD / Maximum values of the error term represent for the average / standard deviation / largest values of error with respect to angle  $\phi$ . And the values in the tables have an order of  $10^{-4}$ .

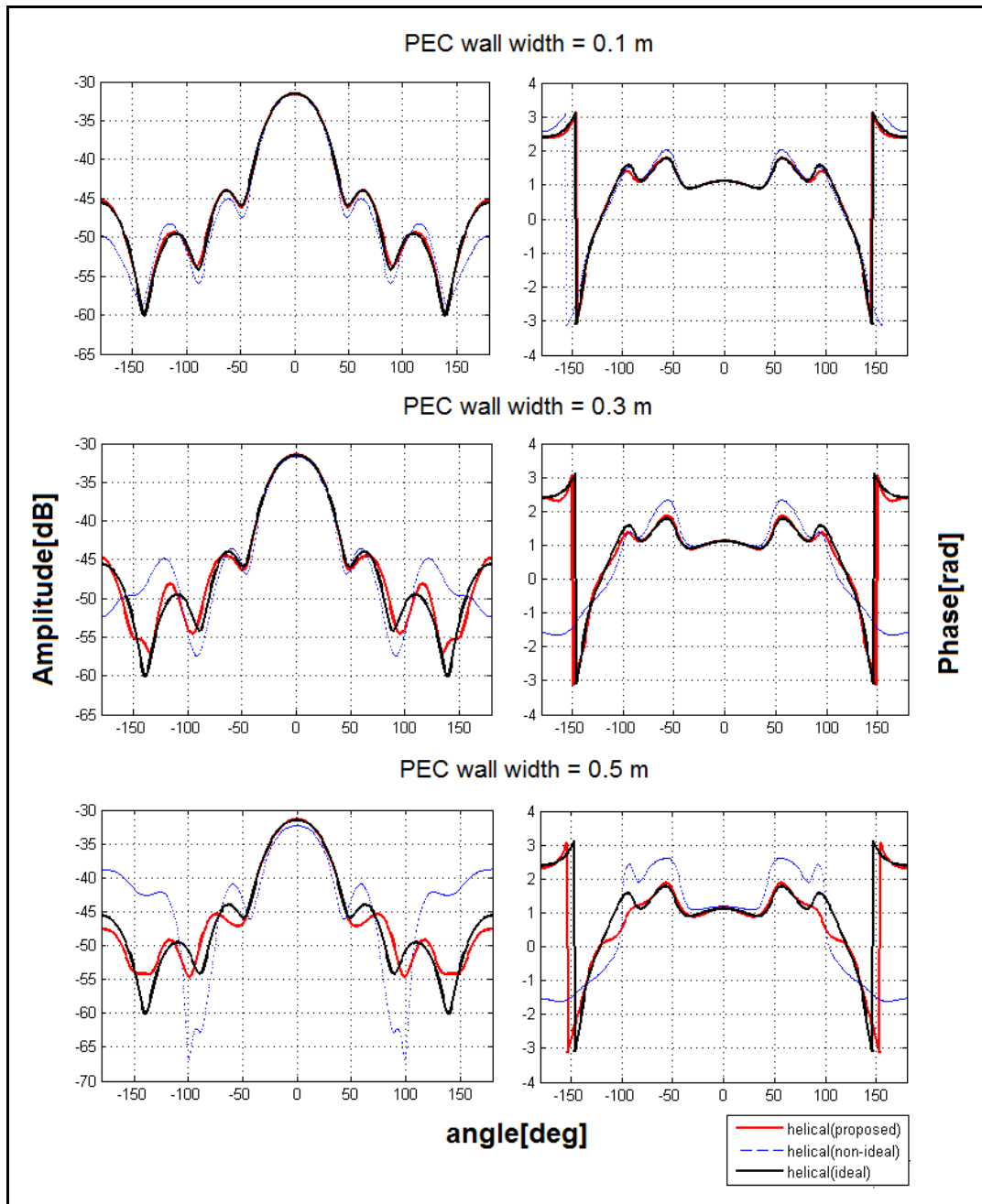


**Figure 4.35** Comparison of the reconstructed patterns for the helical antenna under three PEC plate width settings.

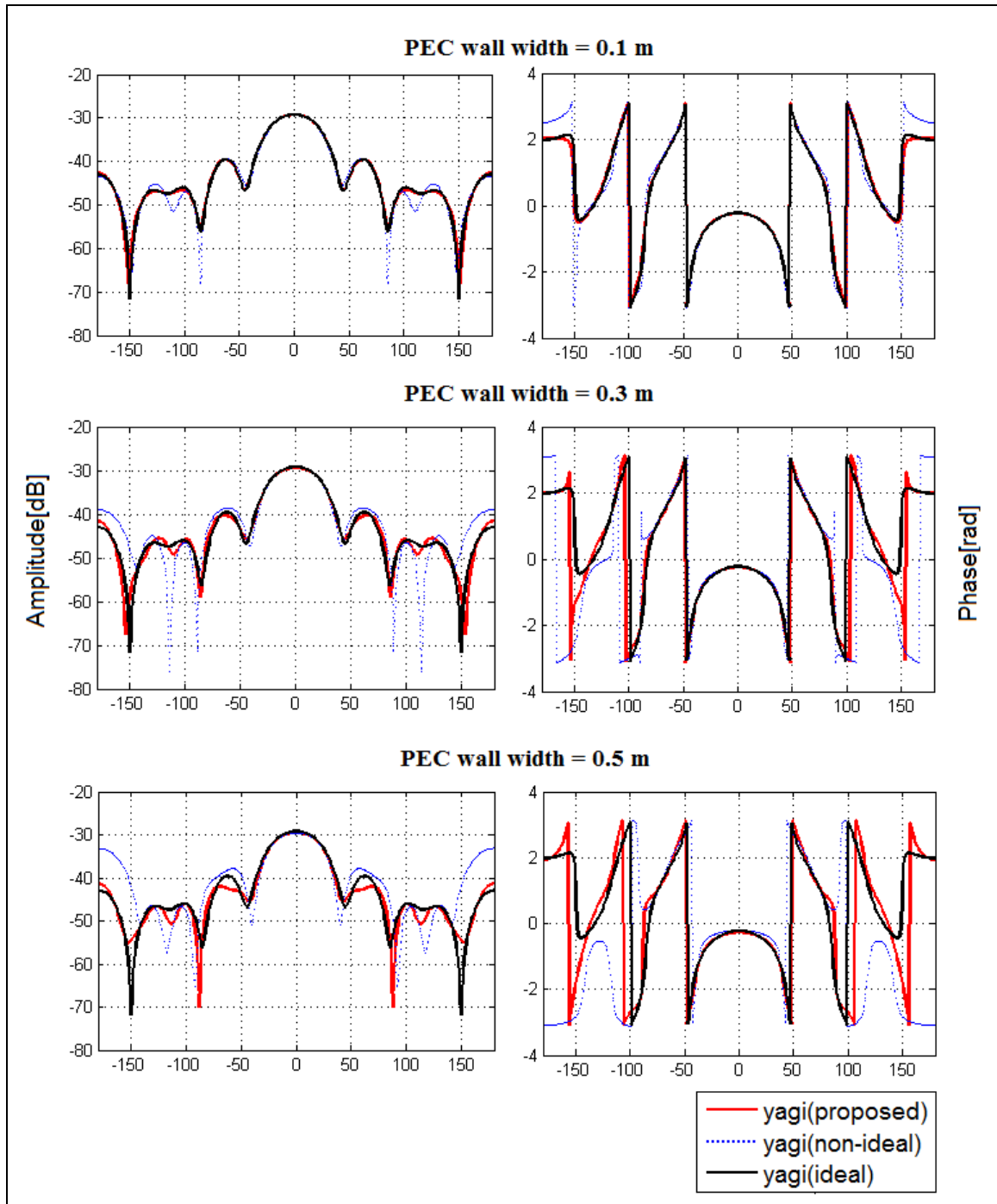


**Figure 4.36** Comparison of the reconstructed patterns for the yagi antenna under three PEC plate width settings.

**Table 4.1** Reconstruction error for the helical antenna in the angular domain at 1.5 GHz

Error ( $e^{-04}$ )	Width = 0.1m	Width = 0.3m	Width = 0.5m
Mean Error level	1.06	3.82	6.55
STD Error level	0.68	2.91	4.80
Maximum Error level	2.55	10.26	18.92

**Table 4.2** Reconstruction error for the yagi antenna in the angular domain at 1.5 GHz

Error ( $e^{-04}$ )	Width = 0.1m	Width = 0.3m	Width = 0.5m
Mean Error level	1.59	5.45	8.99
STD Error level	0.97	3.48	7.07
Maximum Error level	4.28	12.35	31.21

Based on the above examples, we can conclude that when the number of PEC plates increases or the width of the PEC plates gets larger, the environment becomes more complicated and there will be stronger reflections, and the reconstructed results get worse. We can claim that the effectiveness of the pattern reconstruction is inversely proportional to the complexity of the environment.

## Chapter 5

# Extension of the Deconvolution Method to Three-Dimensional Pattern Reconstruction

In the last chapter, models of different sizes are simulated and discussed. Examples in Section 4.3 show that reconstructed results of the model with the plate width of  $0.5 m$  are not as good as for the other examples. And we conclude that the effectiveness of the pattern reconstruction is inversely proportional to the complexity of the environment. So the question comes to our mind naturally: how would the deconvolution method handle the case when the plate width is much larger than the antenna size?

For all previous examples, we constitute the environment such that the PEC plates are around the probe and the AUT. And the PEC plates, whether they have one or two or four plates, whether they are wide or narrow, are always located at the azimuth plane of the antennas. But this would not be the practical case in a real measurement environment. If the measurement is carried out inside a room, there would be concrete plates around the room, the floor, and the ceiling. Therefore, there would be much more reflections from all directions inside the room compared with the examples in Chapter 4. And it would have more practical meaning if the deconvolution method can address this case. This chapter presents the theoretical derivation and numerical examples for a realistic environment.

## 5.1 Equation and Derivation

In Section 3.1, we start by considering an AUT which can generate an ideal pencil beam pattern. As shown in Figure 3.2, the AUT, the probe and two objects are on the same plane, and the received response at the probe is a function of the rotation angle  $\phi$ . So the time domain response along angle  $\phi$  can be described as an impulse response along  $\phi$  or a spatial signature of  $\phi$ . And the equation (3.16),

$$P_{non-ideal\ AUT}(\phi, f) = P_{ideal\ AUT}(\phi, f) \otimes_{\phi} A(\phi, f)$$

reveals that the measured non-ideal signal can be represented as an angular convolution between the ideal signal and the environmental responses. The convolution is in the azimuth angle  $\phi$  domain, while the pattern measurements are considered in 2D (along the azimuth angle only), even through the numerical simulations are carried out in 3D.

In a complicated environment, when objects and antennas are not in the same plane, the impulse response of the environment is not only related to the azimuth angle, but also related to the elevation angle. Similarly, we first assume an AUT generates an ideal pencil beam pattern (the radiated signal will be along one direction in the far field). As shown in Figure 5.1, the gray plane is the azimuth plane where the AUT, the probe and Object 1 are located; while Object 2 is above the plane. It is easy to know that reflections occur in both  $\phi$  and  $\theta$  angles. The received time domain signal at the probe, when the AUT is at the rotation angles  $(\theta, \phi)$ , is unique with respect to other angles and will not be related to the response of the AUT along other angles. Therefore, the received response at the probe will be a function of both the azimuth angle  $\phi$  and the elevation angle  $\theta$ .

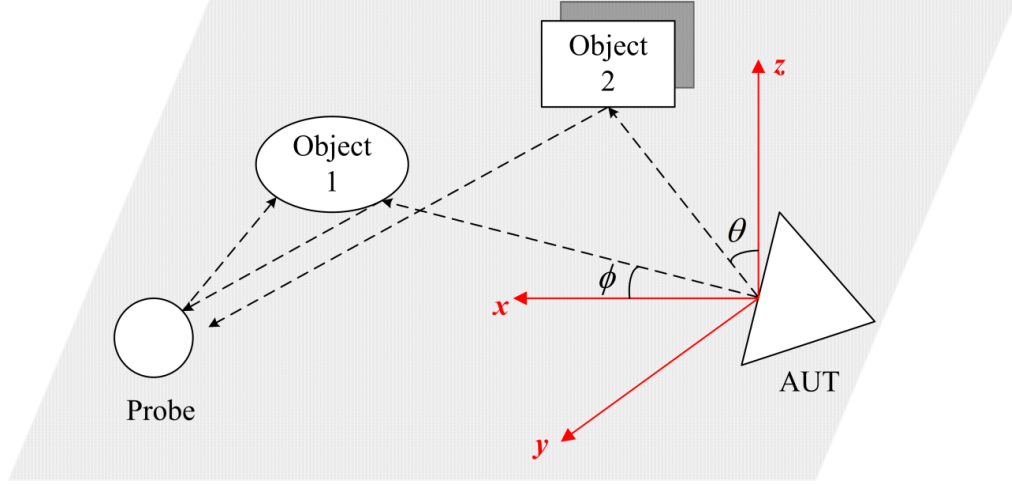


**Figure 5.1** Multiple reflections exist in the whole spatial domain.

The measured signal at the probe, which contains various reflections, can be represented as a convolution in time by the ideal signal (without any reflection) and the impulse response of the environment along the rotation angle  $(\theta_L, \phi_I)$ . It can be written as (similar to previous case):

$$P_{non-ideal}(\theta_L, \phi_I, t) = P_{ideal}(\theta_L, \phi_I, t) \otimes A(\theta_L, \phi_I, t) \quad (5.1)$$

or

$$P_{non-ideal}(\theta_L, \phi_I, f) = P_{ideal}(\theta_L, \phi_I, f) \cdot A(\theta_L, \phi_I, f) \quad (5.2)$$

where  $\otimes$  denotes a time convolution, and

$P_{non-ideal}(\theta_L, \phi_I, t)$  is the non-ideal time domain signal at the probe in the presence of the reflections for the rotation angle  $(\theta_L, \phi_I)$ ;

$P_{non-ideal}(\theta_L, \phi_I, f)$  is the non-ideal frequency domain signal at the probe in the presence of the reflections for the rotation angle  $(\theta_L, \phi_I)$ ;

$P_{ideal}(\theta_L, \phi_I, t)$  is the ideal time domain signal without any reflection for the rotation angle  $(\theta_L, \phi_I)$ ;

$P_{ideal}(\theta_L, \phi_I, f)$  is the ideal frequency domain signal without any reflection for the rotation angle  $(\theta_L, \phi_I)$ ;

$A(\theta_L, \phi_I, t)$  is the impulse response of the environment when the AUT has a ideal pencil beam pattern pointing along the angle  $(\theta_L, \phi_I)$ ;

$A(\theta_L, \phi_I, f)$  is the frequency domain response of the environment when the AUT has a ideal pencil beam pattern pointing along the angle  $(\theta_L, \phi_I)$ .

Note that  $A(\theta_L, \phi_I, t)$  represents the reflection contributions from the environment at the rotation angle  $(\theta_L, \phi_I)$  and is independent of the particular AUT. It is the spatial signature of the environment.

In a real situation, the AUT will radiate towards every direction in the spatial domain and cannot have an ideal pencil beam pattern. We define the impulse response of the environment along the angle  $(\theta_L, \phi_I)$  as  $\hat{A}(\theta_L, \phi_I, f)$  when the AUT does not have an ideal pencil beam pattern. Then, by using (5.2) we have:

$$P_{non-ideal}(\theta_L, \phi_I, f) = P_{ideal}(\theta_L, \phi_I, f) \cdot \hat{A}(\theta_L, \phi_I, f) \quad (5.3)$$

here,  $\hat{A}(\theta_L, \phi_I, f)$  is the impulse response of the environment along the angle  $(\theta_L, \phi_I)$  when the AUT does not have a ideal pencil beam pattern. It is not the true impulse response of the environment but also contains the pattern information of the AUT. For the deconvolution method, we need to know the true impulse response  $A(\theta_L, \phi_I, f)$  of the test environment. Then  $\hat{A}(\theta_L, \phi_I, f)$  can be considered as a convolution in the angular domain of the normalized beam pattern and the true impulse response. That is,

$$\hat{A}(\theta_L, \phi_I, f) = \frac{P_{ideal}(\theta, \phi, f)}{P_{ideal}(\theta_L, \phi_I, f)} \otimes_{\phi, \theta} A(\theta, \phi, f) \Big|_{\theta=\theta_L, \phi=\phi_I} \quad (5.4)$$

Here,  $P_{ideal}(\theta, \phi, f)$  is the ideal pattern without any reflection from the environment at the frequency  $f$ . And  $\otimes_{\phi, \theta}$  is the 2D convolution operator for both the azimuth angle  $\phi$  and the elevation angle  $\theta$ , in other words, this operator is a two-dimensional operator works on each row and column of the matrix. By substituting (5.4) into (5.3), we have:

$$P_{non-ideal}(\theta_L, \phi_I, f) = P_{ideal}(\theta, \phi, f) \otimes_{\phi, \theta} A(\theta, \phi, f) \Big|_{\theta=\theta_L, \phi=\phi_I} \quad (5.5)$$

For a general angle of  $(\theta, \phi)$ , we have:

$$P_{non-ideal}(\theta, \phi, f) = P_{ideal}(\theta, \phi, f) \otimes_{\phi, \theta} A(\theta, \phi, f) \quad (5.6)$$

which is an extension of the equation (3.16). Therefore, the radiation pattern of the AUT in the presence of reflections can be considered as two-dimensional convolution in the angular domain between the ideal pattern of the AUT and the impulse response of the environment. Note that the convolution is now carried out in both the azimuth angle  $\phi$  domain and the elevation angle  $\theta$  domain, thus the 3D pattern measurements (in both azimuth angle and elevation angle) are carried out to form the matrix of  $P_{non-ideal}(\theta, \phi, f)$ ,  $P_{ideal}(\theta, \phi, f)$  and  $A(\theta, \phi, f)$ . And we know that taking the FFT will transform the convolution in the angular domain to the multiplication in the other domain. Thus the impulse response of the environment  $A(\theta, \phi, f)$  can be extracted by taking the Inverse Fourier Transform of (5.6) after a reference antenna is measured in the environment. And the ideal radiation pattern of the AUT  $P_{ideal}(\theta, \phi, f)$  can then be obtained for any AUT measured in the same environment using (5.6).

## 5.2 Steps Summarized for the Methodology

The procedure to carry out the deconvolution method in 3D environments is very similar to the procedure described in Section 3.2. We first carry out the measurement in a 3D non-anechoic environment using two reference antennas, whose ideal patterns are known, and perform a deconvolution to estimate the environmental responses  $A$ . Then, we use the AUT as the transmitter and carry out the measurement in the same environment and estimate the ideal radiation pattern of the AUT. The entire procedure consists of 4 steps:

- 1) At a fixed frequency, measure the reference antenna in a non-anechoic environment and obtain the received response  $P_{non-ideal}(\theta, \phi, f)$ . Also the ideal response for the reference antenna  $P_{ideal}(\theta, \phi, f)$  is known.
- 2) Calculate the environmental effects  $A(\theta, \phi, f)$  using the equation:

$$P_{non-ideal}(\theta, \phi, f) = P_{ideal}(\theta, \phi, f) \otimes_{\phi, \theta} A(\theta, \phi, f)$$

- 3) At the same frequency, use the AUT as the transmitter at the same position and measure the AUT in the same non-anechoic environment as described in step (1), and let  $P_{non-ideal AUT}(\theta, \phi, f)$  be the result.
- 4) By substituting the environmental effects  $A(\theta, \phi, f)$  into the equation one can obtain the ideal response of the AUT  $P_{ideal AUT}(\theta, \phi, f)$  through deconvolution:

$$P_{non-ideal AUT}(\theta, \phi, f) = P_{ideal AUT}(\theta, \phi, f) \otimes_{\phi, \theta} A(\theta, \phi, f)$$

Again, we can see that the deconvolution method only requires a single frequency measurement, and does not need any prior knowledge of the test environment.

## 5.3 Processing of the Data

Section 3.3 gives the data processing procedures for 2D radiation pattern reconstruction. This section gives the following procedures for processing the simulated data for 3D radiation pattern reconstruction. The procedures will be similar to that for 2D pattern reconstruction but rotate the AUT three-dimensionally.

1. First, create the simulation model for the 3D pattern measurement system. For both the reference antenna and the AUT, each antenna needs to have two simulation models. One model only have antennas (the probe and the AUT), and there is no PEC plates as reflectors. Such model is to simulate the free space condition to obtain the ideal pattern of the antenna. The other model has both antennas and PEC plates, and is to simulate the non-anechoic environment to obtain the non-ideal pattern of the antenna.
2. For each model, rotate the AUT along itself for a step of  $10^\circ$  for both the azimuth angle and the elevation angle  $(\theta, \phi)$ , and for each rotation angle the model is simulated and the  $S_{21}$  data is collected. The  $S_{21}$  data along each spatial angle  $(\theta, \phi)$  forms the radiation pattern of the AUT. There are 36 data points along the elevation angle  $\theta$ , i.e.  $0^\circ, 10^\circ, \dots, 350^\circ$ . For each elevation angle, the AUT rotates one loop in the azimuth plane and there will be 36 data points in one loop, i.e.  $-180^\circ, -170^\circ, \dots, 170^\circ$ . One can imagine this as the AUT rotates in a step of  $10^\circ$  in the azimuth plane and changes the elevation angle in a step of  $10^\circ$ . In total, there will be  $36 \times 36$  data points forming a period in the angular domain  $(\theta, \phi)$ , i.e.  $(0^\circ, -180^\circ), (0^\circ, -170^\circ), \dots, (0^\circ, 170^\circ), (10^\circ, -180^\circ), (10^\circ, -170^\circ), \dots, (350^\circ, 160^\circ), (350^\circ, 170^\circ)$  in a two dimensional

matrix form, and then the data will repeat this sequence. The data at the spatial angle of  $(360^\circ, 180^\circ)$  is equal to that of  $(0^\circ, -180^\circ)$  and belongs to the next period. Therefore, the non-ideal pattern  $P_{non-ideal-AUT}(\theta, \phi, f)$ , the ideal pattern  $P_{ideal-AUT}(\theta, \phi, f)$  and the environmental effects  $A(\theta, \phi, f)$  all are two-dimensional periodic sequences in the angular domain  $(\theta, \phi)$ . Note that in the normal Spherical coordinate system, the elevation angle  $\theta$  varies between  $[0^\circ, 180^\circ]$ . Here, the  $\theta$  angle will change its value between  $[0^\circ, 360^\circ]$  to form a period in the spatial angular domain. However, we only need to simulate the model when  $\theta$  varies between  $[0^\circ, 180^\circ]$ , from which the data set of  $\theta$  between  $[180^\circ, 360^\circ]$  can be derived. Since there is no explicit definition for the data set of  $\theta$  between  $[180^\circ, 360^\circ]$  in the normal spherical coordinate system, we need to derive that data through using the conversion between the spherical coordinate system and the Cartesian coordinate system, as shown in the Appendix A. Then, both  $(\theta, \phi)$  change its value within  $2\pi$  range and form a periodic 2D matrix.

3. Simulate the model for the reference antenna in the free space and the desired non-anechoic environment to obtain the ideal and non-ideal patterns of the reference antenna  $P_{ideal-Ref}(\theta, \phi, f)$  and  $P_{non-ideal-Ref}(\theta, \phi, f)$ , respectively. Similarly, by replacing the reference antenna with the desired AUT and carry out the simulation, we can obtain the ideal pattern  $P_{ideal-AUT}(\theta, \phi, f)$  and the non-ideal pattern  $P_{non-ideal-AUT}(\theta, \phi, f)$  for the desired AUT. The ideal pattern of the AUT  $P_{ideal-AUT}(\theta, \phi, f)$  will be the goal of the reconstructed pattern.
4. Now we need to apply (5.6) to reconstruct the 3D radiation pattern of the AUT.

According to Section 3.9 of [40], the convolution of two 2D periodic sequences is the multiplication of the corresponding 2D matrix of discrete Fourier series. Let  $\tilde{x}_1(m, n)$  and  $\tilde{x}_2(m, n)$  be two periodic sequences of period  $N*M$  with the 2D discrete Fourier series denoted by  $\tilde{X}_1(k, l)$  and  $\tilde{X}_2(k, l)$ , respectively. It can be written as:

$$\tilde{x}_3(m, n) = \sum_{q=0}^{M-1} \sum_{r=0}^{N-1} \tilde{x}_1(q, r) \tilde{x}_2(m-q, n-r) \quad (5.7)$$

$$\tilde{X}_3(k, l) = \tilde{X}_1(k, l) \tilde{X}_2(k, l) \quad (5.8)$$

5. From (5.6) we have the following equations:

$$P_{non-ideal-Ref}(\theta, \phi, f) = P_{ideal-Ref}(\theta, \phi, f) \otimes_{\theta, \phi} A(\theta, \phi, f) \quad (5.9)$$

$$P_{non-ideal-AUT}(\theta, \phi, f) = P_{ideal-AUT}(\theta, \phi, f) \otimes_{\theta, \phi} A(\theta, \phi, f) \quad (5.10)$$

Therefore, by taking the 2D-FFT of both sides of (5.9), the angular convolution operator will become the multiplication operator. We can derive the environment effects  $A(\phi, f)$  as:

$$A(\theta, \phi, f) = \text{iff}_2 \left( \frac{\text{fft}_2(P_{non-ideal-Ref}(\theta, \phi, f))}{\text{fft}_2(P_{ideal-Ref}(\theta, \phi, f))} \right) \quad (5.11)$$

where  $\text{fft}_2$  and  $\text{iff}_2$  denote the 2D-FFT and 2D-IFFT operator, respectively.

6. Take the 2D-FFT of both sides of (5.10) and substitute the environment effects

$A(\theta, \phi, f)$  into the equation, we get:

$$\begin{aligned}
P_{ideal-AUT}(\theta, \phi, f) &= \text{iff}_2 \left( \frac{\text{fft}_2(P_{non-ideal-AUT}(\theta, \phi, f))}{\text{fft}_2(A(\theta, \phi, f))} \right) \\
&= \text{iff}_2 \left( \frac{\text{fft}_2(P_{non-ideal-AUT}(\theta, \phi, f)) \cdot \text{fft}_2(P_{ideal-Ref}(\theta, \phi, f))}{\text{fft}_2(P_{non-ideal-Ref}(\theta, \phi, f))} \right)
\end{aligned} \tag{5.12}$$

Note that the division and multiplication in (5.11) and (5.12) are element by element operations on 2D matrices. All data processing will be performed off-line using a commercial software package (MATLAB 7, The MathWorks Inc., Natick, MA, 2000). In MATLAB, the function  $Y=\text{fft2}(X)$  returns the two-dimensional Discrete Fourier Transform of matrix  $X$ , computed with a Fast Fourier Transform algorithm. Similarly, the function  $Y=\text{ifft2}(X)$  returns the two-dimensional Inverse Discrete Fourier Transform of matrix  $X$ . All the data used in (5.12) need to be processed through step 2 first. Note that when the environment setting is symmetrical along the elevation angle  $\theta = 90^\circ$ , some elements of the 2D-FFT of the 2D matrices generate zero values, so in (5.12) there exists  $0 \cdot (0/0)$  value, which should be zero. However, N/A value was generated in MATLAB due to the numerical error. To conduct the 2D-IFFT of the matrix, we manually set those N/A values to be zero, which they should be, as shown in Appendix B.

7. Compare the reconstructed pattern of the AUT from (5.12) with the simulated result

$$P_{ideal-AUT}(\theta, \phi, f).$$

## 5.4 Simulation Examples

In this section, we will show examples of the 3D pattern reconstruction under five different environmental settings by using the yagi antenna and the parabolic reflector antenna as the

AUT. The five environmental settings include: four wide PEC plates around the antennas (shown in Section 5.4.1), four PEC plates as well as the PEC ground (shown in Section 5.4.2), six PEC plates form an unclosed contour around the antennas (shown in Section 5.4.3), six PEC plates forming a closed contour (shown in Section 5.4.4), and six dielectric plates forming a closed contour (shown in Section 5.4.5). Those five environmental settings present a full picture of how the deconvolution method extracts the ideal pattern from the non-ideal signal under 3D environments. For the examples shown below, a 6-element yagi antenna and a new parabolic reflector antenna will be the AUTs. Again, a horn antenna is set to be both the reference antenna and the probe. Dimensions of the horn antenna and the yagi antenna are given in Figures 4.21 and 4.23, respectively. Dimensions of the new parabolic reflector antenna are shown in Figure 5.2. The numerical simulations and the processing of the simulation data will follow the procedures as described in Section 5.3.

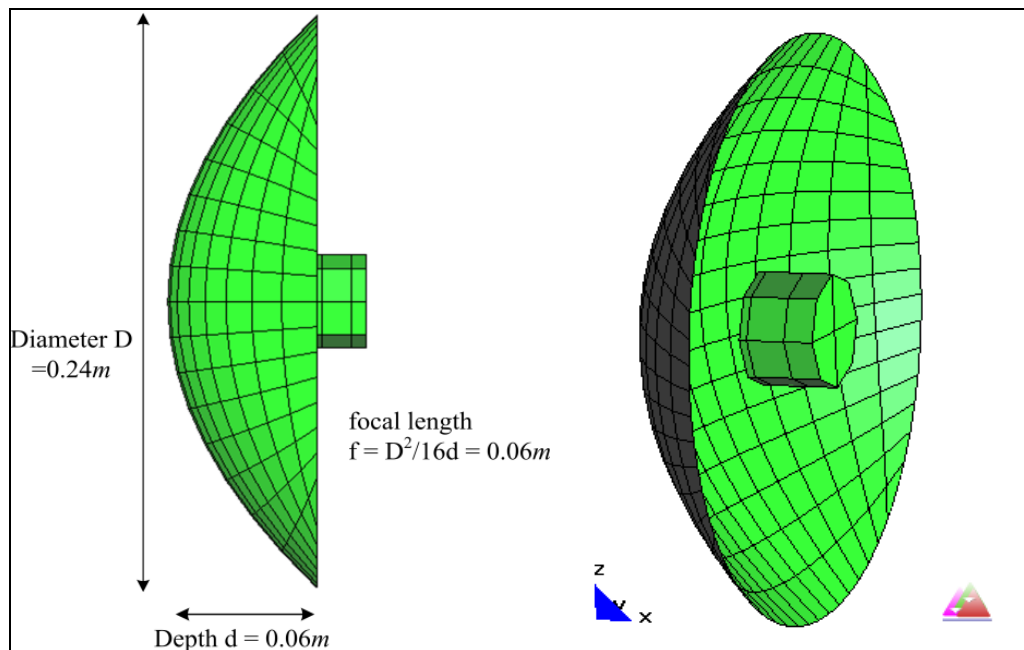


**Figure 5.2** Model of a new parabolic reflector antenna with its feeding component.

### 5.4.1 Example I: Four Wide PEC Plates Serve as Reflectors

The simulation model in this example is similar to the one shown in Figure 4.34. The difference is that the PEC plates have a width of  $2\text{ m}$  and are  $2\text{ m}$  away from the antennas in this example, as shown in Figure 5.3.

The  $S_{21}$  data was collected at each spatial angle  $(\theta, \phi)$  to form the 3D radiation pattern figure. Equation 5.12 was used to calculate the reconstructed 3D pattern for the AUT. And the reconstructed results were compared with the simulated ideal pattern of the AUT to illustrate the performance of the deconvolution method. HOBBIES was used to perform the full wave EM simulation and the operation frequency was  $1.5\text{ GHz}$ .

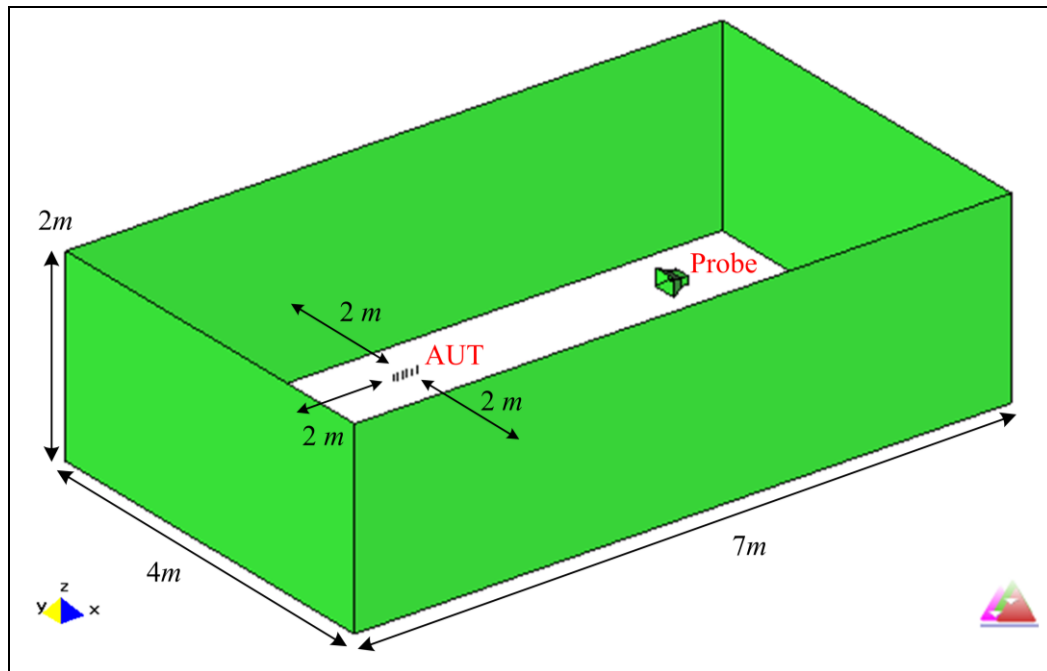


**Figure 5.3** Model of the measurement system with four very wide PEC plates.

The ideal (free space) and non-ideal (under the presence of the PEC plates) radiation patterns of the horn, the yagi, and the parabolic reflector antenna in 3D plot are shown in

Figures 5.4, 5.5 and 5.6, respectively. The vertical axis is the amplitude of  $S_{21}$  in dB scale. It is easy to observe the differences between the ideal patterns and the non-ideal patterns. The back lobes in all three figures have been greatly increased due to the reflections from the PEC plates. Note that at the rotation angle  $(\theta, \phi)=(90^\circ, 0^\circ)$ , the AUT faces toward the probe; while at  $(\theta, \phi)=(90^\circ, 180^\circ)$ , the AUT rotates  $180^\circ$  in the azimuth plane and faces back to the probe. And the back lobe is located around the angle of  $\phi = 180^\circ$ .

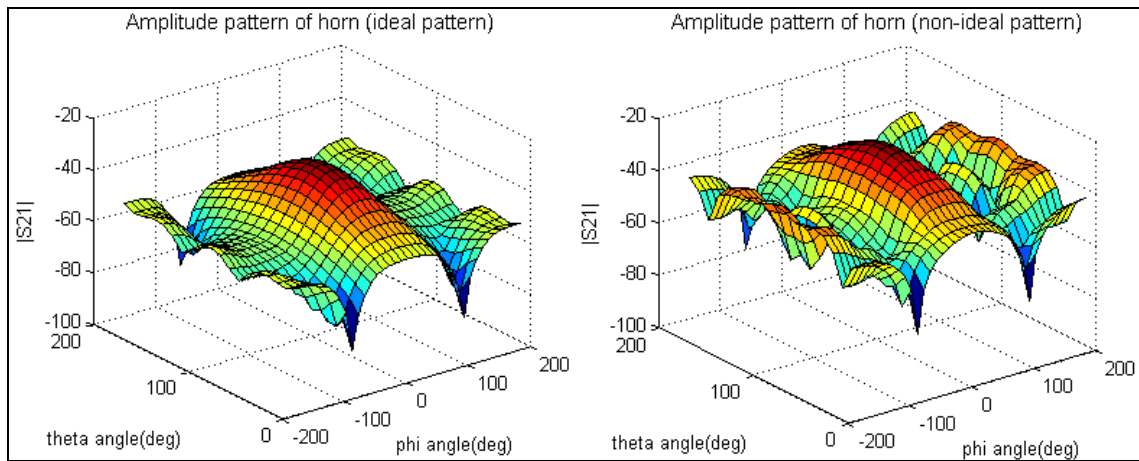


**Figure 5.4** Three-dimensional plot of the ideal and non-ideal radiation patterns of the horn antenna.

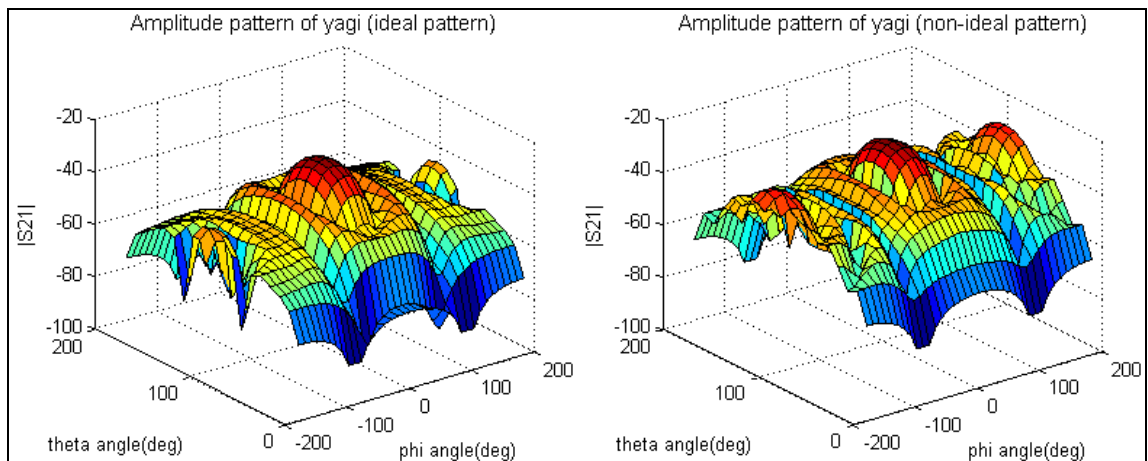


**Figure 5.5** Three-dimensional plot of the ideal and non-ideal radiation patterns of the yagi antenna.

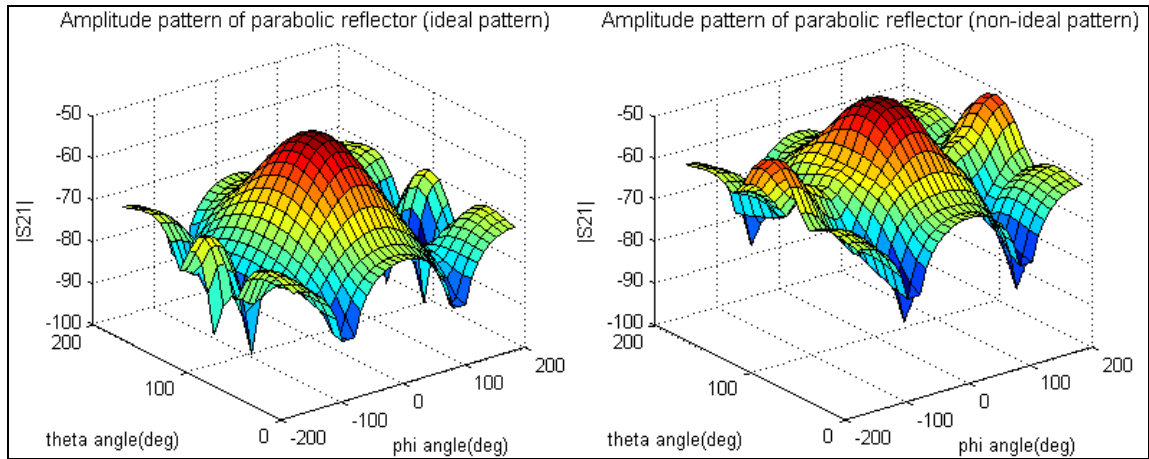


**Figure 5.6** Three-dimensional plot of the ideal and non-ideal radiation patterns of the parabolic reflector antenna.

As mentioned in Section 3.1, one condition needs to be satisfied is that the current distribution on the feed dipole of the AUT should remain close to the ideal one. Figures 5.7 and 5.8 give both the real and imaginary part of the current distribution on the feed dipole of the two AUTs, the yagi antenna and the parabolic reflector antenna, respectively. It shows that the current distribution on the feed dipole of the parabolic reflector is slightly changed (since the feed dipole is located inside the waveguide); while the current distribution of the yagi has been partly affected by the PEC plates. To mitigate this change of the current distribution due to the PEC plates, we need to increase the distance between the plates and the AUT. However, this will dramatically increase the computational size of the problem and make the simulation an infeasible task. Therefore, we will keep the current model settings, but we should expect some level of differences between the ideal pattern and the reconstructed results.

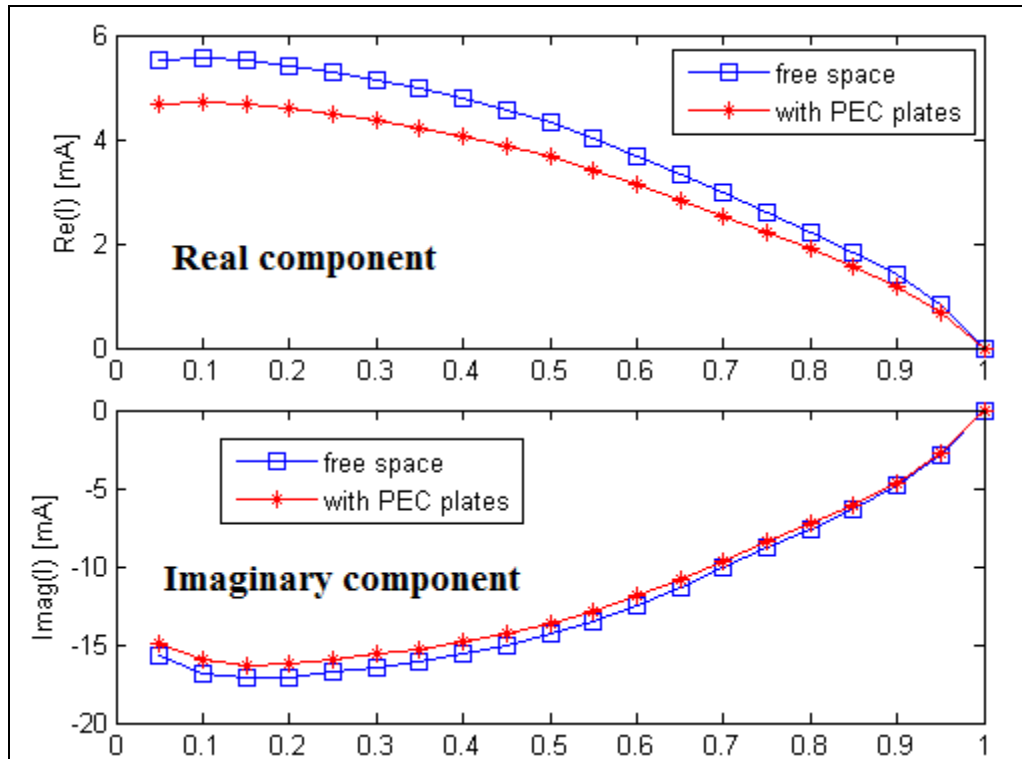


**Figure 5.7** Current distribution on the feed dipole of the yagi antenna with four very wide PEC plates.

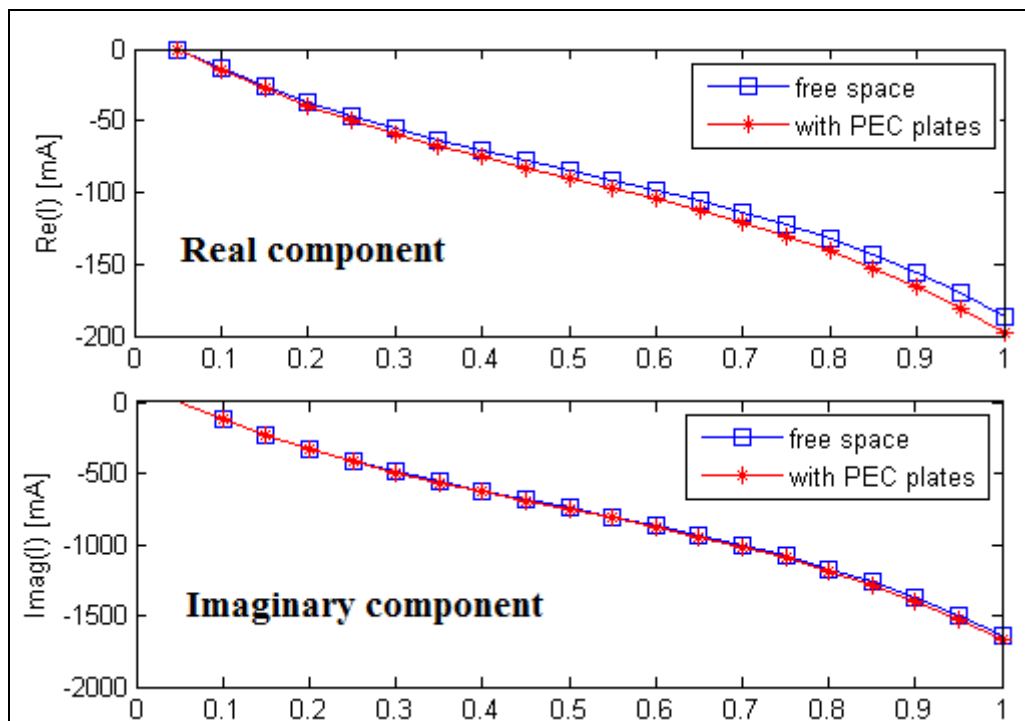


**Figure 5.8** Current distribution on the feed dipole of the parabolic reflector antenna with four wide PEC plates as the reflector.

The pattern reconstruction procedure in 3D environment follows the steps as described in Section 5.2. The 3D reconstructed pattern of the yagi antenna is shown in Figure 5.9. To better illustrate the reconstructed pattern along different spatial angles, the 2D cuts of different phi angles and theta angles are shown in Figures 5.11 and 5.12, respectively. The reconstructed pattern is indicated by the red line while the ideal pattern is indicated by the black line. The blue dash line is for the non-ideal pattern. In Figure 5.11 the  $x$ -axis is the elevation angle  $\theta$ , and the  $y$ -axis is the amplitude of  $S_{21}$  in dB scale. In Figure 5.12 the  $x$ -axis is the azimuth angle  $\phi$ , and the  $y$ -axis is the amplitude of  $S_{21}$  in dB scale. Note that the 2D cuts at  $\phi = 0^\circ$  and  $\theta = 90^\circ$  give the patterns of the principal planes for the AUT, and they are more representative in illustrating the performance of the 3D pattern reconstruction.

Similarly, for the pattern reconstruction of the parabolic reflector antenna, the 3D reconstructed pattern is shown in Figure 5.10; while the 2D cuts of different phi angles and theta angles are shown in Figures 5.13 and 5.14, respectively.

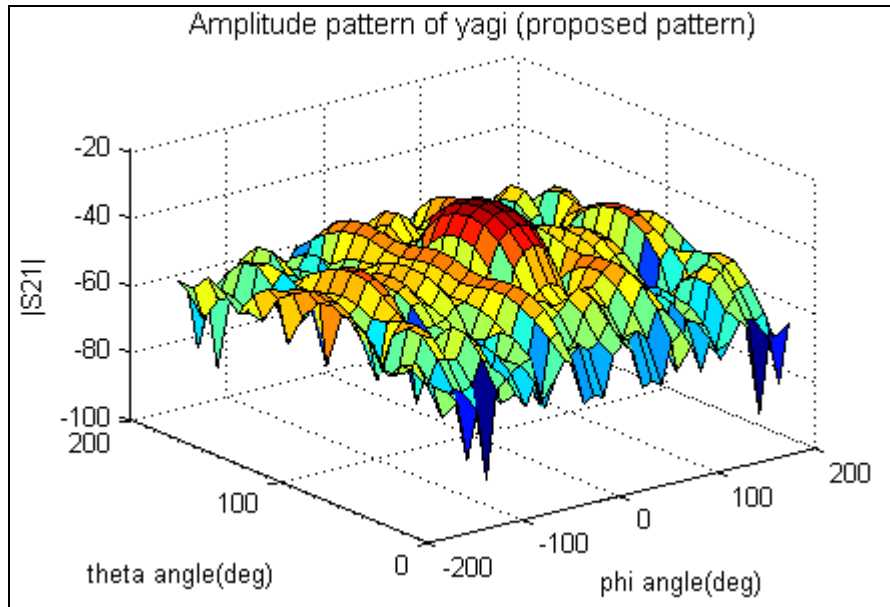


**Figure 5.9** Three-dimensional plot of the reconstructed pattern for the yagi antenna.

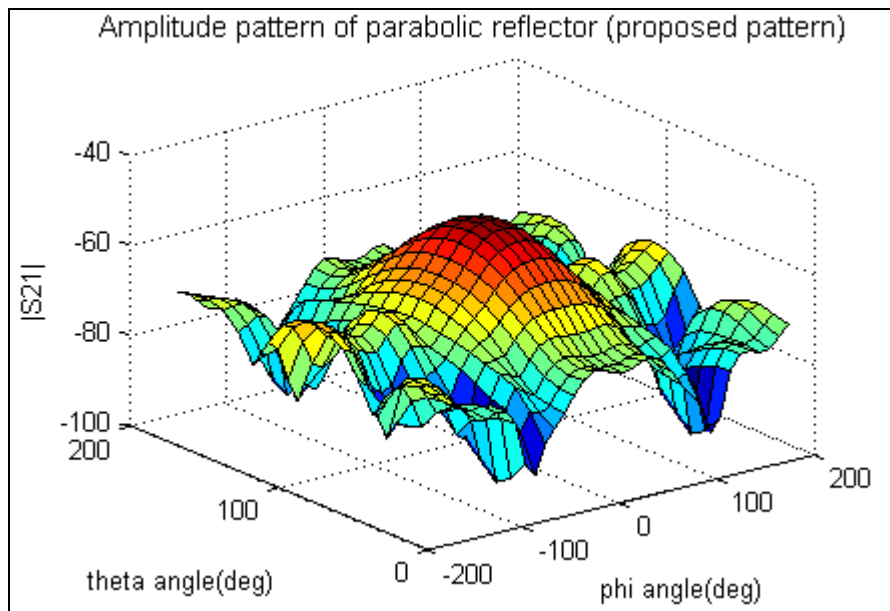


**Figure 5.10** Three-dimensional plot of the reconstructed pattern for the parabolic reflector antenna.

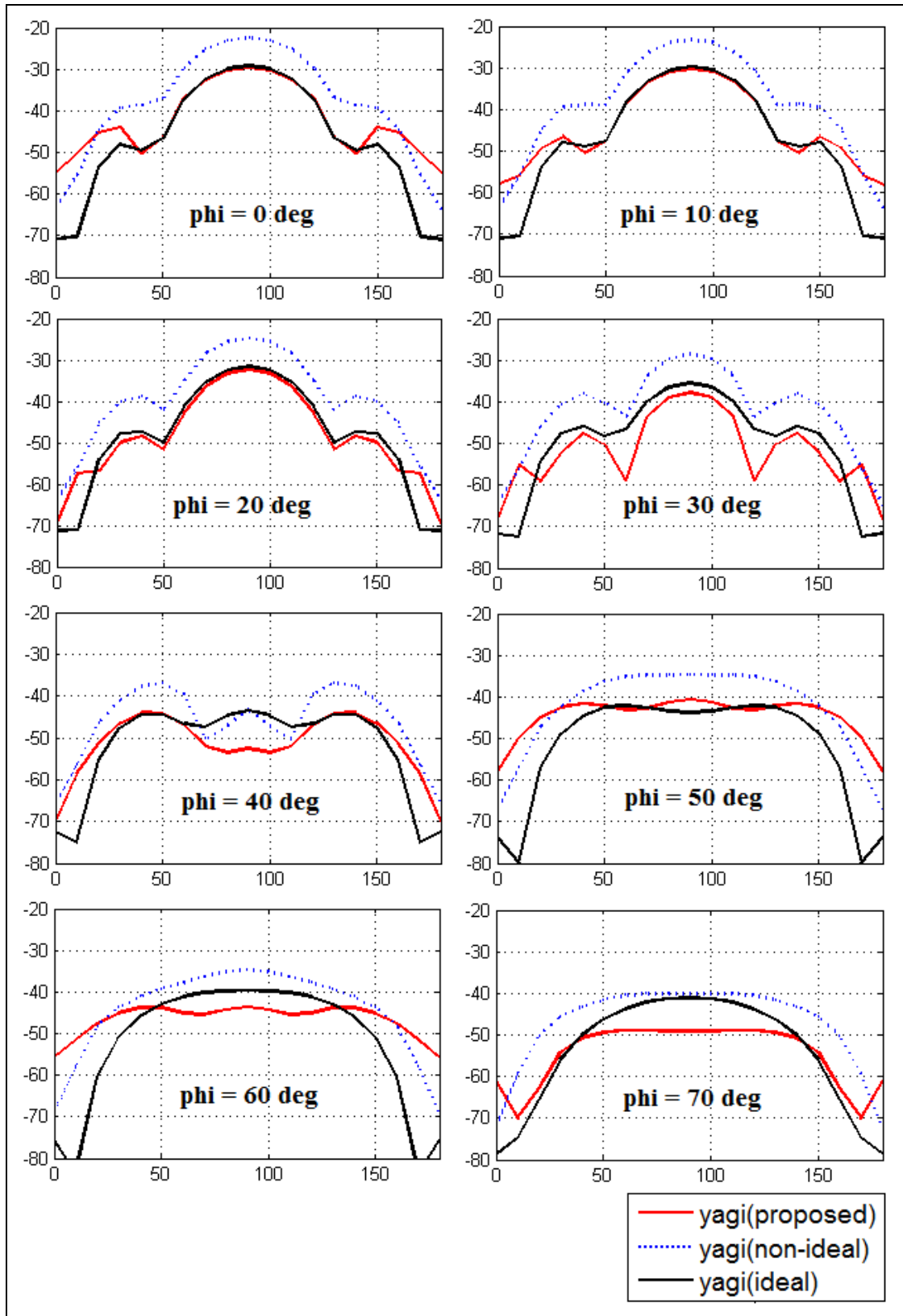


**Figure 5.11** Comparison of the reconstructed patterns for the yagi antenna along different  $\phi$  angles with four wide PEC plates as the reflector.

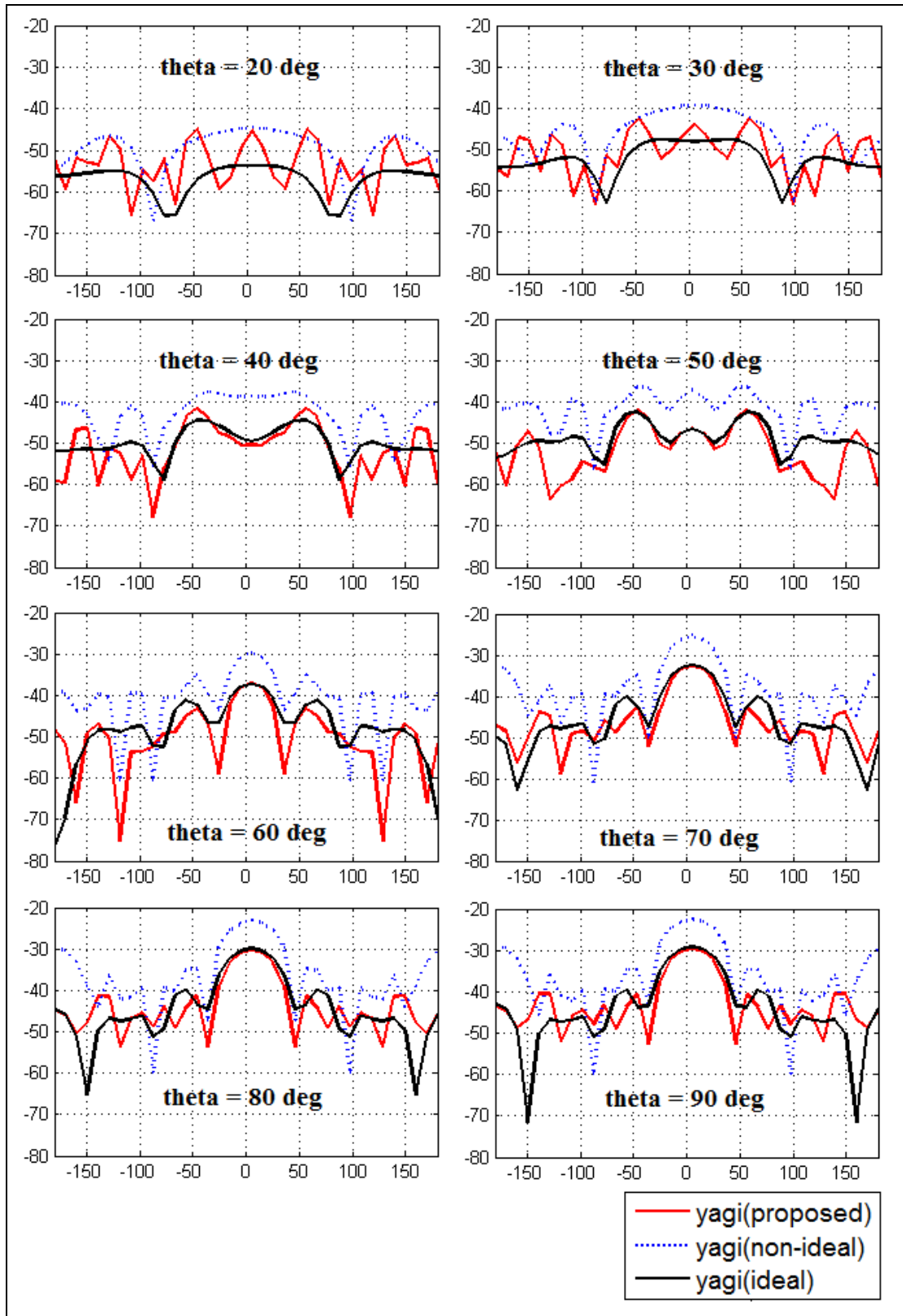


**Figure 5.12** Comparison of the reconstructed patterns for the yagi antenna along different theta angles with four wide PEC plates as the reflector.

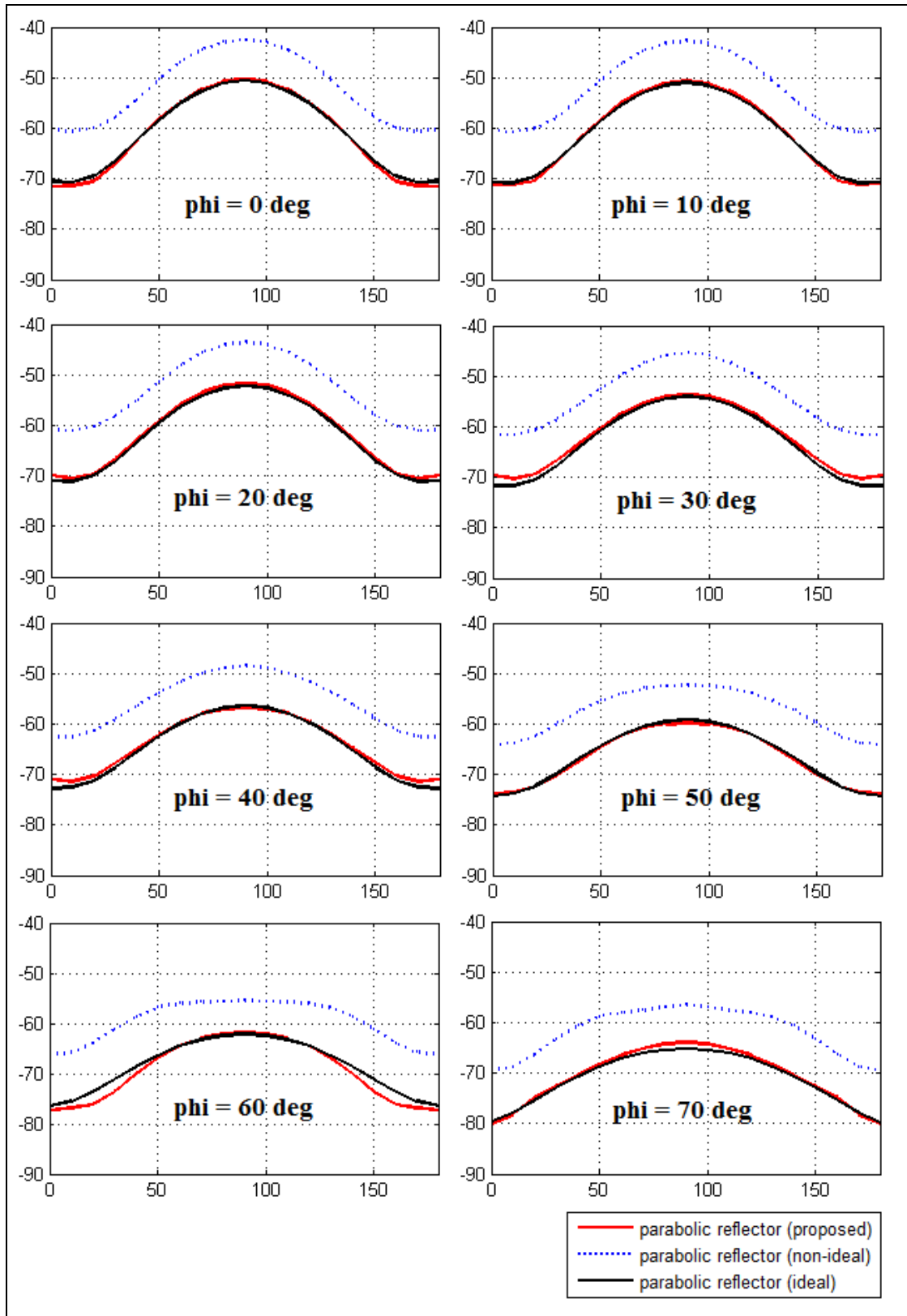


**Figure 5.13** Comparison of the reconstructed patterns for the parabolic reflector antenna along different  $\phi$  angles with four wide PEC plates as the reflector.

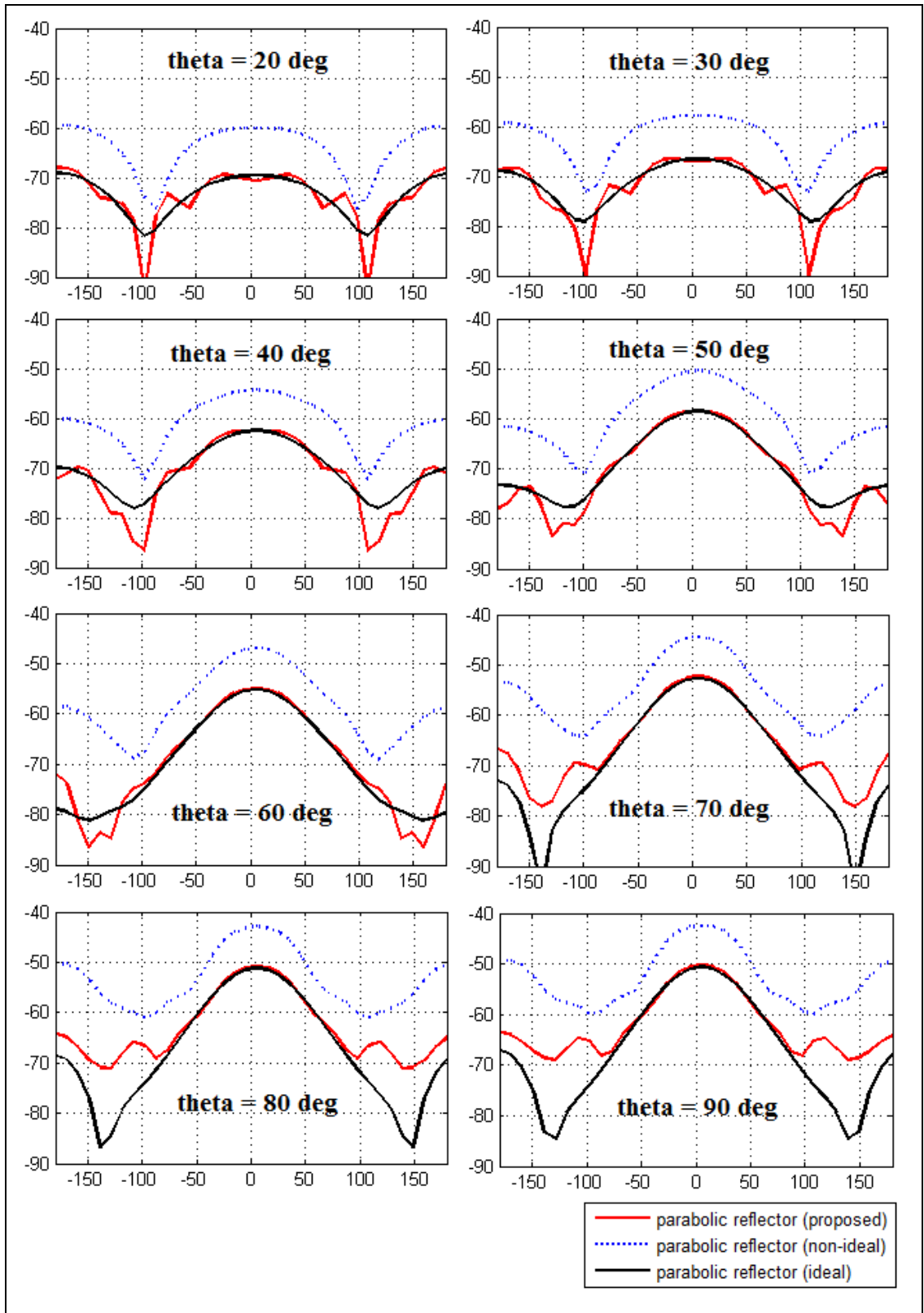


**Figure 5.14** Comparison of the reconstructed patterns for the parabolic reflector antenna along different theta angles with four wide PEC plates as the reflector.

As shown in the figures, the results of the 3D pattern reconstruction for the parabolic reflector antenna are of engineering accuracy. The reconstructed pattern is very close to the ideal pattern. While for the yagi antenna the results are not as good as previous 2D reconstruction examples. The pattern shapes at some 2D cuts are a little different from the ideal ones. But the reconstructed pattern basically follows the trend of the ideal pattern and the undesired reflections have been greatly compensated by using the deconvolution method. One reason for the difference of patterns would be the current distribution on the feed dipole of the AUT has been changed and this leads to the change of the free space radiation pattern of the AUT.

The other possible reason may be due to the lack of the sample data in the angular domain. In previous examples, the 2D reconstruction takes  $1^\circ$  as a step in  $\phi$  angle; while the 3D reconstruction example takes  $10^\circ$  as a step in  $\theta$  angle and  $\phi$  angle. Even though the total number of data points (equals  $36 \times 36$ ) is much larger than that of the 2D examples, the density of data points in the angular domain is much lower. And this low rate of sample points may not sufficiently characterize the environmental effects, especially when the environments are complicated or the reflections are strong.

#### *5.4.2 Example II: Four PEC Plates and the Ground Serve as Reflectors*

The simulation model of this example includes the antenna, four PEC plates and the PEC ground, as shown in Figure 5.15. The PEC plates and the ground serve as the reflectors and reflect the fields from the AUT to all directions. Those four PEC plates all have the same size of  $3\text{ m}$  by  $4\text{ m}$  and are connected with the PEC ground plane (the blue plane in Figure

5.15), just like the four plates and the floor of a room. The AUT and the probe are 2.5 meters away from the PEC ground. The PEC ground is modeled with an infinite large PEC plane. Due to the property of an infinite large PEC plane, the PEC ground can be substituted by adding the image of the model with respect to the PEC ground, as shown in the red circle in Figure 5.15.

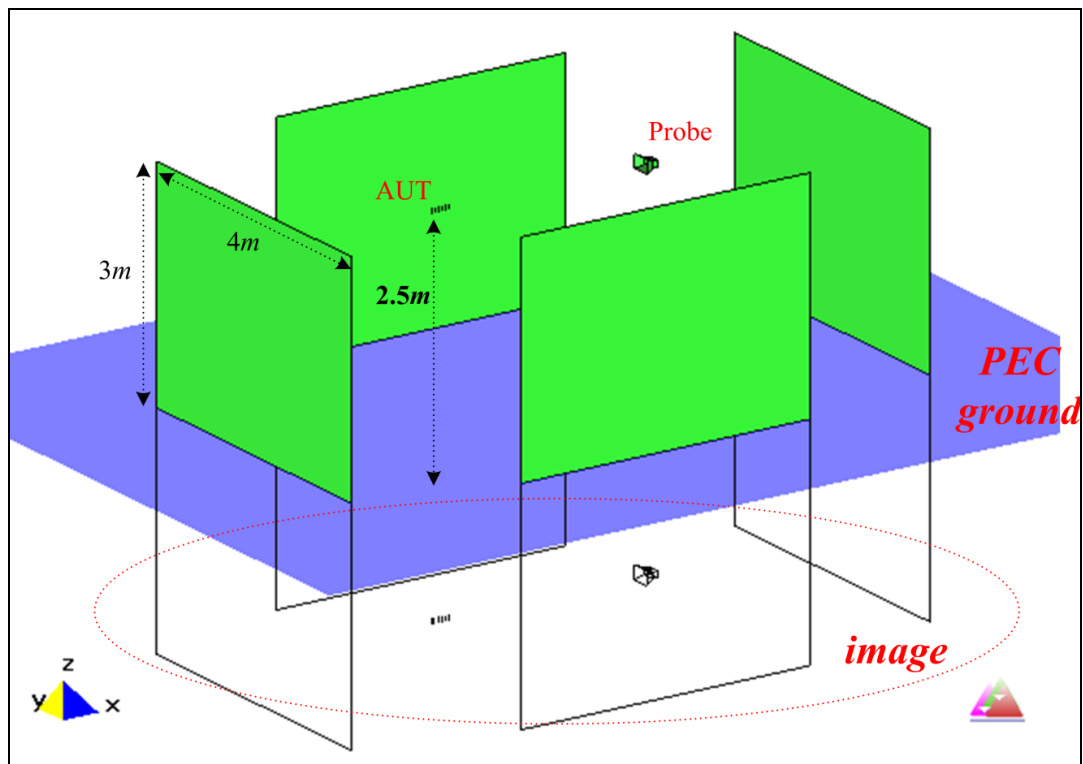


**Figure 5.15** Model of the measurement system with four PEC plates and the ground as the reflector.

The ideal and non-ideal (under the presence of PEC plates) radiation patterns of the horn antenna, the yagi antenna and the parabolic reflector antenna in 3D plot are shown in Figures 5.16, 5.17 and 5.18, respectively. The vertical axis is the amplitude of  $S_{21}$  in dB scale. It is easy to observe the differences between the ideal patterns and the non-ideal patterns. Especially the back lobes of all the three figures are much stronger due to the reflections from the PEC plates and the ground.

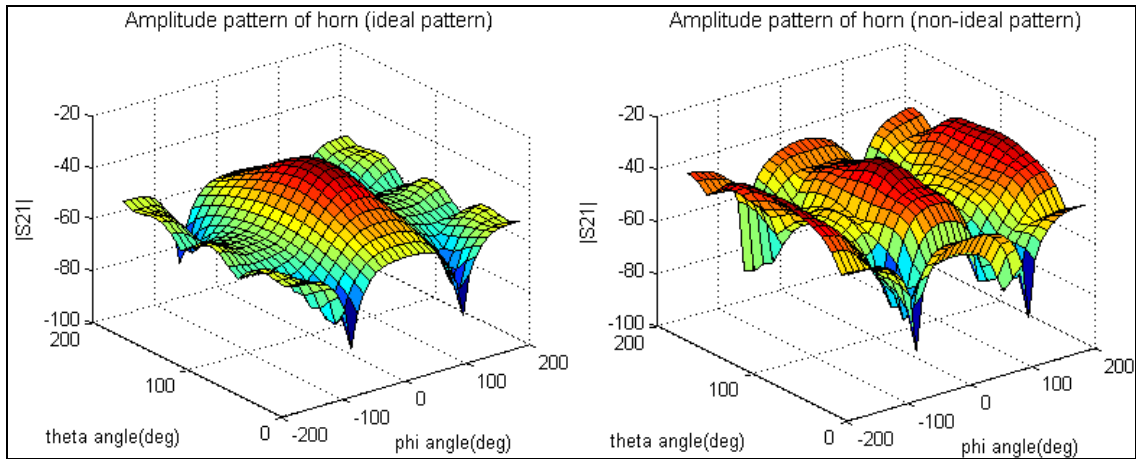


**Figure 5.16** Three-dimensional plot of the ideal and non-ideal radiation patterns of the horn antenna.

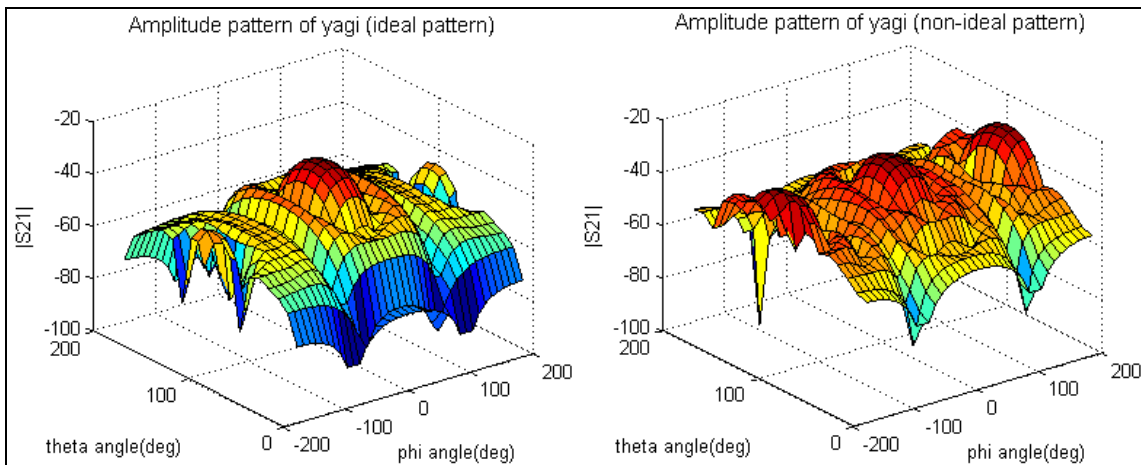


**Figure 5.17** Three-dimensional plot of the ideal and non-ideal radiation patterns of the yagi antenna.

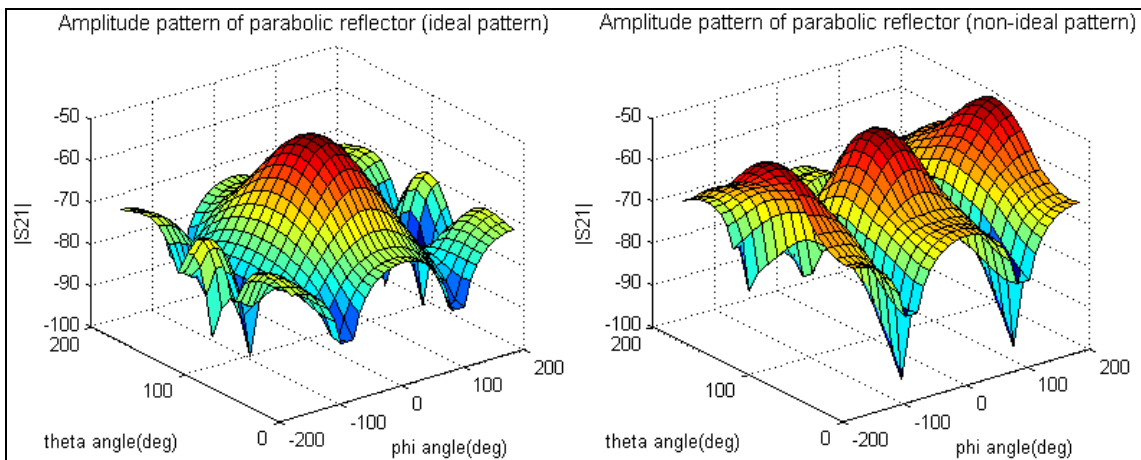


**Figure 5.18** Three-dimensional plot of the ideal and non-ideal radiation patterns of a parabolic reflector antenna.

Now let's look at the current distribution on the feed dipole of the yagi antenna, which is shown in Figure 5.19. It shows that the real part of the current distribution on the yagi has been partly affected by the PEC plates, which means the reconstructed pattern in this environment will be somewhat different from the free space ideal pattern. And we should expect this in the reconstructed results.

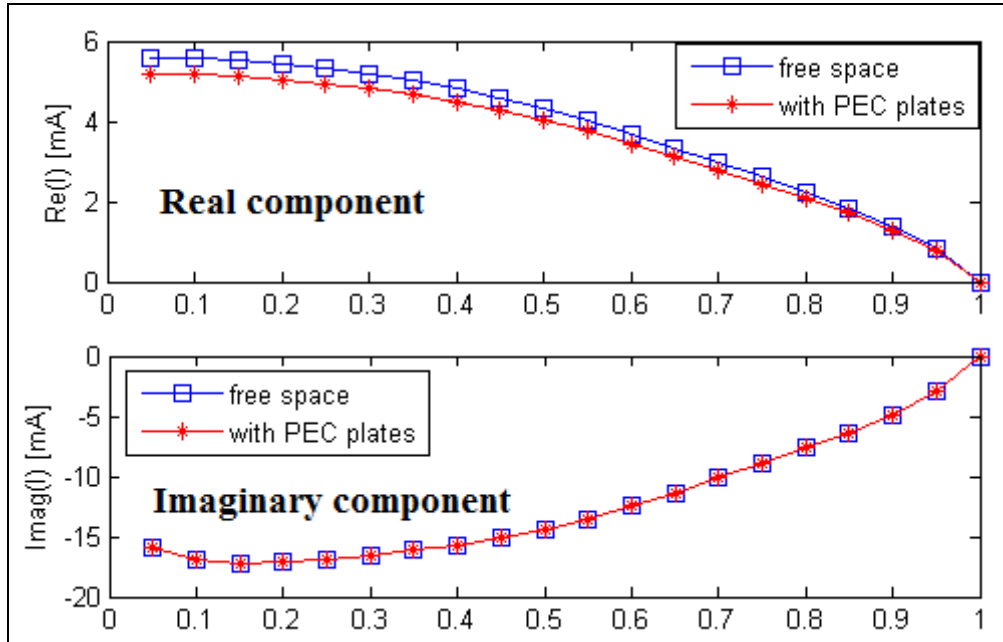


**Figure 5.19** Current distribution on the feed dipole of the yagi antenna with four PEC plates and the ground as the reflector.

The pattern reconstruction procedures follow the steps as described in Section 5.2. And the reconstructed 3D pattern for the yagi antenna is shown in Figure 5.20. To better display the reconstructed pattern along different spatial angles, Figures 5.22 and 5.23 give the 2D cuts of different phi angles and theta angles, respectively. Since the model is not symmetrical in the theta angle domain, the theta cuts plot takes several cut planes around the principal plane ( $\theta = 90^\circ$ ). The reconstructed pattern is indicated by the red line while the ideal pattern is indicated by the black line. The blue dash line is for the non-ideal pattern. In Figure 5.22 the  $x$ -axis is the elevation angle  $\theta$ , the  $y$ -axis is the amplitude of

$S_{21}$  in dB scale. In Figure 5.23 the  $x$ -axis is the azimuth angle  $\phi$ , the  $y$ -axis is the amplitude of  $S_{21}$  in dB scale.

Similarly, for the pattern reconstruction of the parabolic reflector antenna, the 3D reconstructed pattern is shown in Figure 5.21; while the 2D cuts of different phi angles and theta angles are shown in Figures 5.24 and 5.25, respectively.

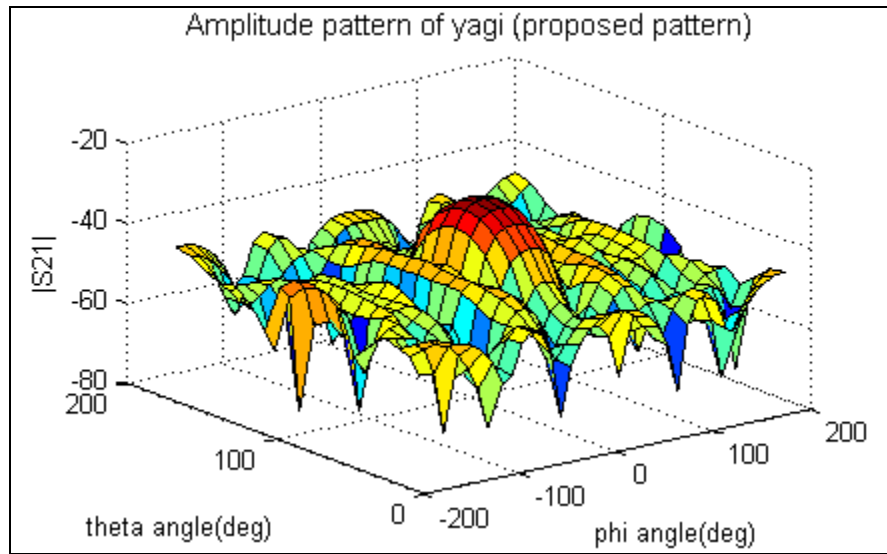


**Figure 5.20** Three-dimensional plot of the reconstructed pattern for the yagi antenna.

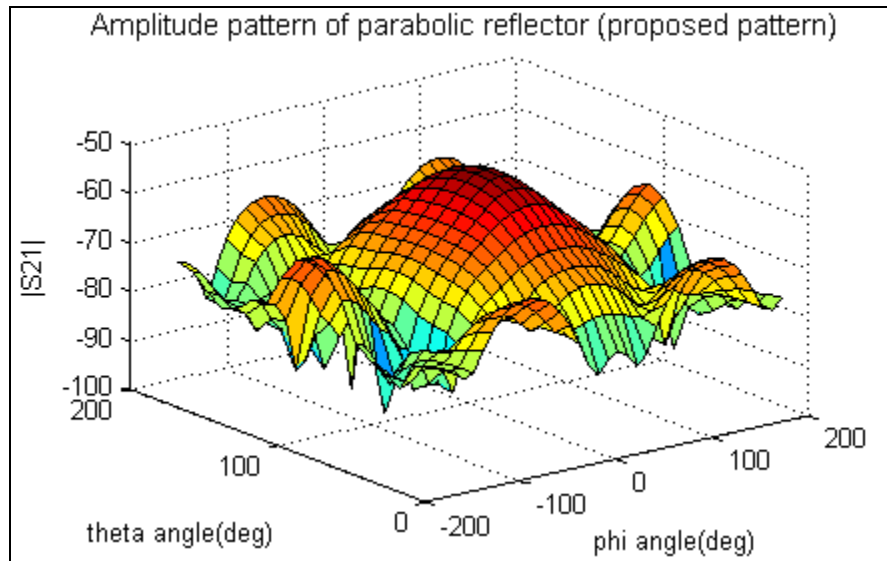


**Figure 5.21** Three-dimensional plot of the reconstructed pattern for the parabolic reflector antenna.

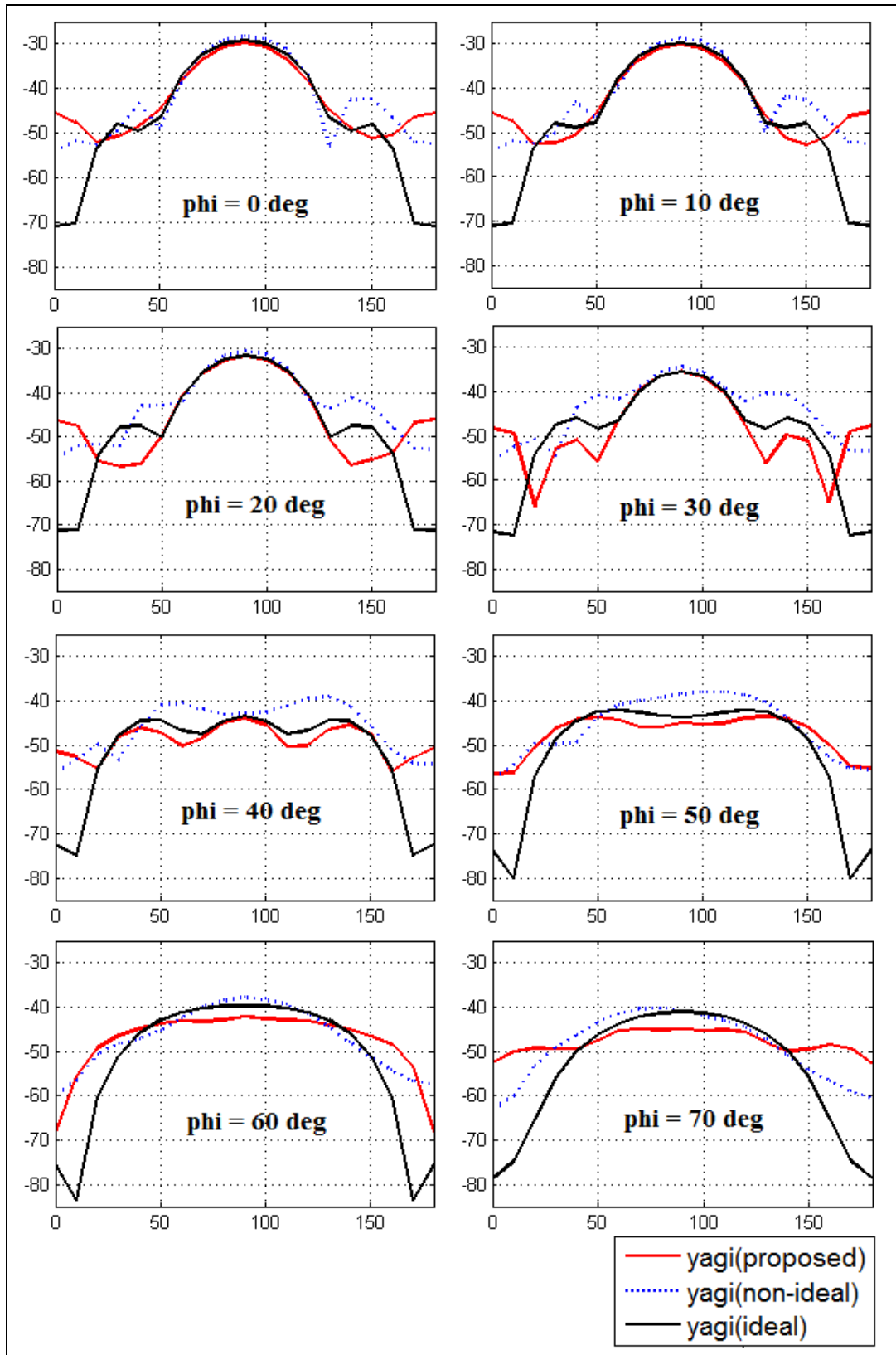


**Figure 5.22** Comparison of the reconstructed patterns for the yagi antenna along different  $\phi$  angles with four PEC plates and the ground as the reflector.

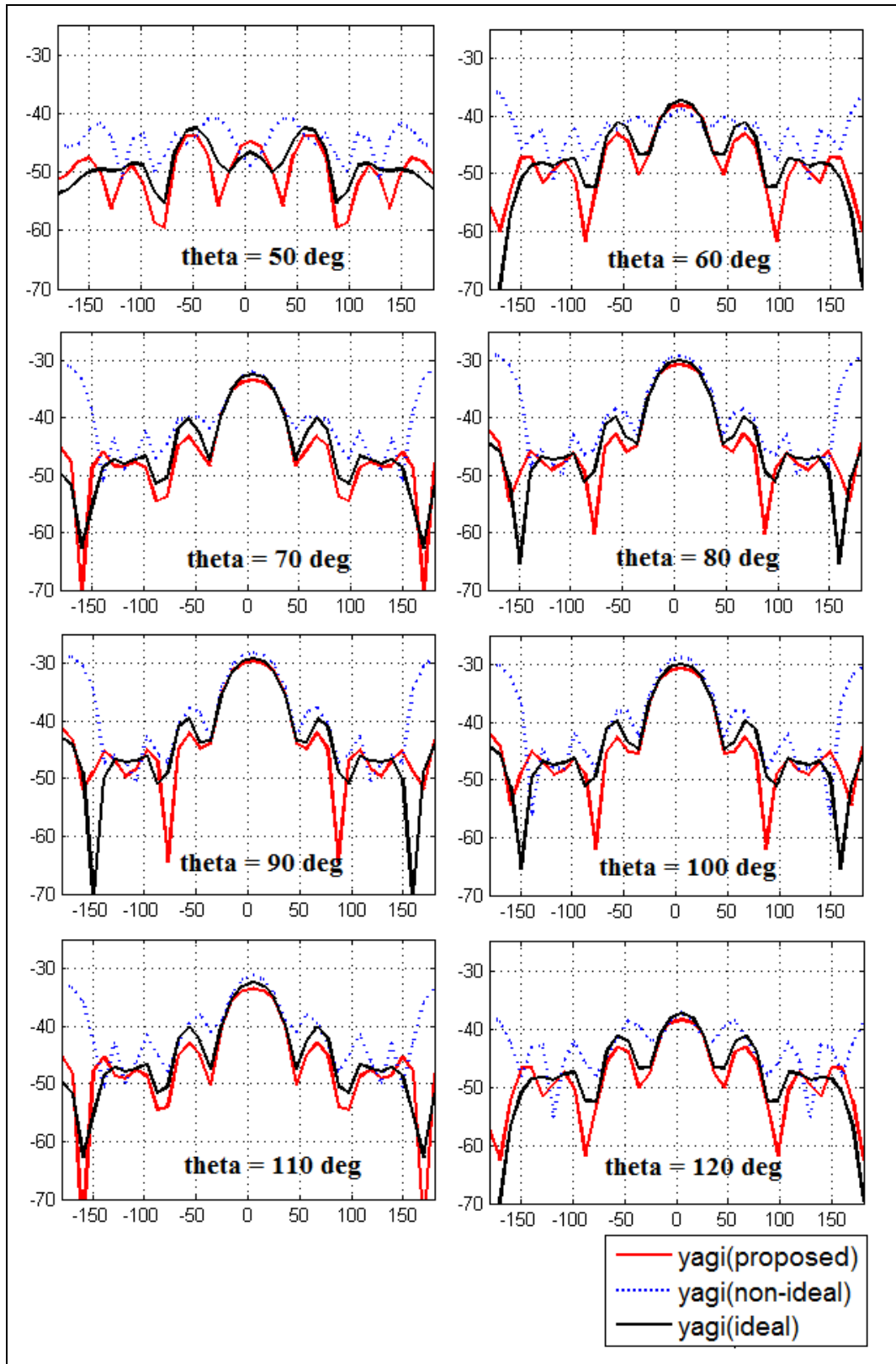


**Figure 5.23** Comparison of the reconstructed patterns for the yagi antenna along different theta angles with four PEC plates and the ground as the reflector.

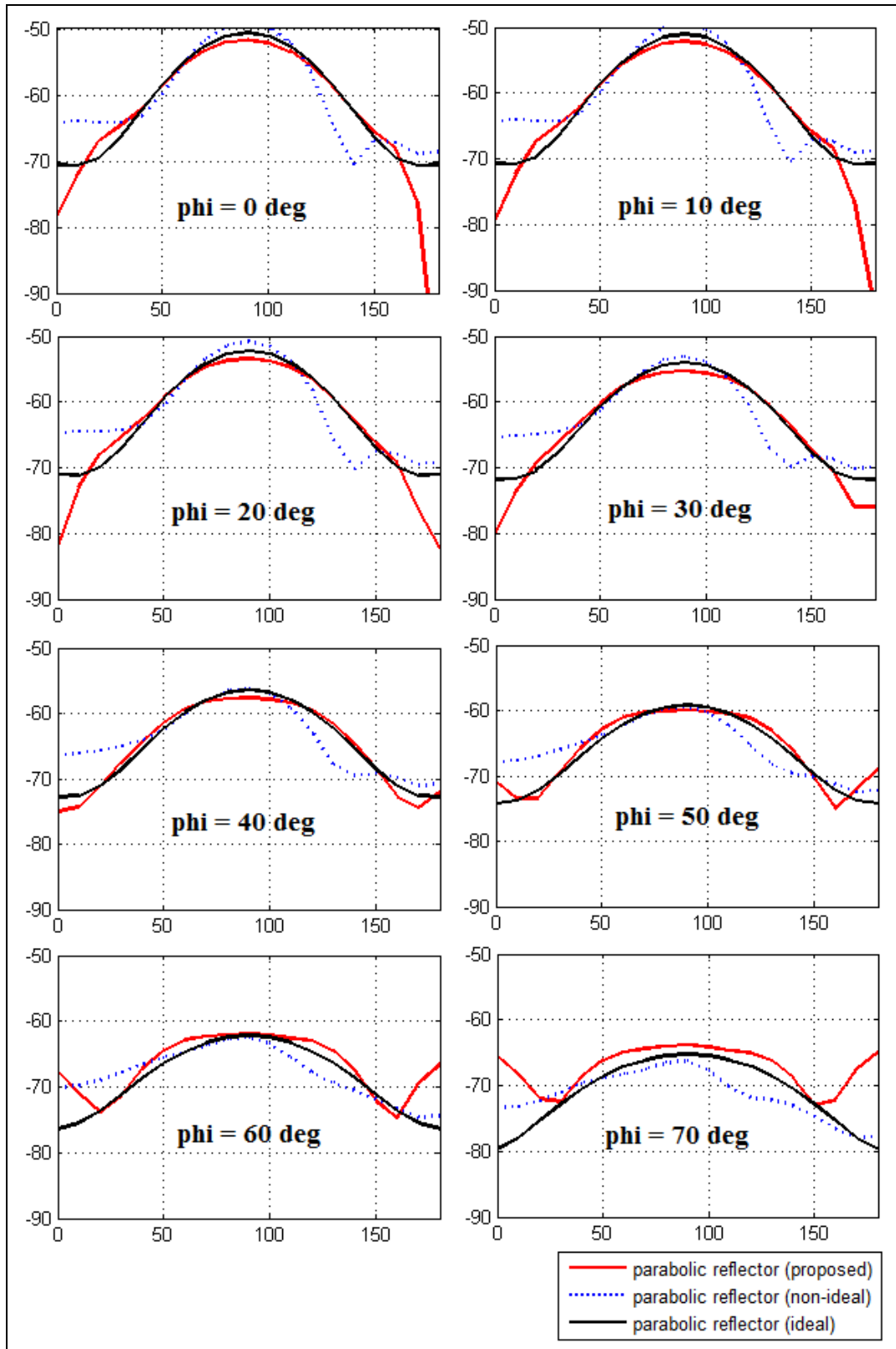


**Figure 5.24** Comparison of the reconstructed patterns for the parabolic reflector antenna along different  $\phi$  angles with four PEC plates and the ground as the reflector.

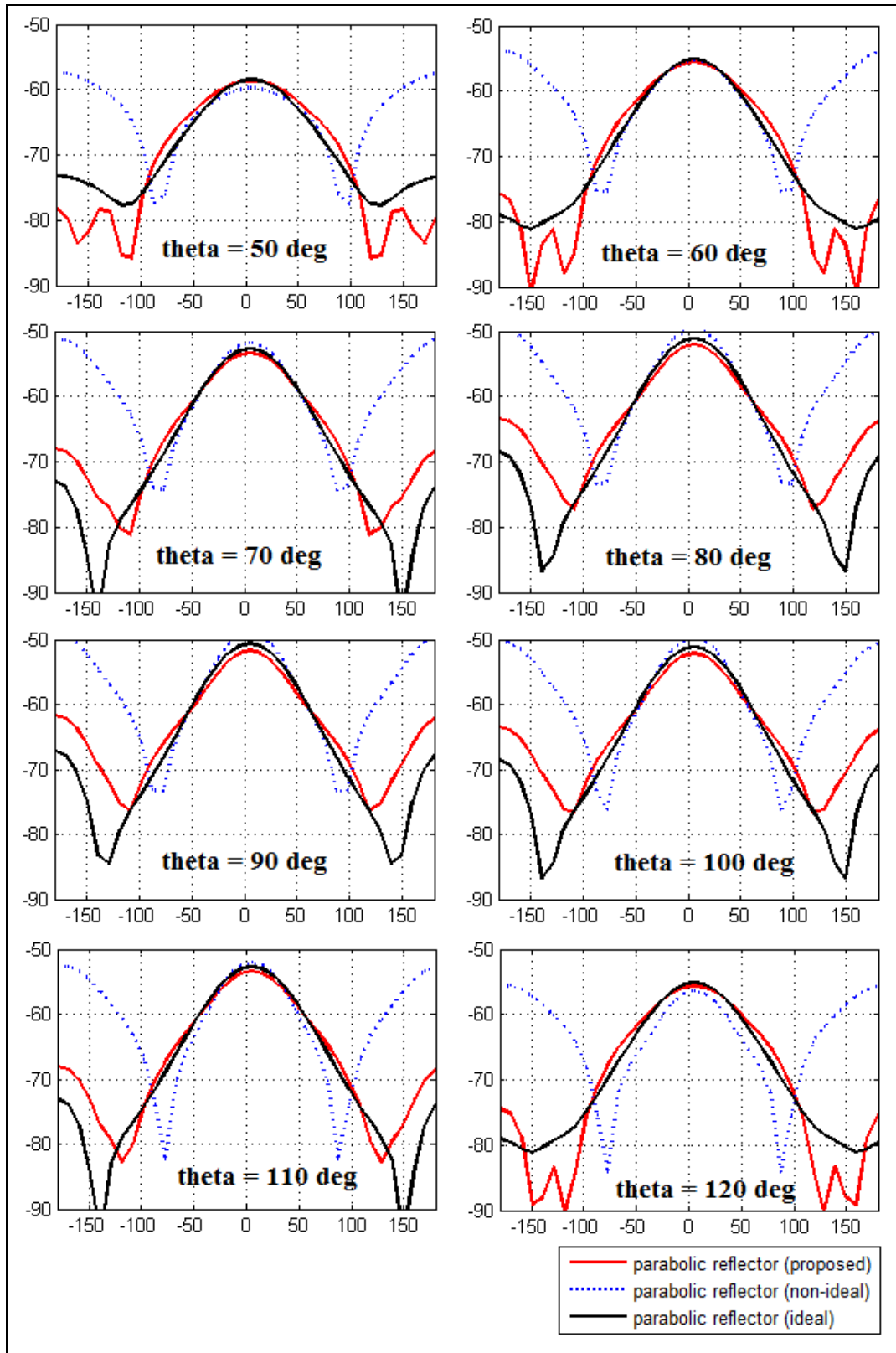


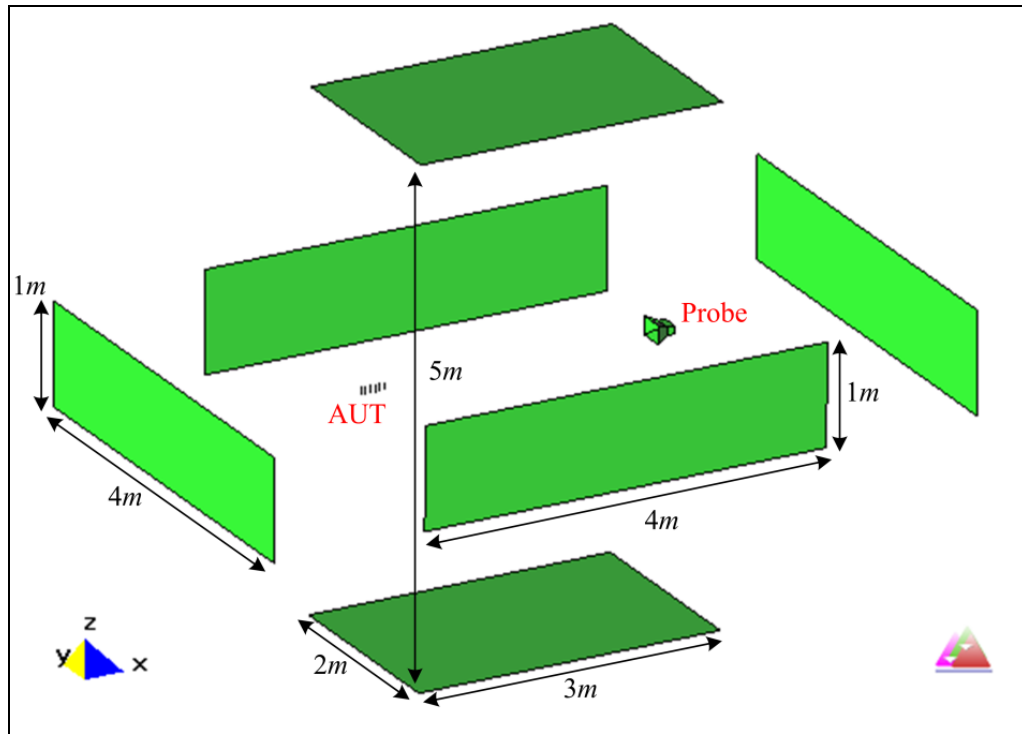
**Figure 5.25** Comparison of the reconstructed patterns for the parabolic reflector antenna along different theta angles with four PEC plates and the ground as the reflector.

As shown in the figures, the reconstructed results for the yagi antenna are not as good as the results shown in Example I (Section 5.4.1). The phi-cuts plot shows that along theta equals  $0^\circ$  and  $180^\circ$  the reconstructed patterns have even stronger reflections than the non-ideal patterns. But the theta-cuts plot still shows that the reconstructed pattern is improved through the deconvolution method. For the parabolic reflector antenna, the reconstructed results are much better. Figures 5.24 and 5.25 clearly illustrate that reflections of the non-ideal patterns have been greatly compensated, and nulls of the reconstructed pattern have been shifted to the right positions.

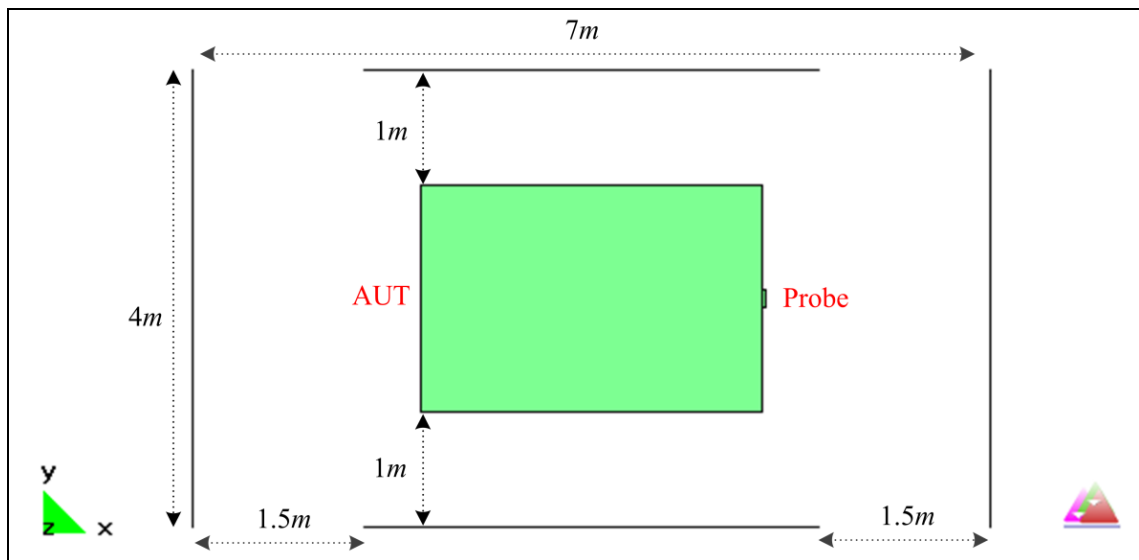
#### *5.4.3 Example III: Six Plates Forming an Unclosed Contour Serve as Reflectors*

The simulation model with six PEC plates forming an unclosed contour is shown in Figure 5.26, which gives a side view and a top-down view of the model. The PEC plates are set in a symmetrical way and have the same size for the four plates at the side. The PEC plates on the bottom and the top also have the same size. These six PEC plates will serve as the reflectors and reflect the fields of the AUT from all directions. The antenna measurement simulation is carried out inside the contour.

The ideal and non-ideal (under the presence of PEC plates) radiation patterns of the horn antenna, the yagi antenna and the parabolic reflector antenna in 3D plot are shown in Figures 5.27, 5.28 and 5.29, respectively. The vertical axis is the amplitude of  $S_{21}$  in dB scale. It is clear to observe the differences between the ideal patterns and the non-ideal patterns. Especially the back lobes of all three figures are much stronger than the ideal ones due to the reflections from the PEC plates.



(a)



(b)

**Figure 5.26** Model of the measurement system with six PEC plates forming an unclosed contour.

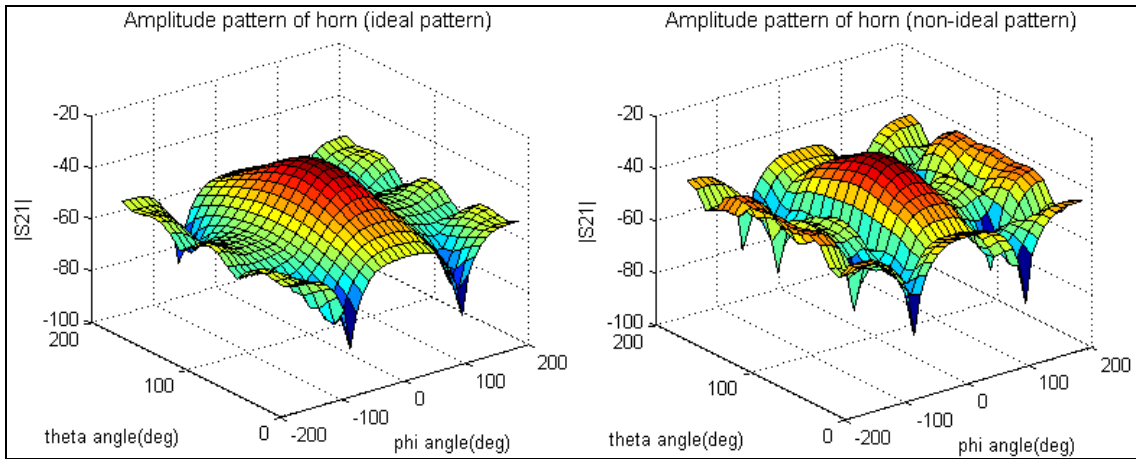


**Figure 5.27** Three-dimensional plot of the ideal and non-ideal radiation patterns of the horn antenna.

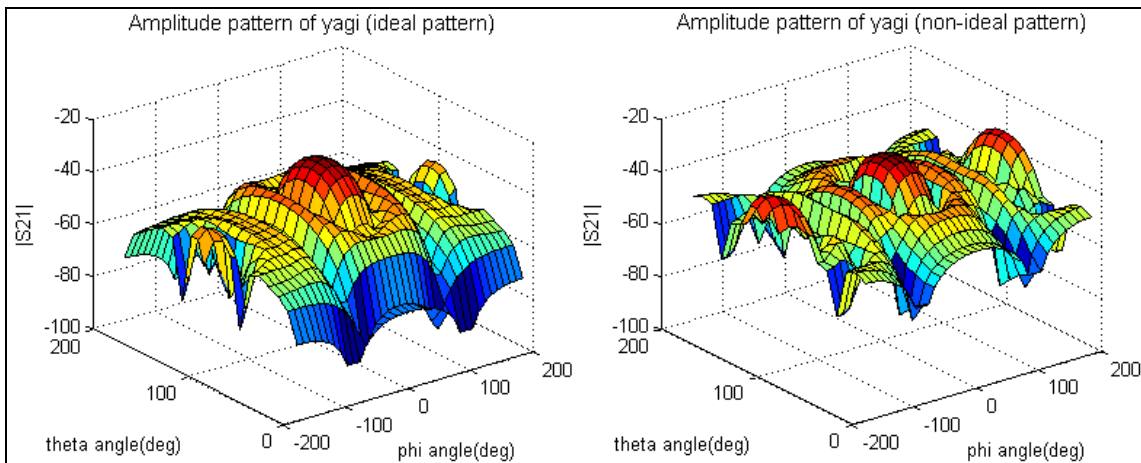


**Figure 5.28** Three-dimensional plot of the ideal and non-ideal radiation patterns of the yagi antenna.

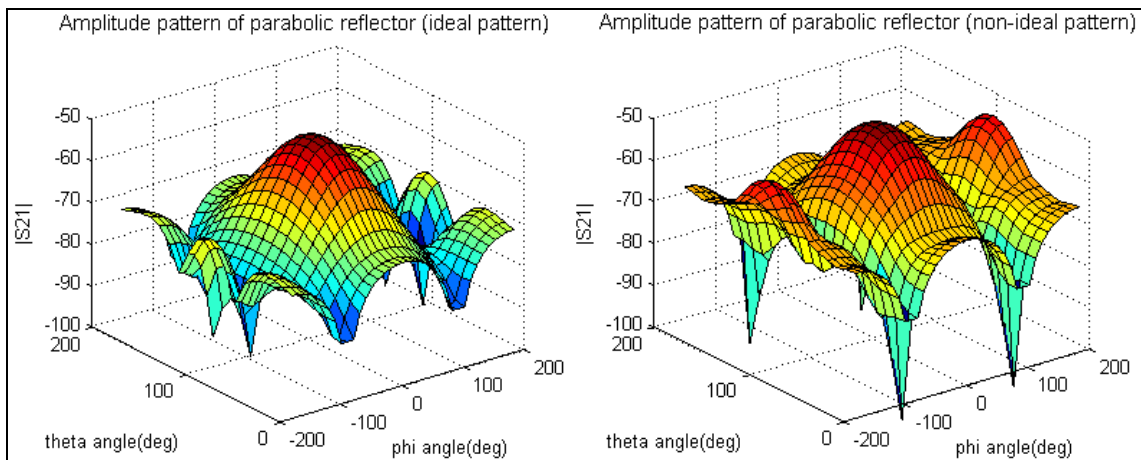


**Figure 5.29** Three-dimensional plot of the ideal and non-ideal radiation patterns of the parabolic reflector antenna.

Now let's look at the current distribution on the feed dipole of the yagi antenna, which is shown in Figure 5.30. It shows that the current distribution on the yagi has been partly affected by the PEC plates.

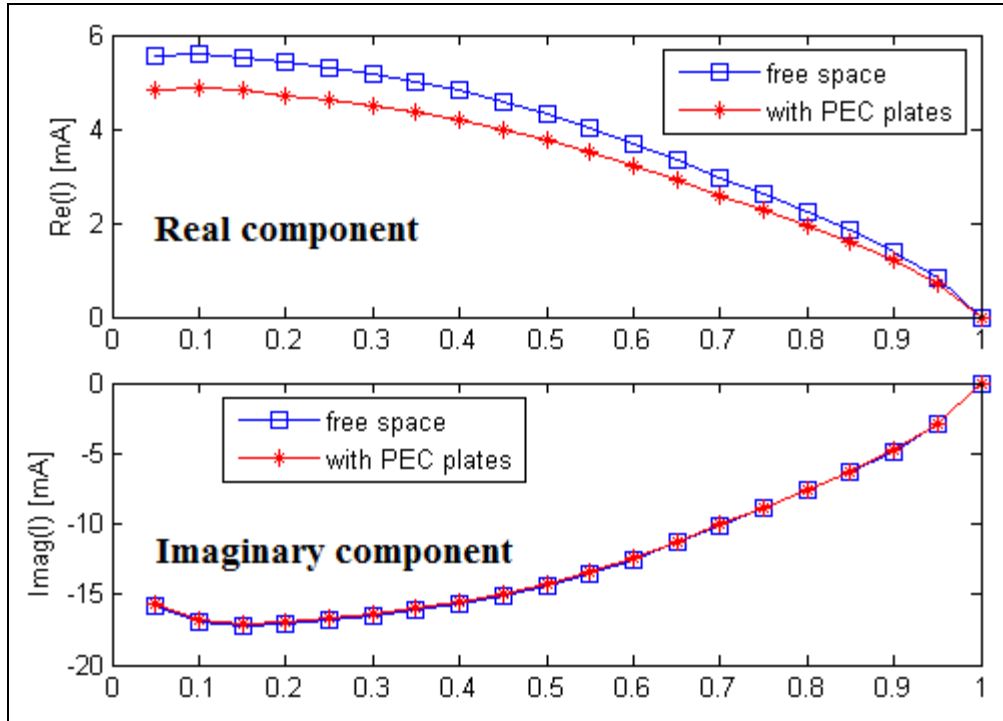


**Figure 5.30** Current distribution on the feed dipole of the yagi antenna with six PEC plates as the reflector.

The pattern reconstruction procedures in 3D environments follow the steps as described in Section 5.2. And the reconstructed 3D pattern for the yagi antenna is shown in Figure 5.31. To better demonstrate the reconstructed results along different spatial angles, Figures 5.33 and 5.34 give the 2D cuts of different phi angles and theta angles, respectively. The reconstructed pattern is indicated by the red line while the ideal pattern is indicated by the black line. The blue dash line is for the non-ideal pattern. In Figure 5.33 the  $x$ -axis is the elevation angle  $\theta$ , the  $y$ -axis is the amplitude of  $S_{21}$  in dB scale. In Figure 5.34 the  $x$ -axis is the azimuth angle  $\phi$ , the  $y$ -axis is the amplitude of  $S_{21}$  in dB scale.

Similarly, for the pattern reconstruction of the parabolic reflector antenna, the 3D reconstructed pattern is shown in Figure 5.32; while the 2D cuts of different phi angles and theta angles are shown in Figures 5.35 and 5.36, respectively.

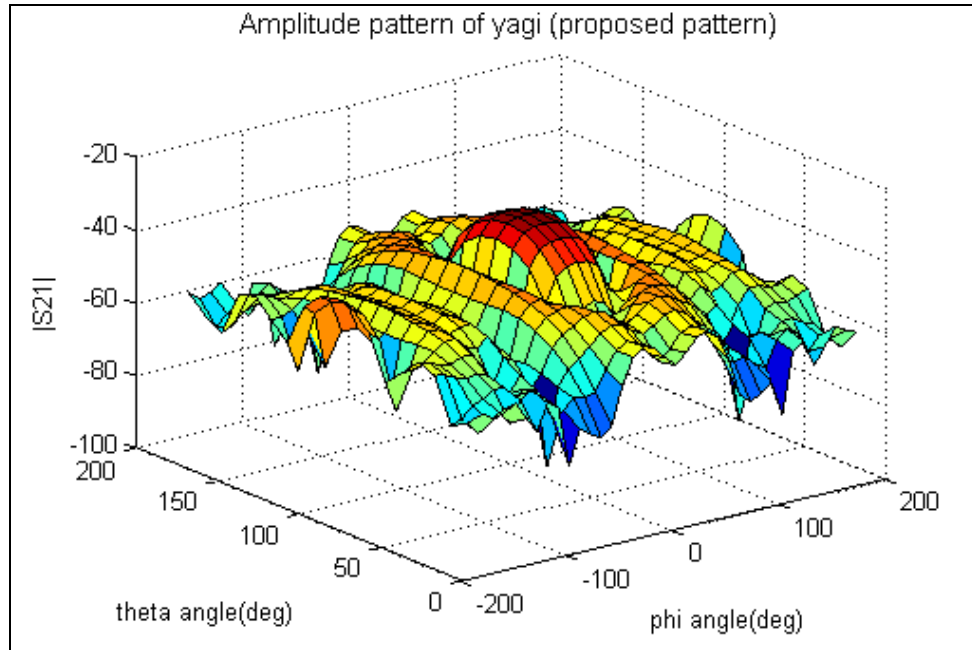


**Figure 5.31** Three-dimensional plot of the reconstructed pattern for the yagi antenna.

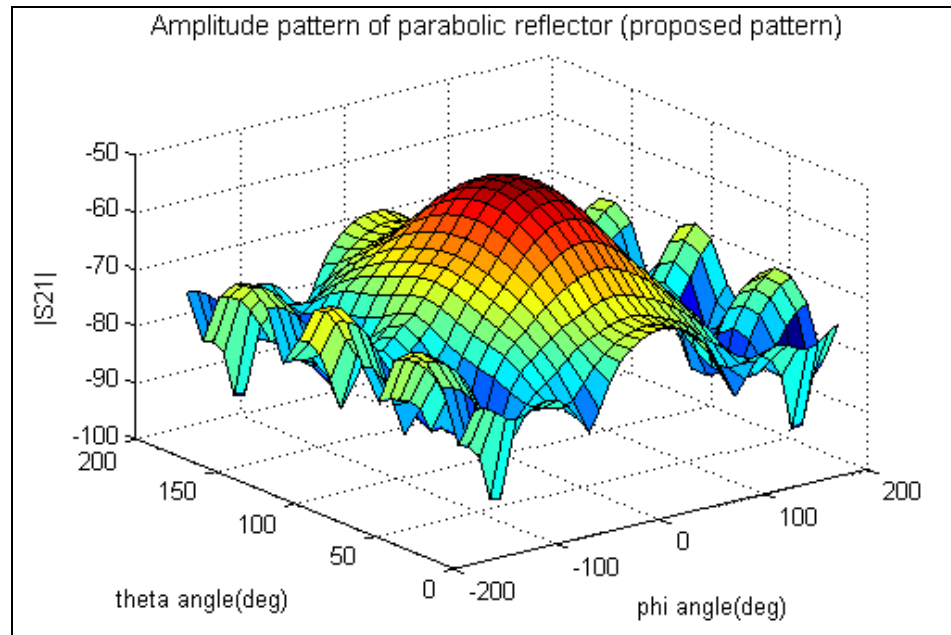


**Figure 5.32** Three-dimensional plot of the reconstructed pattern for the parabolic reflector antenna.

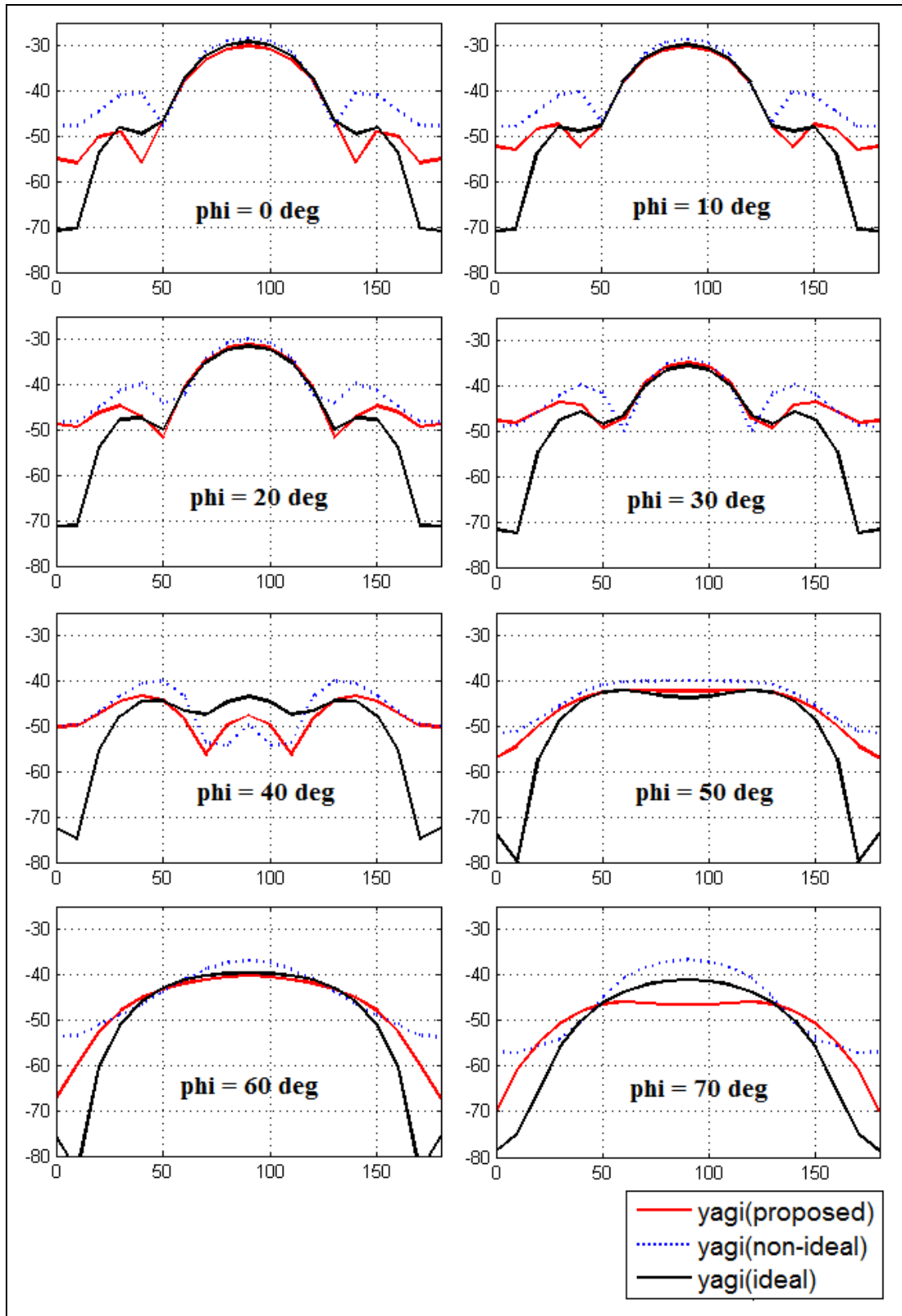


**Figure 5.33** Comparison of the reconstructed patterns for the yagi antenna along different  $\phi$  angles with six PEC plates as the reflector.

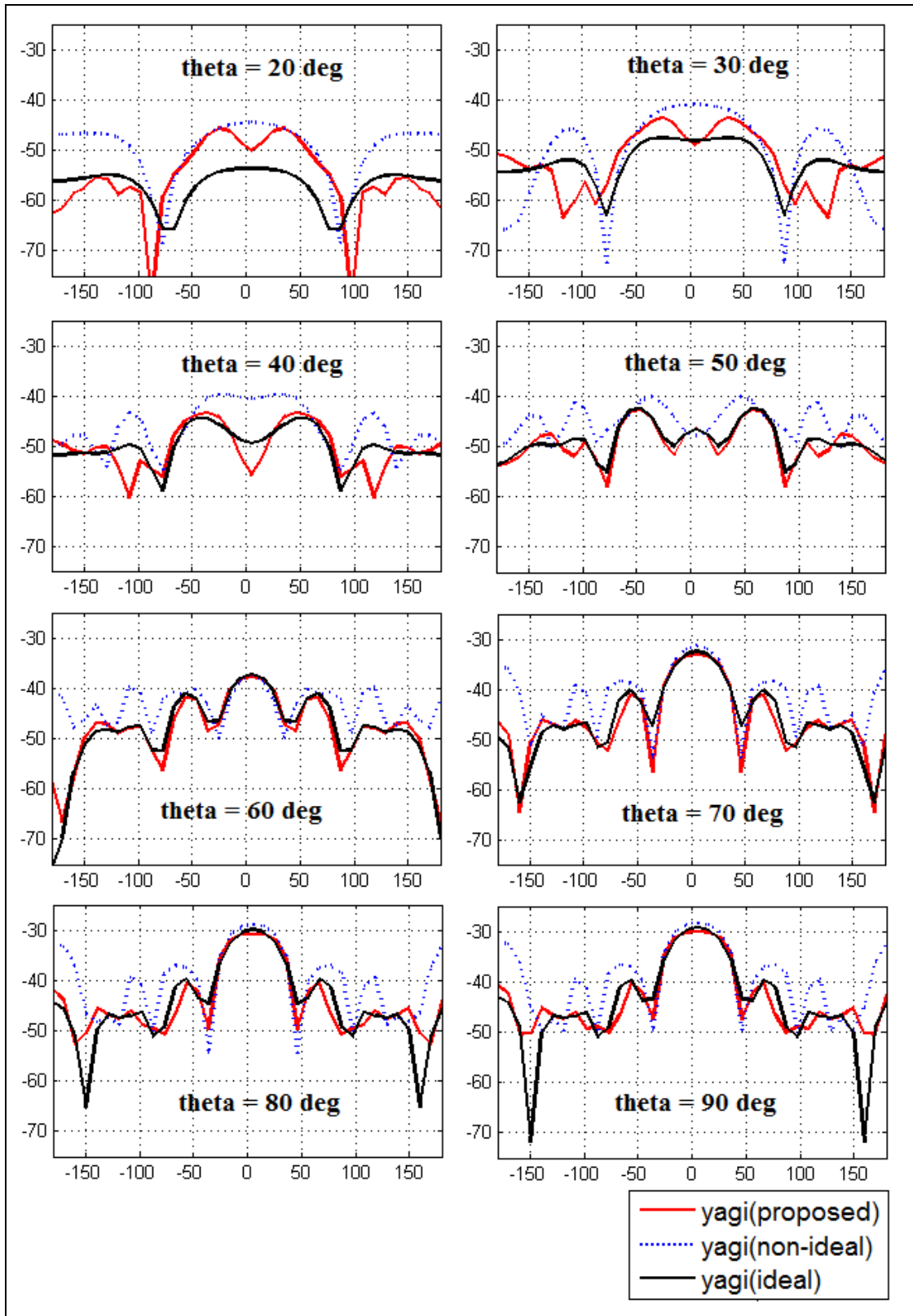


**Figure 5.34** Comparison of the reconstructed patterns for the yagi antenna along different theta angles with six PEC plates as the reflector.

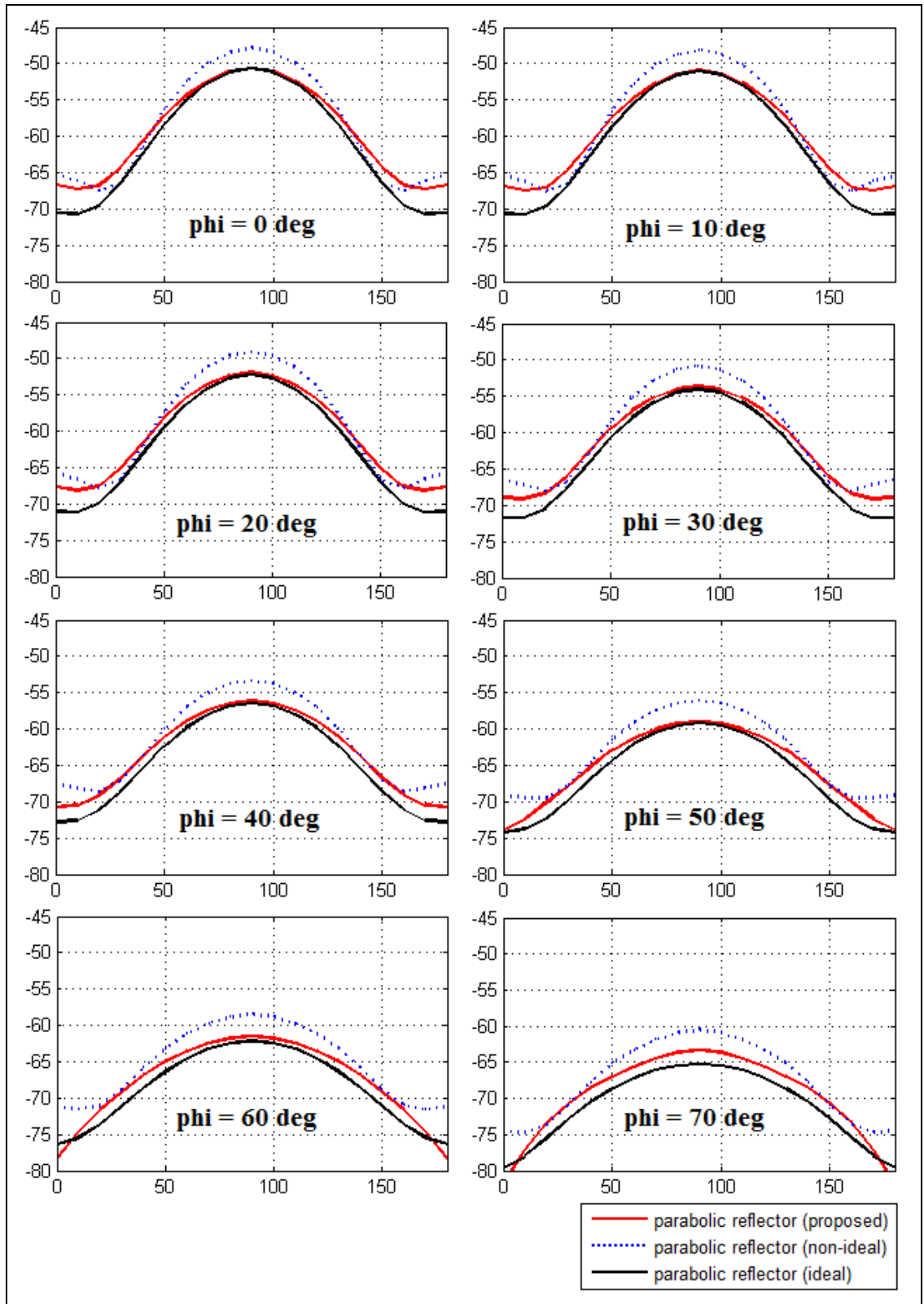


**Figure 5.35** Comparison of the reconstructed patterns for the parabolic reflector antenna along different  $\phi$  angles with six PEC plates as the reflector.

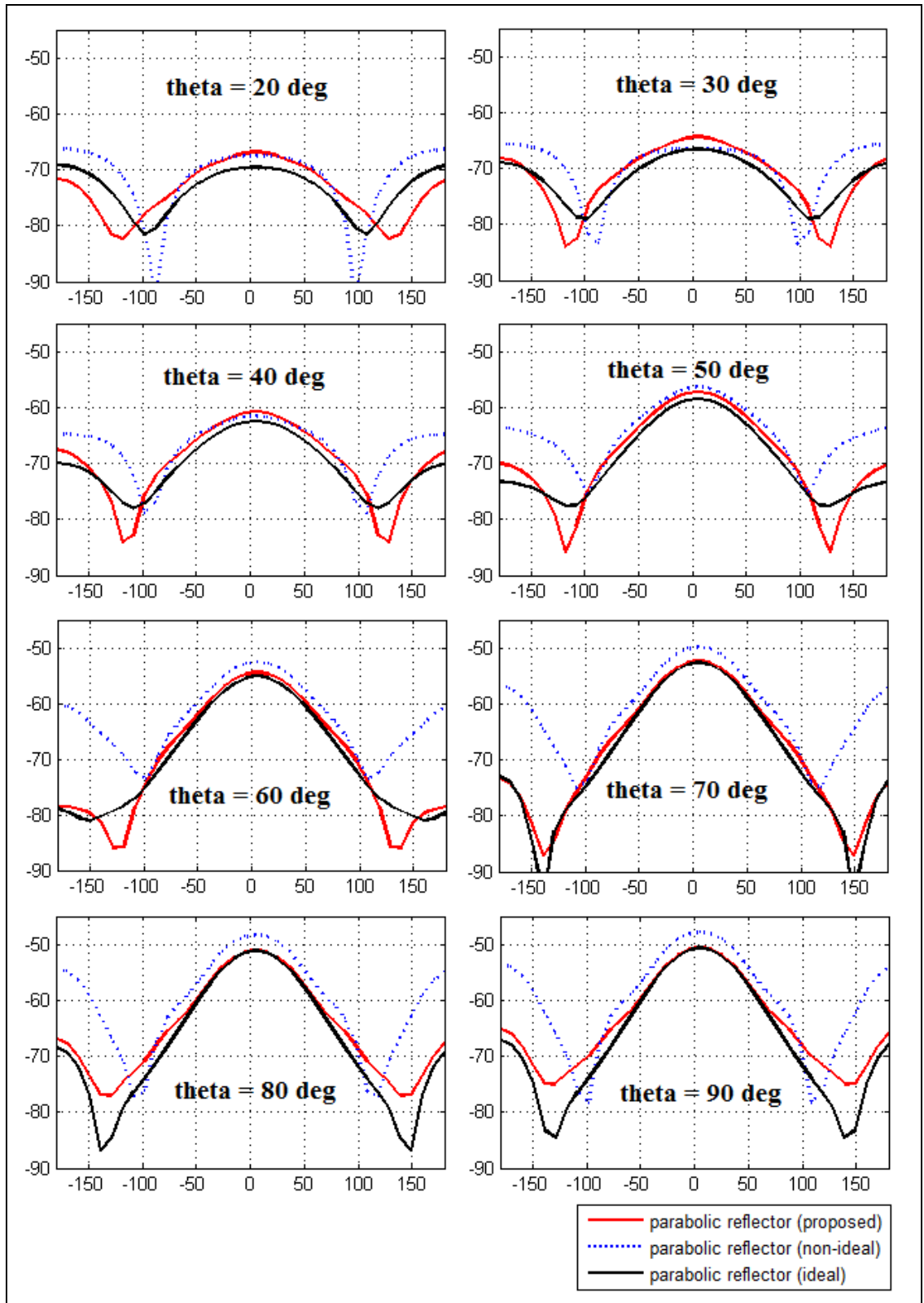


**Figure 5.36** Comparison of the reconstructed patterns for the parabolic reflector antenna along different theta angles with six PEC plates as the reflector.

As shown in the figures, the reconstructed results are not as good as the results shown in Example I in Section 5.4.1. The reconstructed pattern can basically follow the trend of the ideal pattern and compensate the reflections for the main lobe; but the reconstructed results for the side lobes are not good enough. Except the effect of the changes in current distribution shown in Figure 5.30, the two PEC plates at the top and the bottom of the antennas also add the complexity of reflections and thus distort the reconstruction performance.

#### *5.4.4 Example IV: Antenna Measurement in a Closed PEC Box*

The previous three examples have shown the pattern reconstruction under the environments of unclosed PEC contour. This example is to illustrate the case that the antenna measurement is carried out in a closed PEC box, where the deconvolution method fails.

The model of this example is shown in Figure 5.37 (displayed in the transparent mode). The PEC box has the size of 4 m by 4 m by 7 m; while the AUT and the probe antenna have a distance of 3 m between them and they are 2 m away from the surrounding PEC plates. Again, the 6-element yagi antenna and the parabolic reflector antenna are used as the AUT while the horn is used as the probe antenna. The sampling of data points in the angular domain is every 10 degree as a step in both  $\theta$  angle and  $\phi$  angle.

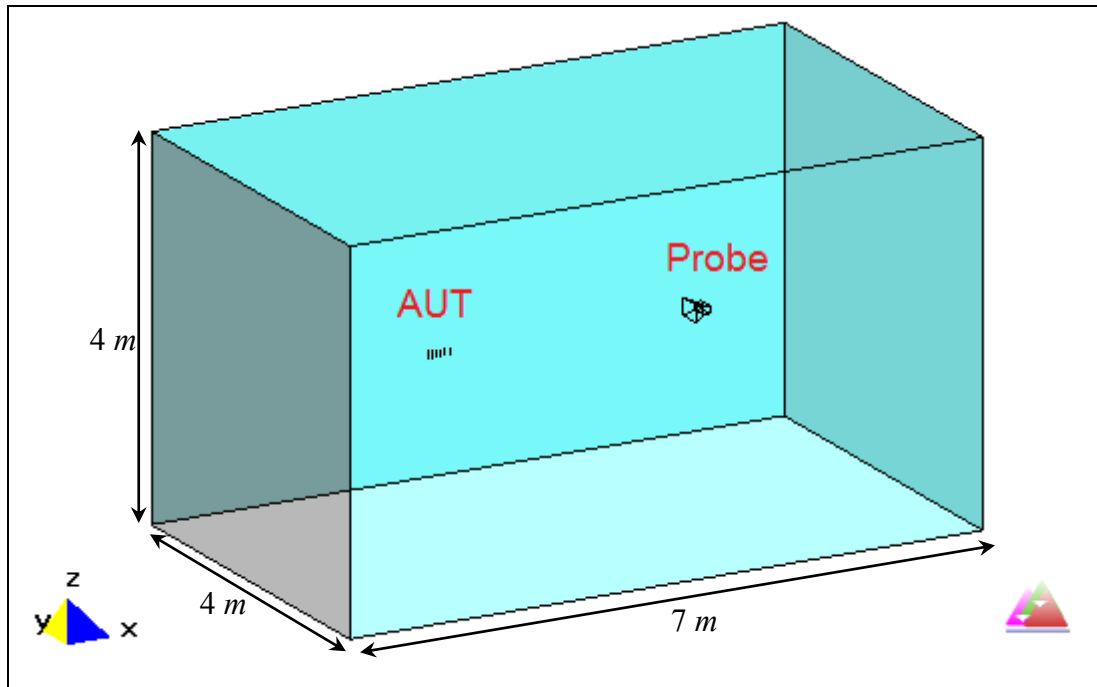


**Figure 5.37** Model of the measurement system within a closed PEC box.

The ideal and non-ideal (under the presence of PEC plates) radiation patterns of the horn antenna, the yagi antenna and the parabolic reflector antenna in 3D plot are shown in Figures 5.38, 5.39 and 5.40, respectively. The vertical axis is the amplitude of  $S_{21}$  in dB scale. It is seen that there are tremendous differences between the ideal patterns and the non-ideal patterns. The non-ideal patterns don't have a regular shape of radiation patterns with the main lobe and the back lobe. They are more like random values. And the average level of the non-ideal patterns is much higher than the ideal patterns. This will be explained later.

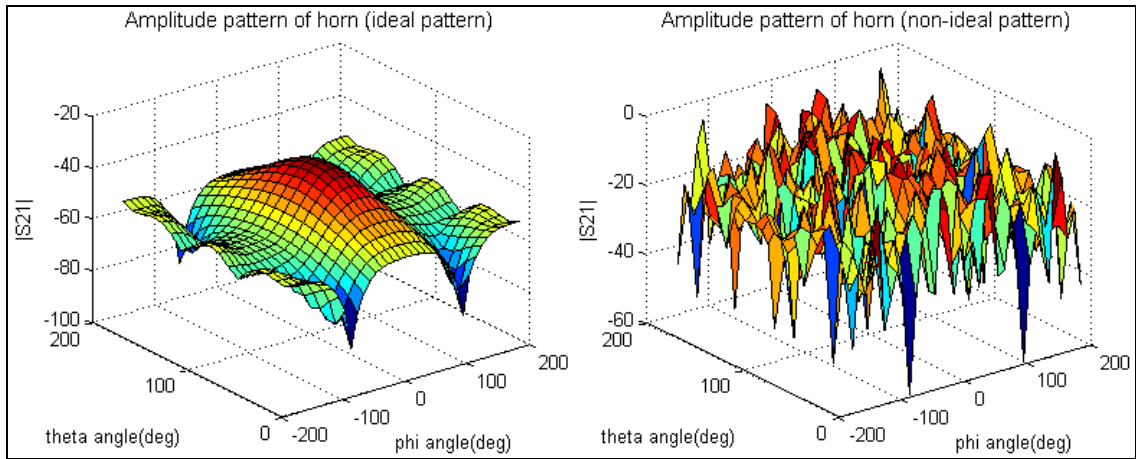


**Figure 5.38** Three-dimensional plot of the ideal and non-ideal radiation patterns of the horn antenna (antenna in a closed PEC box).

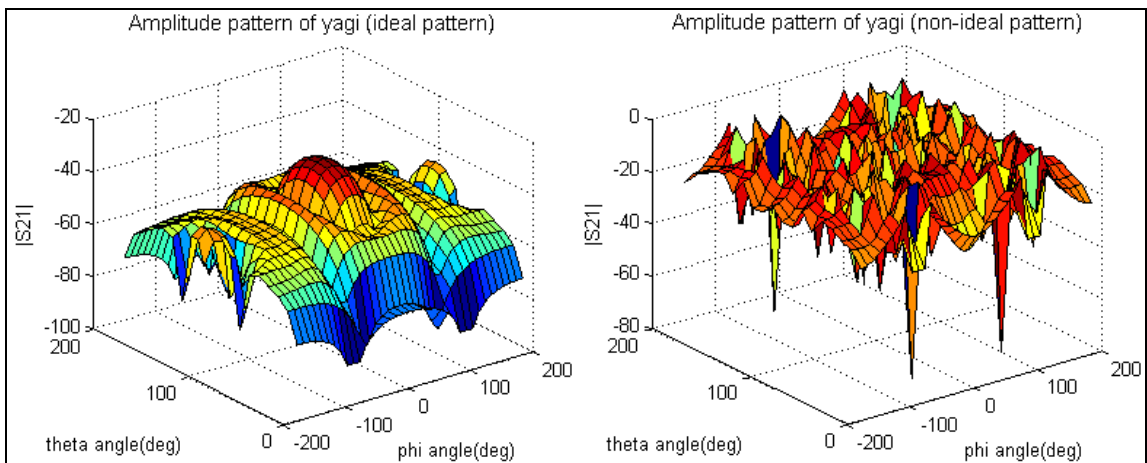


**Figure 5.39** Three-dimensional plot of the ideal and non-ideal radiation patterns of the yagi antenna (antenna in a closed PEC box).

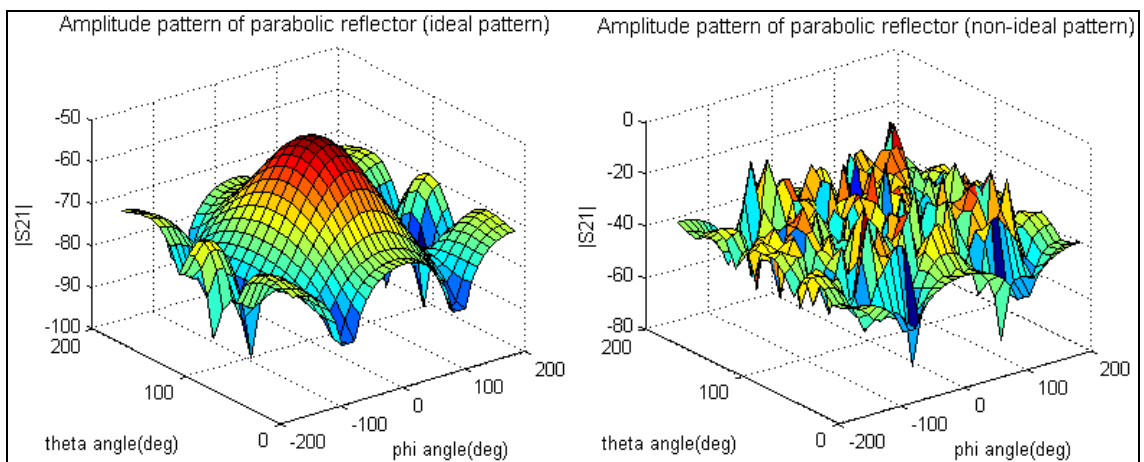


**Figure 5.40** Three-dimensional plot of the ideal and non-ideal radiation patterns of the parabolic reflector antenna (antenna in a closed PEC box).

Let's first look at the current distribution on the feed dipole of the yagi antenna as shown in Figure 5.41. As shown in the figure, the imaginary part of the current distribution within the PEC box is much larger than the ideal one; while the real part of the current distribution within the PEC box is zero value. It is known that inside a closed PEC box, the energy generated by the AUT is pure imaginary, which is induced by the imaginary part of the current. So the field inside the closed PEC box would be near field only, and there would be no far field inside or outside the PEC box, which is why a PEC box is commonly used as the shield box. Therefore the measured pattern under such environment is not the far-field pattern. This also explains why the average level of the non-ideal radiation pattern is much larger than the ideal pattern in Figures 5.27 ~ 5.29. Because all the energy is conserved inside the PEC box as the near-field.

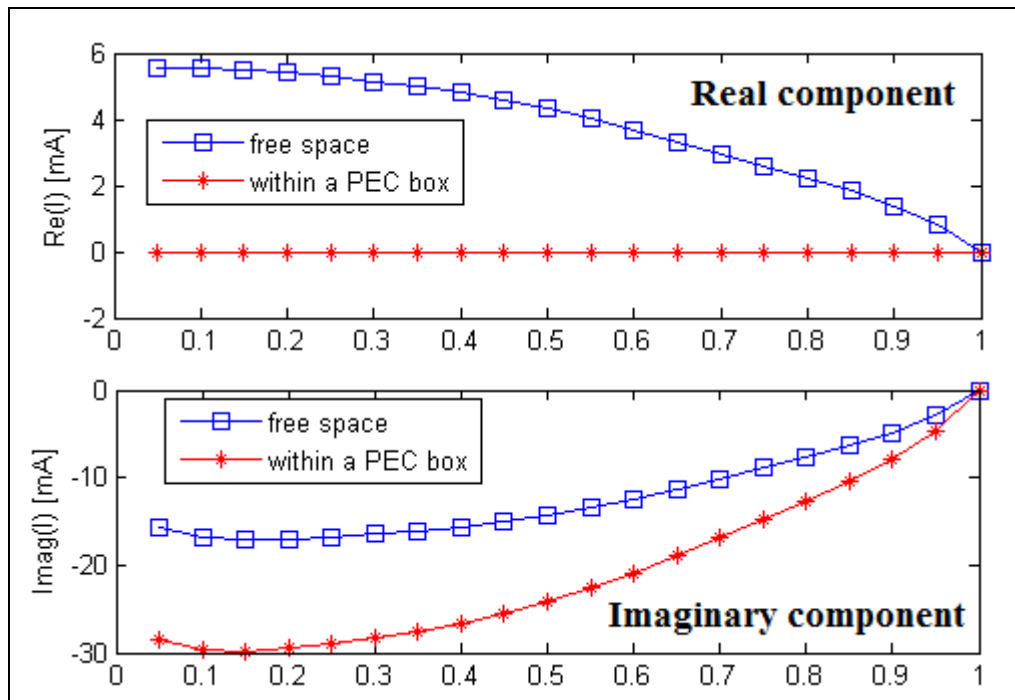


**Figure 5.41** Current distribution on the feed dipole of the yagi antenna. (antenna within a closed PEC box)

To illustrate the deconvolution method fails under such environment, we still tried to reconstruct the radiation pattern of the AUT. The pattern reconstruction procedures still follow the steps as described in Section 5.2. The reconstructed 3D pattern for the yagi antenna is shown in Figure 5.42. And the 2D cuts of different phi angles and theta angles are given in Figures 5.44 and 5.45, respectively. The reconstructed pattern is indicated by the red line while the ideal pattern is indicated by the black line. The blue dash line is for the non-ideal pattern. In Figure 5.44 the  $x$ -axis is the elevation angle  $\theta$ , the  $y$ -axis is the amplitude of  $S_{21}$  in dB scale. In Figure 5.45 the  $x$ -axis is the azimuth angle  $\phi$ , the  $y$ -axis is the amplitude of  $S_{21}$  in dB scale.

Similarly, for the pattern reconstruction of the parabolic reflector antenna, the 3D reconstructed pattern is shown in Figure 5.43; while the 2D cuts of different phi angles and theta angles are shown in Figures 5.46 and 5.47, respectively.

It is seen that the reconstructed results are much worse than the previous examples, and the reconstructed patterns are very different from the ideal ones. This is mainly due to the fact that the current distribution on the AUT has been greatly changed from the ideal one when the AUT radiates in the free space. And the probe is actually measuring within the near field of the AUT, which makes the radiation pattern reconstruction meaningless. Therefore, it is not surprising that the reconstructed patterns are not approximated to the ideal patterns.

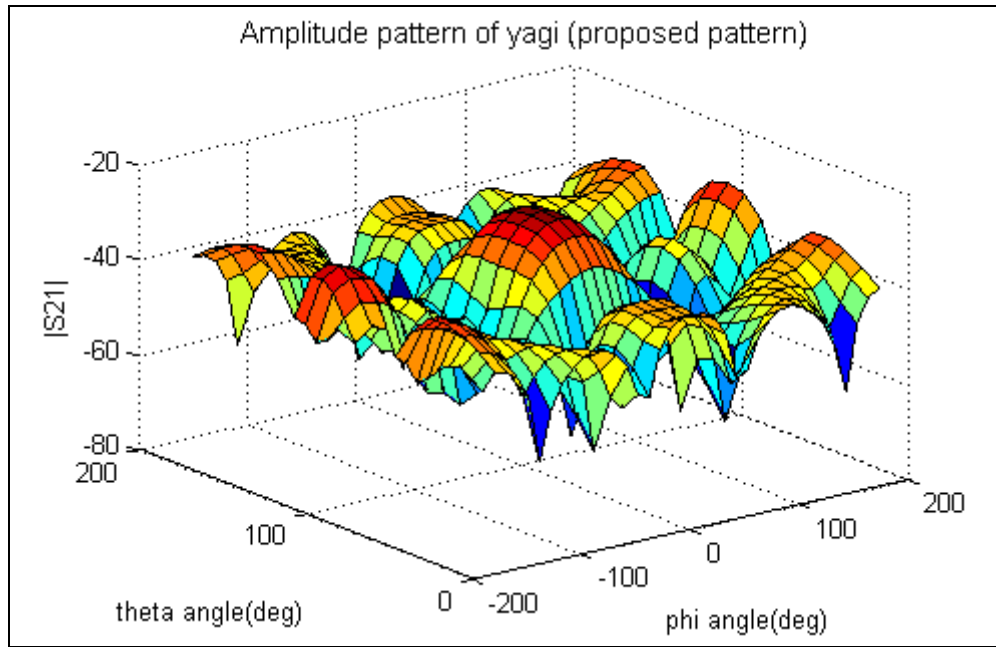


**Figure 5.42** Three-dimensional plot of the reconstructed pattern for the yagi antenna.

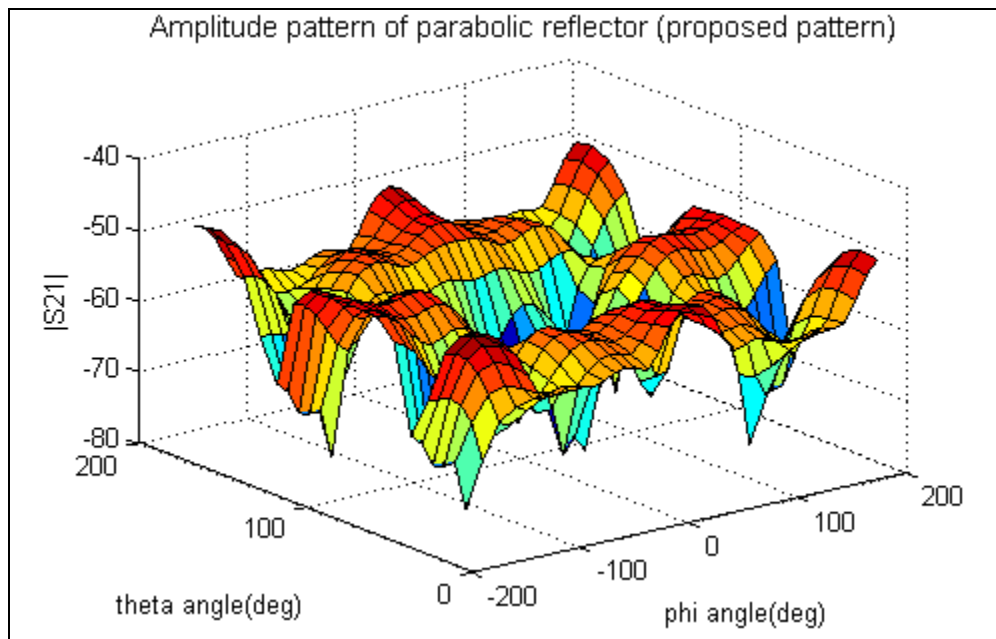


**Figure 5.43** Three-dimensional plot of the reconstructed pattern for the parabolic reflector antenna.

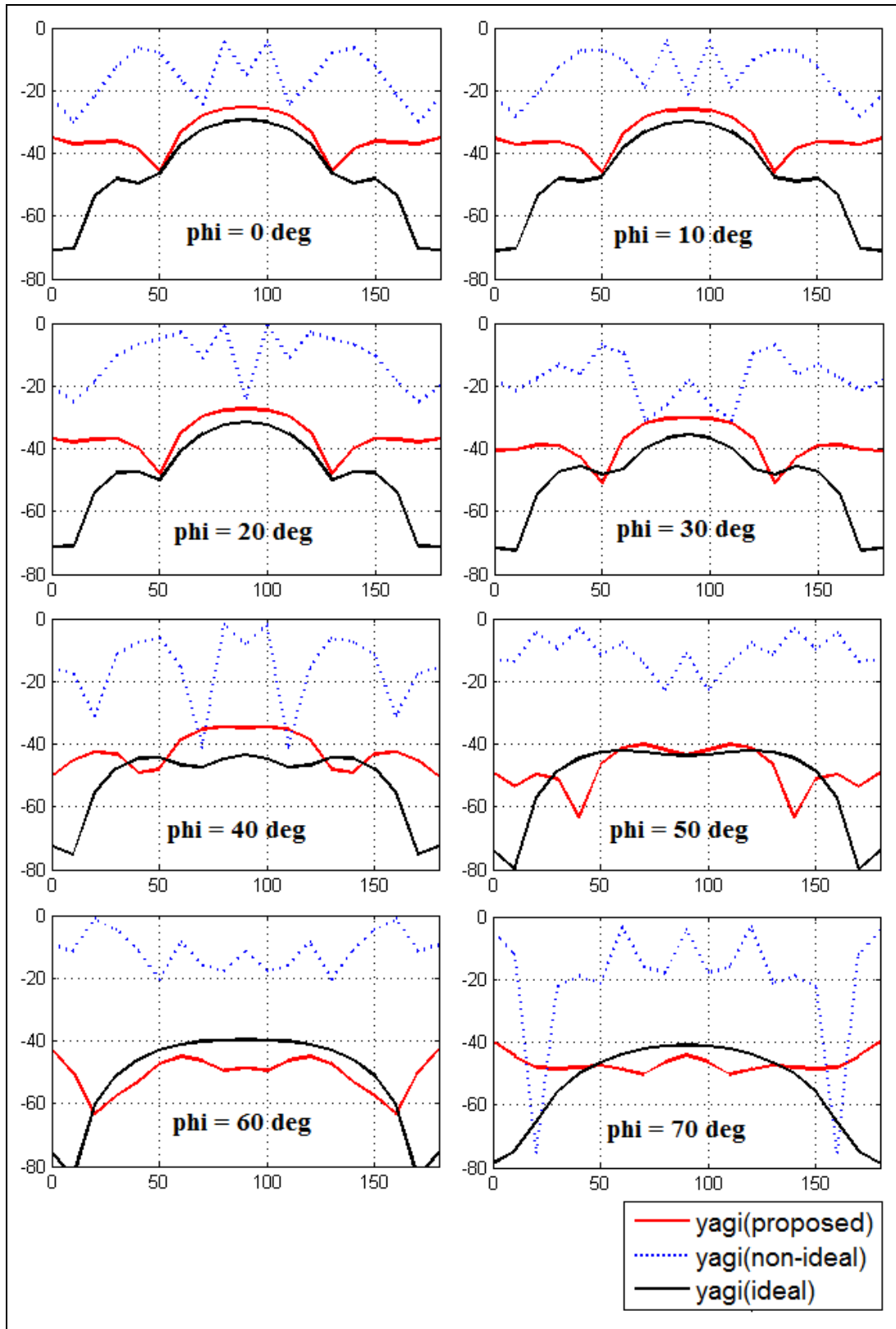


**Figure 5.44** Comparison of the reconstructed patterns for the yagi antenna along different  $\phi$  angles (antennas within a closed PEC box).

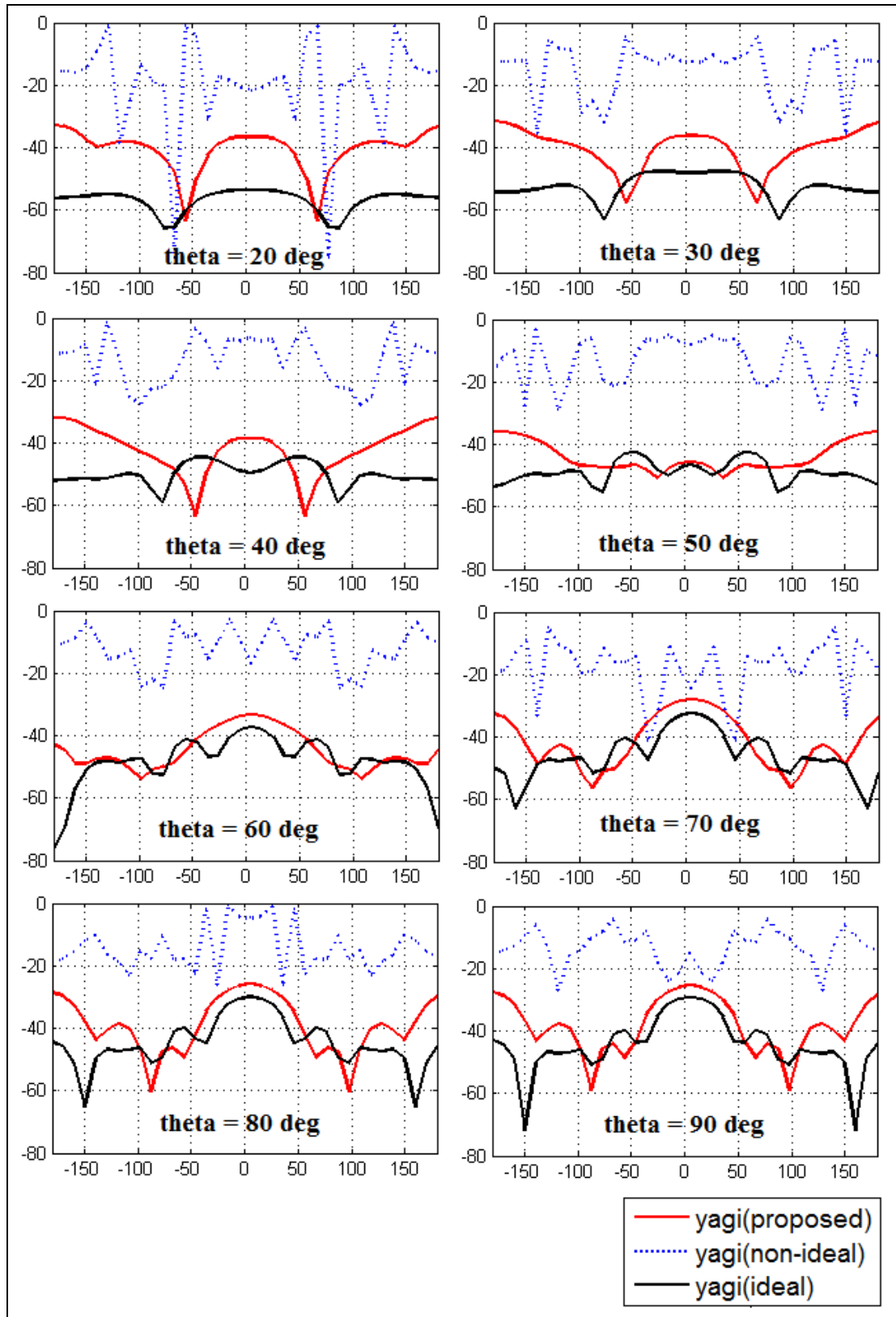


**Figure 5.45** Comparison of the reconstructed patterns for the yagi antenna along different theta angles (antennas within a closed PEC box).

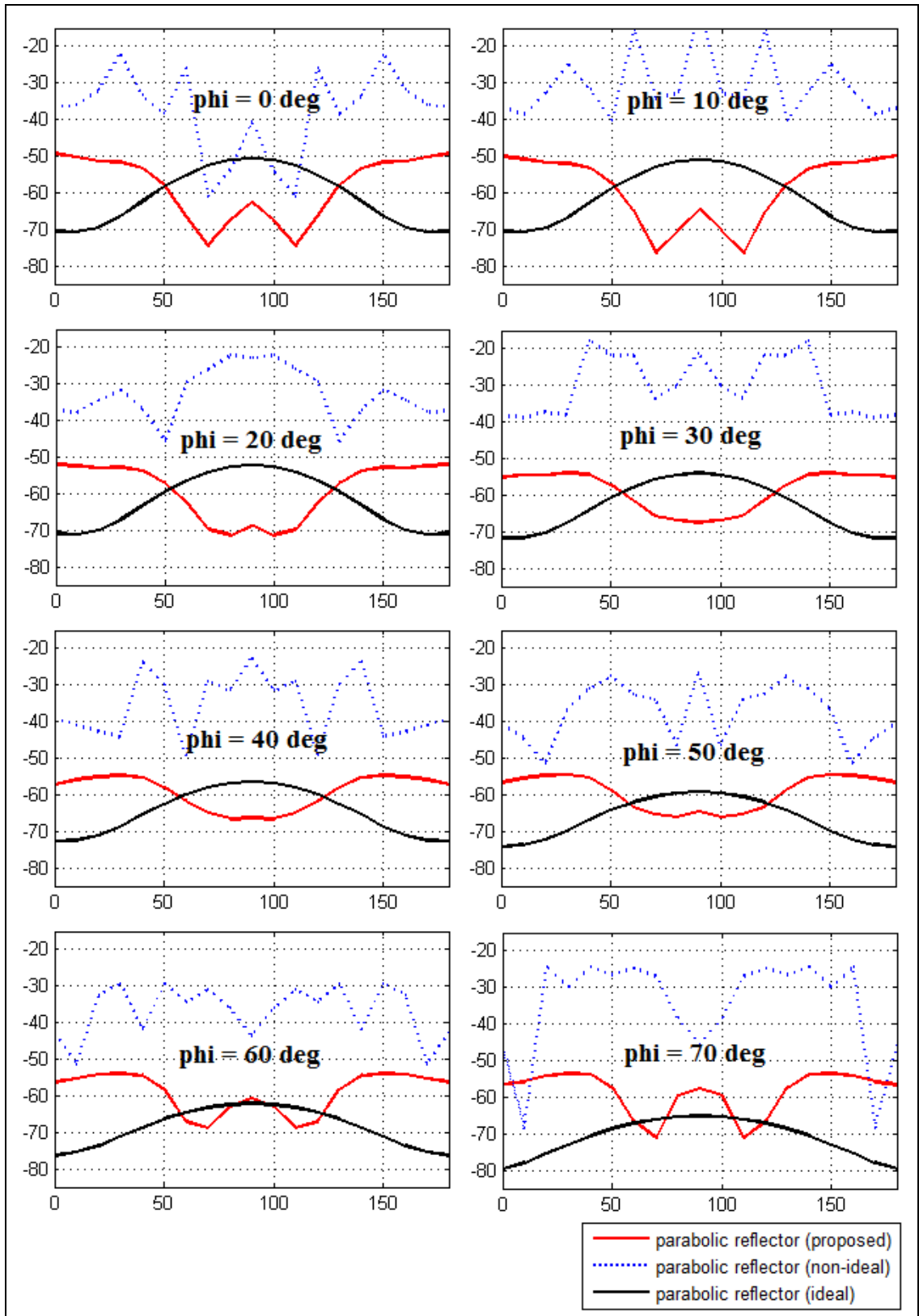


**Figure 5.46** Comparison of the reconstructed patterns for the parabolic reflector antenna along different  $\phi$  angles (antennas within a closed PEC box).

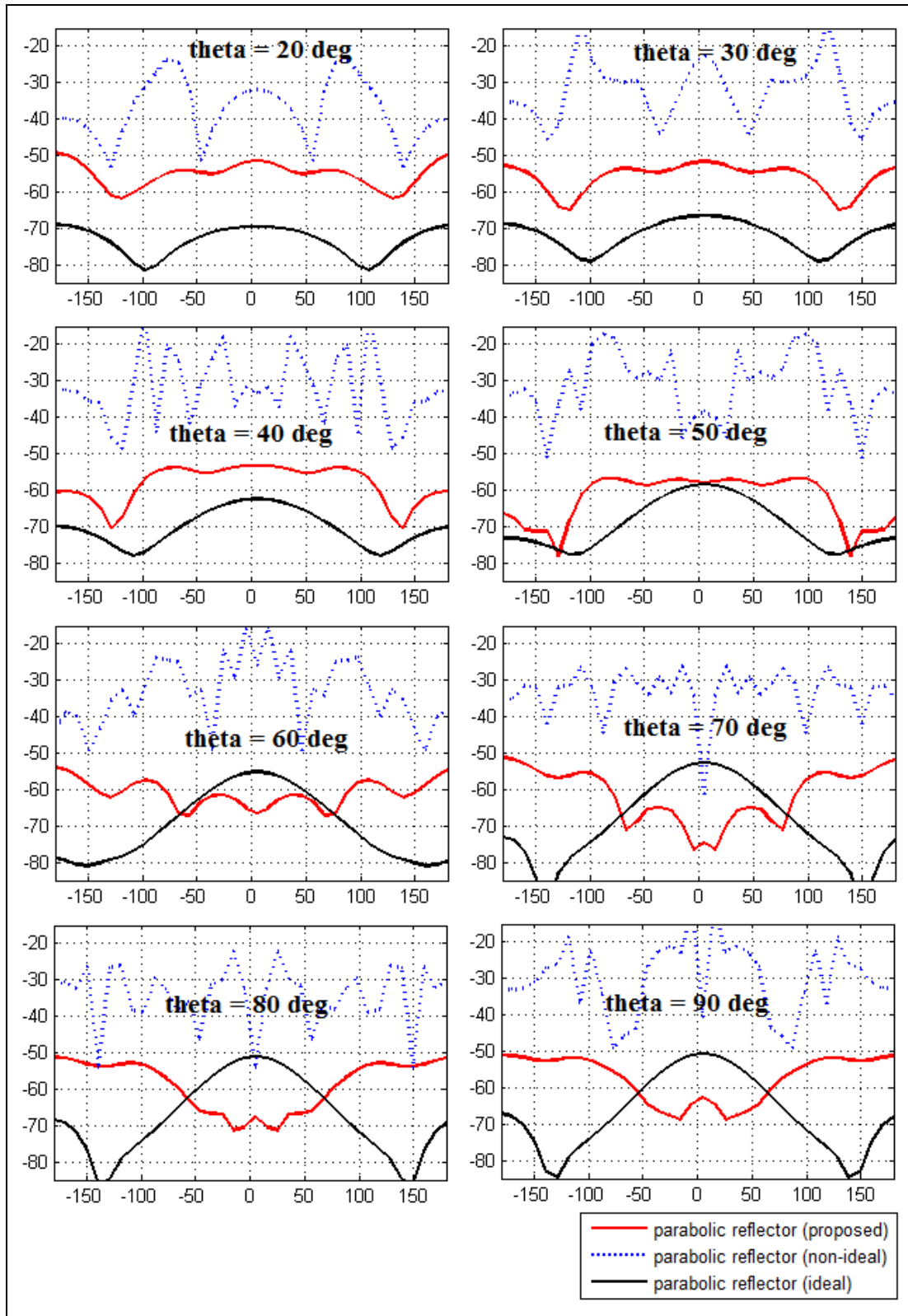


**Figure 5.47** Comparison of the reconstructed patterns for the parabolic reflector antenna along different theta angles (antennas within a closed PEC box).

#### *5.4.5 Example V: Six Dielectric Plates Forming a Closed Contour*

The previous four examples have used PEC plates to model plates of a room, but this is not realistic in a real measurement. The idea of using the PEC plates is to enhance the environmental effects and make it easier to be observed. On the other hand, that greatly increases the difficulty of the reconstruction problem, since the reflection and diffraction components are strong. Actually, they are too strong that the current distribution of the AUT has also been much changed under those environment settings. This example models the environment as a room formed by six dielectric plates, which is much more realistic.

The simulation model of this example includes the AUT, the probe and six dielectric plates around the antennas, as shown in Figure 5.48. The antennas are inside the air box while the dielectric material starts from the plates and extends to the infinity. Therefore, the dielectric plates around the antennas will be infinite thick. This is a simplified model of a regular room where the plates are made of concrete blocks with a thickness of around 1 feet. The radiated fields from the AUT will reflect, diffract and refract on dielectric plates.

The dielectric box has a size of  $2\text{ m}$  by  $2\text{ m}$  by  $4\text{ m}$ , and the six plates separate the air and the dielectric material, which is concrete ( $\epsilon_r = 2.2$ ,  $\tan \delta = 0.011$ ). The AUT and the probe are  $2.5$  meters away from each other and are  $1$  meter away from plates around.

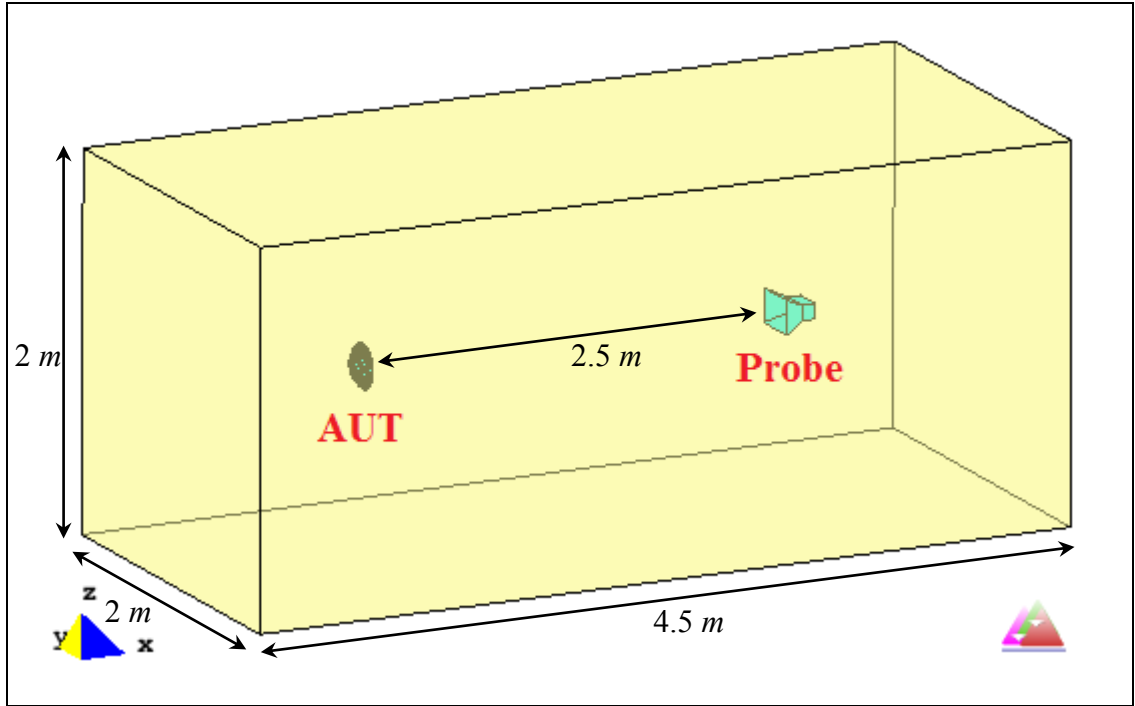


**Figure 5.48** Model of the measurement system within a closed box with 6 dielectric plates.

For this model, the differences between the ideal and non-ideal (under the presence of dielectric plates) radiation patterns are much smaller. We will not show the 3D plot here since they look very close in 3D plot, but we will show comparison of the patterns in 2D cut plots.

First let's check the current distribution on the feed dipole of the yagi antenna, which is shown in Figure 5.49. It shows that the current distribution on the feed dipole of the yagi is very slightly changed by the dielectric plates, which means the reflection and diffraction components are much smaller under this environment compared with previous examples. And we should expect this in the reconstructed results. Based on the experience of previous examples we expect that the reconstructed pattern should be closer to the ideal pattern.

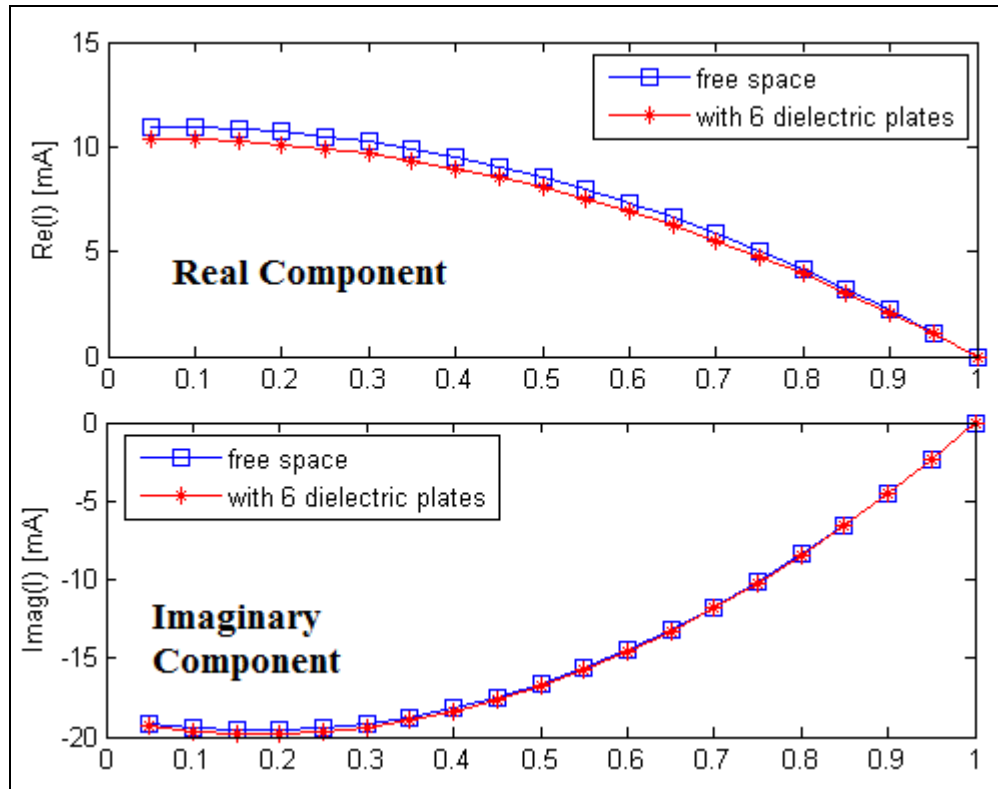


**Figure 5.49** Current distribution on the feed dipole of the yagi antenna when the test environment is a closed box with 6 dielectric plates.

We followed the procedures as described in Section 5.2 and reconstructed the patterns for the yagi antenna and the parabolic reflector antenna. To better display the differences between the ideal pattern, non-ideal pattern, and the reconstructed pattern, 2D cuts along different spatial angles are given in the following figures.

For the yagi antenna, 2D cuts along different phi angles and theta angles are shown in Figures 5.50 and 5.51, respectively. The reconstructed pattern is indicated by the red line while the ideal pattern is indicated by the black line. The blue dash line is for the non-ideal pattern. In Figure 5.50 the  $x$ -axis is the elevation angle  $\theta$ , the  $y$ -axis is the amplitude of  $S_{21}$  in dB scale. In Figure 5.51 the  $x$ -axis is the azimuth angle  $\phi$ , the  $y$ -axis is the amplitude of  $S_{21}$  in dB scale.

Similarly, for the pattern reconstruction of the parabolic reflector antenna, the 2D cuts along different phi angles and theta angles are shown in Figures 5.52 and 5.53, respectively.

The results for both the yagi and the parabolic reflector antenna show that the reconstructed patterns agree very well to the ideal patterns. The differences between the ideal patterns and the reconstructed patterns are mainly located at the region of  $\theta \in [0^\circ, 50^\circ]$ ,  $\theta \in [130^\circ, 180^\circ]$ ,  $\phi \in [-180^\circ, -100^\circ]$ , and  $\phi \in [100^\circ, 180^\circ]$ , which are the side lobes and back lobes.

This example also indicates that under a more realistic environment setting, when the current distribution of the AUT is not much affected by the test environment, the deconvolution method can achieve a very good reconstructed result. For previous four examples, those are the worst scenarios where PEC plates are used as the reflector. The PEC plates generate much more reflections and diffractions than the dielectric plates and affect the current distribution on the AUT a lot.

The previous 2D pattern reconstruction has been extended to 3D environments. The five examples shown above discussed the pattern reconstruction in different 3D environments. The reconstructed results can greatly mitigate the undesired reflections and approximate the ideal patterns. One major reason for the differences between the ideal patterns and the reconstructed patterns is due to the change of the current distribution on the AUT.

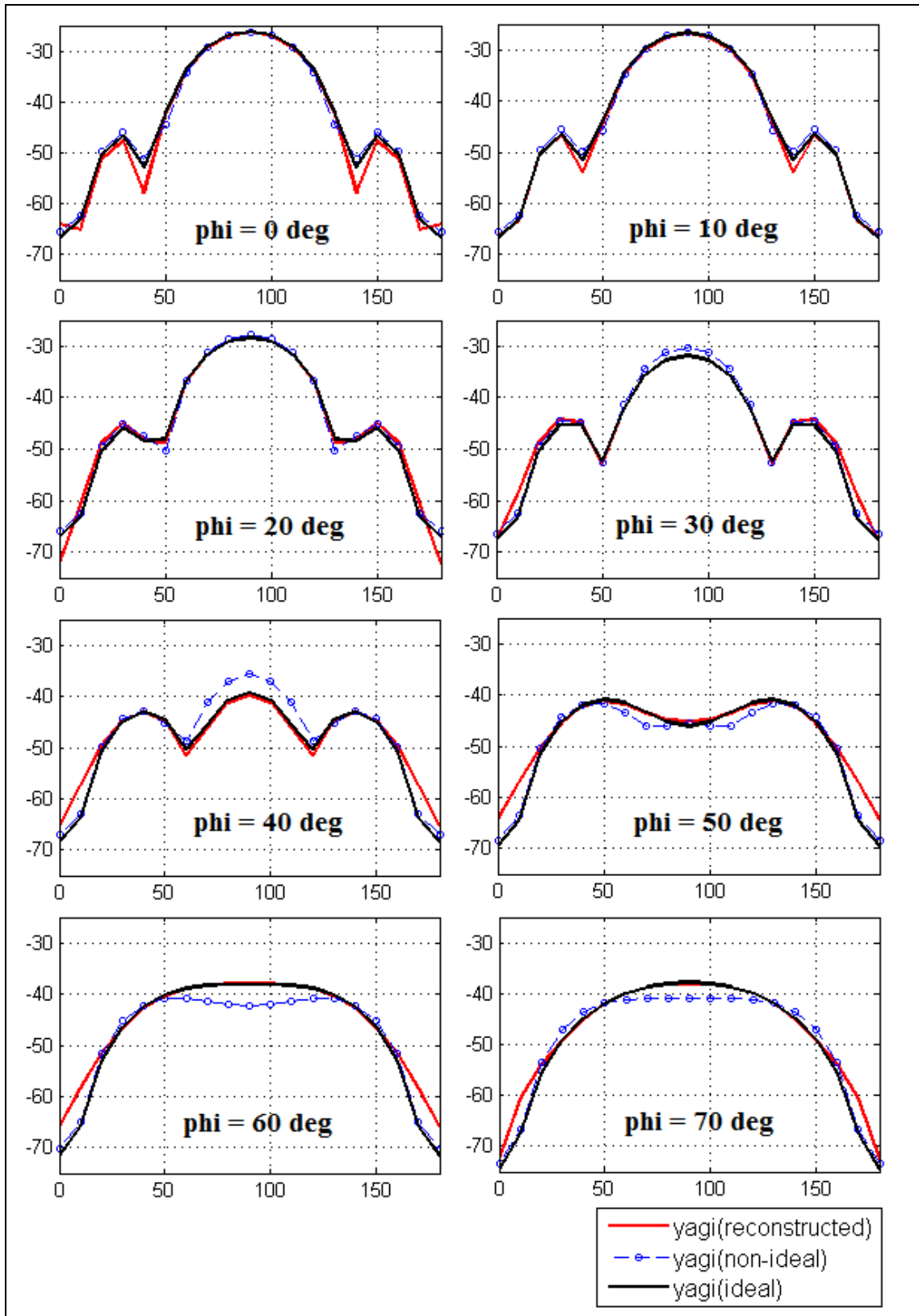


**Figure 5.50** Comparison of the patterns for the yagi antenna along different  $\phi$  angles when the test environment is a closed box with 6 dielectric plates.

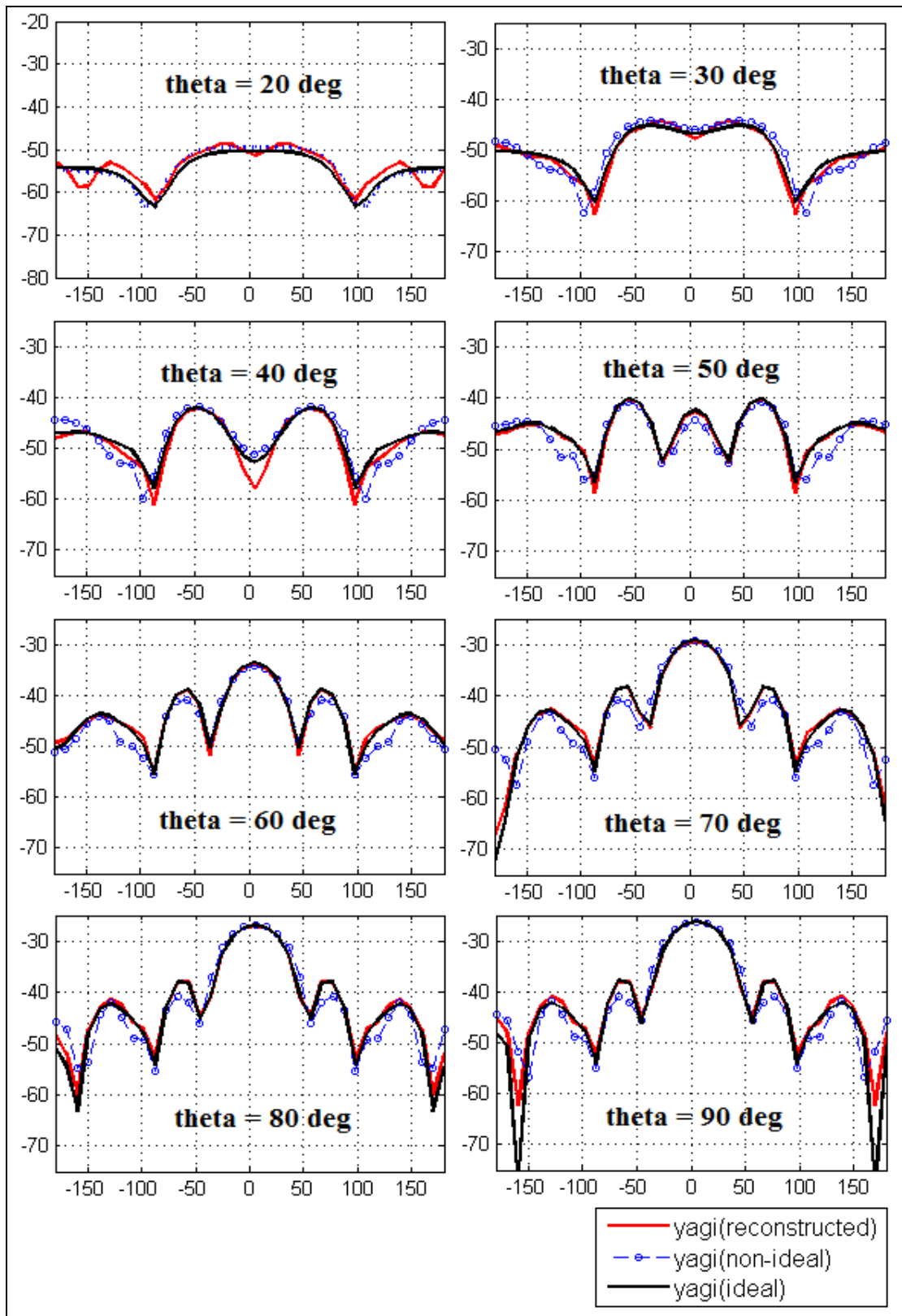


**Figure 5.51** Comparison of the patterns for the yagi antenna along different theta angles when the test environment is a closed box with 6 dielectric plates.

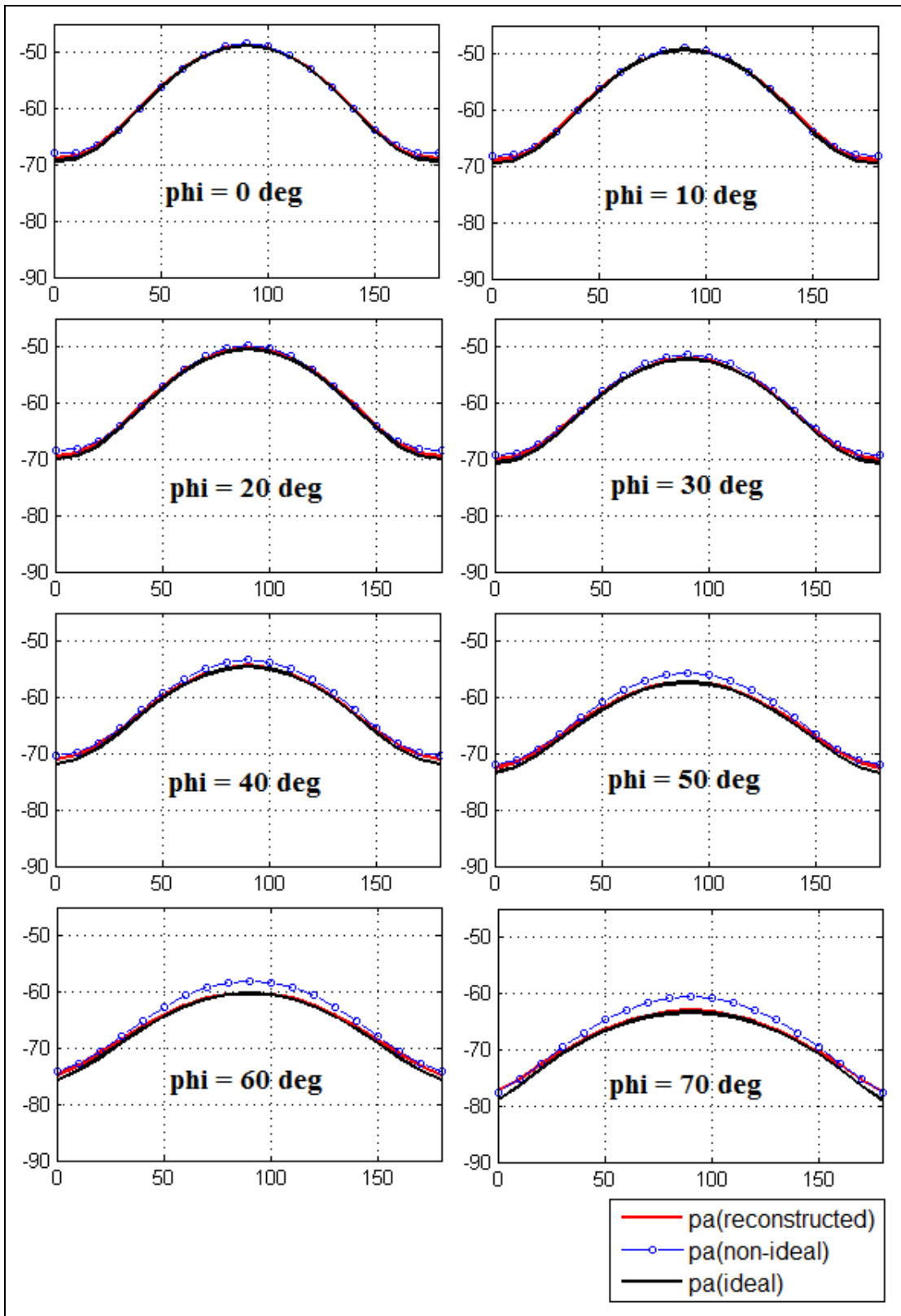


**Figure 5.52** Comparison of the patterns for the parabolic reflector antenna along different  $\phi$  angles when the test environment is a closed box with 6 dielectric plates.

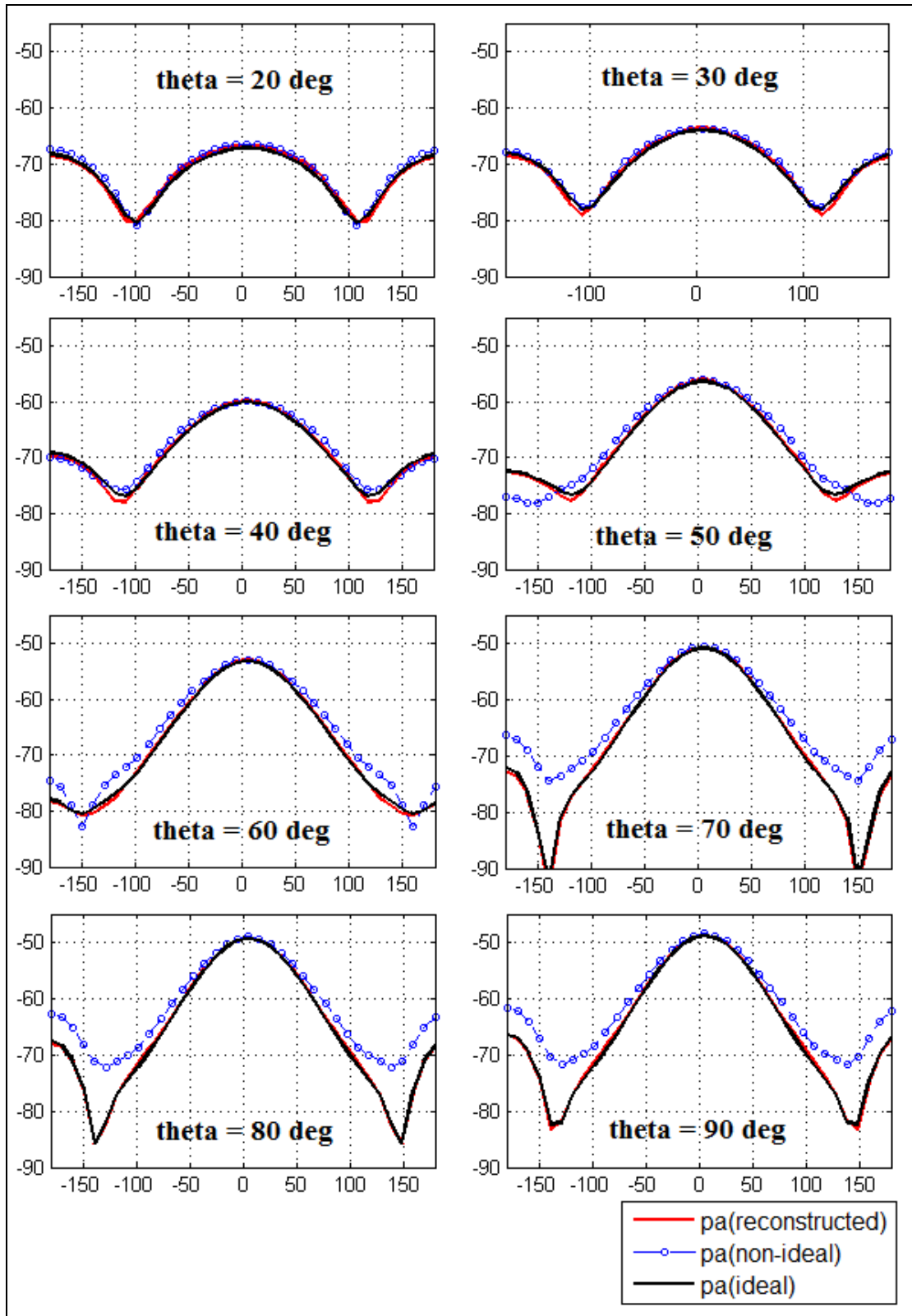


**Figure 5.53** Comparison of the patterns for the parabolic reflector antenna along different theta angles when the test environment is a closed box with 6 dielectric plates.

# Chapter 6

## Conclusion and Future Work

This work focuses on illustrating and extending a deconvolution algorithm to retrieve the free space far-field pattern of an AUT from its measured radiation pattern in a non-anechoic environment. Extensive numerical examples are given for illustration.

We model the environmental effects as an impulse response of the test environment in the spatial domain. And the measured non-ideal pattern under the environment is an angular convolution between the ideal pattern (free space far-field pattern) of the AUT and the environmental responses. Therefore, under any test environment, one can obtain the free space far-field pattern for an unknown antenna with two antenna measurements. One measurement is for the calibration of the environment using a reference antenna whose pattern is known, and the other is for the measurement of an AUT in the same test environment. This requires two assumptions that the environment is unchanged during measurements for two antennas and sizes of the reference antenna as well as the AUT need to be similar.

The proof of the concept and the derivation of the governing equations are given in Chapter 3 for the 2D situation. Then, numerical examples with different environmental settings and AUTs are presented to illustrate how the deconvolution method works. These examples show that through the deconvolution method, the reconstructed patterns of the AUTs are well approximated to the free space radiation patterns.

Further analysis is made in Chapter 4 to explore the limitations and effectiveness of the deconvolution method. Numerical examples indicate that the method is not limited to the sizes of the antennas or the frequencies under test, as long as the current distribution on the AUT is not much affected by the environments. However, the method does have a limitation to the choice of the probe antenna. The failure of the dipole antenna example shows that the probe needs to be a directional antenna. And the performance of the method is inversely proportional to the complexity of the environments. The complexity of the environments shows in two ways in our simplified models, the number of PEC objects and the width of PEC plates.

The deconvolution method is extended to three-dimensional environments in Chapter 5 to reconstruct the 3D radiation pattern for an AUT, with both azimuth angle and elevation angle considered. Numerical examples are given to evaluate the 3D pattern reconstruction under five different environmental settings. Those settings cover different 3D environments and present a full picture of how the deconvolution method retrieves the ideal pattern from the non-ideal pattern. Results indicate that with PEC plates as the reflector, the reconstructed patterns are roughly approximated to the ideal patterns, but are not as good as the results shown in 2D examples. And for the environment of a closed PEC box, the reconstruction will fail since there will be no far-field inside a closed PEC box. While for the example with dielectric plates as the reflector, reconstructed results are much improved and are very well approximated to the ideal pattern of an AUT. We find that one major reason for the differences between the ideal patterns and the reconstructed patterns is due to the change of the current distribution on the AUT. When PEC plates are used as the reflector, they cause much more reflections and diffractions than the dielectric

plates and affect the current distribution on the AUT a lot. The current distribution change directly affects the radiation pattern of the AUT. However, an environment with dielectric plates is more realistic than an environment with large PEC plates. Therefore, we can expect a better reconstructed result from the deconvolution method under realistic environment settings.

In this work, we didn't consider interference signals (i.e., the radio noise), which is not practical in the real measurements. One important function of the anechoic chamber is to shield the measurements from the outside signals and provide an accurate result of the radiation pattern, especially for side lobes. However, the main goal of the deconvolution method is not to provide a reconstructed result as accurate as that measured in an anechoic chamber but to provide an approximated radiation pattern. Even we didn't consider the effect of the radio noise, the low level noise will not make a significant change to the reconstructed results according to the measurement results of man-made noise in VHF and UHF bands [41]-[42]. Therefore, it is reasonable to neglect the effect of interference signals.

So far, multiple numerical examples are presented to model the antenna radiation pattern measurement system and test the effectiveness of the deconvolution method. Those examples have shown the method can achieve a good approximation of the free space radiation pattern of the AUT from the data measured in non-anechoic environments. From those examples, we can observe some good features or advantages of the deconvolution method comparing to other pattern reconstruction methods in the literature. First, this method is independent of the bandwidth of an antenna and there is no

requirement of prior knowledge of the system or the test environment. Also, this method not only provides an approximated free space radiation pattern, but also provides the knowledge of the phase component of the pattern. And this phase knowledge is necessary for some applications.

Still, there are lots of work can be done to improve the deconvolution method:

1. Besides the measurement of a single AUT, the deconvolution method is also useful and promising for measurements of a large target, especially for antennas mounted on large platforms. For those large targets, indoor measurements inside an anechoic chamber are very difficult. The deconvolution method provides a way to obtain a quick and relative accurate estimation of the radiation pattern for such large targets. Due to the limited time and computational resources, we are currently unable to simulate the pattern reconstruction for antennas mounted on large platforms. This situation is suggested to be evaluated in real measurements.
2. The deconvolution method is not only useful in antenna pattern measurements in non-anechoic environments, but also could be applied in characterizing the reflection level of an anechoic chamber. It will be very interesting to model an anechoic chamber with absorbing materials and simulate the antenna measurements in such environment. And the deconvolution method can be used to extract the reflections and diffractions within the anechoic chamber.
3. As shown previously, we choose PEC plates and dielectric plates as the reflector. For realistic measurements in a large room, the radiated fields would reflect on wooden tables, concrete walls around the room, the floor, and the ceiling of the room. Therefore, a more realistic numerical simulation needs to add these realistic objects

into the model. And the reconstructed results would be more convincing.

4. So far, we have evaluated deconvolution method through numerical simulations. A better way is to test the method in real measurements. This requires one to choose an environment and carry out a real antenna pattern measurement. Then, follow procedures of the deconvolution method to measure the received response at the probe and extract the environmental effects from measured result of a reference antenna. And use it in a subsequent measurement for an AUT to extract its ideal pattern, and compare the reconstructed pattern with that measured in an anechoic chamber.

We hope the deconvolution method could be applied into the real antenna measurements, and can be used to save the expenses on building an anechoic chamber. So the antenna pattern measurement could be more affordable and flexible.

# Appendix A

## Data Mapping Using the Conversion between the Spherical Coordinate System and the Cartesian Coordinate System

As mentioned in Section 5.3, the FFT transforms the convolution of 2D periodic sequences into the multiplication of their corresponding discrete Fourier series. And the sequences that we select should be a period of the 2D periodic sequences. For example, if we take a step of  $10^\circ$  along the azimuth angle  $\phi$ , the data at  $\phi = -180^\circ, -170^\circ, \dots, 160^\circ, 170^\circ$  should be a period of the periodic sequences, as shown below:

$$\phi = -\infty, \dots, -180^\circ, -170^\circ, \dots, 170^\circ, 180^\circ, 190^\circ, \dots, 530^\circ, \dots, +\infty$$



Also notice that the end point of one period should be continuous to the start point of the next period, like the transition from  $\phi = 170^\circ$  to  $180^\circ$ . These two properties can be visualized as: we rotate an object along the azimuth angle and the object will return to its original starting place after rotating one loop and then it starts to rotate the next loop. This is the case for our 1D pattern reconstruction in Chapter 3.

These two properties also apply to the 2D situation. For example, if you change both  $\phi$  and  $\theta$  in a step of  $10^\circ$ , we form a 2D matrix by listing the  $(\theta, \phi)$  in a plane, as shown below ( $\theta$  varies along the column and  $\phi$  varies along the row):

$$\begin{bmatrix} (0^\circ, -180^\circ) & (0^\circ, -170^\circ) & \dots & (0^\circ, 170^\circ) \\ (10^\circ, -180^\circ) & (10^\circ, -170^\circ) & \dots & (10^\circ, 170^\circ) \\ \vdots & \vdots & \ddots & \vdots \\ (170^\circ, -180^\circ) & (170^\circ, -170^\circ) & \dots & (170^\circ, 170^\circ) \\ (180^\circ, -180^\circ) & (180^\circ, -170^\circ) & \dots & (180^\circ, 170^\circ) \end{bmatrix}_{19 \times 36}^{\theta \times \phi}$$

We would think this is also a period of the 2D periodic sequences, and it should be continuously transited to the next period along either  $\phi$  or  $\theta$ . However, it turns out to be not true.

If we duplicate this matrix and pad it at its side as shown below, we see that the two adjacent data  $(\theta, \phi)$  of  $(180^\circ, -180^\circ)$  and  $(0^\circ, -180^\circ)$  should have a step difference of  $10^\circ$ , which is not. Therefore, the original 2D matrix cannot satisfy our requirement.

$$\begin{array}{c} \begin{bmatrix} (0^\circ, -180^\circ) & (0^\circ, -170^\circ) & \dots & (0^\circ, 170^\circ) \\ (10^\circ, -180^\circ) & (10^\circ, -170^\circ) & \dots & (10^\circ, 170^\circ) \\ \vdots & \vdots & \ddots & \vdots \\ (170^\circ, -180^\circ) & (170^\circ, -170^\circ) & \dots & (170^\circ, 170^\circ) \\ (180^\circ, -180^\circ) & (180^\circ, -170^\circ) & \dots & (180^\circ, 170^\circ) \end{bmatrix}_{19 \times 36} \\ \hline \begin{bmatrix} (0^\circ, -180^\circ) & (0^\circ, -170^\circ) & \dots & (0^\circ, 170^\circ) \\ (10^\circ, -180^\circ) & (10^\circ, -170^\circ) & \dots & (10^\circ, 170^\circ) \\ \vdots & \vdots & \ddots & \vdots \\ (170^\circ, -180^\circ) & (170^\circ, -170^\circ) & \dots & (170^\circ, 170^\circ) \\ (180^\circ, -180^\circ) & (180^\circ, -170^\circ) & \dots & (180^\circ, 170^\circ) \end{bmatrix}_{19 \times 36} \end{array}$$

However, if we complete the data matrix by padding the data in the elevation angle  $\theta$ , specifically adding  $\theta$  between  $[180^\circ, 360^\circ)$ , we can guarantee that the above two

properties can be satisfied. Since there is no explicit definition for the data set of  $\theta$  between  $[180^\circ, 360^\circ]$  in the normal spherical coordinate system, we need to derive that data by using the conversion between the Spherical coordinate system and the Cartesian coordinate system, as shown below:

$$\begin{cases} x = r \sin \theta \cos \phi \\ y = r \sin \theta \sin \phi \\ z = r \cos \theta \end{cases} \quad (\text{A.1})$$

One can verify that the data in the region  $\theta \in [0^\circ, 180^\circ]$  and  $\phi \in [-180^\circ, 180^\circ]$  can be fully mapped to the data in the region  $\theta \in [180^\circ, 360^\circ]$  and  $\phi \in [-180^\circ, 180^\circ]$  by using the angular conversion (A.2):

$$(r, \theta, \phi) = (r, 2\pi - \theta, \phi \pm \pi) \quad (\text{A.2})$$

It is easy to see the Cartesian coordinates generated by the two sides of the (A.2) are the same. Therefore, the data set of  $\theta$  between  $[180^\circ, 360^\circ]$  can be derived. Then, both  $\theta$  and  $\phi$  change its value within  $2\pi$  range and form a periodic 2D matrix.

This data mapping process is shown in Figure A.1. The lower layer data blocks are the original data when  $\theta$  is between  $[0^\circ, 180^\circ]$  while the upper layer data blocks are the mapped data when  $\theta$  is between  $[180^\circ, 360^\circ]$ . The data blocks with the same color indicate the mapping location for the spatial angle  $(\theta, \phi)$ . And the dashed lines show two examples of data mapping using (A.2), i.e., the spatial angle  $(\theta, \phi)$  at  $(-120^\circ, 120^\circ)$  should be mapped to  $(60^\circ, 240^\circ)$ ; while the angle at  $(150^\circ, 60^\circ)$  should be mapped to  $(-30^\circ, 300^\circ)$ .

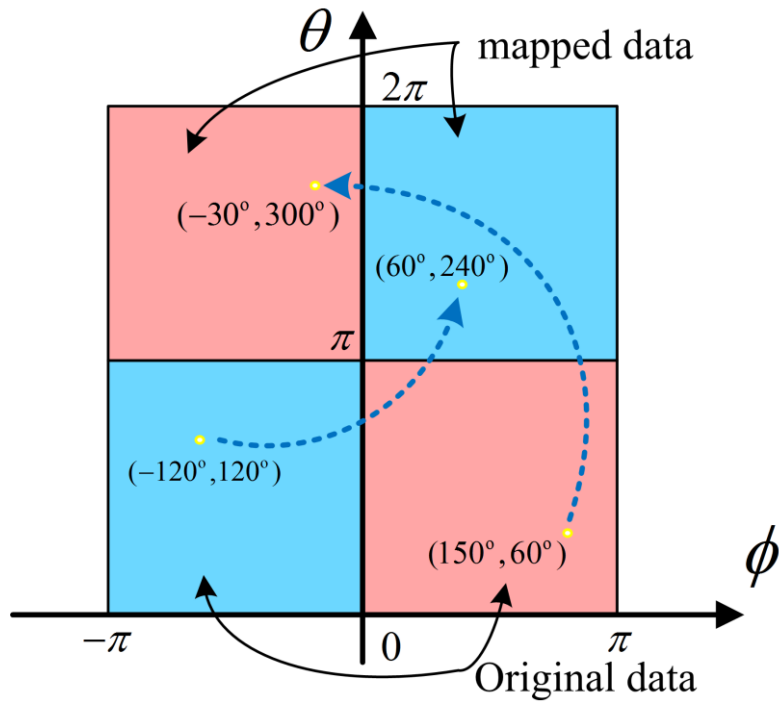


**Figure A.1** Data mapping illustration.

## Appendix B

### A Side Note of the 2D-FFT during the Data Processing

As mentioned in Section 5.3, we need to perform the 2D-FFT on matrices and transform the angular convolution into the multiplication in the other domain. According to (5.12), the ideal pattern of the AUT can be calculated as below:

$$\text{fft}_2(P_{\text{ideal-AUT}}(\theta, \phi, f)) = \frac{\text{fft}_2(P_{\text{non-ideal-AUT}}(\theta, \phi, f)) \cdot \text{fft}_2(P_{\text{ideal-Ref}}(\theta, \phi, f))}{\text{fft}_2(P_{\text{non-ideal-Ref}}(\theta, \phi, f))} \quad (\text{B.1})$$

and the 2D-FFT is defined as:

$$X(m, n) = \sum_{q=1}^M \sum_{r=1}^N x(q, r) W_M^{(m-1)(q-1)} W_N^{(n-1)(r-1)} \quad (m = 1, \dots, M; n = 1, \dots, N) \quad (\text{B.2})$$
$$W_N = e^{-j(2\pi/N)}$$

where  $M$  and  $N$  are the dimensions of the matrix, and  $X(m, n)$  denotes the DFT of  $x(q, r)$ . In our examples, we take a step of  $10^\circ$  in the spatial domain, and the matrix will be padded to be a 36 by 36 square matrix (as shown in Appendix A), i.e.,  $M = N = 36$ . And both  $x(q, r)$  and  $X(m, n)$  should be a matrix with the dimension of 36 by 36.

When the environment is symmetrical along the plane with the elevation angle  $\theta = 90^\circ$ , and the dimension  $N$  is even, it can be proved that some elements of  $X(m, n)$  should be zero when  $m$  is even and  $n$  is odd. The proof is shown as below.

If we set  $m = 2k$ ,  $n = 2t - 1$ , ( $k, t = 1, 2, \dots, N/2$ ), then  $m$  is even and  $n$  is odd. So we have:

$$X(2k, 2t - 1) = \sum_{q=1}^N \sum_{r=1}^N x(q, r) W_N^{(2k-1)(q-1)} W_N^{(2t-2)(r-1)} \quad (k, t = 1, \dots, N/2) \quad (\text{B.3})$$

By separating the summation operator, we have:

$$X(2k, 2t - 1) = \sum_{q=1}^N W_N^{(2k-1)(q-1)} \sum_{r=1}^N x(q, r) W_N^{(2t-2)(r-1)} \quad (\text{B.4})$$

We can separate (B.4) as:

$$X(2k, 2t - 1) = \sum_{q=1}^N W_N^{(2k-1)(q-1)} C_q \quad (\text{B.5})$$

$$C_q = \sum_{r=1}^N x(q, r) W_N^{(2t-2)(r-1)} \quad (\text{B.6})$$

For a fixed value of  $q$ , (B.6) is a weighted summation of row elements at row  $q$ , which can be viewed as a constant. Also, the terms  $W_N^k = e^{-j(2\pi/N)k}$  are the complex roots of the unit circle, as shown in Figure B.1.

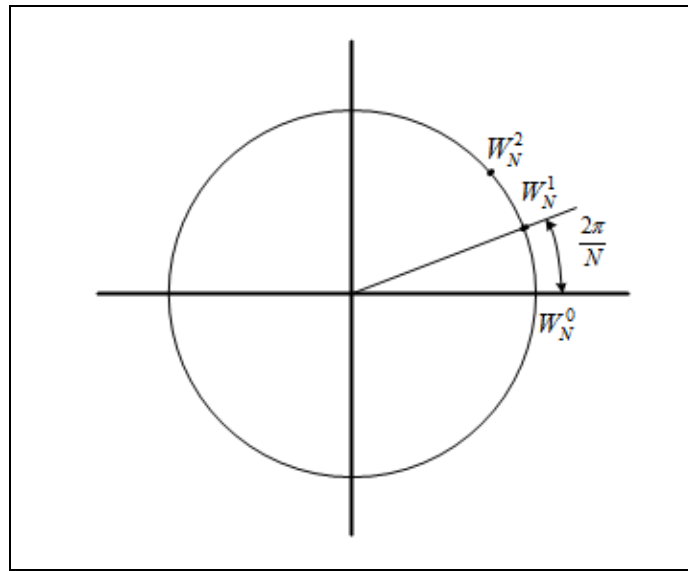


**Figure B.1** Points of complex roots at the unit circle.

If  $C_q$  have the value of 1, we will have  $X(2k, 2t-1)=0$  from the Summation lemma:

$$\sum_{q=1}^N W_N^{-(k-1)(q-1)} = 0, \quad (k = 1, 2, \dots, N) \quad (\text{B.7})$$

Due to the symmetrical environment setting, for any  $r = 1, 2, \dots, N$ , we have:

$$x(1, r) = x(19, r), x(2, r) = x(18, r), \dots, x(9, r) = x(11, r) \quad (\text{B.8})$$

Therefore,  $C_q$  have the value:

$$\text{at the upper unit circle: } C_1 = C_{19}, C_2 = C_{18}, \dots, C_9 = C_{11} \quad (\text{B.9})$$

$$\text{at the lower unit circle: } C_{20} = C_{36}, \dots, C_{27} = C_{29} \quad (\text{B.10})$$

$$C_{10} \text{ and } C_{28} \text{ are at the positive axis and negative axis, respectively} \quad (\text{B.11})$$

And (B.5) can be expanded as the following summation of 8 terms in 4 lines:

$$X(2k, 2t-1) = \text{sum} \left\{ \begin{array}{l} \sum_{q=2}^9 W_N^{(2k-1)(q-1)} C_q + \sum_{q=11}^{18} W_N^{(2k-1)(q-1)} C_q \\ W_N^{(2k-1)(1-1)} C_1 + W_N^{(2k-1)(19-1)} C_{19} \\ W_N^{(2k-1)(10-1)} C_{10} + W_N^{(2k-1)(28-1)} C_{28} \\ \sum_{q=20}^{27} W_N^{(2k-1)(q-1)} C_q + \sum_{q=29}^{36} W_N^{(2k-1)(q-1)} C_q \end{array} \right. \quad (\text{B.12})$$

The 4 terms in the center cancel out to be zero; while the first line and the 4<sup>th</sup> line also cancel out to be zero. Therefore  $X(2k, 2t-1)$  will becomes zero value.

Thus  $\text{fft}_2(P_{\text{ideal-AUT}}(\theta, \phi, f))$  in (B.1) will be  $0 \cdot (0/0)$  value, which should be zero.

But N/A value was generated in MATLAB due to the numerical error. To conduct the 2D-IFFT of the matrix, we manually set those N/A values to be zero, which they should be.

# Bibliography

- [1] C.A. Balanis, *Antenna Theory: Analysis and Design, 3rd Edition*. John Wiley & Sons, Inc., New York, 2005.
- [2] P. W. Arnold, "The slant antenna range," *IEEE Trans. Antennas Propagat.*, Vol. AP-14, No. 5, pp. 658-659, September 1966.
- [3] R. C. Johnson and R. J. Poinsett, *Compact antenna range techniques*, Technical Report, 1966.
- [4] E. B. Joy, W. M. Leach, Jr., G. P. Rodrigue, "Applications of probe-compensated near-field measurements," *IEEE Trans. Antennas Propagat.*, Vol. 26, No. 3, pp. 379-389, May 1978.
- [5] W.L. Stutzman, and G.A. Thiele, *Antenna Theory and Design, 2nd Edition*, John Wiley & Sons, New York, 1998.
- [6] V. Viikari, J. Mallat, J. Ala-Laurinaho, et al., "New pattern correction techniques for submm-wave CATRs," *Proceedings of The European Conference on Antennas and Propagat.(EuCAP)*, 2006.
- [7] D. N. Black, E. B. Joy, M. G. Guler, and R. E. Wilson, "Range field compensation," in *Proc. Antenna Measurement Techniques Assoc. Symp.*, pp. 3B-19 to 3B-24, 1991.
- [8] D.N. Black and E.B. Joy, "Test zone field compensation," *IEEE Trans. on Antennas and Propagation*, Vol. 43, No.4, pp. 362-368, 1995.
- [9] J. T. Toivanen, T. A. Laitinen, S. Pivnenko, and L. Nyberg, "Calibration of multi-probe antenna measurement system using test zone field compensation," *3rd European Conference on Antennas and Propagation (EuCAP'09)*, Berlin, Germany, pp. 2916-2920, 2009.
- [10] J. T. Toivanen, T. A. Laitinen, and P. Vainikainen, "Modified Test Zone Field Compensation for Small Antenna Measurements," *IEEE Trans. on Antennas and Propagation*, Vol. 58, No. 11, pp. 3471-3479, 2010.

- [11] R. Pogorzelski, "Extended Probe Instrument Calibration (EPIC) for Accurate Spherical Near-Field Antenna Measurements," *IEEE Trans. on Antennas and Propagation*, Vol. 57, No. 10, pp. 3366-3371, 2009.
- [12] R. Pogorzelski, "Experimental Demonstration of the Extended Probe Instrument Calibration (EPIC) Technique," *IEEE Trans. on Antennas and Propagation*, Vol. 58, No. 6, pp. 2093-2097, 2010.
- [13] S. Raz, R. Kastner, "Pattern reconstruction from distorted incident wave measurements", *Antennas and Propagation Society International Symposium*, vol.14, pp.280, Oct. 1976
- [14] J. C. Bennet and A. Griziotis, "Removal of environmental effects from antenna radiation patterns by deconvolution processing", *Proceedings of the IEE Conference*, Pub. 219, Pt. 1, pp. 224–228, 1983
- [15] P. L. Garcia Muller, J. L. Cano, and R. Torres, "A deconvolution method for correcting antenna measurement errors in compact antenna test ranges," *Proceedings of the 17th Annual Antenna Measurement Techniques Association (AMTA) Meeting & Symposium*, USA, pp. 509-514, Nov. 1995
- [16] Koh Jinhwan, A. De, T. K. Sarkar, Moon Hongsik, Zhao Weixin, M. Salazar-Palma, "Free Space Radiation Pattern Reconstruction from Non-Anechoic Measurements Using an Impulse Response of the Environment," *IEEE Trans. on Antennas and Propagation*, Vol. 60, No. 2, pp. 821-831, Feb. 2012.
- [17] S. Loredó, M. R. Pino, F. L.-Heras, and T. K. Sarkar, "Echo Identification and Cancellation Techniques for Antenna Measurement in Non-Anechoic Test Sites," *IEEE Antennas & Propagation Magazine*, Vol. 46, No. 1, pp.100-107, Feb. 2004.
- [18] S. Loredó, G. Leon, S. Zapatero, F. Las-Heras, "Measurement of Low-Gain Antennas in Non-Anechoic Test Sites through Wideband Channel Characterization and Echo Cancellation," *IEEE Antennas and Propagat. Magazine*, Vol. 51, No. 1, pp. 128-135, Feb. 2009.
- [19] A. V. Kalinin, "Anechoic chamber wideband antenna measurements," *IEEE Aerospace and Electronic Systems Magazine*, Vol. 21, No. 1, pp. 21- 24, Jan. 2006.

- [20] M. E. Sr. Hines, H. E. Stinehelfer, "Time-Domain Oscillographic Microwave Network Analysis Using Frequency-Domain Data," *IEEE Trans. on Microwave Theory and Techniques*, Vol. 22, No. 3, pp. 276-282, Mar 1974.
- [21] J. Marti-Canales, L. P. Ligthart, "Modeling and pattern error correction of time domain far-field antenna measurements," *IEE Proceedings on Microwaves, Antennas Propagation*, Vol. 148, No. 2, pp.133-136, Apr. 2001.
- [22] B. Fourestie, Z. Altman, and M. Kanda, "Anechoic Chamber Evaluation using the Matrix Pencil Method," *IEEE Trans. on Electromagnetic Compatibility*, Vol. 41, No. 3, pp.169–174, Aug. 1999.
- [23] B. Fourestie, Z. Altman, J. Wiart, and A. Azoulay, "On the Use of the Matrix-Pencil Method to Correlate Measurements at Different Test Sites," *IEEE Trans. on Antennas and Propagation*, Vol. 47, No. 10, pp. 1569-1573, Oct. 1999.
- [24] B. Fourestie, Z. Altman, and M. Kanda, "Efficient detection of resonances in anechoic chambers using the matrix pencil method," *IEEE Trans. on Electromagnetic Compatibility*, Vol. 42, No. 1, pp.1-5, Feb 2000.
- [25] B. Fourestie and Z. Altman, "Gabor schemes for analyzing antenna measurements," *IEEE Trans. on Antennas and Propagation*, Vol. 49, No. 9, pp.1245-1253, Sept. 2001.
- [26] P. S. H. Leather and D. Parson, "Equalization for Antenna-Pattern Measurements: Established Technique - New Application," *IEEE Antennas & Propagation Magazine*, Vol. 45, No. 2, pp.154-161, April 2003.
- [27] P. S. H. Leather, D. Parsons, J. Romeu, S. Blanch, A. Aguasca, "Correlation techniques applied to antenna pattern measurement," *Electronics Letters* , Vol. 40, No. 10, pp. 572-574, May 2004.
- [28] P. S. H. Leather, J. D. Parsons, "Plane wave spectra, test-zone fields and simulation of antenna-pattern measurements," *Electronics Letters*, Vol. 39, No. 25, pp. 1780-1782, Dec. 2003.
- [29] P. S. H. Leather, D. Parsons, "Improved Antenna Pattern Measurements using Equalization," *IEE Antennas and Propagation Newsletter*, pp. 4-7, Oct. 2002.
- [30] P. S. H. Leather, D. Parsons, "Equalization: a technique to improve the accuracy of antenna radiation pattern measurements," Vol. 1, pp. 102-106, *ICAP 2003*.

- [31] P. S. H. Leather, D. Parsons, J. Romeu, "Signal processing techniques improve antenna pattern measurement," pp. 97-100, *IEE AMS 2004*.
- [32] J. Appel-Hansen, "Reflectivity level of radio anechoic chambers," *IEEE Trans. on Antennas and Propagation*, Vol. 21, No. 4, pp. 490-498, Jul. 1973.
- [33] W. D. Burnside, I. J. Gupta, "A method to reduce stray signal errors in antenna pattern measurements," *IEEE Trans. on Antennas and Propagation*, Vol. 42, No. 3, pp. 399-405, Mar. 1994.
- [34] M. D. Migliore, "Filtering environmental reflections in far-field antenna measurement in semi-anechoic chambers by an adaptive pattern strategy," *IEEE Trans. on Antennas and Propagation*, Vol. 52, No. 4, pp. 1112-1115, April 2004.
- [35] V. Viikari, J. Mallat, J. Ala-Laurinaho, et al., "A feed scanning based APC technique for compact antenna test ranges," *IEEE Trans. on Antennas and Propagation*, Vol. 53, No. 10, pp. 3160-3165, Oct. 2005.
- [36] V. Viikari, J. Mallat, J. Ala-Laurinaho, et al., "A Frequency Shift Technique for Pattern Correction in Hologram-Based CATRs," *IEEE Trans. on Antennas and Propagation*, Vol. 54, No. 10, pp. 2963-2968, Oct. 2006.
- [37] V. Viikari, V.-M. Kolmonen, J. Salo, A. V. Raisanen, "Antenna Pattern Correction Technique Based on an Adaptive Array Algorithm," *IEEE Trans. on Antennas and Propagation*, Vol. 55, No. 8, pp. 2194-2199, Aug. 2007.
- [38] Yu Zhang, T. K. Sarkar, et al., *Higher Order Basis Based Integral Equation Solver (HOBBIES)*, John Wiley & Sons, NJ, 2012.
- [39] A. V. Oppenheim, A. S. Willsky, and I. T. Young, *Signals and Systems*, Prentice Hall, Englewood Cliffs, NJ, 1983.
- [40] A. V. Oppenheim, Ronald W. Schaffer, *Digital Signal Processing*, Prentice Hall, Englewood Cliffs, NJ, 1975.
- [41] R. Dalke, R. Achatz, Y. Lo, P. Papazian, and G. Hufford, "Measurement and analysis of man-made noise in VHF and UHF bands", *Wireless Communications Conference*, pp. 229-233, 1997.
- [42] Robert J. Achatz, Roger A. Dalke, "Man-Made Noise Power Measurements at VHF and UHF Frequencies", page 9 of NTIA Technical Report 02-390, National Telecommunications and Information Administration, December 2001.

# VITA

Weixin Zhao was born in Wuxi, China. He received the B.S degree in Electrical Engineering and Information Science from University of Science and Technology of China, Hefei, China, in 2007. He is currently working toward the Ph.D. degree in the Department of Electrical Engineering at Syracuse University, Syracuse, NY. He has been a Research Assistant at Syracuse University since 2007. His current research interests include antenna design and optimization.

## PUBLICATIONS

- [1] **Weixin Zhao**, “HOBBIES Optimizer and Its Applications”, Chapter 10 of *Higher Order Basis Based Integral Equation Solver (HOBBIES)*, JohnWiley&Sons, Hoboken, NJ, USA, 2012.
  
- [2] Jinhwan Koh, De, A., T. K. Sarkar, Hongsik Moon, **Weixin Zhao**, M. Salazar-Palma, “Free Space Radiation Pattern Reconstruction from Non-Anechoic Measurements Using an Impulse Response of the Environment,” *IEEE Transactions on Antennas and Propagation*, vol.60, no.2, pp.821-831, Feb. 2012
  
- [3] Ying Yan, **Wei-Xin Zhao**, Xun-Wang Zhao, Yu Zhang, and Chang-Hong Liang, “Parallel Computation of RCS of Electrically Large Platform with Coatings Modeled with NURBS Surfaces,” *International Journal of Antennas and Propagation*, vol. 2012, Article ID 348052, 10 pages, 2012

- [4] **Weixin Zhao**, HongSik Moon, T. K. Sarkar, “Retrieval of free space radiation pattern through non-anechoic data”, IEEE AP-S International Symposium, Chicago, USA, July, 2012
- [5] **Weixin Zhao**, De, A., Zicong Mei, Yu Zhang, T. K. Sarkar, “Design of a two-element folded-Yagi antenna with super-directivity”, IEEE AP-S International Symposium, Spokane, USA, July, 2011
- [6] Daniel García-Doñoro, **Weixin Zhao**, Yu Zhang, Tapan K. Sarkar, Luis Emilio García-Castillo and Magdalena Salazar-Palma, “Automatic Goal Oriented Optimization Using Parallel Higher Order Basis Based Integral Equation Solver”, European Conference on Antennas and Propagation, Roma, Italia, April 2011
- [7] Hong-Wei Zhang, Xun-Wang Zhao, Yu Zhang, Daniel García-Doñoro, **Weixin Zhao**, Chang-Hong Liang, “Analysis of a Large Scale Narrow-Wall Slotted Waveguide Array by Parallel MoM Out-of-Core Solver Using the Higher Order Basis Functions”, *Journal of Electromagnetic Waves and Applications*, Vol. 24, 1953–1965, 2010
- [8] **Weixin Zhao**, Daniel García-Doñoro, Yu Zhang, Xunwang Zhao, Tapan K. Sarkar, “Optimization of Radiation Pattern for Narrow-wall Slotted Waveguide Arrays Using HOBBIES”, International Symposium on Antennas and Propagation, Macao, China, November 2010
- [9] **Weixin Zhao**, Yu Zhang, Daniel García-Doñoro, Tapan K Sarkar, “Optimizing Narrow-wall Slotted Waveguide Arrays Using HOBBIES”, IEEE AP-S International Symposium, Toronto, Canada, July 2010
- [10] Daniel García-Doñoro, **Weixin Zhao**, Yu Zhang, Tapan K. Sarkar, Luis Emilio García Castillo, Magdalena Salazar Palma, “HOBBIES: A new electromagnetic simulator”, IEEE AP-S International Symposium, Toronto, Canada, July 2010

- [11] Daniel García-Doñoro, Yu Zhang, **Weixin Zhao**, Sarkar, T.K., Garcia-Castillo L.E., Salazar-Palma M., “HOBBIES: Higher Order Basis Based Integral Equation Solver with Automatic Goal Oriented Optimization”, Biennial IEEE Conference on Electromagnetic Field Computation, Chicago, May 2010
- [12] Daniel García-Doñoro, **Weixin Zhao**, Yu Zhang, Tapan K. Sarkar, Luis Emilio García Castillo, Magdalena Salazar Palma “HOBBIES: Electromagnetic Simulator Using GiD”, Conference on Advances and Applications of GiD, Barcelona, Spain, May 2010
- [13] **Weixin Zhao**, Arijit De, Daniel García-Doñoro, Yu Zhang, Tapan K Sarkar, “Antenna Optimization by Using NEWUOA”, IEEE AP-S International Symposium, Charleston, SC, June 2009
- [14] **Weixin Zhao**, Arijit De, Yu Zhang, Xiaomin Lin, Tapan K Sarkar, “Optimization of the End-fire Beam Pattern of Two-Dimensional Dipole Array”, IEEE AP-S International Symposium, San Diego, CA, July 2008